

GPS Reflectometry: Innovative Flood Monitoring at the Mekong Delta

vorgelegt von
Dipl. – Ing.
Jamila Beckheinrich
geb. in Tangerang

von der Fakultät VI - Planen Bauen Umwelt
der Technischen Universität Berlin
zur Erlangung des akademischen Grades

Doktorin der Ingenieurwissenschaften
- Dr.-Ing. -

genehmigte Dissertation

Promotionsausschuss:

| | |
|---------------|-------------------------|
| Vorsitzender: | Prof. Dr. Martin Kada |
| Gutachter: | Prof. Dr. Harald Schuh |
| Gutachter: | Prof. Dr. Steffen Schön |
| Gutachter: | Prof. Dr. Jens Wickert |

Tag der wissenschaftlichen Aussprache: 14. Juni 2016

Berlin 2016

Abstract:

Ground-based gauge instrumentation enables a high altimetric accuracy with high temporal resolution, but for a point location only. However, the number of gauge instruments is decreasing worldwide due to high maintenance costs. Global Positioning System-Reflectometry (GPS-R) reveals new perspectives for water level monitoring, since water surfaces show a high reflectivity for the GPS L-band signal. To test the possibility of using this innovative technique as a gauge instrument, two field campaigns were conducted in Vietnam, in February 2012 and March 2013 respectively, within the Water related Information system for the Sustainable Development Of the Mekong delta (WISDOM) project. As the use of phase observations has the potential to offer more accurate results, a new generation of GNSS Occultation, Reflectometry and Scatterometry (GORS) receiver has been successfully tested. Several reflection traces on the 150 m wide Can Tho River section have been recorded.

GPS-R phase-based altimetry implies continuous coherent phase observations. Due to the high sampling rate of the recorded data (200 Hz), a new automated algorithm, based on an ellipse fitting, is proposed to extract coherent phase observations. A hit rate of 82% could be reached. To test the geometrical impact of the antenna position on quality and quantity of the recorded coherent observations, two different antenna heights were used. For the first time, a detailed analysis of the recorded observations was performed and correction techniques were developed and applied. The results of the analysis show that the roughness of the water surface, caused primarily by ship traffic, had a major influence on loss of coherency. Additionally, the surroundings of the antennas and the river geometry restrict the use of reflection events within the interval of 3 to 29 deg. The analysis also showed the presence of multipath effects other than the water surface in the direct and the reflected signals, thus deteriorating the results. A phenomena that was already found in other research activities but not resolved. These multipath effects are mitigated and filtered based on an adjusted Empirical Mode Decomposition Method showing an improvement of several centimetres in the obtained water level results. The data also reveals the strong presence of cycle slips that distort the results, so that a preprocessing of the data is mandatory. A cycle slip detection strategy was therefore proposed. The challenge here, was to develop an algorithm based on GPS L1 observations only as they form 95% of the coherent phase observations. The detected cycle slips reveal a strong correlation with the surroundings of the antennas.

To extract water level changes, a Least-Squares method is used. As the accuracy of the extracted altimetric heights are strongly dependent on the accurate calculation of the geometrical excess paths between the direct and the reflected signal, effort was made to analyse the impact of systematic errors that influence the signals. For this purpose, different tropospheric correction strategies are compared, showing that atmospheric height layer and total zenith delay have to be precisely calculated. Additionally, the impact of the mostly ignored phase wind-up effects in GPS-R applications is underlined. As the recorded coherent phase observations are ambigu-

ous, an ambiguity fixing strategy for different satellite redundancy is proposed. Mostly, only L1 coherent phase observations from a single satellite are present. The most challenging problem in this case arises due to the lack of redundancy and slowly changing satellite geometry. In this case, water level heights within the set goal of decimetre level of accuracy can be calculated with an interval of 10 min. In the most desirable case, with the presence of more than one satellite tracked simultaneously, water level heights could be estimated at the centimetre level of accuracy.

To test the general applicability of the proposed algorithm, recorded observations during a measurement campaign, conducted 2014 within the Programme Marocco-Allemand de Recherche Scientifique (PMARS) project in Midelt, Morocco, were used. The obtained results within the decimetre level of accuracy, underline the applicability of the proposed algorithm to other ground and phase-based GPS-R altimetry applications.

All the obtained results are verified by comparing them with tide gauge measurements in the vicinity of the antennas.

Zusammenfassung:

Bevölkerungswachstum und Klimawandel haben tiefgreifende Veränderungen im Mekong Delta, einer natürlichen Ressource für Millionen von Einwohnern, verursacht. Eine dieser Veränderungen betrifft das zunehmende Auftreten extremer Hochwasserereignisse. Um das Leben der Menschen, insbesondere in den Küstenbereichen, während solcher Ereignisse zu schützen, ist es von großer Bedeutung, die Wasserstandshöhe in diesen Bereiche kontinuierlich zu überwachen. Standardmäßig kommen dafür Pegelmessstationen zum Einsatz. Sie ermöglichen die Bestimmung der Wasserstandshöhe mit großer Genauigkeit und hoher zeitlichen Auflösung. Ein Nachteil dieser Methode liegt in der lediglich punktuellen Verfügbarkeit von Messwerten. Aufgrund steigender Wartungskosten wird die Anzahl der Messstationen ferner kontinuierlicher verringert. Eine zukunftssträchtige Alternative stellt die Global Positioning System-Reflectometry (GPS-R) dar, da Wasseroberflächen eine hohe Reflektivität für GPS L-band Signale zeigen. Im Vergleich zur Codebeobachtungen, haben Phasenbeobachtungen das Potenzial, genauere Ergebnisse zu liefern, ihre Kohärenz und Kontinuität vorausgesetzt. Um die Möglichkeit des Einsatzes eines darauf beruhenden Verfahrens als Pegelmessinstrument zu prüfen, wurden zwei 14-tägige Messkampagnen, im Februar 2012 und im März 2013, im Mekong-Delta durchgeführt. Dabei kam eine neue Generation von GNSS Occultation, Reflectometry and Scatterometry (GORS)-Empfänger zum Einsatz. Mit ihnen konnten erfolgreich mehrere Reflexionsspuren auf dem 150 m breiten Can Tho River registriert werden.

Um eine Aussage über den Einfluss der Antennenposition auf Qualität und Quantität der registrierten kontinuierlichen, kohärenten Phasenbeobachtungen treffen zu können, wurden zwei unterschiedliche Antennenhöhen verwendet. Die Ergebnisse der Analyse zeigen, dass hauptsächlich die Rauheit der Wasseroberfläche, in erster Linie verursacht durch den Schiffsverkehr, für den Verlust der Kohärenz der Phasenbeobachtungen verantwortlich ist. Bedingt durch die hohe Datenrate, ein neuer Algorithmus zur automatisierte Extraktion von kohärente Phasenbeobachtungen wird vorgestellt. Dabei zeigt die Analyse der Ergebnisse eine Übereinstimmung von 82%. Die Analyse zeigte ferner die Präsenz von Mehrwegeeffekten, hervorgerufen durch Reflexionen an anderen Objekten als der Wasseroberfläche. Dieses bereits in anderen Veröffentlichungen festgestellte Phänomen stellt weiterhin eine offene Fragestellung dar. In der vorliegenden Arbeit werden diese Effekte durch die Anwendung einer adaptierten Version der empirischen Modenzerlegung Empirical Mode Decomposition reduziert, was zu einer deutlichen Erhöhung der Genauigkeit bei der Bestimmung der Wasserstandshöhen führt. Des Weiteren kann durch die Analyse der Daten das Vorhandensein einer Vielzahl von Phasensprüngen und deren hohes Maß an Korrelation mit der Umgebung der Antenne nachgewiesen werden. Da die Phasensprünge zu erheblichen Genauigkeitsverlusten führen, ist deren Detektion von großer Bedeutung. Die Herausforderung im Rahmen dieser Arbeit besteht dabei in der Entwicklung eines dafür geeigneten Algorithmus, der allein auf GPS L1 Beobachtungen basiert, da diese 95% der kohärente Phasenbeobachtungen ausmachen.

Um den Höhenunterschied zwischen Empfänger und Wasseroberfläche zu bestimmen, wird eine Ausgleichsrechnung nach der Methode der kleinsten Quadrate durchgeführt. Da die Genauigkeit des geschätzten Höhenunterschieds von der Genauigkeit der berechnete Entfernungsdifferenz zwischen dem direkten und dem reflektierten Signal abhängig ist, muss der Einfluss von systematischen Fehlern, die die Signale beeinflussen, minimiert werden. Für diesen Zweck, werden zum einen verschiedene Strategien für die Korrektur des durch die Troposphäre verursachten Fehlers verglichen, wobei gezeigt wird, dass atmosphärische Höhengschicht und die Gesamtzenitverzögerung genau berechnet werden müssen. Zum anderen werden die Einflüsse des Phase Wind-up sowie von Antennenphasenzentrumsvariationen und -offset analysiert und entsprechende Korrekturverfahren vorgestellt. Für eine erfolgreiche Bestimmung der Wasserstandshöhe ist neben der Korrektur systematischer Fehler die korrekte Festsetzung der Mehrdeutigkeiten in den Phasenbeobachtungen erforderlich. Die Besonderheit bei der Lösung dieser Aufgabe besteht im Rahmen dieser Arbeit darin, dass größtenteils nur L1 Phasenbeobachtungen von jeweils einem einzelnen Satelliten zur Verfügung steht. Die Herausforderung ergibt sich in diesem Fall aus der fehlenden Redundanz an Beobachtungen, sodass eine Auflösung der Mehrdeutigkeiten allein auf Basis der sich langsam ändernden Geometrie der Satelliten Konstellation realisiert werden muss.

Als Ergebnis dieser Arbeit kann festgehalten werden, dass unter diesen Voraussetzungen die Bestimmung der Wasserstandhöhen mit einer Auflösung von 10 Minuten und einer Genauigkeit im dm-Bereich möglich ist. Es konnte ferner gezeigt werden, dass bei gleichzeitigem Vorliegen von Daten mehrerer Satelliten Genauigkeiten im cm-Bereich erzielt werden können. Während die größtenteils nicht vorhandene Redundanz den Hauptgrund für die eingeschränkte Genauigkeit darstellt, liegt dieser für die fehlende Kontinuität in dem häufig auftretenden Verlust der Kohärenz der Phasenbeobachtungen.

Darüber hinaus, wurde die Methode auf Daten einer in 2014 durchgeführte Messung in Midelt, Marokko, angewandt, um die allgemeine Anwendbarkeit des entwickelten Algorithmus zu überprüfen. Die dabei erreichten Genauigkeiten bei der Wasserstandmessung im dm-Bereich, zeigen die Anwendbarkeit des entwickelten Algorithmus auf andere phasen- und grundbasierte GPS-R Anwendungen.

Acknowledgments:

This dissertation was made possible by Prof. Jens Wickert and Prof. Harald Schuh. I thank them for giving me this opportunity and their unconditional support. The daily supervision was taken care by Prof. Steffen Schön. I am grateful for his trust, support and great engagement. Without his help, this work would not have been possible. Financial support for this study was provided by the Federal Ministry of Education and Research (BMBF) and by the GFZ. This support is greatly appreciated. I would like to thank Dr. Georg Beyerle for his great work on the GORS receiver hard- and software, his genius ideas, patience and fruitful discussions without which this work would not exist. My special thanks also goes to Angelika Hirrle, for her support, the fruitful discussions and for reading and commenting the drafts of the doctoral thesis. I thank Dr. Maximilian Semmling for his support especially at the beginning of this thesis and for his great help preparing and testing all the conducted experiments. My thank goes also to Dr. Heiko Apel, Marcel Ludwig and Dr. Markus Ramatschi for their technical and logistical support by preparing all the conducted experiments. I thank Dr. Florian Zus for the very helpful discussions and making his ray-tracing based tropospheric correction model available for this thesis. Within this context, I thank Dr. Torsten Schmidt for providing ECMWF data via the German Weather Service from which meteorological analysis was made possible. I would also like to thank Dr. Tobias Kersten for determining the Phase Centre Corrections of the antennas used within this thesis. I would also like to thank Dr. Christina Arras for her help commenting and correcting a part of this thesis. My thanks go also to all my other GFZ colleges especially to Dr. Svetozar Petrovic, Dr. Zhiguo Deng, Dr. Galina Dick, Dr. Mathias Fritsche and Kirstin Winkler for all their help and support. Finally, my thanks go to all the colleges for their help and support during the experiment conducted in Morocco especially Prof. Driss Ouazar, Prof. Abderrahmane Touzani and Dr. Sybille Vey.

To my parents Abdessalam and Ilonka-Kyra, without your sacrifices and efforts, I would not have come so far. To my sister and best friend Nadia, my husband Hubert and his family, all of whom I own a great personal debt for the investment they have made in me and their patience during the compilation of this thesis. To my sons Elias and Jonas for their unbelievable comprehension. This dissertation is dedicated to all of you.

Contents

| | |
|--|-----------|
| Acronyms and abbreviations | 11 |
| 1 Introduction | 15 |
| 2 Theory and Definitions | 19 |
| 2.1 Fundamentals of the Global Positioning System | 19 |
| 2.1.1 GPS System | 20 |
| 2.1.2 GPS Signal Structure | 21 |
| 2.1.3 Basic Architecture of a GPS Receiver | 22 |
| 2.1.4 GPS Signal Processing | 24 |
| 2.2 GPS as a Remote Sensing Tool | 28 |
| 2.2.1 GPS-Reflectometry Motivation | 28 |
| 2.2.2 GPS-R Altimetry Principle | 29 |
| 2.2.3 GPS-R Altimetry Methods | 33 |
| 2.3 Reflection Process | 36 |
| 2.3.1 Coherent Phase Observations | 36 |
| 2.3.2 Fresnel Coefficient | 40 |
| 2.4 GPS Phase and Code Observation and their Systematic Errors | 42 |
| 2.4.1 Tropospheric Delay | 43 |
| 2.4.2 Phase Wind-up | 45 |
| 2.4.3 Antenna Phase Centre Offset and Variation | 48 |
| 2.4.4 Cycle slip | 50 |
| 2.4.5 Multipath | 51 |
| 2.4.6 Remaining Systematic Errors | 54 |
| 2.4.7 Final GPS Phase and Code Observation Equation | 55 |
| 3 Experimental Set-up | 57 |
| 3.1 Experimental Set-up in Vietnam | 58 |
| 3.2 Experimental Set-up in Morocco | 63 |
| 3.3 GNSS-Reflectometry Receiver | 65 |
| 4 Data Analysis | 67 |
| 4.1 Coherent Observation Extraction Algorithm | 67 |
| 4.1.1 Ellipse Fitting | 68 |
| 4.1.2 Performance of the Coherency Extraction Algorithm | 72 |

| | | |
|----------|---|------------|
| 4.2 | Coherent Data Analysis | 74 |
| 4.3 | Cycle slips | 83 |
| 4.3.1 | Cycle Slip Detection Algorithm | 84 |
| 4.3.2 | Algorithm Performance | 85 |
| 4.3.3 | Cycle Slip Occurrence Analysis | 86 |
| 4.4 | Multipath Effects | 88 |
| 4.4.1 | Empirical Mode Decomposition | 89 |
| 4.4.2 | Efficiency Analysis | 93 |
| 4.5 | Preprocessing Algorithm | 99 |
| 5 | Least-Squares Phase Based GPS-R Altimetry | 101 |
| 5.1 | Functional Model of a Phase Based GPS-R Altimetry | 102 |
| 5.1.1 | Impact of Excess Path Errors on Altimetric Determination | 103 |
| 5.1.2 | Planar versus spherical Earth Model | 104 |
| 5.1.3 | GPS-R Mathematical Model | 104 |
| 5.1.4 | GPS-R Tropospheric Model | 106 |
| 5.1.5 | Antenna Phase Centre Offset and Variation | 110 |
| 5.2 | GPS-R Ambiguity Fixing | 114 |
| 5.2.1 | Ambiguity Fixing Methods | 115 |
| 5.2.2 | Analysis of the Vietnam Data with Regard to the Ambiguity Problematic | 119 |
| 5.3 | Water Level Height Determination | 122 |
| 5.4 | Result Analysis | 124 |
| 5.4.1 | Solution gaps | 124 |
| 5.4.2 | Impact of undetected Cycle slips | 127 |
| 5.4.3 | Impact of the proposed Empirical Mode Decomposition Method on the results | 129 |
| 5.4.4 | Impact of the available satellite redundancy | 130 |
| 6 | Conclusion and Outlook | 135 |

Acronyms and abbreviations

| | |
|-----------------|--|
| ACC | Accuracy |
| ADC | Analogue-to-Digital Converter |
| APC | Antenna Phase Centre |
| ARP | Antenna Reference Point |
| ANTEX | ANTenna EXchange format |
| BPSK | Binary Phase Shift Keying |
| BMBF | German Federal Ministry of Education and Research |
| B-Method | Beta-Method |
| C/A-code | Coarse/Acquisition code |
| CDMA | Code Division Multiple Access |
| CIR | Cascading Integer Resolution |
| CM | Center of Mass |
| CNO | Carrier-to-NOise |
| CP | Circular Polarized |
| CS | Cycle Slip |
| DLL | Delay Lock Loop |
| DIA | Detection Identification Adaptation |
| DOP | Dilution Of Precision |
| DOY | Day of the Year |
| ECMWF | European Centre for Medium-range Weather Forecasts |
| EM | Electromagnetic |
| EMD | Empirical Mode Decomposition |
| EMI | Mohammedia School of Engineers |
| ENVISAT | ENVIronmental SATellite |
| ERS | European Research Satellite |
| FFT | Fast Fourier Transform |
| FBMWA | Forward and Backward Moving Window Averaging |
| FP | False Positive |
| FN | False Negative |
| GFZ | German Research Centre for Geosciences, Germany |
| GOM | Global Overall Model |
| GLONASS | GLObal NAvigation Satellite System |
| GFS | Global Forecast System |
| GMF | Global Mapping Function |
| GNSS | Global Navigation Satellite System |
| GNSS-R | Global Navigation Satellite System-Reflectometry |
| GNSS-Ri | GNSS-R interferometric |
| GORS | GNSS Occultation, Reflectometry and Scatterometry |
| GPS | Global Positioning System |
| GPS-R | Global Positioning System-Reflectometry |

| | |
|---------------------|--|
| GITEWS | German Indonesian Tsunami Early Warning System |
| HF | High Frequency |
| I | In-phase |
| IB | Integer Bootstrapping |
| IF | Intermediary Frequency |
| IGS | International GNSS Service |
| ILS | Integer Least-Squares |
| IMF | Intrinsic Mode Function |
| INS | Inertial Navigation System |
| IR | Integer Rounding |
| IRNSS | Indian Regional Navigation Satellite System |
| LAMBDA | Least-squares AMBIGUITY Decorrelation Adjustment |
| LEO | Low Earth Orbit |
| LHEP | Left Hand Elliptical Polarized |
| LHCP | Left Hand Circular Polarized |
| LNA | Low Noise Amplifier |
| LO | Local Oscillator |
| LOS | Line-Of-Sight |
| LS | Least-Squares |
| MCS | Master Control Station |
| MDB | Minimal Detectable Bias |
| MEO | Medium Earth Orbit |
| MF | Mapping Function |
| MP | Multipath |
| MPC | Mean Phase Centre |
| MOST | Vietnamese Ministry of Science and Technology |
| NAVSTAR | NAVigation Satellite Timing And Ranging |
| NCO | Numerically Controlled Oscillator |
| NMF | Niell Mapping Function |
| NWM | Numerical Weather Model |
| OSTM/Jason-2 | Ocean Surface Topography Mission |
| PCC | Phase Centre Correction |
| P-code | Precision code |
| PARIS | PAssive Reflectometry and Interferometric System |
| PLL | Phase Lock Loop |
| PN | Product Number |
| PRN | Pseudo Random Noise |
| PCO | Phase Centre Offset |
| PCV | Phase Centre Variation |
| PMARS | Programme Marocco-Allemand de Recherche Scientifique |
| PWU | Phase Wind Up |
| Q | Quadrature |
| QZSS | Quasi-Zenith Satellite System |

| | |
|---------------|---|
| RF | Radio Frequencies |
| RHEP | Right Hand Elliptical Polarized |
| RHCP | Right Hand Circular Polarized |
| RMS | Root Mean Square |
| RMSE | Root Mean Square Error |
| RO | Radio Occultation |
| SDT | Semi Diurnal Tide |
| SIR-C | Shuttle Imaging Radar with payload C |
| SMAP | Soil Moisture Active Passive |
| SMOS | Soil Moisture and Ocean Salinity |
| SNR | Signal-to-Noise Ratio |
| STD | Slant Total Delay |
| STEC | Slant Total Electron Content |
| TCAR | Three Carrier Ambiguity Resolution |
| TEC | Total Electron Content |
| TP | True Positive |
| TPR | True Positive Rate |
| TN | True Negative |
| TNR | True Negative Rate |
| TSS | True Skill Statistic |
| UTC | Universal Time Coordinated |
| VMF1 | Vienna Mapping Function |
| VTEC | Vertical Total Electron Content |
| WL | Wide-Lane Linear Combination |
| WISDOM | Water related Information system for the Sustainable Development Of the Mekong delta |
| WGS84 | World Geodetic System 1984 |
| ZHD | Zenith Hydrostatic Delay |
| ZTD | Zenith Total Delay |
| ZWD | Zenith Wet Delay |

Chapter 1

Introduction

Over recent decades, the global challenge for Earth and environmental research has been tackling problems such as the growing vulnerability of countries to natural events, risks related to climate changes and the shortage of usable land, resources and energy sources resulting from rapid population growth, industrialisation and changes in ecosystems and air quality affecting the natural function of human life. The central challenges of the 21st century are thus to develop strategies for the prevention and management of natural hazards and climate change, and to find the right balance for a sustainable and efficient use of geo- and ecosystems. One ascertained consequence of Global climate change is the sea level rise (Wassmann et al., 2004) that in turn causes an increase in extreme flood events. The United Nations stated that more people died due to floods than due to any other natural hazard and that they cause the most economic damage (Long and Trong, 2001), especially in developing or least developed countries where inadequate coverage of flood warning and monitoring systems exist (Grasso, 2012). One of these countries is Vietnam. Each year, half of the Vietnamese Mekong Delta area is inundated during the flood season causing extreme economic damage (Danh and Mushtaq, 2011).

Between 2007 and 2014, a German Vietnamese WISDOM research project was conducted. The goal of the project, funded by the German Federal Ministry of Education and Research (BMBF) and the Vietnamese Ministry of Science and Technology (MOST), is to develop an information system containing hydrologic, ecologic, and sociologic data to support and assist planners and authorities for an optimized regional planning of water and land resources (Gebhard et al., 2008). As observational data is an essential component of this information system, the focus of this thesis is to investigate the possibility of using the innovative phase-based GPS-R altimetry method as an observation and monitoring technique to derive accurate and continuous water level measurements of the flood risk area of the Mekong Delta.

Ground-based instrumentation, for example pressure or radar water level gauges, offer high altimetric accuracy of a few centimetres with high temporal resolution in 15 - 30 minutes, but for a point location only, which restricts its use for large rivers (Apel et al., 2010) like the Mekong Delta. Additionally, the maintenance of this instrumentation is cost-intensive, therefore the number of ground-based networks for the monitoring of water level is decreasing worldwide (Grasso, 2012).

For several years the Global Navigation Satellite System (GNSS) has not only been solely used for positioning tasks but also widely spread in geoscientific research fields. From the satellite to the receiver, the signal traverses through different atmospheric layers. An appropriate analysis of these signals has contributed immensely to the development of accurate ionospheric and tropospheric models that in turn are of great importance to ameliorate weather models. Currently, there are more than 75 GNSS satellites in orbit. Their deployment enables the reception of at least 4 signals simultaneously everywhere on Earth and at any time. Therefore, GNSS signals are an ideal tool for remote sensing and Earth observation. These properties have promoted for a new research field called Global Navigation Satellite System-Reflectometry (GNSS-R). This time, it is not the propagation properties of the signal through the atmosphere that are analysed but rather the reflection of the signal on the surface of interest, for example water, ice, snow or wet soils. Here the idea is to use the scattered signals to estimate characteristics of the reflecting surface such as roughness, dielectric properties or height, from which geophysical parameters such as ocean surface wind intensity and direction, sea ice stages, soil moisture and vegetation growth can be deduced. The focus of this thesis is the determination of altimetric water level.

As with in GNSS positioning, two GNSS-R altimetry methods exist: a code-based method and a phase-based method. In the first case, the altimetric excess range with respect to the direct Line-Of-Sight (LOS) (caused by the reflection), is measured through the delay between the recorded code of the reflected signal and the code of the direct one. This delay corresponds to the range between the peaks of the two correlation functions. By using the Coarse/Acquisition code (C/A-code), the range can only be measured within the smallest chip unit, mostly 0.1 chip (Van Dierendonck et al., 1992), restricting the achievable accuracy at meter level (Martín-Neira et al., 2001). An alternative offers the use of the Precision code (P-code). Due to the smaller chip width, a centimetre level of accuracy can be achieved (Lowe et al., 2002). In this thesis, the phase-based approach is applied for observing water reflected Global Positioning System (GPS) signals. The main observable is the altimetric excess range that is derived by using the observed phase delay between the direct and the reflected signals which can be measured within millimetre of precision. Several research have been done on this topic reaching the centimetre level of accuracy. However, these results are mostly reached under a free view of the water level surface allowing the use of a large elevation angle range. In contrast, the geometry of the observed 150 m large river section within this thesis restrict the elevation range strongly leading to a reduction of the observable reflected signals. Second, a high number of coherent phase observations are available. Due to the surrounding of the used antenna and the high roughness of the sensed water surface, a high loss of coherent observations is observed. These two factors, lead to a reduction of the number of simultaneously observed satellites, so that mostly only L1 phase observations are available to estimate the water level height. Another challenge is to correct all systematic errors that the signal contains after passing the Earth's atmosphere. One of the key tasks of this thesis is to discuss these effects systematically. As a result, the appropriate models are ultimately selected.

The surrounding of the antenna and the geometry of the observed river section increased the number of cycle slips and multipath effects present in the observations. Undetected cycle slips

lead to an error in the water level height estimation of several then a metres. Uncorrected multipath effects, mostly ignored in other proposed research, show an error of several centimetres. Thus, another task of the thesis is to develop appropriate algorithms based on L1 phase observations only for the detection of cycle slips and the isolation of multipath signals. Based on this analysis, a complete Least-Squares based GPS-R algorithm is presented. Additionally, as the Mekong Delta is an important mean of transportation for local people and merchandise, the high number of passing ships increases the roughness of the water surface causing a loss of phase coherency. This fact will be revealed as the most limiting but uninfluenceable factor in the proposed method. To highlight this, collected data under smooth water conditions of a measurement campaign conducted 2014 within the PMARS project in Midelt, Morocco, are used.

This thesis has the following structure. First an introduction to the theory and definitions behind GPS-R are given in Chapter 2 with some general background information about the GPS, the GPS signal structure, the GPS antenna and the GPS receiver acquisition and tracking technique. The differences between the two existing GPS-R altimetric methods with their advantages and disadvantages are presented. Diffuse and specular reflection with their relation to signal coherency are outlined. Systematic error sources that influence the signals are also discussed to finally end with the equation of GPS phase observations that are used within this thesis.

In Chapter 3, the used experimental set-up in Vietnam and Morocco will be presented. In this chapter, a description of the, specially for GNSS-R applications, modified JAVAD receiver can also be find.

To benefit from the potential precision of phase-based GNSS-R altimetry, coherent, continuous and outlier free observations are needed. A loss of observation coherency, a high number of cycle slips and the presence of reflections other than those coming from the water surface are observed in the recorded data. All these effects that deteriorate the results, are directly related to the water surface conditions and objects obstructing the signal in the vicinity of the antenna. These issues are addressed in Chapter 4. As water irregularities are unpredictable, a new method is presented in this chapter that enables one to distinguish between coherent and incoherent observations showing that 82% of the data could be extracted correctly. Based on the data analysis, preprocessing strategies are also proposed. In GNSS based positioning, several algorithms were developed to detect and correct cycle slip events or multipath effects. Concerning the presence of cycle slips, the majority of the proposed approaches involve forming cycle-slip-sensitive linear combinations of the available code and/or phase observations (Bisnath, 2000). However, in the present study, only phase observations are available, therefore a cycle slips detection method is developed. Regarding multipath effects, the challenge here is to isolate the reflections of interest from those resulting from objects surrounding the antenna. The use of the Empirical Mode Decomposition (EMD) method is also proposed here.

Based on a Least-Squares (LS) method that offers the advantage to give precision and reliability specification on the extracted unknown parameters, the preprocessed data is used to extract water level heights in Chapter 5. In recent decades, the functional model of GPS based

positioning, has been continuously improved (Hofmann-Wellenhof et al., 2008; Teunissen and Kleusberg, 1998; Xu, 2007). Nevertheless, for GPS-R applications the functional model has to be adapted and contains deficiencies in terms of modelling phase wind-up effects or atmospheric propagation delays for low-elevation data. Based on an analysis of the impact of excess path errors on altimetric determination, the functional model is developed. The ambiguity fixing problem suffers under the same conditions as the cycle slips detection. In precise GPS based positioning, on average seven different satellites are simultaneously observed, and multi-frequency code and phase observations are available. An overdetermined observation system is thus available to determinate a single three dimensional position, namely the receiver position, and to facilitate the fixing of the ambiguity. In GPS-R altimetry, each observed satellite link represents one reflection height that differs from one reflection point to another. Additionally, continuous and simultaneous observations are not always available. It will be shown in Chapter 5 that this constellation leads to a reduction of the water level height accuracy from centimetre to decimetre.

The main challenge of this thesis is the development of algorithms for GPS-R phase-based water surface parameter and water level observation in banks and near-coastal areas. Under the condition of coherent phase observations, it will be demonstrated that GPS-R could complement conventional altimetric sensors by filling the gap of observation data with an interval of 10 min and with an accuracy at the decimetre level.

However, the method also presents challenges: the phase-based GPS-R technique depends on the presence of continuous coherent phase observations. As mostly only L1 phase observations are available and their continuous coherency is mostly restricted to a length of 10 minutes the ambiguity fixing rely on the geometrical change of the satellites leading to a decimetre level of accuracy. In the rare cases where coherent observations from several satellites in parallel are also available, the centimetre level can be reached. The coherency is, as shown by the comparison of two different measurement campaigns under different water surface conditions, strongly dependent on the roughness of the water surface. The presented algorithm showed better results on smooth water surfaces.

Nevertheless, GPS-R is a promising altimetry remote sensing tool, yet it still requires further research to resolve remaining scientific and technical uncertainties especially in the optimization of receivers and antennas for GPS-R applications.

Chapter 2

Theory and Definitions

The objective of this chapter is to give the reader the necessary theory and definitions behind the Global Positioning System-Reflectometry (GPS-R) based altimetry which is the focus of this thesis. But first, the functionality of the GPS system as an instrument for positioning and timing will be outlined in Section 2.1. This will allow for a better understanding of the GPS-R altimetry motivation and the existing processing methods, namely the code and the phase-based, that are presented in Section 2.2. Within this thesis, the phase-based method is used because it has the potential to offer results with high accuracy. But one of the mandatory condition of this method, is the continuous measurement of reflected coherent phase observations. In Section 2.3.1, the properties of coherent phase observations will be introduced as well as his relation to specular and diffuse reflection. In Section 2.3.2, the impact of the reflection on the signal overall electric field will be presented. Until this point of the theory, both methods (GPS based positioning and GPS-R based altimetry) are intentionally described in their idealised form ignoring the existing systematic errors that falsify the obtained observations. These errors are described in Section 2.4 with focus on those systematic errors that are relevant for a GPS-R based altimetry. For the sake of completeness, the remaining systematic errors sources are presented in Section 2.4.6. With all this theoretical background, the GPS phase and code observation equations are given in the last section of this chapter (Section 2.4.7) that will be the core of the proposed algorithm.

2.1 Fundamentals of the Global Positioning System

As the theory behind GPS is very large, this section aims to concentrate on the relevant fundamentals needed within this thesis. For this purpose, Section 2.1.1 introduces the primary goal of GPS as well as the different segments composing the system. To provide the user with the necessary informations to solve for their positioning and timing, the used signal structure is outlined in Section 2.1.2. The following two sections present, in a compact view, the flow of the transmitted GPS navigation signal from his reception via an antenna till his processing in a GPS receiver (Section 2.1.3) to finally end as a ranging observation (Section 2.1.4).

2.1.1 GPS System

The NAVigation Satellite Timing And Ranging (NAVSTAR)-GPS, commonly known as GPS, is a one way ranging and timing system operated and maintained by the U.S. Department of Defence. Based on the trilateration principle, its use permits to obtain accurate and continuous three-dimensional position and velocity information but also highly accurate timing information. To reach this, the GPS system is composed of the space, the control and the user segment.

The original space segment consists of a nominal constellation of 24 satellites equally-spaced on six Earth-centred orbital planes with four satellites in each plane, see Xu (2007, pp. 23) for an illustration. The ascending nodes of the orbital planes are equally spaced by 60 deg. The orbital planes are inclined by 55 deg with respect to the equator and the GPS satellites are placed at an altitude of about 20 160 km above the Earth's surface. This constellation guarantees a global coverage with four to eight simultaneously observable satellites above 15 deg of elevation at any time of day (Hofmann-Wellenhof et al., 2008, chap. 2). In June 2011, the U.S. Air Force successfully completed a new GPS constellation expansion to improve the global coverage¹. Three of the 24-slots were expanded with a satellite. For this purpose, six satellites, originally used as system backup to maintain the coverage whenever the baseline satellites are serviced or decommissioned, were repositioned. As a result, GPS now effectively operates with a 27-slot satellite constellation. The GPS satellites have a sidereal revolution period of approximately 11 hours 58 minutes (half a sidereal day) so that the same satellite configuration is repeated four minutes earlier every day for one and the same location. Each satellite carries highly accurate and ultra-stable atomic clocks that form the heart of the system as they produce the fundamental used frequency (Section 2.1.2).

The control segment is comprised of three major components: a Master Control Station (MCS), ground antennas, and monitoring stations. The MCS, located in Colorado Springs, commands and controls the GPS satellite constellation, generates and uploads ephemerides and clock adjustments to the satellites. This task is assisted by 16 monitoring stations that are used to track the GPS satellites and collect atmospheric data.

Finally, the user segment consists of receivers and processors able to track and proceed the GPS navigation signals.

A detailed description of the GPS system can be found in Hofmann-Wellenhof et al. (2008); Parkinson (1996); Spilker Jr. (1996c).

For the sake of completeness, one has to mention here that five other satellite navigation systems exist (status July 2015): the Russian GLObal NAVigation Satellite System (GLONASS), the European Galileo, the Chinese BEIDOU/COMPASS, the Indian Regional Navigation Satellite System (IRNSS) and the Japanese Quasi-Zenith Satellite System (QZSS).

¹<http://www.gps.gov/systems/gps/space>

2.1.2 GPS Signal Structure

The structure of the GPS signal have been selected in order to satisfy several requirements. First, to get accurate positioning information, the signal frequency should be chosen that way that atmospheric induced delays can be minimized. Second, since real-time positioning is seek and it is based on the trilateration principle, simultaneous measurements to different positioned satellites are required. There is thus a need to identify unambiguously the transmitting satellite as well as his position during the transmission. Third, no limitation is made on the number of parallel users (Multi-user system). Finally, different codes are required to provide differential access to civilian and military/authorized users.

At the time of this thesis, five types, called blocks, of the second generation of GPS satellites exist (Table 2.1). All of them continuously transmit two carrier Radio Frequencies (RF) in the L-band (L1 and L2). The use of two frequencies permits to correct for ionospheric induced delays (Section 2.4.6). Since 2010, the new generation of satellites transmit a third carrier RF, labelled L5, which is broadcast in a radio band reserved exclusively for safety-of-life systems, for example aviation safety services and other high-performance applications. All these frequencies are coherent with a 10.23 MHz atomic clock and have a centre frequency at

$$\begin{aligned} L1 &= 1575.42 \text{ MHz} &= & 154 \times 10.23 \text{ MHz} & \text{ with a wavelength of } 0.1904 \text{ m,} \\ L2 &= 1227.60 \text{ MHz} &= & 120 \times 10.23 \text{ MHz} & \text{ with a wavelength of } 0.2445 \text{ m,} \\ L5 &= 1176.45 \text{ MHz} &= & 115 \times 10.23 \text{ MHz} & \text{ with a wavelength of } 0.2550 \text{ m.} \end{aligned}$$

These L-band carrier signals are modulated by a binary code, the Pseudo Random Noise (PRN), that is unique for each satellite. This allows the receiver to identify the transmitting satellite by correlating the incoming PRN with the internally stored replicas of all possible PRN's. The generation of the PRN code relies on a well-defined mathematical method: the Gold Code, used because of its correlation properties. Indeed, the PRN sequences of each satellite are nearly orthogonal to each other so that the correlation function exhibits a sharp peak only when the receiver generated code is aligned with the incoming code from the satellite otherwise the correlation is nearly zero. This coding method, known as the Code Division Multiple Access (CDMA), permits all satellites to transmit on the same frequency. Each satellite sends two different PRN codes: the Coarse/Acquisition code (C/A-code) and the Precision code (P-code).

The C/A-code, designed for the civil user, is a sequence of 1023 bits that are modulated on the L1 (abbr. L1 C/A) carrier signal frequency. As these bits do not carry any information, they are commonly called chip. The chipping rate of a complete PRN sequence is 1.023 MHz and thus repeats periodically each millisecond, so that it has a width of approximately 300 m. Since 2005, a second civilian GPS signal on the L2 radio frequency (abbr. L2C) is broadcast, to permit users with dual-frequency GPS receivers to correct for the ionospheric induced error (Section 2.4.6) and so increase their positioning accuracy (Dunn, 2013).

The P-code is restricted to military use and is modulated on the L1 (abbr. L1P) and on the L2 (abbr. L2P) carrier signal with a chipping rate of 10.23 MHz. It has thus a ten times higher

resolution than the C/A-code and thereby the determination of the pseudoranges can be done more precisely (de Jonge, 1998). The code length is slightly longer than 38 weeks. However the actual length is one week as the code is reset every week (Tsui, 2005, chap. 5.4).

| Block IIA | Block IIR | Block IIR(M) | Block IIF | GPS III |
|---------------|----------------|---------------|---------------|-------------------|
| 1990 - 1997 | 1997 - 2004 | 2005 - 2009 | 2010 | Now in production |
| L1 C/A | L1 C/A | L1 C/A | L1 C/A | L1 C/A |
| L1P/L2P | L1P/L2P | L1P/L2P | L1P/L2P | L1P/L2P |
| | | L2C | L2C | L2C |
| | | | L5 | L5 |
| 4 operational | 12 operational | 7 operational | 8 operational | |

Table 2.1: GPS Block satellites. Status on January 2016.

The L-band frequencies are also used to broadcast the navigation data which is a 50 Hz binary-coded and time-tagged message. It contains information on the transmitting time, the satellite health status, and ephemeris parameters, permitting the user receiver to calculate position, velocity, time, and ionospheric corrections.

To modulate all these binary data onto the carriers, the Binary Phase Shift Keying (BPSK) technique is used. Thereby, only one sinusoid is taken as basis function. The modulation itself is achieved by varying the phase of the basis function in dependency of the chip.

More detailed information on the GPS signal structure can be found in Spilker Jr. (1996b); ICD-GPS-200D (2010); Misra and Enge (2011, chap. 2); Doberstein (2012).

2.1.3 Basic Architecture of a GPS Receiver

Now that the goal and the signal structure of GPS have been defined, the basic architecture with the various components of a GPS receiver will be presented in the next two subsections (Figure 2.1). However, as the signal processing is the core of the GPS receiver, an extra section will be dedicated to this subject (Section 2.1.4).

GPS Antenna

The first component is an antenna that receives the GPS RF signals. An antenna is an important part of any wireless communication system as it converts the electronic signals into Electromagnetic (EM) waves optimally. The radiation, the polarization of the EM waves, and the frequency band define the antenna design.

The L-band transmitting antenna of a GPS satellite are pointing to the Earth's centre with a one sided beam angle of 21.3 deg for the L1 and 23.4 deg for the L2 band (Spilker Jr., 1996a, pp. 84-86). This permits to illuminate the complete Earth's surface in view of the satellite. Furthermore, as it is desirable to receive signals from different satellites with similar strength,

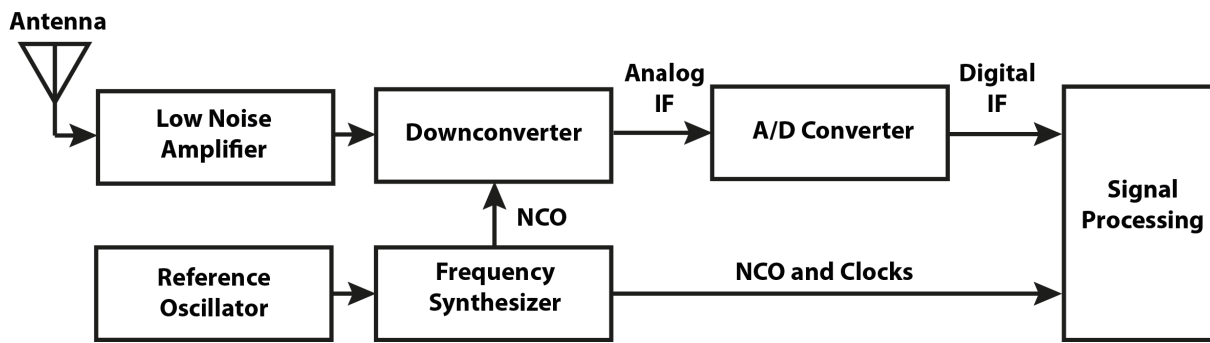


Figure 2.1: Simplified schematic representation of the elements composing a GPS receiver. The weak GPS signals, received by an antenna, are amplified by a Low Noise Amplifier (LNA). A reference oscillator provides time and frequency reference used in the frequency synthesizer to generate Numerically Controlled Oscillator (NCO)s and clocks. The NCOs produced frequencies are mixed with the amplified RF to down-convert the signal to an analogue Intermediary Frequency (IF). These are then converted into digital IF by an Analogue-to-Digital Converter (ADC) that is used in the signal processing step.

the beam is slightly weaker at the centre. This in turn means for the GPS receiving antenna, that it should be able to receive a maximum number of signals and thus cover a wide spatial angle. But, as the transmitted signals come from the top side of the antenna, it should ideally only cover one half of the hemisphere thus from the zenith to the horizon for all azimuths. However, in GNSS positioning, an antenna should also be able to reject or minimize reflections coming from the ground upon the antenna from below (Section 2.4.5). This can be controlled by the polarization design of the antenna.

The polarization of EM waves is defined as the locus traced by the extremity of the time-varying electric field vector \mathbf{E} (vectors will be written in bold within this thesis), at a fixed observation point (Ilcev, 2005). Depending on the shape of this trace, three types of polarization exist: linear, circular and, elliptical. Furthermore, depending on the relation between the direction of propagation and the direction of observation, it is then distinguished as right-handed (clockwise) or left-handed (counter-clockwise) polarisation.

Concerning the GPS signals, they are transmitted as Right Hand Circular Polarized (RHCP). Essentially, to reduce polarization changes associated with Faraday rotation due to free electrons in the ionosphere (Flock, 1987). The polarization of a reflected or refracted EM wave in dependency of the reflecting surface properties and the incident angle wave may changes to Left Hand Circular Polarized (LHCP) (Section 2.3.2). To exclude to the greatest possible extent these undesirables signals (the reflected ones), a RHCP antenna is commonly used as it has a higher gain for the direct signals and a lower gain for the reflected LHCP signals. Additionally, if a ground reflection occurred, the direction of the incoming signal is known (from the ground), that is why the antenna have a low back lobe. In contrast, in GNSS-R applications, we are especially interested in reflected signals mostly arriving from low elevations. Thus a LHCP or a combination of LHCP/RHCP antennas are used.

Finally, if all frequencies are used, the antenna can either have a wide bandwidth covering the entire frequency range or have different narrow bands that cover the desired frequency range. Narrow bandwidths can be used to avoid interference in between the selected bands.

GPS Receivers

Through an RF front-end, the received GPS signals of all satellites in view are amplified to a proper amplitude by a Low Noise Amplifier (LNA). Sometimes a bandpass filter is set between the antenna and the LNA in order to filter out the interfering signals in adjacent frequency bands by decreasing the bandwidth of the received signal. The reference oscillator, that has a key function in the receiver, provides time and frequency reference. This is used in the frequency synthesizer from which Numerically Controlled Oscillators (NCO) and clocks are derived. To be able to work with the incoming signal, the frequency of around 1.5 GHz is down-converted to an Intermediary Frequency (IF), typically around 80 MHz, which is obtained by mixing frequencies generated by the NCOs with the amplified RF (Eissfeller, 1997). After these steps, the analogue IF signal is converted into digital IF using an Analogue-to-Digital Converter (ADC). These digitized IF signals are now ready to be processed by each of the N correlation channels of the receiver (Kaplan and Hegarty, 2006, chap. 5). A modern geodetic receiver has at least 12 such channels.

2.1.4 GPS Signal Processing

Signal processing is the core of a GPS receiver as it permits the user to get access to the necessary information contained in the GPS signals to perform a navigation solution or other applications function. For this purpose, first an acquisition and tracking process in the code and carrier dimension is started.

Acquisition

The basic idea of the acquisition process is to despread the input signal and find the carrier frequency and code phase. Indeed, the modulation of the C/A-code on the carrier frequency spreads the total signal power over a wide bandwidth making the signal virtually undetectable unless the C/A-code with the correct phase is found. For this purpose, the receiver correlates the incoming IF signal with receiver-generated delayed replicas of the C/A-code for all possible satellites (Figure 2.2).

The search step depends on the desired power density loss due to misaligned spreading code phases. The typical step for GPS is 0.1 chip. Concerning the length of the used signal, the navigation data is 20 ms or 20 C/A-codes long. If there is a navigation data transition, it will spread the spectrum which will degrade the acquisition result. Thus, the appropriate length of the data has to be selected. Since the C/A-code is 1 ms long, it is reasonable to perform the acquisition on at least 1 ms of data. However, a navigation data phase transition can occur. Therefore, at least two consecutive data sets should be taken into account. Alternatively, using a 10 ms long data set ensures that only one data transition can occur (Tsui, 2005, pp. 131-132). In this case, the power density is improved but the acquisition takes longer.

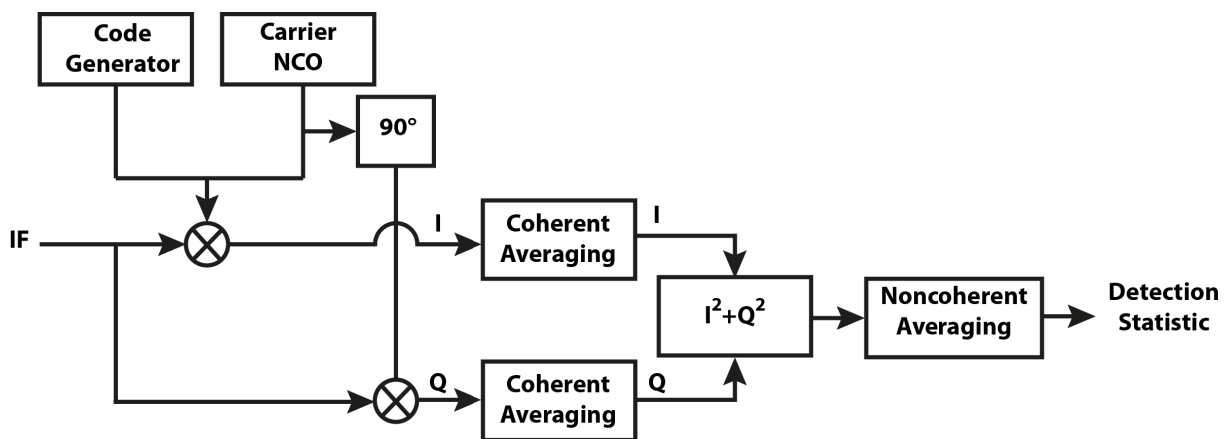


Figure 2.2: Simplified schematic representation of the acquisition step. To track and decode the information contained in the GPS signal, a two dimensional code and frequency search process is started. The incoming IF is correlated with delayed receiver-generated codes whereat the Doppler induced shift is considered in parallel. Each alignment is averaged and accumulated to form a detection statistic that will be largest when the selected code and frequency match those of the incoming IF signal. Similar block diagram can be found in Weill (2011).

The relative motion of satellite and receiver produces a Doppler frequency shift of the IF and the C/A-code that has to be accounted for. For a stationary observer, the maximum Doppler frequency shift due to satellite motion is approximately 5 kHz for the L1 and 4 kHz for the L2 frequencies (Tsui, 2005, pp. 34-38). This causes a Doppler frequency shift on the C/A-code in the order of 3.2 Hz (Tsui, 2005, pp. 40) for a stationary user. Thus, in addition to the code search, the receiver also needs to search in the frequency domain.

The frequency search band, generated by a NCO, is divided in frequency bins with the size depending on the desired integration time and power density loss due to frequency mismatch. A commonly used Doppler frequency bin size is 500Hz.

Rough information about receiver location and approximate time of day reduce the code and frequency search space as only expected visible satellites will be investigated and approximate Doppler ranges can be calculated.

This search process, provides the In-phase (I) and Quadrature (Q). For each alignment (carrier frequency and C/A-code), the signal is coherently averaged over a sufficiently long time period, typically 1 ms determined by the C/A-code repeat sequence, to build up the power density to a usable level (Weill, 2011).

The key feature of a coherent averaging process is the timing used to sample the original signal. Multiple sets of the signal plus noise samples are collected, though the time phase at the beginning of each sample set is the same (Lyons, 2004).

The accumulated power $I^2 + Q^2$ is averaged non coherently to form a detection statistic that will tend to be largest when both the selected code delay and frequency closely match those of the IF input signal.

Tracking

Once the signal is detected, the tracking process starts. The main purpose of this step, is to refine the coarse values of code phase and frequency obtained in the acquisition step, to keep the replica and the received codes aligned and to correct frequency if a Doppler shift change occurs. Two coupled loops are used: one loop that tracks the C/A-code referred to as Delay Lock Loop (DLL) and one loop that tracks the carrier frequency of the IF referred to as Phase Lock Loop (PLL) (Figure 2.3).

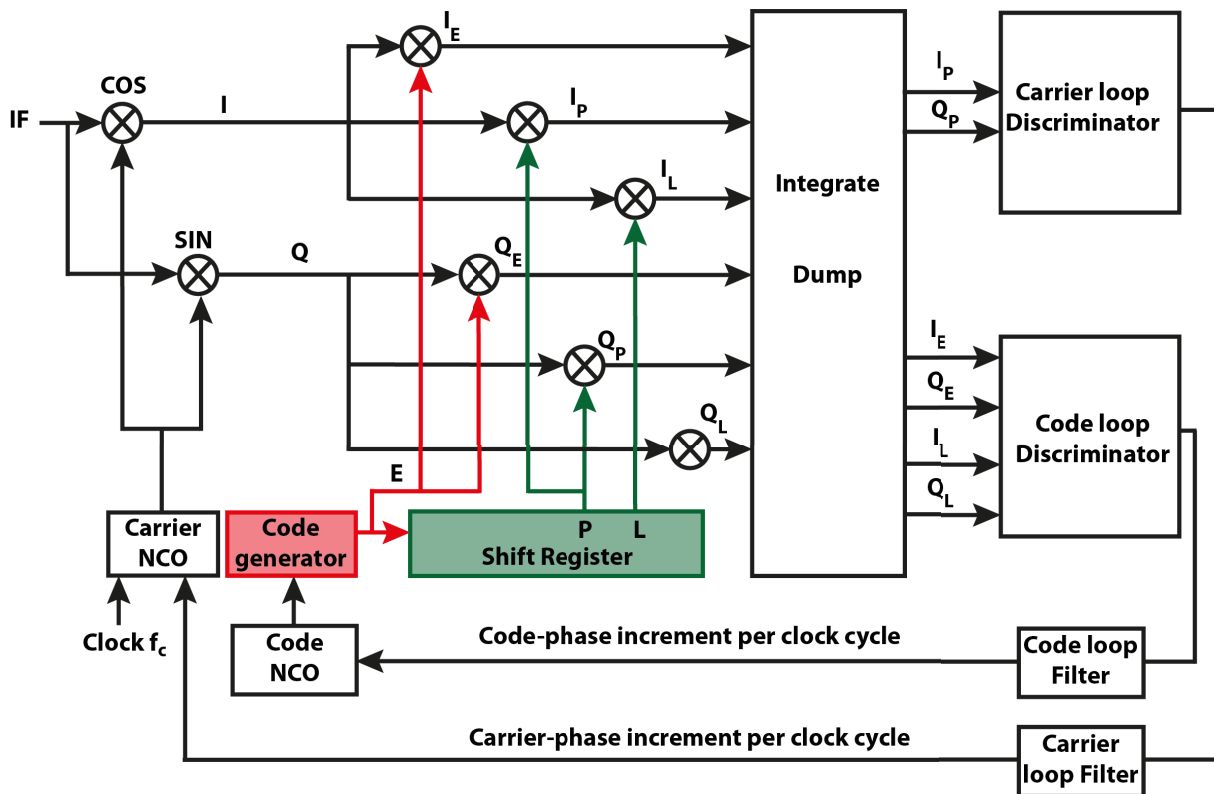


Figure 2.3: Simplified schematic representation of the Delay and Phase Lock Loop. The NCO synthesized carrier replica is stripped of the incoming carrier. The obtained I and Q are correlated with three code replicas (Early (E), Prompt (P), Late (L)) and coherently accumulated and stored. If P is aligned with the incoming signal, a maximum correlation occurs. Any misalignment is fed-back (closed-loop) to the code and phase NCO that accordingly adjusts the code and the phase replica. A similar diagram can be found in (Kaplan and Hegarty, 2006).

The digital IFs are stripped of the carrier by the NCO synthesized carrier replica to produce I and Q samples (Kaplan and Hegarty, 2006, chap. 5). The obtained I and Q signals are then correlated with three different displaced versions of the replica code designed as early (E), prompt (P) and, late (L) which are synthesized by the code generator and the code NCO controlled by the code tracking loop in the receiver processor. E and L are typically separated in phase by 0.1 chip and P is in the middle (Van Dierendonck et al., 1992). By integrating the resulting data streams over an integration time interval, maximum of 20 ms, three In-phase (I_E , I_P , I_L) and three Quadrature-phase (Q_E , Q_P , Q_L) components are formed. If the prompt replica code P is aligned with the incoming code phase, it produces a maximum correlation. Any misalignment produces a difference in the vector magnitude of the early and

late correlated outputs. Code and phase discriminator are used to compute the mismatch amount and direction which is fed back (closed loop) to the code and carrier NCO that adjust accordingly the code and phase replicas to maintain that code, phase and frequency is locked (Irsigler, 2008). When the signals are properly tracked, the C/A-code and the carrier wave can be removed from the signal leaving the navigation data bits from which the ephemeris data for the satellite can be decoded.

Output

Contrary to popular belief, the natural measurements of a GPS receiver are not pseudoranges but replica code phase and replica carrier Doppler frequency (Ward et al., 2006, pp. 200-219).

Indeed, the replica code phase determined during the tracking process is converted into satellite transmitting time as each chip of the PRN code is linear to the satellite clock time. This is then used to compute the pseudorange (PR)

$$PR_{rcv}^{sat_i}(t_r, t_e) = c(t_r - t_e) + c(\delta t_r - \delta t_e) + \delta, \quad (2.1)$$

where subscript rcv and superscript sat_i denote the receiver and the i th satellite respectively, c is the speed-of-light, t_r the reception time based on the receiver clock in seconds, t_e the emission time based on the satellite clock in seconds, δt_r and δt_e the receiver and satellite clock errors and δ other systematic errors in meters that influence the signal including noise (Section 2.4). The de-synchronisation between the satellite and the receiver clocks is the reason why the expression "pseudorange" instead of "range" is commonly used.

The replica carrier Doppler frequency is converted into highly precise integrated carrier Doppler phase measurements. These are extracted from the carrier tracking loop using a carrier accumulator that consists of the fractional cycle count of the carrier Doppler phase measurement and the integer cycle count. Indeed, during the first signal tracking, the number of full carrier waves (cycles) between the receiver and the satellite is unknown and the receiver can only measure a fraction of the cycle. After this first signal tracking, the receiver starts to count for the full cycles but the ambiguous number of full cycles during the first signal tracking remains unknown. This is called ambiguity and has the following three properties. First, it stays constant as long as no signal interruption has occurred (Section 2.4.4), otherwise the receiver interprets the interruption as a new signal tracking and thus a new ambiguity occurs. Second, as the ambiguity is a number of full cycle it has an integer value. Finally, for each receiver satellite link the integer ambiguity value differs. The carrier phase in cycles is thus

$$\Phi_{rcv}^{sat_i}(t_r) = \Phi_{rcv}(t_r) - \Phi^{sat_i}(t_r) + N_{amb,rcv}^{sat_i} + \delta, \quad (2.2)$$

where Φ_{rcv} denotes the phase of the receiver's oscillator, Φ^{sat_i} represents the received signal phase of the i th satellite, $N_{amb,rcv}^{sat_i}$ denotes the ambiguity related to receiver rcv and satellite sat_i and δ the systematic errors including noise in cycles.

The advantage of using phase observations is that the fraction of the cycle can be measured with a precision better than 1% of the wavelength thus within the millimetre. However, to be able to take advantage of this precision the ambiguity has to be resolved.

More detailed information can be found in: Kaplan and Hegarty (2006); Tsui (2005).

2.2 GPS as a Remote Sensing Tool

Nowadays, the use of GPS in geosciences is widely recognized, mainly for precise positioning. Particularly in recent years, GPS has also become a powerful remote sensing tool for the direct monitoring of geophysical parameters. The most prominent examples are the ground and space based GPS atmosphere soundings. These techniques are based on the fact that the GPS signals are delayed, while propagating through the atmosphere. Related atmospheric data products are currently widely used and can be operated to improve numerical weather forecasts or for climatological investigations and space weather observation (Wickert et al., 2009; Arras et al., 2008; Jakowski et al., 2005; Gendt et al., 2004).

Indeed, GPS offers several advantages for remote sensing: the freely available signals are of high quality (multi-frequency), the measurements are calibration free and the GPS system have been designed for long term availability and stability. But the most important characteristic is the satellite constellation that allows the continuous tracking of GPS signals transmitted from various satellites orbiting at different positions simultaneously. Furthermore, if the current GNSS constellation is considered (status 2015), more than 75 satellites are available: GPS with 32 operational Medium Earth Orbit (MEO) satellites, GLONASS with 29 MEO transmitters, Galileo currently with four satellites, planned to be fully operational by 2019 with 30 satellites, and COMPASS/Beidou-2 currently with 14 spacecraft and foreseen to be fully operational with 30 satellites offering a width global coverage. All these properties makes GNSS an ideal remote sensing tool and essentially is the motivation for the outcome of a new research field called Global Navigation Satellite System-Reflectometry (GNSS-R). As only GPS signals are used within this thesis, the focus will be made on the GPS based Reflectometry.

In the following sections, the motivation behind the innovative GPS-R method with his two main applications will be presented (Section 2.2.1). Although emphasis will be made on the altimetric application, the field of interest of this thesis, so that a separate section will be devoted to this subject (Section 2.2.2). The following Section 2.2.3, will then present the two main exiting methods to extract water level height informations with there pros and cons.

2.2.1 GPS-Reflectometry Motivation

In GPS-R, not the directly transmitted signals play the principal performing role but the reflected ones received simultaneously from different reflection points on the surface of interest such as water, ice or wet soils.

The idea of using reflections to extract information on the reflecting surface, has already been proposed by Cox and Munk (1954). The method consists of photographing the Sun's glitter pattern on the sea surface from an aeroplane and translating the statistics of the glitter into the roughness of the sea surface for different wind speeds and directions. In 1988, Hall and Cordy already proposed the use of GPS signals as a multi-static ocean scatterometer, but the decisive starting point of GNSS-R as a remote sensing tool for ocean altimetry, was given by Martín-Neira (1993) within the PAssive Reflectometry and Interferometric System (PARIS) project. The goal was to define a system with the ability to carry out high precision ocean altimetry with high spatial and temporal resolution to improve mesoscale eddy measurements. Such a system would offer the possibility to understand ocean circulation on a scale that cannot be resolved with standard satellite based altimeters. Indeed, satellite altimetry offers a high accuracy of a few to tens of centimetres for oceans but typically with a repeat period of 10 (OSTM/Jason-2) to 35 (ERS/ENVISAT) days (Fu et al., 2010) and a spatial resolution of 200 km. In comparison, GNSS-R has the potential to map the Earth in about a day or two with a spatial resolution of 25 km (Gleason and Gebre-Egziabher, 2009). Since then, intensive theoretical and experimental work has been completed and tested with different receiver designs at diverse observation heights and platforms for two main applications namely: scatterometry and altimetry. A good overview can be found in Wickert et al. (2012).

In the scatterometry stream, methods are developed to recover, for example, the sea state conditions by determining wind speed and wind direction (Soulat et al., 2004; Garrison and Katzberg, 2000). Soil dielectric properties and thus the degree of moisture is estimated using the temporal variation of the reflected signal amplitude (Zavorotny et al., 2010; Larson et al., 2010). Polarimetric measurements of reflected signals are used in Egido et al. (2012) to extract soil moisture and vegetation development conditions or sea ice conditions (Fabra et al., 2012). Larson et al. (2009) showed the possibility of using GNSS-R to measure snow depth. A good overview of the different experimental results in GNSS-R scatterometry can be found in Cardellach et al. (2011).

2.2.2 GPS-R Altimetry Principle

The main objective of the GPS-R based altimetry stream, the application used within this thesis, is the monitoring of water level heights using GPS reflected signals. When a GPS wavefront scatters on the Earth's surface, the reflection process is typically not a point-shaped one. Depending on surface irregularities (roughness), the elevation angle E and the signal wavelength, an active scattering region contributes to the total received field called the glistening zone (Figure 2.4 in grey). The point on the reflecting surface, labelled **S** in Figures 2.4 and 2.5, that minimizes the Transmitter-Earth-Receiver distance and that satisfies Snell's Law, i.e. where the elevation angle E between the direct and the reflected signal with respect to the surface normal are equal, is located at the centre of the glistening zone and is called the specular point (Gleason and Gebre-Egziabher, 2009, chap. 16). The glistening zone with his specular point, are the primary surface respectively point of reference for model applications and measurements.

Due to the reflection of the GPS signal on the water surface, the reflected signal has to travel a longer path compared to the direct one. The determination of this excess path ($\Delta\rho$, bold line in Figure 2.4) permits to derive the relative height h between the receiver height H_{rcv} and the reflecting surface height H_S . For this purpose, two models of different complexity can be used.

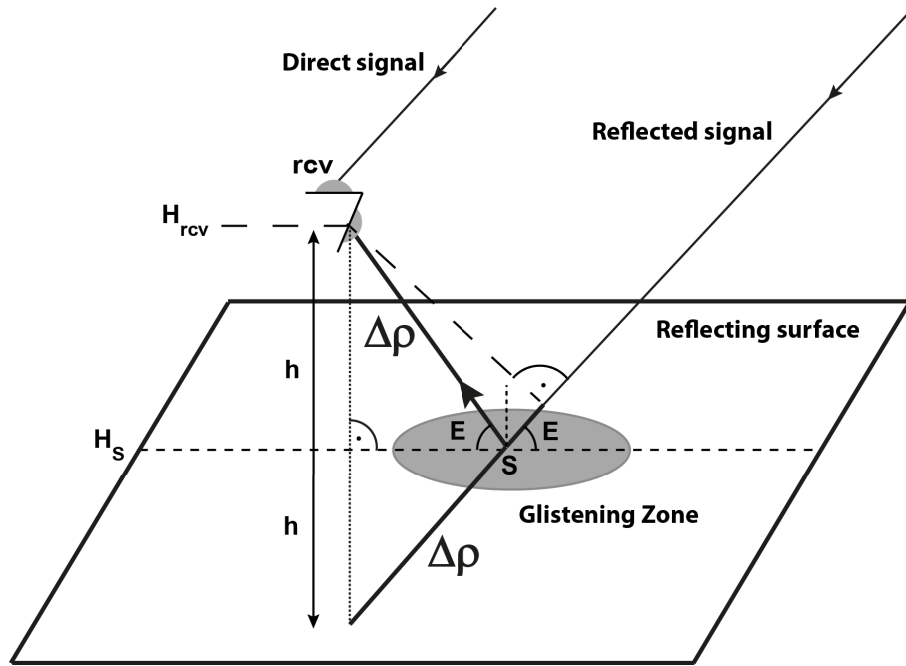


Figure 2.4: Schematic representation of the GNSS-R principle. Two main research field exist: scatterometry and altimetry. In scatterometry, through the active scattering region called glistening zone (in grey), surface properties can be extracted. In altimetry, the excess geometric path travelled by the reflected signal compared to the direct one can be modelled in terms of relative height h between the receiver height H_{rcv} and the reflecting surface height H_S at the specular point S which is at the centre of the glistening zone.

In the simplified model, a planar Earth is assumed. In this case, the geometric excess path of the reflected signal $\Delta\rho$ can be modelled as

$$\Delta\rho = 2(H_{rcv} - H_S) \sin E = 2h \sin E . \quad (2.3)$$

To calculate the required elevation angle E , the satellite and the receiver position are needed. The satellite position is computed using the broadcast ephemeris. The receiver position is taken from the standard navigation output of the receiver.

In the second method, a more complex Earth model is assumed: a spherical one. Following Martín-Neira (1993); Helm (2008); Roussel et al. (2014), the excess path length $\Delta\rho$ has to be calculated iteratively through the determination of the specular point vector \mathbf{S} on a Gaussian osculating sphere that best fits the World Geodetic System 1984 (WGS84) ellipsoid and that fulfils the condition of a specular reflection i.e. the incident angle E equals the reflected one (Figure 2.5).

To reach this, a system coordinate (x,y) is first defined so that the receiver rcv , the transmitter sat and the specular point S lie in one plane with the origin defined at the centre of the sphere.

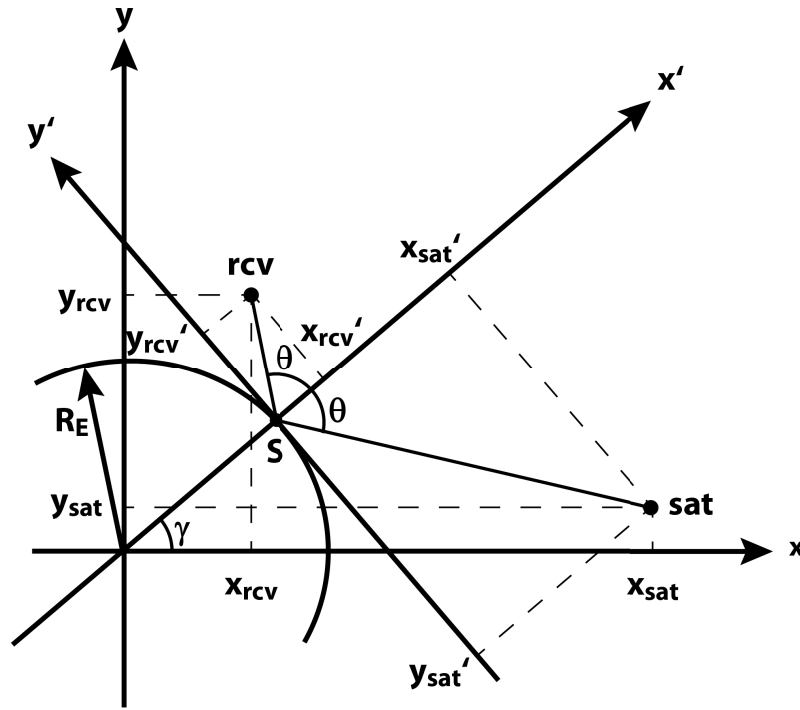


Figure 2.5: System geometry to calculate the coordinates of the reflection point S . The main issue is to find the angle γ so that the incident angle θ equals the reflected one. Similar figure can be found in Martín-Neira (1993)

The Gaussian mean radius of the sphere R_E is calculated as

$$R_E = \sqrt{MN}, \quad (2.4)$$

with M the curvature of the meridian ellipse and N the radius of curvature in the prime vertical

$$M = \frac{a^2 \cdot b^2}{\sqrt{(a^2 \cos^2 \phi_{rcv} + b^2 \sin^2 \phi_{rcv})^3}}, \quad N = \frac{a^2}{\sqrt{a^2 \cos^2 \phi_{rcv} + b^2 \sin^2 \phi_{rcv}}}, \quad (2.5)$$

where a respectively b represent the values of the semi-major and semi-minor axis as defined for the WGS84 ellipsoid in (ICD-GPS-200D, 2010) and ϕ_{rcv} the receiver latitude.

The receiver and satellite position coordinates (x_{rcv}, y_{rcv}) and (x_{sat}, y_{sat}) respectively, are then transformed to a system of coordinates (x'_{rcv}, y'_{rcv}) and (x'_{sat}, y'_{sat}) respectively, by rotating the system around the z-axis with an angle γ and translating the new +x-axis with a distance equal to the radius of the sphere R_E

$$\begin{pmatrix} x'_{rcv} \\ y'_{rcv} \end{pmatrix} = \begin{pmatrix} \cos \gamma & \sin \gamma \\ -\sin \gamma & \cos \gamma \end{pmatrix} \begin{pmatrix} x_{rcv} \\ y_{rcv} \end{pmatrix} - \begin{pmatrix} R_E \\ 0 \end{pmatrix}, \quad \begin{pmatrix} x'_{sat} \\ y'_{sat} \end{pmatrix} = \begin{pmatrix} \cos \gamma & \sin \gamma \\ -\sin \gamma & \cos \gamma \end{pmatrix} \begin{pmatrix} x_{sat} \\ y_{sat} \end{pmatrix} - \begin{pmatrix} R_E \\ 0 \end{pmatrix}. \quad (2.6)$$

To insure that the incident angle equals the reflected one, Snell's Law is used

$$\frac{x'_{sat}}{y'_{sat}} = -\frac{x'_{rcv}}{y'_{rcv}}. \quad (2.7)$$

Substituting Equation (2.6) into Equation (2.7) and setting $t = \tan \frac{\gamma}{2}$, the following equation is obtained after some arrangements

$$c_4 t^4 + c_3 t^3 + c_2 t^2 + c_1 t + c_0 = 0, \quad (2.8)$$

with

$$\begin{aligned} c_0 &= (x_{sat} y_{rcv} + y_{sat} x_{rcv}) - R_E (y_{sat} + y_{rcv}), & c_1 &= -4 (x_{sat} x_{rcv} + y_{sat} y_{rcv}) + 2 R_E (x_{sat} + x_{rcv}), \\ c_2 &= -6 (x_{sat} y_{rcv} + y_{sat} x_{rcv}), & c_3 &= 4 (x_{sat} x_{rcv} + y_{sat} y_{rcv}) + 2 R_E (x_{sat} + x_{rcv}), \\ c_4 &= (x_{sat} y_{rcv} + y_{sat} x_{rcv}) + R_E (y_{sat} + y_{rcv}). \end{aligned}$$

To calculate the distance between the receiver to the point of specular reflection S as a function of the elevation of the transmitter above the local horizon, the receiver position \mathbf{r}_r is defined that way that it is located along the y -axis at an altitude H_s meters above the Earth surface so that

$$\mathbf{r}_r = \begin{pmatrix} x_{rcv} \\ y_{rcv} \end{pmatrix} = \begin{pmatrix} 0 \\ R_E + H_s \end{pmatrix}. \quad (2.9)$$

The position vector of the GPS transmitter \mathbf{r}_t expressed in terms of the elevation angle E above the local horizon plane at the receiver location and the angle τ formed by the triangle RTO' (stressed in red in Figure 2.6) is

$$\mathbf{r}_t = \begin{pmatrix} x_{sat} \\ y_{sat} \end{pmatrix} = \begin{pmatrix} r_t \cos(E + \tau) \\ r_t \sin(E + \tau) \end{pmatrix}, \quad (2.10)$$

with r_t is the orbital radius of the transmitter.

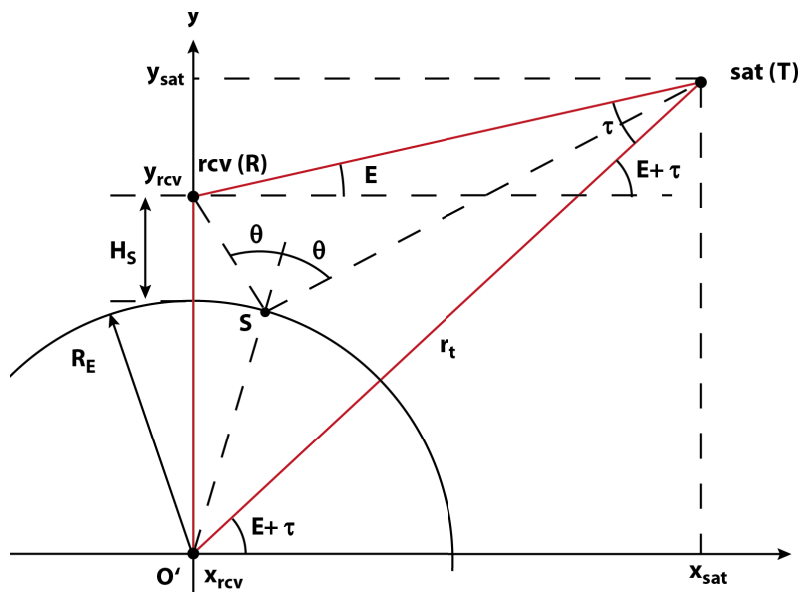


Figure 2.6: Geometry used to express the transmitter coordinates as a function of his elevation above the local horizon. Similar figure can be found in Martín-Neira (1993).

Using the trigonometric sine formula in the RTO' triangle

$$\frac{\sin\left(\frac{\pi}{2} + E\right)}{r_t} = \frac{\sin \tau}{R_E + H_s},$$

we finally obtain

$$\begin{pmatrix} x_{sat} \\ y_{sat} \end{pmatrix} = \begin{pmatrix} r_t \cos E \sqrt{1 - \frac{R_E + H_s}{r_t^2} \cos^2 E} - (R_E + H_s) \sin E \cos E \\ r_t \sin E \sqrt{1 - \frac{(R_E + H_s)^2}{r_t^2} \cos^2 E} + (R_E + H) \cos^2 E \end{pmatrix}. \quad (2.11)$$

An iterative scheme based on the modified Newton-method is used to solve for a solution of the angle γ that fulfils the condition of equal angle of incidence $\theta = 90 - E$. With a solution for γ , the position of the specular reflection point S is

$$\begin{pmatrix} x_s \\ y_s \end{pmatrix} = \begin{pmatrix} R_E \cos \gamma \\ R_E \sin \gamma \end{pmatrix}. \quad (2.12)$$

2.2.3 GPS-R Altimetry Methods

Like in positioning, two different GPS-R methods exist to derive water level heights: the code and the phase based.

Indeed, the geometric path delay $\Delta\rho$ of the reflected signal with respect to the direct one, can also be expressed in terms of the recording time-delay Δt between the time-of-arrival of the direct t_{drct} and the reflected signal t_{refl}

$$\Delta\rho = c\Delta t = c(t_{refl} - t_{drct}), \quad (2.13)$$

where c denotes the speed-of-light.

Moreover, the relative time-delay in the reception of the signal also causes a phase difference $\Delta\varphi$ between the measured phase of the reflected φ_{refl} and the direct φ_{drct} signal which in turn can also be expressed as geometric excess path $\Delta\rho$ in metres

$$\Delta\varphi = \varphi_{refl} - \varphi_{drct}, \quad (2.14)$$

$$\Delta\rho = \lambda_i \Delta\varphi + \lambda_i N_{amb}, \quad (2.15)$$

where N_{amb} is the ambiguity (Section 2.1.4) and λ stands for the used wavelength with subscript i indicating the signal frequency L1 or L2.

Code based GPS-R Altimetry

The primary observation of the code based GPS-R is the time-delay Δt . As described in Section 2.1.2, the direct signal undergoes an acquisition and tracking process from which a

replica code of the incoming PRN is determined. Based on the transmitter-surface-receiver geometry, delay and Doppler shift of the reflected signal can be approximated. These are added to the determined replica code of the direct signal and are used to initiate an acquisition process of the reflected signal. After the reflected signal is coarsely defined in delay and frequency, it is cross-correlated over a range of delays and frequencies and averaged over consecutive coherent correlations. For a mirror-like surface, the result of this cross-correlation process in the time domain, called waveform, is a very sharp triangle. The searched time-delay is given by the peak-to-peak measurement between the reflected and the direct correlation function (Figure 2.7). However due to the reflection process, the waveform of the reflected signal becomes wider and smoother as the roughness of the reflecting surface increases (Rius et al., 2002). The challenge of the method is thus to accurately determine the peak of the reflected signal.

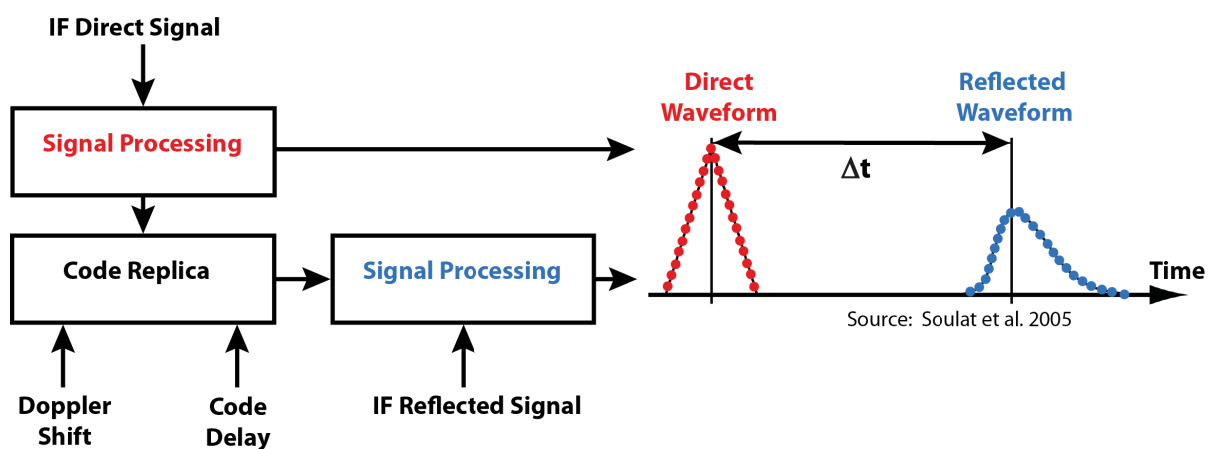


Figure 2.7: Simplified scheme of code based GPS-R altimetry. The geometrical excess path from which the relative height between receiver and reflecting surface is calculated, corresponds to the time-delay Δt given by the peak-to-peak distance between the waveform of the reflected and the direct signal multiplied with the speed-of-light.

Martín-Neira et al. (2001) was the first to present results of a ground GPS L1 C/A-code-based GPS-R experiment over the Zeeland Bridge in The Netherlands. The proposed method uses a Peak-to-Peak detection algorithm for each pair of cross-correlation signals (replica-direct signal and replica-reflected signal) based on an interpolation around the correlation spike. A Root Mean Square Error (RMSE) of the estimated sea surface height with respect to the true value of 3.3 m could be reached. Ruffini et al. (2004) obtained during a flight at an altitude of 1 km, an altimetric accuracy of 1 dm with a spacial resolution of 20 km. The used method consists of tracking the GPS L1 C/A-code peak of the direct signal with the software receiver and fitting the reflected correlation function to a theoretical model waveform. The accuracy of the two cited examples are restricted by the chipping rate of the C/A-code leading to a narrow bandwidth of approximately 2-MHz (Section 2.1.2). To overcome this limitation, Martín-Neira et al. (2011) proposed a so called GNSS-R interferometric (GNSS-Ri) approach. The main difference in the used template is to determine the waveform of the reflected signal. In the conventional C/A-code-based GNSS-R, the reflected signal is correlated with an internally stored PRN replica in the receiver that is associated to a particular satellite. In the case of GNSS-Ri, the observations are obtained by directly cross-correlating the direct and reflected signals so

that no replica is needed. The discrimination is provided by a high-gain, directivity and narrow beam antenna and a relative delay and Doppler shifts estimation. The primary advantage of GNSS-Ri is that it allows the use of the full power spectral density of all the transmitted GNSS signals whether the codes are known or not. The resulting waveform presents a sharper leading edge allowing one to determinate the time-delay with approximately twice the precision than with the C/A-code based method (Cardellach et al., 2014). Rius et al. (2012) demonstrated the proof of the concept in a ground-based experiment and reached a 7.5 cm uncertainty in 1 sec. of measurements. The main difficulty encountered was the contamination of the altimetric observations by multiple correlated signals from more than one satellite because of the minimal differences in delay and Doppler shift values due to the low altitude of the receiver antenna. Another disadvantage, is the large signal loss that results from correlating two weak signals compared to the correlation with a model (Lowe et al., 2014). This loss is compensated through the use of a high-gain, directivity and narrow beam antenna that could be a limitation in space-based applications.

Phase based GPS-R Altimetry

In the phase based GNSS-R approach (the method utilized in this thesis), phase observations are used. The main advantage of this method is that the variations in the range can be extracted with much better precision than the code based one. Indeed, an entire cycle corresponding to a wavelength of λ of approximately 19 cm for L1 frequency, permits a measurement of around 0.5 mm per carrier phase degree. The acquisition and tracking process is the same as the code based method (Figure 2.7). However, the main difference is that not the average of consecutive correlation power is used but rather the average of consecutive correlation sums of the I and Q signal components from which a carrier phase angle Φ is computed

$$\Phi = \text{atan}(Q, I). \quad (2.16)$$

Thus the primary observation of both methods are different (time-delay and phases) but from the signal processing not independent from each other.

Treuhaft et al. (2001), demonstrated the use of phase observations with a ground-based GPS altimetric experiment over Crater Lake, in Central Oregon, with an altitude of 480 m over the lake surface. A physical model of the complex GPS cross-correlation was used to extract the differential delay of the reflected and direct signal. Altimetric information over 12 min. of data length, was estimated for two GPS satellites showing a 2.5 cm precision. Cardellach et al. (2004) calculated phase delay altimetry by analysing the interferences found in radio occultation data from the CHAMP satellite (Beyerle et al., 2005). Topographic ice-profiles at the North Pole have been generated with a vertical precision of 0.7 m at approximately 1 km of horizontal sampling. Helm (2008) extracted relative altimetric heights with 2 cm precision using an open-loop tracking of GPS L1 reflected signals. During the experiment, an antenna was tilted toward and placed 599 m above the lake Kochelsee in the Bavarian Alps. Semmling et al. (2011) estimated sea level heights in Greenland with a Root Mean Square (RMS) of 9.7 cm for L1 and 22.9 cm

for L2 using an altimetric model based on ray tracing and Fourier analysis. Fabra et al. (2012) retrieved, for an observation period of 7 months, absolute ellipsoidal heights over sea ice with an RMS of 15.4 cm averaged over one-day. This developed method uses the coherent differential phase between direct and reflected signals collected from a fixed platform placed at 650 m above sea surface in Greenland. Löfgren (2014) extracted sea level observations at the observatory of Onsala in Sweden, by analysing the phase-delay between the direct and the reflected signals as well as the Signal-to-Noise Ratio (SNR) of the direct signals recorded by a standard geodetic receiver. He reached a RMS of 3.0 to 5.0 cm for one month of observation.

The accuracy of the phase-based GNSS-R method is limited by the difficulty of resolving the ambiguous integer number of cycles N_{amb} in Equation (2.15). Semmling et al. (2014) uses reference height tracks by linear interpolating between the water gauge stations located in the vicinity of the experiment. At crossover points of reflection tracks with height reference tracks, a phase ambiguity estimate is determined and used to extract water level heights.

2.3 Reflection Process

A mandatory condition of the phase-based GPS-R method, is the continuous measurement of reflected phase observations. GPS-R reflected signals contain a coherent and an incoherent component that correlates with the roughness of the reflecting surface. When the surface is very rough, the coherent part of the signal becomes very small and introduces random phase behaviour that will be explained in the next Subsection 2.3.1. Additionally, the more the surface roughness increases the more the reflected signal power decreases. A process that can be approximate with the fresnel coefficient presented in the Subsection 2.3.2.

2.3.1 Coherent Phase Observations

The definitions and relationships described within this section are taken from Beckmann and Spizzichino (1987).

The shape of the reflecting surface, (dependent on the EM wavelength λ and the angle of incidence θ) determines two different reflection types: specular and diffuse.

For visualization purposes of both types of reflections, a Cartesian coordinates system x, y, z is defined with the origin at the specular point S and with unit vectors $\mathbf{x}_0, \mathbf{y}_0, \mathbf{z}_0$ (Figure 2.8). The surface is represented by the function $\zeta = \zeta(x, y)$ that describes the statistical distribution of the surface irregularities (roughness) and their deviation from a mean surface height defined by the plane $z = 0$. The direct ray \mathbf{k}_1 always lies in the xz plane and the incidence angle θ_1 is defined between \mathbf{k}_1 and \mathbf{z}_0 . The scattering angle θ_2 is situated between \mathbf{z}_0 and the scattering vector \mathbf{k}_2 . For lateral scattering out from the plane of incidence ($\mathbf{k}_1, \mathbf{z}_0$), a third angle θ_3 is defined. However only one-dimensionally rough surfaces will be taken into account, so that $\zeta(x, y) = \zeta(x)$ and $\theta_3 = 0$ and thus \mathbf{k}_2 lies in the xz plane.

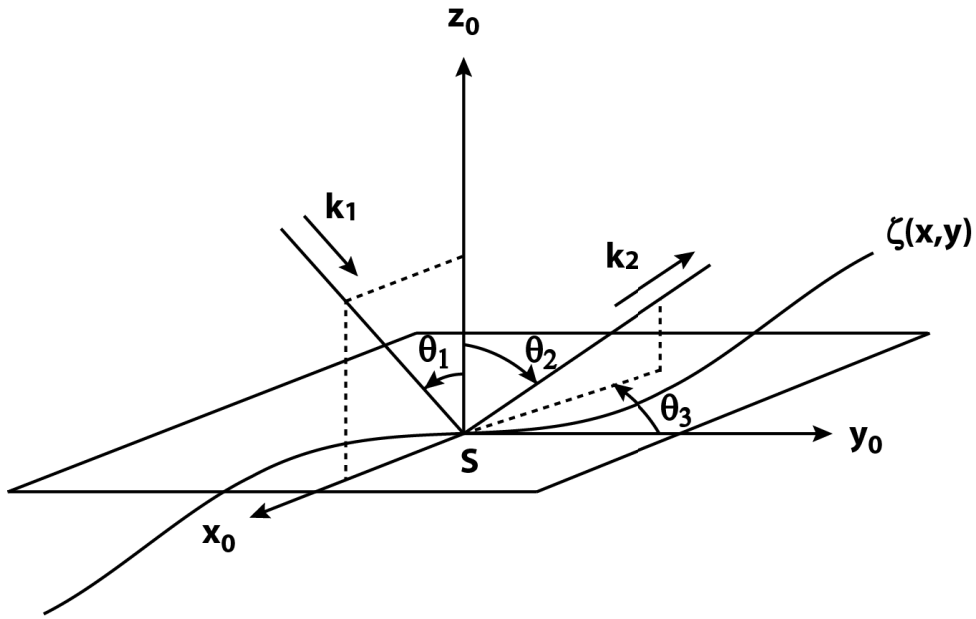


Figure 2.8: Scattering geometry. The incident ray \mathbf{k}_1 , lying in the (x, z) plane, is reflected at the specular point S as a single ray \mathbf{k}_2 . The angle of incidence θ_1 is defined between the \mathbf{z}_0 and \mathbf{k}_1 and the scattering angle θ_2 between \mathbf{k}_2 and \mathbf{z}_0 (but measured in opposite from the positive z axis). For lateral scattering the angle θ_3 is defined. Similar graphic can be found in Beckmann and Spizzichino (1987).

In a very general manner, a specular reflection is the reflection of an EM wave on a mirror-like surface so that the incoming and reflecting EM waves obey the laws of classical ray optics. One can visualize the incoming ray \mathbf{k}_1 as a single ray that reflects as another single ray \mathbf{k}_2 at the specular point S (Figure 2.9A).

The particularity of such a reflection is that it has a well defined phase φ

$$\mathbf{E} = \mathbf{E}_0 e^{i\varphi} = \mathbf{E}_0 e^{i(\mathbf{k}\cdot\mathbf{r} - \omega\mathbf{t})}, \quad (2.17)$$

where $\mathbf{k} = \frac{2\pi}{\lambda}$ is the wave number defined as the number of complete wave cycles of an EM field that exists in one meter of linear space, ω the angular frequency of the carrier and \mathbf{r} the position vector along the ray trajectory

$$\mathbf{r} = x\mathbf{x}_0 + \zeta(x)\mathbf{z}_0. \quad (2.18)$$

In contrast, a rough surface scatters diffusely the incident ray \mathbf{k}_1 , in i different single rays \mathbf{k}_i in different directions. In this case, the reflecting surface can be visualized as a composition of n facets with different orientation that individually act as a mirror-like surface (Figure 2.9B). In a diffuse reflection, each scattered ray introduces its own phase-offset ϕ_i

$$\mathbf{E} = \sum_{k=1}^n \mathbf{E}_i e^{i(\mathbf{k}\cdot\mathbf{r} - \omega\mathbf{t} + \phi_i)}. \quad (2.19)$$

Generally, the scattering process is a mix of both types of reflections with different proportions depending on the irregularities of the reflecting surface.

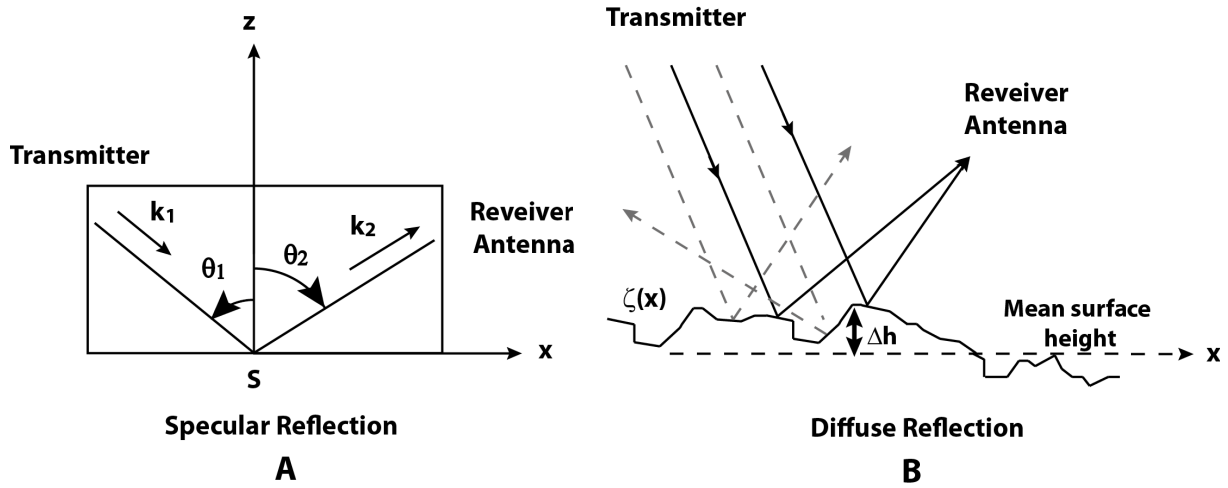


Figure 2.9: Illustration of: **A** a specular reflection where the incoming ray can be visualized as a single ray that reflects as another single ray and **B** a diffuse reflection where the incoming ray is scattered in different directions due to the irregularities of the surface.

Following Beckmann and Spizzichino (1987) (pp. 149-151), the phase difference $\Delta\phi$ between two waves 1 and 2 at the points $\zeta(x_1)$ and $\zeta(x_2)$ of the surface is considered as

$$\Delta\phi = \frac{2\pi}{\lambda} [(x_1 - x_2) (\sin\theta_1 - \sin\theta_2) + (\zeta_1 - \zeta_2) (\cos\theta_1 + \cos\theta_2)] , \quad (2.20)$$

with $\zeta_1 = \zeta(x_1)$, $\zeta_2 = \zeta(x_2)$.

For $\theta_1 \neq \theta_2$, $\Delta\phi$ will always vary over many intervals 2π independently of the distribution of ζ . The phases of the individual scattered waves will be uniformly distributed over the basic phase cycle. In this case the phases are incoherent. Thus, the field scattered in the non-specular direction ($\theta_1 \neq \theta_2$) is always incoherent.

For $\theta_1 = \theta_2 = \theta$, a reflection in the specular direction, the phase of each elementary wave is

$$\phi = \frac{4\pi}{\lambda} \zeta(x) \cos\theta , \quad (2.21)$$

with variance

$$\sigma_\phi = \frac{(4\pi)^2}{\lambda^2} \cos^2\theta \sigma_\zeta . \quad (2.22)$$

If there are no irregularities, for example a reflection on a perfectly mirror-like surface, then $\sigma_\zeta = 0$ and all σ_ϕ are equal to zero. In this case the phase is coherent.

If the variance of the surface irregularities $\sigma_\zeta \gg \lambda^2/\cos^2\theta$, then the variance of the resulting phase $\sigma_\phi \gg 4\pi^2$. In this case, the phase of the individual scattered waves ϕ in the specular direction are uniformly distributed over an interval length of $[0, 2\pi]$ and there is no phase coherency.

Now, let the resulting vector of a reflected signal in the specular direction be described as the

sum of n coplanar vectors (Figure 2.10); c.f. Beckmann and Spizzichino 1987, pp. 119-123

$$U = Ae^{i\varphi} = \sum_{j=1}^n r_j e^{i\phi_j}, \quad (2.23)$$

with A and φ the resulting amplitude and phase, r_j the amplitudes of each n scattered waves and ϕ_j their individual phases.

Transformed to polar coordinates with $I = A \cos \varphi$ and $Q = A \sin \varphi$, we obtain

$$A^2 = I^2 + Q^2. \quad (2.24)$$

Assuming that the I and Q components of A are normally distributed and uncorrelated, then the mean squared amplitude $\langle A^2 \rangle$ is defined as

$$\begin{aligned} \langle A^2 \rangle &= \alpha^2 + s_1 + s_2, \\ \langle A^2 \rangle &= n^2 e^{-\sigma^2} + n(1 - e^{-\sigma^2}), \end{aligned} \quad (2.25)$$

with α the mean value of I , s_1 and s_2 the variance of I and Q respectively and $\sigma = \sqrt{\sigma_\zeta}$ the standard deviation of the reflecting surface from the mean surface level.

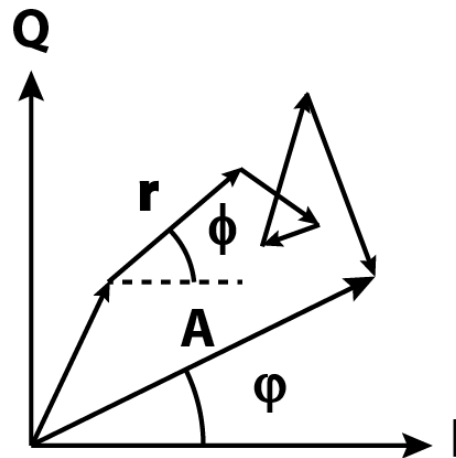


Figure 2.10: Reflected vector of amplitude A and phase φ in the specular direction represented as the sum of n coplanar random vectors with their individual amplitude r and phases ϕ . Similar graphic can be found in Beckmann and Spizzichino (1987).

From Equation (2.25), one can see that the scattered total field in the specular direction is composed of two components. If $\sigma^2 = \sigma_\zeta = 0$, (thus with no irregularities) only the first term remains (n^2) - the coherent one. In this case, the waves interfere and an interferometric fringe becomes visible (Figure 2.11A). This is due to the fact that the mean phase of the reflected wave is known in every point in space. This causes the typical rotation of the receiver complex phasor (Figure 2.11B). If $\sigma^2 \rightarrow \infty$ (very rough surface), the first term vanishes and the second remains (n), the incoherent component. The phase is randomly and normally distributed over an interval length of $[0, 2\pi]$. There is no phase coherency and the power is directly proportional to the number of scatterers. This causes fading and an arbitrary rotation of the receiver phasor,

so that random-phase contributions are added to the total amplitude field A , destroying the interferometric pattern (Figure 2.11C and D).

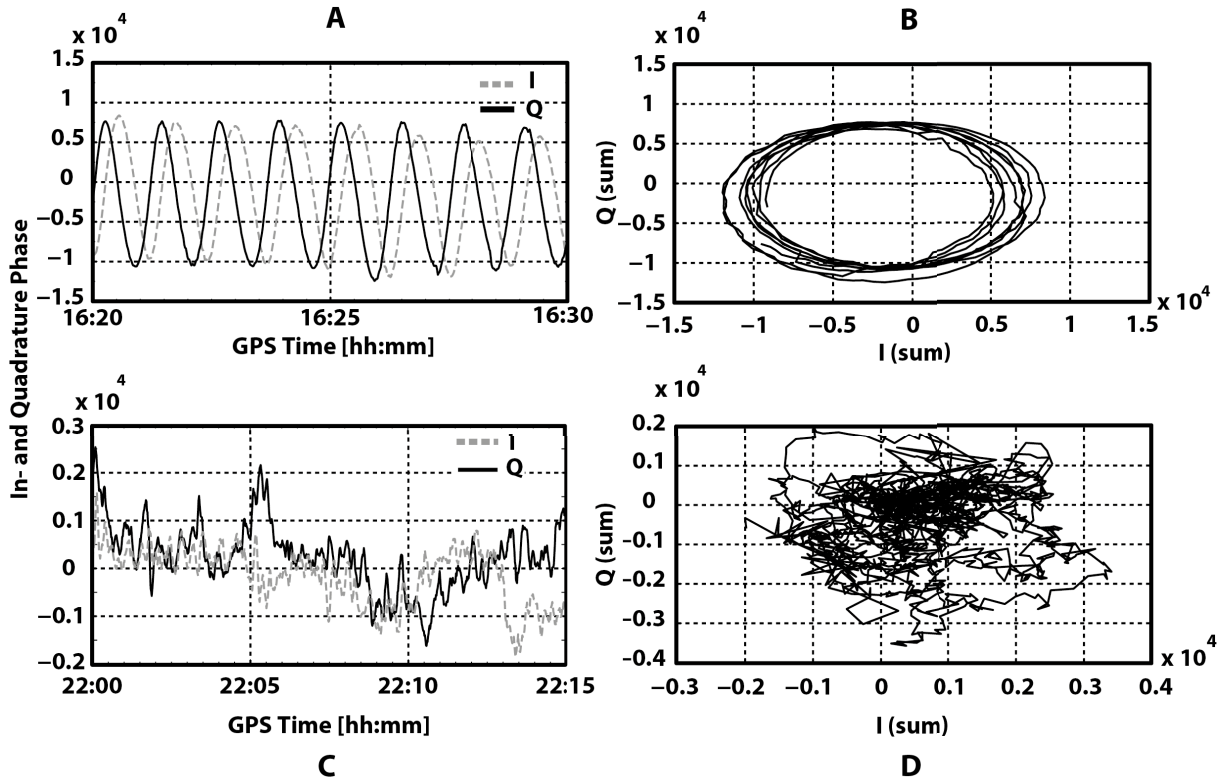


Figure 2.11: **A:** If the reflecting surface is considered to be smooth or slightly rough, the reflected waves interfere and an interferometric fringe is visible. The phase is predominantly coherent. **B:** This causes the typical rotation of the receiver complex phasor. **C:** In contrast, if the surface is very rough, there is no phase coherence. **D:** This causes fading and an arbitrary rotation of the receiver phasor. Data source (A) and (B): Midelt, Morocco, 16 December 2013, PRN 2. Data source (C) and (D): An Bihn hotel, Vietnam, February 25, 2012, PRN 26.

2.3.2 Fresnel Coefficient

The overall electric field \mathbf{E} of a signal is the sum of the horizontal \mathbf{E}_h and vertical \mathbf{E}_v component:

$$\mathbf{E} = \mathbf{E}_h + \mathbf{E}_v, \quad (2.26)$$

where the horizontal component lies within the incidence plane and the vertical component perpendicular to the plane of incidence. Because of it, the horizontal component is also called parallel component and the vertical one perpendicular.

The addition of the two components shows that three different polarization types exist. If one of the electric field components vanish, a linear polarization occurs. If \mathbf{E}_h and \mathbf{E}_v are equal, the resulting vector \mathbf{E} traces a circle and a circular polarization occurs. If \mathbf{E}_h and \mathbf{E}_v have different values, the vector \mathbf{E} traces an ellipse so that an elliptical polarization occurs. Depending on the direction of rotation, as viewed from the receiving antenna, a distinction is made. If \mathbf{E} rotates in a counter clock direction, the polarization is right-handed otherwise it is left-handed.

The GPS signals are transmitted as RHCP (Section 2.1.2). However, when the signal reflects over a surface, each of the \mathbf{E}_h and \mathbf{E}_v encounters an attenuation depending on the surface properties.

For a plane and smooth Earth surface, the characteristics of the reflection is described by the reflection coefficients Γ_h and Γ_v

$$\Gamma_h = \frac{\mathbf{E}_h^i}{\mathbf{E}_h^o} = \frac{\sin E - \sqrt{K^2 - \cos^2 E}}{\sin E + \sqrt{K^2 - \cos^2 E}}, \quad (2.27)$$

$$\Gamma_v = \frac{\mathbf{E}_v^i}{\mathbf{E}_v^o} = \frac{K^2 \sin E - \sqrt{K^2 - \cos^2 E}}{K^2 \sin E + \sqrt{K^2 - \cos^2 E}}, \quad (2.28)$$

where E represents the elevation angle, the superscript i and o the incoming and reflected signal, respectively, and K the normalized admittance of the medium.

This reflects the dielectric properties of the reflecting surface and is defined as (Beyerle, 2009):

$$K \equiv \frac{n_2}{n_1}, \quad (2.29)$$

$$n_2 = \sqrt{\frac{\epsilon}{\epsilon_0} + i60\lambda\sigma}, \quad (2.30)$$

where $\epsilon_{rc} = \epsilon/\epsilon_0$ is the relative complex permittivity, σ the conductivity and n_1 is the refractive index of air (≈ 1.0004).

These reflection coefficients can also be represented as the sum of two circularly polarized signals: one containing the component of the original circular polarisation Γ_0 called co-polarisation and a component of orthogonal polarization Γ_x called cross-polarisation (Hannah, 2001):

$$\Gamma_0 = \frac{\Gamma_H + \Gamma_V}{2}, \quad (2.31)$$

$$\Gamma_x = \frac{\Gamma_H - \Gamma_V}{2}. \quad (2.32)$$

Figure 2.12 in red, illustrates the circular Fresnel coefficient for an incident RHCP L1 GPS signal on a perfectly smooth surface. For the calculation, a relative dielectric constant of $\epsilon_{rc} = 80$ and a conductivity of $\sigma = 4$ mho/m is used (Helm, 2008).

For an elevation angle of 0 deg, the reflected signal is RHCP. Thus, the horizontal and vertical components (Γ_h, Γ_v) are equal, the co-polar component Γ_0 is 1 and the cross-polar component Γ_x is zero. For elevation angles under 6 deg, the co-polar component decreases and the cross-polar component increases. At 6 deg, both components have the same power (50%). This angle is called the Brewster angle. For elevation angles exceeding 6 deg, the reflection is essentially cross-polar (LHCP). For elevation angle between 6 and 30 deg, the reflected LHCP signal power lies between 50 and 78%.

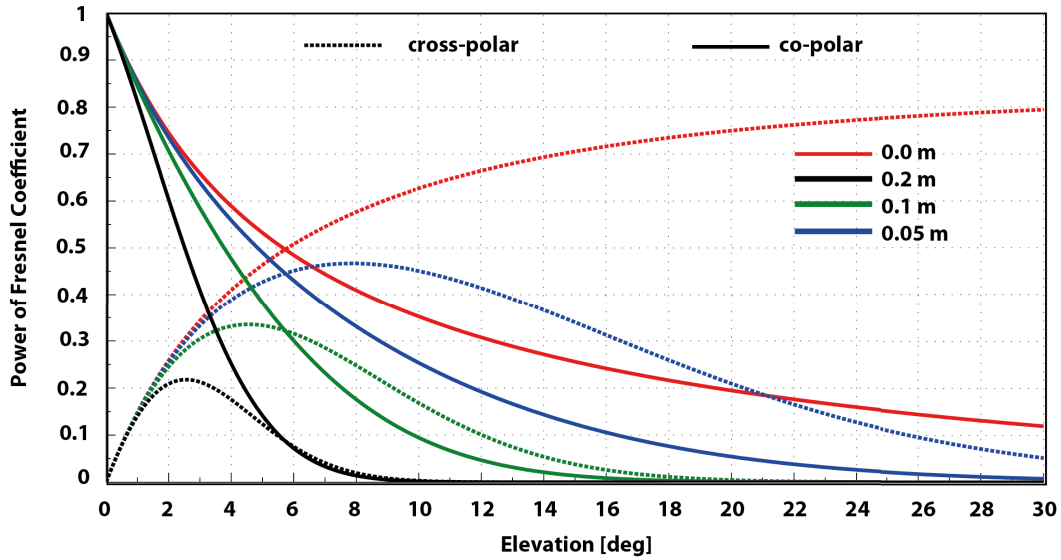


Figure 2.12: Power of Fresnel Coefficients for L1 GPS signals in relation to different water roughness values.

In case of a diffuse reflection, a magnitude reduction factor that considers the roughness of the surface has to be applied to the Fresnel coefficient. Considering only the coherent reflection, the horizontally and vertically polarized components change to:

$$\hat{\Gamma}_h = \langle \rho_{spec} \rangle \Gamma_h, \quad (2.33)$$

$$\hat{\Gamma}_v = \langle \rho_{spec} \rangle \Gamma_v, \quad (2.34)$$

with ρ_{spec} defined as:

$$\rho_{spec} = \exp \left[-\frac{1}{2} \left(\frac{4\pi \Delta h \cos \theta}{\lambda} \right)^2 \right]. \quad (2.35)$$

Figure 2.12 illustrates the power of the Fresnel coefficients for different mean sea surface heights (0.2 m, 0.1 m and 0.05 m). For a σ_h of 0.2 m, the power of the cross-polar (LHCP) and the co-polar (RHCP) component, drops about 50% and 40%, respectively, by elevation angle around 7 deg so that only approximately 5% of the LHCP and RHCP signal power remains (Fig. 2.12 black). Only for elevation angles lower than 6 deg, coherent reflection can be expected. Similarly, for σ_h of 0.1 m, 5% of the LHCP signal power remains for an elevation angle of 14 deg. For the RHCP signal for an elevation angle of 11 deg. For σ_h of 5 cm, the power of the LHCP remains over 5%, for elevation angle exceeding 30 deg but for the RHCP at 20 deg of elevation.

2.4 GPS Phase and Code Observation and their Systematic Errors

The GPS-R phase based altimetric method is based on the determination of the geometric excess path between the transmitter and the receiver. Until now, the receiver outputs are

considered in their idealized form. Recalling the discussion in Section 2.1.3, Equations (2.1) and (2.2), the GPS code pseudorange PR in meters and carrier phase observations Φ in cycles are formulated as

$$PR_{rcv}^{sat_i}(t_r, t_e) = c(t_r - t_e) + \delta, \quad (2.36)$$

$$\Phi_{rcv}^{sat_i}(t_r) = \Phi_{rcv}(t_r) - \Phi^{sat_i}(t_e) + N_{amb,rcv}^{sat_i} + \delta', \quad (2.37)$$

where subscript rcv and superscript sat denote the receiver and the i th satellite respectively, t_r and t_e the reception and emission time respectively, c the speed-of-light, N_{amb} the ambiguity related to the receiver rcv and the satellite sat^i and δ , δ' systematic errors including noise.

The signal encounter propagation effects due to the crossing of the ionosphere and troposphere, the magnitude of which depends on the elevation angle of the signal path and the atmospheric environment where the receiver is located. Instrumental components like antenna phase centre offset and variations and phase wind-up effect, falsify additionally the issued receiver ranges.

In the present section, the relevant systematic error sources within this thesis are defined. For completeness, the remaining ones will also be presented but in a compact way. At the end of this section, the final phase observation equation used within this thesis will be presented.

2.4.1 Tropospheric Delay

In this section, the delay effect on the GPS signal propagation caused by the troposphere is presented. Actually, the term tropospheric delay is misleading because roughly 25% of the delay is caused by atmospheric gases above the troposphere, namely from the tropopause and the stratosphere (Spilker Jr., 1996d, chap. 13).

The neutral atmosphere that consists of dry gases and water vapour, is a non-dispersive medium for microwave signals and thus invariant to GPS frequencies. Therefore, the code and carrier phase observations are delayed by the same amount and the tropospheric effects can not be removed by combining different frequencies as in the case of the ionospheric delay (Section 2.4.6).

The troposphere produces delay effects in the order of 2-25 m depending on the incoming elevation angle of the signal and the location of the receiver (Spilker Jr., 1996d, chap. 13). This path delay can be divided into a dry, also called hydrostatic, and a wet component. The dry component represents $\approx 90\%$ of the entire path delay and can be easily modelled because of its slow temporal and spatial variations. The wet component is caused by water vapour in the lower troposphere. Though the wet component is much smaller, (from a few mm in the dry Arctic areas or in deserts to 0.4 m in tropical regions (Andrei and Chen, 2009)) it is more difficult to model because of his high variability with position and time.

Following (Hofmann-Wellenhof et al., 2008, pp. 109-116), the tropospheric delay in the zenith direction, called the Zenith Total Delay (ZTD), is defined as the difference between the optical

path and the geometrical path for a given receiver position P_1 and satellite position P_2

$$ZTD = \int_{P_1}^{P_2} n ds - \int_{P_1}^{P_2} ds = \int_{P_1}^{P_2} (n - 1) ds, \quad (2.38)$$

with n the refractive index and s the curvilinear index along the actual signal path.

Usually, instead of the refractive index n , the refractivity N is used

$$N = (n - 1) 10^6, \quad (2.39)$$

so that Equation (2.38) becomes

$$ZTD = 10^{-6} \int_{P_1}^{P_2} N ds. \quad (2.40)$$

The refractivity is composed of a wet N_{wet} and dry N_{dry} refractivity component

$$N = N_{dry} + N_{wet}. \quad (2.41)$$

According to this decomposition, the total tropospheric zenith path delay is

$$ZTD = 10^{-6} \int_{P_1}^{P_2} N_{dry} ds + 10^{-6} \int_{P_1}^{P_2} N_{wet} ds = ZHD + ZWD, \quad (2.42)$$

where ZHD and ZWD denote respectively, the Zenith Hydrostatic Delay and the Zenith Wet Delay.

However, the GPS signals do not arrive from the zenith but from slant directions. Mapping Functions (MF) are used to project the a-priori zenith hydrostatic and wet delay to any given satellite elevation angle E

$$STD = ZHD \cdot MF_{dry}(E) + ZWD \cdot MF_{wet}(E), \quad (2.43)$$

where STD denotes the Slant Total Delay.

The Mapping Function (MF) are based on a functional formulation that describes how the slant delay varies with respect to a set of parameters. These parameters are calculated on the foundation of atmospheric data sources, parameterization and ray-tracing algorithms for their calibration (Urquhart et al., 2013). The lower the elevation angle E is, the longer the GPS signals have to travel through the troposphere to reach the receiver antenna. Consequently, the impact of tropospheric refractivity is higher. Indeed, the Slant Total Delay is about 2.30 m close to the zenith (Businger et al., 1996) and reaches about 23 m for a satellite at an elevation angle of 5 deg (Foelsche and Kirchengast, 2001).

More details can be found in Spilker Jr. (1996d); Hofmann-Wellenhof et al. (2008).

2.4.2 Phase Wind-up

Phase wind-up effects are due to the electromagnetic nature of the circularly polarised waves of the GPS signals and affect only the carrier phase measurements. The phase wind-up depends on the relative orientation of the satellite and receiver antennas, and the direction of the Line-Of-Sight (LOS). For a ground-based receiver, phase wind-up results from satellite orbital motion. As the satellite moves along its orbit, it must constantly perform a rotation (yaw) to ensure that the solar panels are facing the Sun to optimally collect the solar energy while the satellite antenna keeps pointing to the Earth's centre (Wu et al., 1993). This rotation changes the reference direction of the antenna and induces variations in the observed carrier phase values, that the receiver misunderstands as a range variation (up to one cycle for a complete revolution of the antenna) (Beyerle, 2009).

For positioning tasks a correction is only needed if very high precision is required. However, this error completely cancels out for double differential phase observations (Kouba, 2009). Beyerle (2009) showed that for GNSS-R applications, the phase wind-up of coherently reflected signals (Section 2.3.1) differs by up to several centimetres from the value experienced by the direct signal and thus needs to be taken into account.

Based on Beyerle (2009), the orientation of the transmitter antenna \mathbf{t} is described by the following unit vectors: \mathbf{t}^a , \mathbf{t}^t and \mathbf{t}^b with the subscript a , t and b standing for aligned, transverse and bore-sight respectively. This forms a right-hand orthonormal coordinate system (Figure 2.13A).

The antenna bore-sight unit vector \mathbf{t}^b points to the centre of the Earth and is defined as

$$\mathbf{t}^b = \frac{-\mathbf{r}_{\text{Sat}}}{\|\mathbf{r}_{\text{Sat}}\|}, \quad (2.44)$$

with vector \mathbf{r}_{Sat} representing the satellite coordinates in the ECEF coordinate system.

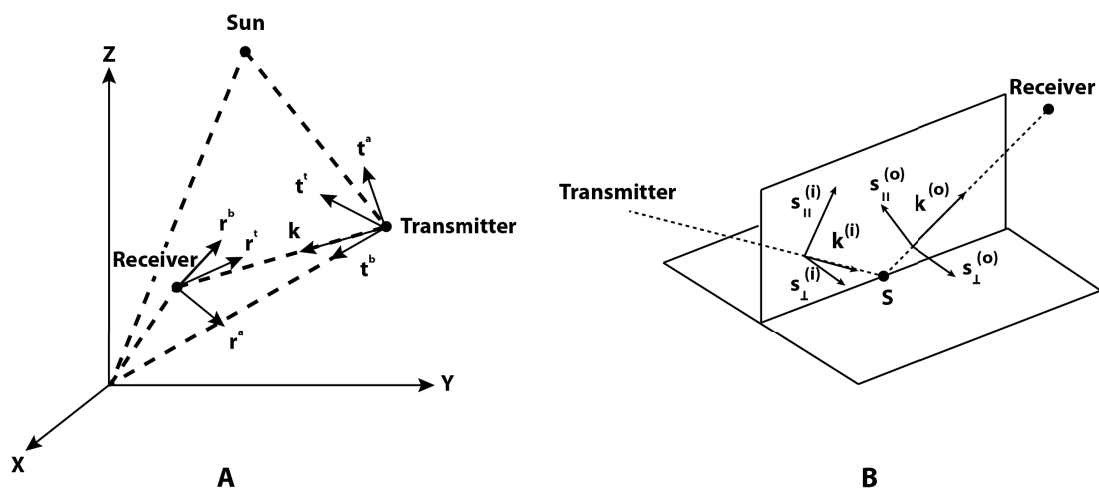


Figure 2.13: **A:** Schematic representation of the transmitter and receiver antenna unit vectors describing the aligned (index a), transverse (index t) and bore-sight (index b) directions in the ECEF coordinate system. **B:** Schematic representation of the incoming (index i) and reflected (index o) unit vectors of the signal ray. Similar graphics can be found in Beyerle (2009).

The aligned transmitter antenna unit vector \mathbf{t}^a is the cross-product of the \mathbf{t}^b vector with the unit vector from the satellite to the Sun $\hat{\mathbf{e}}$

$$\hat{\mathbf{e}} = \frac{\mathbf{r}_{\text{Sun}} - \mathbf{r}_{\text{Sat}}}{\|\mathbf{r}_{\text{Sun}} - \mathbf{r}_{\text{Sat}}\|}, \quad (2.45)$$

$$\mathbf{t}^a = \hat{\mathbf{e}} \times \mathbf{t}^b, \quad (2.46)$$

where \mathbf{r}_{Sun} is the sun position in the ECEF coordinate system.

As the vectors form a right-hand orthonormal coordinate system, the transversal vector \mathbf{t}^t is

$$\mathbf{t}^t = \mathbf{t}^a \times \mathbf{t}^b. \quad (2.47)$$

Similarly, the receiver antenna vector \mathbf{r} can be described by the unit vectors $[\mathbf{r}^a, \mathbf{r}^t, \mathbf{r}^b]$ with $\mathbf{r}^b = \mathbf{r}^a \times \mathbf{r}^t$.

In GNSS-R applications, the antenna is tilted toward the reflecting surface, therefore the orientation of the antenna has to be accounted for (Chapter 3).

Finally, we define the normalized wave vector \mathbf{k}

$$\mathbf{k} = \frac{\mathbf{r}_{\text{rcv}} - \mathbf{r}_{\text{Sat}}}{\|\mathbf{r}_{\text{rcv}} - \mathbf{r}_{\text{Sat}}\|}. \quad (2.48)$$

Based on Beyerle (2009), where a detailed derivation of the formulas can be found, the phase wind-up for the direct LHCP and RHCP signal is

$$\Phi_{RHCP}^{Dir} = \text{atan}(\mathbf{T}^t(\mathbf{k}) \cdot \mathbf{r}^a + \mathbf{T}^a(\mathbf{k}) \cdot \mathbf{r}^t, \mathbf{T}^a(\mathbf{k}) \cdot \mathbf{r}^a - \mathbf{T}^t(\mathbf{k}) \cdot \mathbf{r}^t), \quad (2.49)$$

$$\Phi_{LHCP}^{Dir} = \text{atan}(\mathbf{T}^t(\mathbf{k}) \cdot \mathbf{r}^a - \mathbf{T}^a(\mathbf{k}) \cdot \mathbf{r}^t, \mathbf{T}^a(\mathbf{k}) \cdot \mathbf{r}^a + \mathbf{T}^t(\mathbf{k}) \cdot \mathbf{r}^t), \quad (2.50)$$

with

$$\mathbf{T}^t(\mathbf{k}) \equiv (\mathbf{k} \times \mathbf{t}^t) \times \mathbf{k}, \quad (2.51)$$

$$\mathbf{T}^a(\mathbf{k}) \equiv (\mathbf{k} \times \mathbf{t}^a) \times \mathbf{k}. \quad (2.52)$$

The phase wind-up for the reflected LHCP and RHCP signal

$$\Phi_{RHCP}^{Refl} = \text{atan}(\mathbf{S}^t \cdot \mathbf{r}^a + \mathbf{S}^a \cdot \mathbf{r}^t, \mathbf{S}^a \cdot \mathbf{r}^a - \mathbf{S}^t \cdot \mathbf{r}^t), \quad (2.53)$$

$$\Phi_{LHCP}^{Refl} = \text{atan}(\mathbf{S}^t \cdot \mathbf{r}^a - \mathbf{S}^a \cdot \mathbf{r}^t, \mathbf{S}^a \cdot \mathbf{r}^a + \mathbf{S}^t \cdot \mathbf{r}^t), \quad (2.54)$$

with

$$\mathbf{S}^t = \Gamma_h (\mathbf{T}^t(\mathbf{k}) \cdot \mathbf{s}_{\parallel}^{(i)}) \mathbf{s}_{\parallel}^{(o)} + \Gamma_v (\mathbf{T}^t(\mathbf{k}) \cdot \mathbf{s}_{\perp}) \mathbf{s}_{\perp}, \quad (2.55)$$

$$\mathbf{S}^a = \Gamma_h (\mathbf{T}^a(\mathbf{k}) \cdot \mathbf{s}_{\parallel}^{(i)}) \mathbf{s}_{\parallel}^{(o)} + \Gamma_v (\mathbf{T}^a(\mathbf{k}) \cdot \mathbf{s}_{\perp}) \mathbf{s}_{\perp}, \quad (2.56)$$

where Γ_h and Γ_v represent the horizontal and vertical Fresnel coefficient respectively, as defined

in Section 2.3.2 Equation (2.34), and

$$\mathbf{s}_{\perp} = \frac{\mathbf{k}^{(i)} \times \mathbf{k}^{(o)}}{\|\mathbf{k}^{(i)} \times \mathbf{k}^{(o)}\|}, \quad (2.57)$$

$$\mathbf{s}_{\parallel}^{(i)} = \mathbf{s}_{\perp} \times \mathbf{k}^{(i)}, \quad (2.58)$$

$$\mathbf{s}_{\parallel}^{(o)} = \mathbf{s}_{\perp} \times \mathbf{k}^{(o)}, \quad (2.59)$$

where \mathbf{s}_{\parallel} and \mathbf{s}_{\perp} are the parallel and perpendicular components of the incoming and reflected signal, respectively.

To underline the impact of phase wind-up on a phase-based GPS-R altimetric application, a standard GPS-R antennas arrangement is simulated (Figure 2.14). Two antennas are used: a horizontally placed antenna oriented to the north to track the direct signals (Figure 2.14A and D) and a second antenna also oriented to the north but tilted toward the reflecting surface with different zenith angles (45 deg, 90 deg, -45 deg and -90 deg) (Figure 2.14B and E). For the reflected signals, a distinction is made between the different polarizations of the signals due to the reflection (Section 2.3.2). For the simulation, a relative dielectric constant of water $\epsilon_r = 80$ and a refractive index of air 1.0004 is used. As demonstrated in Beyerle (2009), the difference in the carrier phase wind-up effect between direct and reflected signals can cause a significant error of up to several centimetres depending on the relative orientation of the antennas and the used signal polarization (Figure 2.14C, F).

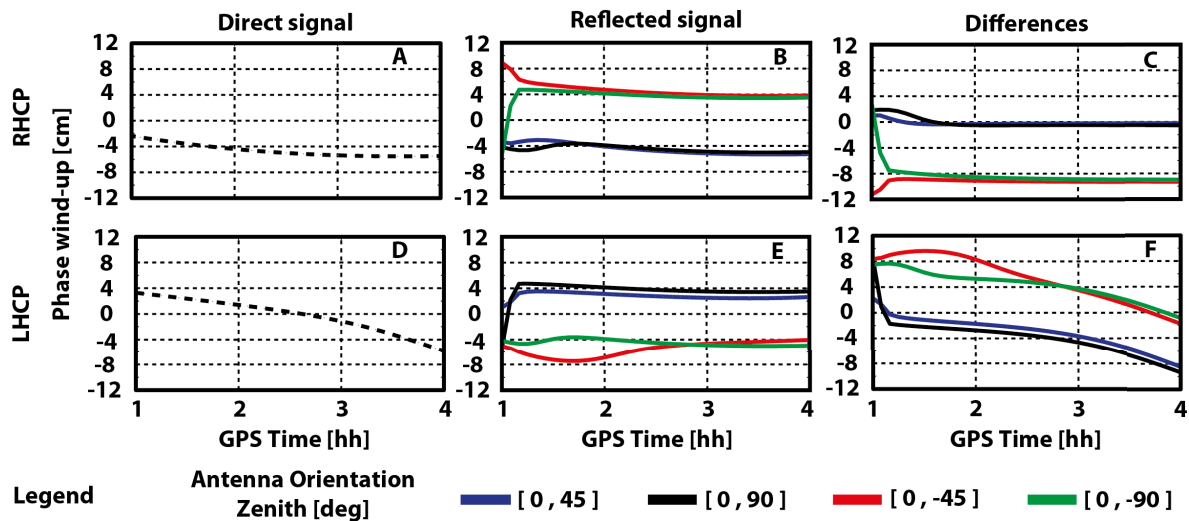


Figure 2.14: Simulated phase wind-up effects in centimetres. **Top:** Panel **A:** Phase wind-up effect for the direct signal using a horizontally placed RHCP antenna. Panel **B:** Phase wind-up effect for the reflected signal using a RHCP antenna tilted with different zenith angles: 45 (blue), 90 (black), -45 (red) and -90 (green) deg. Panel **C:** Phase wind-up effect difference between the reflected and direct signal using RHCP antennas. **Bottom:** Panels **D, E** and **F:** Same simulations using LHCP antennas. Data Source: PRN 29, February 28, 2012, An Bihn hotel, Vietnam.

It can thus be concluded that in phase based GPS-R altimetric applications, with different antennas orientations, the phase wind-up effects have to be corrected.

2.4.3 Antenna Phase Centre Offset and Variation

The calculated geometric distance between satellite and receiver is related to the electrical phase centre of the transmitting GPS satellite antenna and the user receiving antenna. In reality, these phase centres are not identical with the physical centre of the antennas (Hofmann-Wellenhof et al., 2008, pp. 125-130). Since this deviation introduces an error of up to 0.1 m in the height, an adequate calibration of the antennas is necessary (Rothacher, 2001, pp. 88).

A complete description of the antenna phase centre is realized via three closely related definitions that are illustrated in Figure 2.15:

1. The Antenna Reference Point (ARP) which is the physical reference point of the antenna. For a GPS satellite, this point is the Center of Mass (CM) of the spacecraft that describes the motion of the satellite. For a GPS receiver antenna, usually the centre of the antenna screw is used, as the calculated position for that location. The following corrections refer to this point.
2. The Phase Centre Offset (PCO) (Figure 2.15 blue) describes the vector from the ARP to a virtual point called Mean Phase Centre (MPC), which is the midpoint of a hypothetical sphere that approximate the radiation behaviour of a point source with equi-phase wave-fronts (Figure 2.15 green).
3. The Phase Centre Variation (PCV) describes the variation of the real wave-front from the idealized sphere in function of the direction of the incoming/outcoming signal, with regards to the satellite nadir angle and the receiver azimuth and zenith angle, and the signal frequency (Figure 2.15 red).

Regarding the receiver antenna, the values of the phase centre depend on the selected antenna type. Several methods have been developed in order to determine absolute phase centre variations like anechoic chamber measurements or absolute field calibrations (Schmid et al., 2005).

For the commonly used antenna types, the PCO and PCV values are listed and provided by the International GNSS Service (IGS). To standardize the use of these correction terms, an ANTenna EXchange format (ANTEX) was developed. Depending on the selected frequency, the PCO values are given in the local topocentric coordinate system of the antenna defined by three unit vectors East-North-Up ($\mathbf{e}_e, \mathbf{e}_n, \mathbf{e}_u$) and the PCV in function of the azimuth and zenith angle as viewed from the receiver (Figure 2.15). The zenith angles are given in an increasing order with a step of 5 deg starting from 0 to 90 deg and from 90 to 0 deg in a decreasing order for elevation angle. The azimuth angles are also given in an increasing order with an increment of 5 deg starting from 0 to 360 deg.

The carrier phase correction sum of PCO and PCV, called Phase Centre Correction (PCC), for the receiving antenna is calculated as follow (Kersten, 2014)

$$\delta_{PCC_{f,rcv}}(A, E) = r_f + \underbrace{\mathbf{p}_{f,rcv} \cdot \mathbf{e}^{sat}}_{PCO_{f,rcv}} - \underbrace{\Delta\phi_{f,rcv}(A, E)}_{PCV_{f,rcv}(A, E)} \quad (2.60)$$

where A and E represent the azimuth and elevation angle respectively, the subscript f and rcv denote the signal frequency and receiver respectively, $\mathbf{p}_{f,rcv}$ the PCO vector, \mathbf{e}^{sat} the LOS unit vector to the observed satellite and $\Delta\phi$ the phase centre variations.

The term r_f is a constant offset that cannot be determined by any of the up to date calibration methods. It is absorbed by receiver clock offset and float ambiguities or eliminated by forming single or time differences (Schön and Kersten, 2013). For the phase-based GPS-R altimetry method described in this thesis, the value r_f is eliminated by forming single differences.

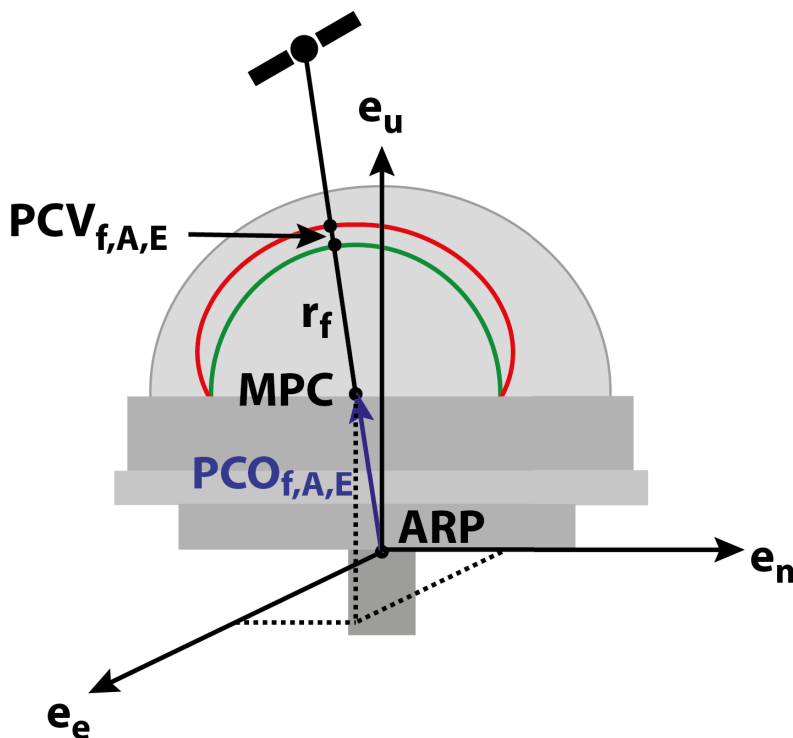


Figure 2.15: Schematic representation of the antenna Phase Centre Correction. The PCC is characterized by (1) the ARP which is the mechanical reference point of the antenna, (2) the PCO that represents the vector from the ARP to the MPC. The MPC is the centre of a sphere that approximates the receiving antenna behaviour. (3) The PCV that gives the variation from the idealized sphere depending on the elevation, azimuth, signal frequency and the signal polarization.

Concerning the antenna phase centre of the satellites, each block (Section 2.1.1) of GPS satellite possesses its own correction terms that are listed by the IGS². The listed PCO values are based on manufacturer specifications. However, the centre of mass of the satellite changes during the lifetime of the satellite (fuel quantity, material ageing) changing the PCO value too. The listed PCV values are given in dependency of the nadir direction α of the satellite to the receiver in a range from 0 to 17 deg. From figure 2.16, the nadir angle α and the zenith angle z as viewed from the receiver antenna, are related by

$$\alpha = \sin^{-1} \left(\frac{R_E}{r} \sin z \right), \tag{2.61}$$

where R_E is the Earth’s radius and r is the geocentric distance to the satellite.

²<http://igsb.jpl.nasa.gov/igsb/station/general/igs08.atx>

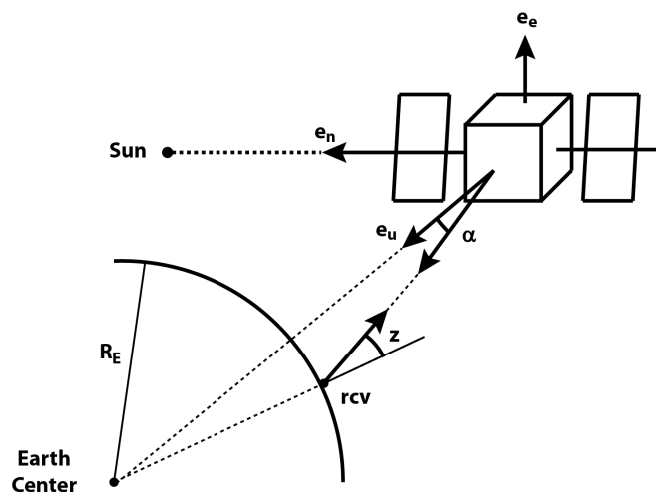


Figure 2.16: Local topocentric coordinate system defining the orientation of the satellite. α is the nadir direction of the satellite to the receiver and z is the zenith angle from the receiver to the satellite. (Not scaled)

Additionally the PCV data is, other than the receiver antennas, not determined in a field calibration or chamber measurement but calculated after the satellite launch from different GNSS institutions using a linear combination of L1 and L2 observations. The obtained PCV values are thus not applicable to single frequency L1 or L2 observations (personal communication M. Fritsche, GFZ Potsdam). It is thus extremely difficult to determine the absolute PCC values of the different satellite blocks.

Fortunately, in the case of the GPS-R altimetric ground based application conducted within this work, the horizontal distance between the reflection point and the antennas do not exceed 350 m (Chapter 3) so that the nadir angle of the direct and the reflected signal can be considered as the same and thus is eliminated by building differences between reflected and direct observations.

2.4.4 Cycle slip

As discussed in Section 2.2.3, carrier phase observations are much more precise than code observations. However, carrier phase based GPS-R requires continuous observations and the resolution of the constant integer ambiguities.

The GPS receiver can keep track of the integer number of cycles as long as the receiver maintains a lock to the satellite signal (Karaim et al., 2014). The temporary loss-of-lock of GPS satellite signals by the receiver leads to a discontinuity of an integer number of cycles in the measured time series of carrier phase measurements called cycle slip (Figure 2.17). In this case, the integer counter of the receiver is reinitialized and consequently a new unknown integer ambiguity have to be determined. Thus, undetected cycle slips affect not only the current measurement, but also all following epochs. However, code observations are not affected by the occurrence of cycle slips.

Cycle slips occur when the signal between satellite and receiver is obstructed by obstacles as well as internally by rapid Signal-to-Noise Ratio (SNR) variations due to strong disturbances in the ionosphere or multipath (Hofmann-Wellenhof et al., 2008, pp. 206-214). If a cycle slip is successfully detected, two options exist, either the ambiguities need to be resolved again or cycle slips need to be corrected. The first option is the safest but implies a new initialisation time to fix for the ambiguities. The second option is faster in processing time but hides some risks. If the cycle slips are wrongly corrected, the induced error propagates through all of the following epochs. In GNSS based positioning, diverse strategies were developed to deal with cycle slips like the use of the Inertial Navigation System (INS)-GPS combination (Karaim et al., 2013), by using phase combinations or by forming a combination of phase and code ranges as the code observations are unaffected by cycle slips (Blewitt, 1990; Cai et al., 2013).

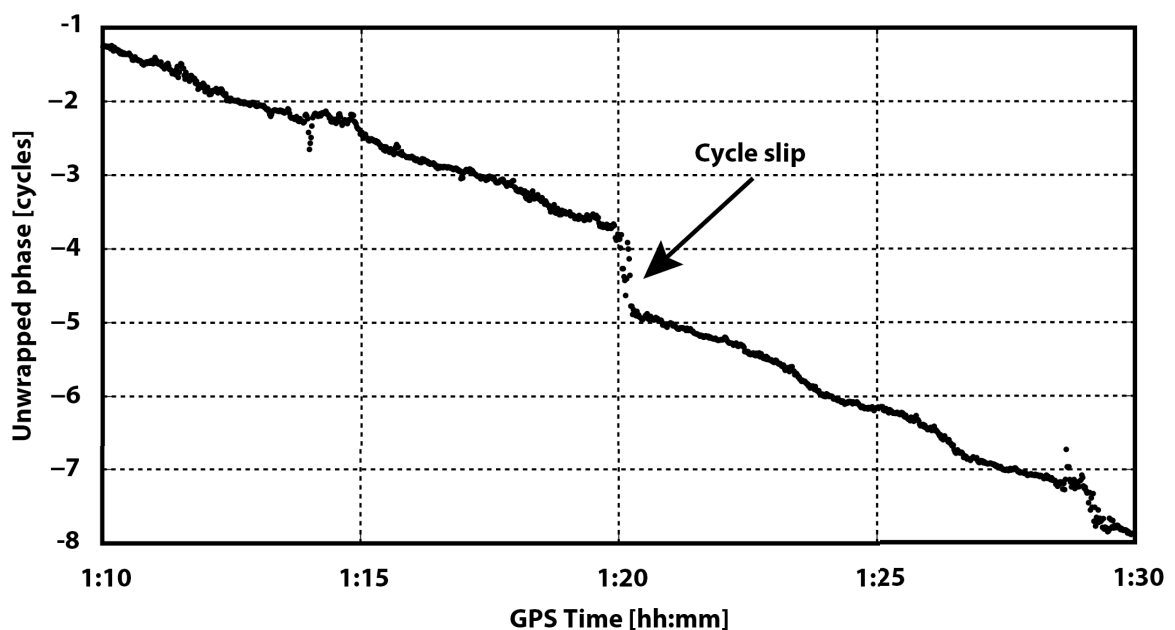


Figure 2.17: Example of a cycle slip causing a jump of one cycle in the accumulated phase observations. Data: Vietnam, An Bihn hotel, February 28, 2012, PRN 27.

A good overview on the different GPS cycle slip detection and correction strategies can be found in Karaim et al. (2014).

2.4.5 Multipath

Multipath (MP) effects occur when the GPS signals are reflected by the surrounding objects in the vicinity of the antenna so that these signals interfere with those received directly from the satellites. GPS-R uses MP effects to extract information from the reflecting surface.

To avoid confusion within this thesis, the term "Multipath" effect will only be used in conjunction with reflections at objects other than the water surface.

In the presence of MP, the direct signal is superposed by an unknown number N of multipath signals. Following Smyrnaiois et al. (2013), this superposition leads to a deformation of the

resulting correlation outputs I_P and Q_P of the prompt replica of the PRN code

$$I_P = A_{drct}P(\tau)D(\tau) \cos(\phi_{drct}) + A_{drct} \sum_1^N \alpha_N P(\tau)D(\tau - \Delta\tau_N) \cos(\phi_{drct} + \Delta\phi_r), \quad (2.62)$$

$$Q_P = A_{drct}P(\tau)D(\tau) \sin(\phi_{drct}) + A_{drct} \sum_1^N \alpha_N P(\tau)D(\tau - \Delta\tau_N) \sin(\phi_{drct} + \Delta\phi_r), \quad (2.63)$$

where A_{drct} is the amplitude of the direct signal, α is an attenuation factor of the signal due to the reflection, D is the navigation bit ($=\pm 1$), P is the correlation function ($=\pm 1$), $\Delta\tau$ is the code tracking error, ϕ_{drct} is the phase of the direct signal and $\Delta\phi_r$ is the relative phase between the direct and the reflected signal.

Figure 2.18 illustrates a phasor diagram for the superposition of the direct signal with one MP signal. From this figure, the resulting signal amplitude A_c is

$$A_c^2 = A_{drct}^2 + A_r^2 + 2A_{drct}A_r \cos \Delta\phi_r. \quad (2.64)$$

where A_r is the amplitude of the MP signal.

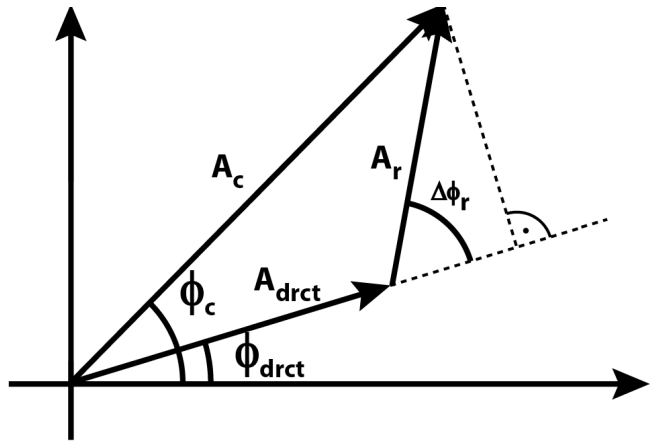


Figure 2.18: Phasor diagram representing the superposition of the direct signal (index drct) with one MP signal (index r) leading to the compound signal (index c) with phase ϕ_c and amplitude A_c . The relative phase between the direct and the MP signal being $\Delta\phi_r$. A Similar graphic can be found in Smyrnaiois et al. (2013).

Due to the constant motion of the satellites and the receiver, the phase shift $\Delta\phi_r$ changes with time. The vector of the reflected signal undergoes a circular motion causing the phase of the tracked signal ϕ_c to show periodic variations. This in turn, can be observed in the amplitude variations of the signal (Figure 2.19).

Assuming a planar Earth surface and a single horizontal reflector, the frequency f_i of the MP variation is

$$\begin{aligned} \frac{\Delta\rho}{dt} &= \lambda_i \frac{\Delta\phi_r}{dt}, \\ f_i(t) &= \frac{d(2h \sin(E))}{dt}, \\ &= \frac{2h \cos(E) dE}{\lambda_i dt}. \end{aligned} \quad (2.65)$$

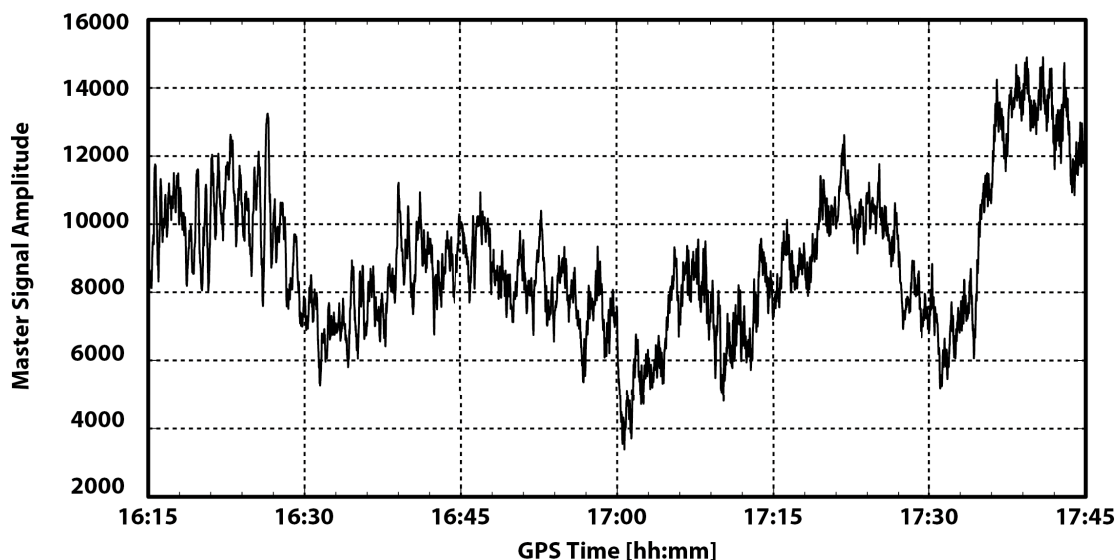


Figure 2.19: The motion of the satellite and the receiver causes the variation of the relative phase between direct and multipath signal. This can be observed in the amplitude variation of the compound signal. Data source. Vietnam, An Bihn hotel, February 25, 2012, PRN 17.

Thus, the frequency of the occurring multipath variations depends on the satellite, reflector and receiver geometry. Figure 2.20 illustrates the expected frequencies in the case of a single horizontal reflector. For a horizontal reflector with a relative height of 10 m and 20 m respectively, a mean frequency of 0.01 Hz and 0.02 Hz is expected.

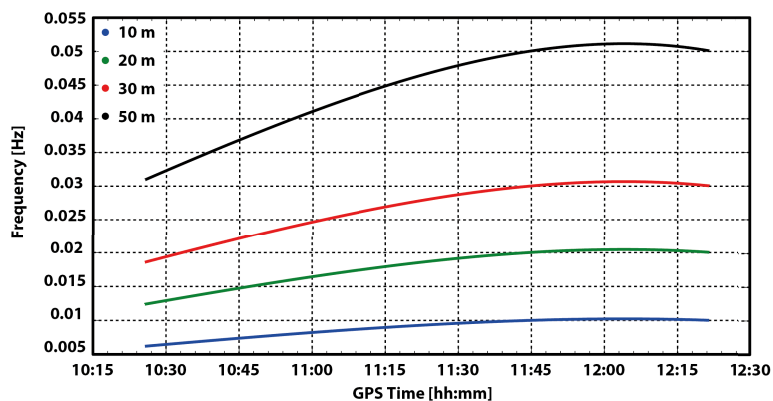


Figure 2.20: Example of frequency variations of Multipath effect for different horizontal reflector height: 10, 20, 30 and 50 m. Data Source: February 25, 2012, PRN 3, An Bihn hotel, Vietnam, PRN3.

In high-accuracy GPS positioning applications, MP is an error source that remains a challenge to this day. Two main techniques are mostly used. The first technique acts at the antenna and receiver baseband signal processing level. The second, on the estimation of multipath induced error using the receiver data output. In GPS-R, we aim to track reflected signals and consequently filtering out these signals on the antenna or receiver level is not desired.

2.4.6 Remaining Systematic Errors

For completeness of the previous sections, remaining errors sources are briefly mentioned.

1. The Earth's ionosphere is part of the upper atmosphere that extends from approximately 50 km to 1000 km above the surface of the Earth. In the ionosphere, a certain fraction of the gas molecules are ionised by solar ultraviolet- and X-ray radiation (Pröller, 2004). This dispersive effect causes a variation in the speed of propagation of the GNSS EM waves, depending on the signal frequency and the number of free charge carriers along the propagation trajectory. This delay can reach in the worst case, more than 300 ns which corresponds to range errors of 100 m (Klobuchar, 1987). In order to nearly eliminate the ionospheric effects, a second frequency L2 was specifically incorporated into the GPS system to allow users to automatically correct for such effects through a linear combination of both frequencies (L1 and L2) called ionosphere free linear combination; c.f. see Xu (2007).

For a receiver placed on a space platform or at large altitudes above the reflecting surface, the direct and the reflected signal cross two different regions of the ionosphere and this must be taken into account. For low altitude receivers near the Earth's surface, the influence of the ionosphere can be neglected (Semmling et al., 2011), as the direct and the reflected signal travel approximately through the same area of the ionosphere.

2. Although the satellite clocks are highly precise, instrumental errors still exist. Correction terms are broadcasted with satellite ephemeris or are available via IGS.
3. GPS broadcast ephemeris are predicted or extrapolated satellite orbital data, thus orbital errors remain. The accuracy of the ephemeris data is ~1 m. Precise GPS orbits are available through the IGS with different latency and accuracies: real-time (~5 cm), Ultra-rapid (~3 cm), Rapid (~2.5 cm) and Final (~2.5 cm)³.
4. Due to the gravitational force of the Moon and the Sun, the elastic body of the Earth undergoes a deformation that can reach up to 60 cm (Xu, 2007, pp. 67-72). The ocean loading, causes a similar effect called ocean loading tide effects and can reach up to 10 cm in coastal regions. For short baseline both effects can be considered to be the same and nearly eliminated by building differences.
5. Instrumental biases are systematic errors that differ depending on the used frequency, the used observations (code or phase) and instrumental induced temperature variations. However, these biases are assumed to be constant for a given receiver and satellite.
6. As the clock installed in the receiver do not have the same stability as the one installed in satellites, a de-synchronisation occurs. This can be corrected for by determining the receiver clock error or by eliminating it through building single differences if the same receiver is used.

³<http://igsceb.jpl.nasa.gov/components/prods.html>

2.4.7 Final GPS Phase and Code Observation Equation

Based on the analysis presented from Section 2.4.1 until Section 2.4.6, the final GPS phase and code observations equation in meters are

$$PR_{rcv}^{sat_i}(t_r, t_e) = \rho_{rcv}^{sat_i}(t_r, t_e) + c \left(\delta t_{rcv} + B_{rcv,PR,f} - \delta t^{sat_i} - B_{PR,f}^{sat_i} \right) + I_{rcv}^{sat_i} + T_{rcv}^{sat_i} + M_C + \delta_{tide} + \delta_{rel} + \epsilon_c, \quad (2.66)$$

$$\lambda_i \Phi_{rcv}^{sat_i}(t_r, t_e) = \rho_{rcv}^{sat_i}(t_r, t_e) + c \left(\delta t_{rcv} + B_{rcv,\Phi,f} - \delta t^{sat_i} - B_{\Phi,f}^{sat_i} \right) - I_{rcv}^{sat_i} + T_{rcv}^{sat_i} + M_p + PWU(A, E) + PCC(A, E, f) + \lambda_i N_{amb,rcv}^{sat_i} + \delta_{tide} + \delta_{rel} + \epsilon_p, \quad (2.67)$$

where λ is the wavelength for the used frequency i , $\rho_{rcv}^{sat_i}$ represents the geometrical distance between the receiver and the satellite at the reception and transmission time, δt_{rcv} and δt^{sat_i} the clock errors of the receiver and the satellite respectively, $I_{rcv}^{sat_i}$ the ionospheric effect, $T_{rcv}^{sat_i}$ the tropospheric effect, δ_{tide} the Earth and loading tide effects, δ_{rel} the relativistic effects, M_C and M_p the multipath effect on the code and phase respectively, PCC antenna phase centre correction in function of the elevation angle E , the azimuth A and the used frequency f , PWU the phase wind-up effect in function of the azimuth A and the elevation angle E , N_{amb} the ambiguity, B_{PR} and B_Φ the instrumental biases for the code and the phase observations, respectively and ϵ_c and ϵ_p , the respective code and phase observations noise.

Chapter 3

Experimental Set-up

Every year in the flood seasons, various regions throughout the Mekong Delta in Vietnam fall victim to extreme flood events causing huge economic damages and losses of human lives. The tidal amplitude can reach a magnitude of up to 4 m in the wet season and up to 2 m in the dry season.

Between 2007 and 2014, a German Vietnamese Water related Information system for the Sustainable Development Of the Mekong delta (WISDOM) project was conducted with the aim to build an information system containing all the necessary data to support decision makers for an optimized water and land resource management outcome. As water level observations are an important task within the project, the feasibility of using the innovative GPS-R technique as a gauge instrument was tested. In February 2012 and March 2013, two week long measurement campaigns were conducted at the An Bihn hotel in Can Tho, the biggest city in the Mekong Delta. In order to analyse the impact of the geometry on the quality and quantity of the recorded reflection events (on the 150 m wide observed river segment of the Mekong Delta), two different antenna heights were used. In the first week of measurements, the antennas were placed 10 m above the reflecting surface. During the second week, the antennas were raised to 20 m above the water surface.

In order to receive information on the accuracy of the proposed water level derivation algorithm as well as its applicability to other GPS-R collected data, a second measurement campaign was conducted in Midelt, Morocco at a dam. Here, nearly optimal conditions were found, since the water surface is smooth preserving the coherency of the phase observations (Section 2.3.1).

Morocco is an agricultural country with limited water resources. Therefore a large number of dams were built and it is important to observe and manage the available water resources. Within the PMARS project, the use of GPS-R as a water level monitoring instrument was tested.

In the first two sections of this chapter (Section 3.1 and 3.2), the experimental set-ups in Vietnam and Morocco are illustrated and the available validation gauge instrument is introduced. To record the reflection tracks, a specially modified JAVAD™ receiver for the German Research Centre for Geosciences, Germany (GFZ) was used enabling its use in a GPS-R mode. The functionalities will be described in the last section of this chapter (Section 3.3).

3.1 Experimental Set-up in Vietnam

The Mekong Delta is the granary of South East Asia. Over thousands of years, the annual flooding of the Mekong River during the monsoon season created a high fertile plain which is, particularly in the Vietnamese part of the delta, used for intensive agriculture. Due to the large areas and multiple harvests per year, the Mekong Delta ensure the basic supply of rice for the Vietnamese population and also provides 20% of the global trade volume of rice. For this purpose, 70% of the population lives on the banks of the Mekong Delta. The basis for this high productivity is the adequate water supply and the sediments that are annually deposited during the floods. However, in recent years, these fundamentals have become endangered. Climate change causing sea level rise combined with the increasing number of hydropower plants cause changes in the hydrological regime of the Mekong River influencing the dynamics and strength of the monsoonal flooding, as well as the sedimentation patterns (Manh et al., 2015). Between 2007 and 2014, a German Vietnamese funded Water related Information system for the Sustainable Development Of the Mekong delta (WISDOM) project was conducted. The goal was to build an information system containing hydrological, economical and social data to assist the authorities and planners with the management of water and land resources. As the monitoring of water level data is an important task within the project, one of WISDOM's work objectives was to test the possibility of using GPS-R as a water level gauging instrument for the Mekong Delta.

With its tropical monsoon climate, the south of Vietnam has two main seasons: the wet season from May to November and the dry season between December and April (Hashimoto, 2001). Due to strong rainfall in the wet season, the Mekong Delta is heavily affected by floods with tidal amplitudes in some regions of up to 3.5 m (Son and Tung, 2011, chap. 18, pp. 316). For security reasons, measurements were not performed in the wet season. The campaigns were conducted during the dry season with expected tidal amplitudes lying between 0.5 m and 2 m (Figure 3.1).

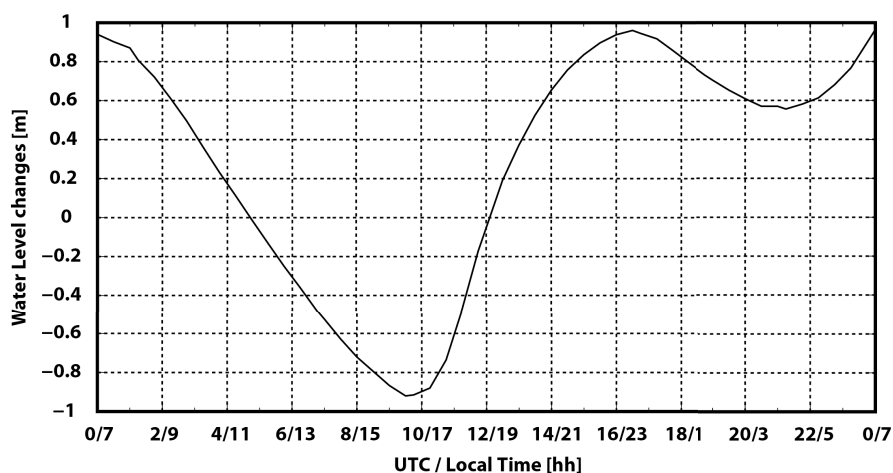


Figure 3.1: A representative example of "24 hours" water level change measurements of the Can Tho River in Can Tho City during the dry season. A tidal amplitude between 0.5 and 2 m can be expected. Data Source: gauge instrument placed 8 km away from the An Bihn hotel, February 4, 2011.

In February 2012 and March 2013 respectively, a two weeks lasting measurement campaign was performed each year in Can Tho, in the south of Vietnam. With a total area of 140 000 ha and 1.2 millions of habitants, it is the fourth biggest city in Vietnam and the biggest in the Mekong Delta. It is located on the south bank of the Hau River which is a distributary of the Mekong River that traverses Vietnam.



Figure 3.2: Location of the GPS-R experimental set-up in Vietnam. The measurement campaigns were conducted in Can Tho City, located on the Hau River. The An Bihn hotel (red dot) was selected to install the GPS-R instrumentation. With a height of approximately 20 m, it is the second highest building with a direct view on the 150 m wide Can Tho River. Source: www.earth.google.de

For the GPS-R instrumental installation, the Kim Tho hotel was originally intended as it is the highest building (~ 40 m) with a free view on the Can Tho River. However, unfortunately, due to government buildings surrounding the hotel, the installation of a GPS-R receiver was not approved from the authorities. As an alternative, the An binh hotel (9.99° N, 105.74° E), the second highest building (~ 20 m) located along the ~ 150 m wide Can Tho River, was selected (Figure 3.2 right, red dot). The location is not optimal as an approximately 20 m wide garden lies between the hotel building and the beginning of the river section. Additionally, high palm trees and constructions in the surrounding of the antenna exist leading to strong signal obstructions (Chapter 4).

To be able to capture the direct and the reflected signals separately and simultaneously, at least two antennas are used. One antenna is placed horizontally to capture the direct signals and the other one(s) is/are tilted toward the reflecting surface to receive the reflected signals. To distinguish between the antennas, the horizontal one will be called "Master antenna" and the tilted one(s) "Slave antenna(s)".

To investigate the impact of the antennas geometry on the quality and quantity of the recorded coherent observations (Chapter 4), two measurement time series were recorded at two different antenna heights (Table 3.1). During the first time series, the antennas were fixed on the balustrade of the terrace with an approximate height of 10 m above the Can Tho River and an approximate horizontal distance of 20 m from the beginning of the river section. In the second

time series, the antennas were placed on the roof of the hotel with an approximate height of 20 m above the reflecting surface and approximately 25 m away from the riverside (Figure 3.3).

Vitenam, Can Tho City, An Bihn Hotel, Experimental Setup

| Year | Time series | Antenna height | Used antennas | |
|------|---------------|----------------|---------------|-------------|
| | | | Master | Slave |
| 2012 | 25.02 - 03.03 | Terrace ~10 m | RHCP | LHCP |
| | 04.03 - 08.03 | Roof ~20 m | RHCP | LHCP |
| 2013 | 03.18 - 03.20 | Terrace ~10 m | RHCP | LHCP / RHCP |
| | 03.11 - 03.17 | Roof ~20 m | RHCP | LHCP / RHCP |

Table 3.1: During the measurement campaigns in 2012 and 2013, two different antenna heights and constellations were used. During the first period, the antennas were placed on the terrace of the An Bihn hotel ~10 m above the Can Tho River. For the second period they were placed on the roof of the hotel ~20 m above the reflecting surface. For each measurement campaign, a different antenna constellation was used to capture the reflected signals: 2012, only a LHCP slave antenna was used, 2013 two slave antennas were used, a LHCP and a RHCP antenna.



Figure 3.3: Antenna placement during the measurement campaigns 2012 and 2013. To analyse the impact of the geometrical position of the antennas on the quality and quantity of recorded coherent reflections, two different antenna heights were used. Bottom left: on the balustrade of the hotel ~10 m above the Can Tho River, Bottom right: on the roof of the hotel ~20 m above the reflecting surface.

The GPS signals are sent as RHCP (Section 2.1.2). Depending on the elevation angle and the dielectric properties of the reflecting surface, the polarization of the reflected signal changes (Section 2.3.2). Therefore during the first measurement campaign in 2012, two antennas were

used: a L1/L2 RHCP antenna oriented to the zenith to track the direct signals and a L1/L2 LHCP antenna oriented southwards (170 deg azimuth) and tilted with an angle of -98 deg with respect to the horizon in the direction of the river to track the reflected signals (Figure 3.4A). During the second measurement campaign in 2013, three antennas were used: a RHCP antenna that tracks the direct signals and a LHCP and RHCP antenna to track the reflected signals (Figure 3.4B). The same antenna position (terrace and roof), inclination and orientation was used.

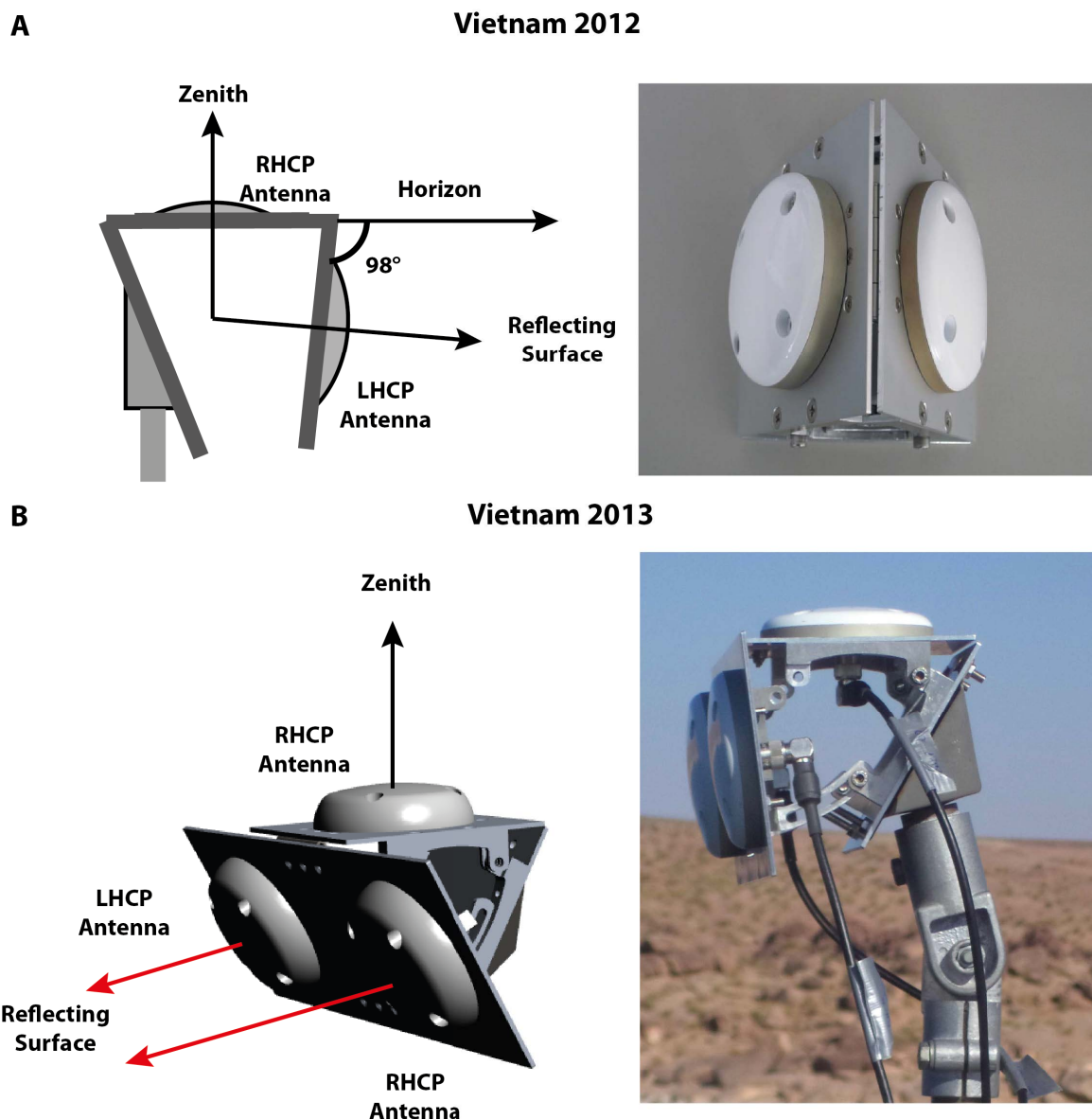


Figure 3.4: The used antennas mounting and configuration during the measurement campaigns in Vietnam. **A:** Schematic representation (left) and a picture (right) of the antenna mounting and configuration used during the measurement campaign of 2012. Two antennas were used: a RHCP L1/L2 GPS antenna in zenith direction to track the direct signals and a LHCP L1/L2 GPS antenna tilted toward the reflecting surface to track the reflected signals. **B:** Schematic representation (left) and a picture (right) of the antenna mounting and configuration used during the measurement campaign of 2013. This time two antennas are used to track the reflected signals: a RHCP and a LHCP antenna. All the used antennas are manufactured by Antcom. Sketch panel **B** left, was created by M. Ludwig, GFZ.

All the antennas used during the measurements are manufactured by Antcom™. They have a diameter of 88.90 mm, a hemispheric field-of-view and are able to receive the GPS L1 and L2 signals.

The following instruments were additionally used to record the data: a control-unit, a laptop, an external hard disk, a GNSS-Reflectometry receiver and a standard GNSS geodetic receiver. The control-unit is a computer manufactured by "Plug in" (Figure 3.5D). It commands the GNSS-R receiver (Figure 3.5C). Indeed, based on a predefined azimuth and elevation mask, it controls which satellites should be tracked in order to record reflection events. Following a schedule of simulated GPS reflection tracks, that takes the Can Tho River geometry and the approximate antenna position into account, only elevation angles between 0 and 30 deg are used. For the azimuth mask, observations between 80 and 260 deg are considered in order to restrict reflections coming only from the Can Tho River. The measurement stops if the receiver loses track of the direct signal or if the tracked GPS satellite leaves the defined visibility mask.

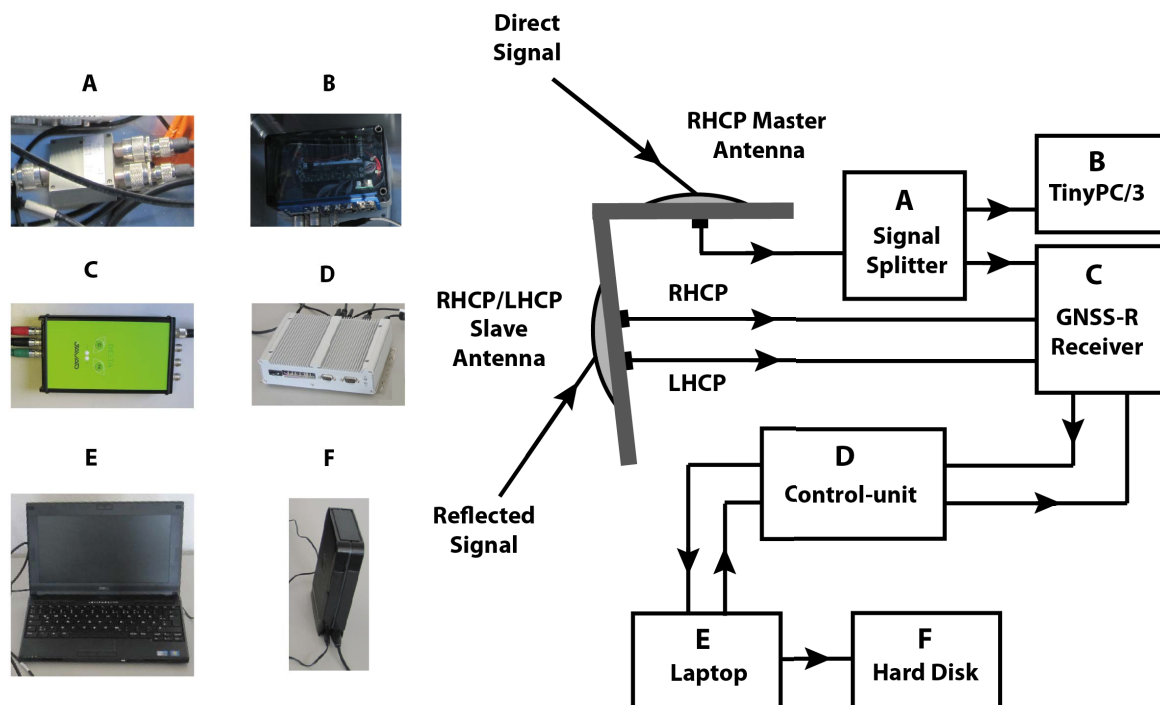


Figure 3.5: The hardware connection used during the Vietnam measurement campaign of 2012 and 2013. The incoming direct signal is captured by the RHCP Master antenna and split by a signal-splitter (A) between the TinyPC/3 (B) and the GNSS-R receiver (C). The TinyPC/3 then permits to calculate the position of the Master antenna. It is a GFZ internally built box that contains a geodetic JAVAD™ receiver as well as a processor. The GNSS-R receiver is custom-designed with a specially modified software for GNSS-R applications. The incoming reflected signals are captured in parallel by Slave antennas and then processed by the GNSS-R receiver. A control-unit (D) commands the GNSS-R receiver to track specific satellites in view and thus reflection events should be tracked based on a set elevation and azimuth mask. A laptop (E) is used as an interactive communication interface between the operator and the Control-unit. Finally, an external hard disk (F) is used to back-up the data.

The GNSS-R receiver is a custom-designed JAVAD receiver with a modified software enabling its use in Reflectometry mode (Section 3.3). A laptop was used as an interface between the control-unit and the GNSS-R receiver (Figure 3.5E). The GPS direct and reflected obser-

uations were recorded in the control-unit and in parallel backed-up on an external hard disk (Figure 3.5F).

As a precise position of the Master antenna is needed, a second GPS receiver, called TinyPC, is used (Figure 3.5B). The used TinyPC/3 box of the third generation, is a compact GNSS station developed by GFZ¹. It contains a JAVAD OEM board that allows for the tracking of GPS, GLONASS and Galileo signals as well as an integrated 800 MHz processor with a power consumption of only 2.5 Watts. For this purpose, the incoming direct signal was separated with a splitter-signal between the TinyPC/3 and the GNSS-R receiver (Figure 3.5A).

To obtain reference measurements of the water level changes, the Xuanh Khan pump station installed 8 km eastern from the An Bihn hotel is used. The water level changes are given with an interval of 15 min and are measured using a pressure gauge instrument from the manufacturer SEBA Hydrometrie™ with an accuracy of 1 cm.

3.2 Experimental Set-up in Morocco

Morocco is a country where agriculture plays an important economic role, employing around 42% of the country's workforce, thus the biggest employer in the country (Requier-Desjardins, 2010). However, several recent studies show that agriculture is greatly affected by the impacts of climate changes causing a reduction in available water resources (decrease of precipitation) as well as degradation of land and ecosystems (desertification) (Magnan et al., 2009; Requier-Desjardins, 2010). At the same time, an increasing demographic trend can be observed that causes an expansion of irrigated agricultural land (to ensure basic provision for the population) and thus an overexploitation of ground-water and water reservoirs. Therefore local, regional and global monitoring of water resources becomes increasingly important.

Within the Programme Marocco-Allemand de Recherche Scientifique (PMARS) research project, funded by the German and Moroccan Ministry of Education and Research, a measurement campaign, jointly organized by the Mohammedia School of Engineers (EMI) in Rabat, Morocco and the GFZ, in Potsdam, Germany, was conducted in Morocco from the 13th to the 19th of December, 2013. The mission's main aim was to install the first GPS-R station in Morocco to extract the degree of soil moisture. But the opportunity was also used to test the developed GPS-R phase based algorithm to extract water level heights under near optimal conditions.

For this purpose, a GPS-R station was installed at the Hassan II dam near the city of Midelt. This location was selected as the Moroccan project partners are developing hydrological models for the basin "la Moulouya" and the water surface of the dam offers a almost optimal reflecting surface. This region accurately represents well the agricultural situation in Morocco. More than half of the agriculture is run in zones with low precipitation (under 400 mm per year) where a Mediterranean semi-arid/arid climate dominates (Ibouhouten et al., 2010). Therefore,

¹<http://www.gfz-potsdam.de/forschung/ueberblick/departments/departement-1/gpsgalileo-erdbeobachtung/projekte/gnss-infrastruktur/>

irrigation of the fields is necessary, based on existing ground water and hydraulic engineering that is filled from snow melt from the atlas mountains. From a technical point of view, the choice of the dam offers the advantage that all dams in Morocco are controlled areas with access only for authorized persons. This permits a supervision of the installed instruments.

The basin "La Moulouya" with a surface area of 55 860 km² extends between the parallel 32° 18' and 35° 8' N and the meridians 1° 11' and 5° 37' W. It is flanked to the Northwest by the Mediterranean coast, to the west by the basins of Sebou and Oum Er-Rebia, south by the basins of the Ziz and Guir and in the East by Algeria (Figure 3.6 left).

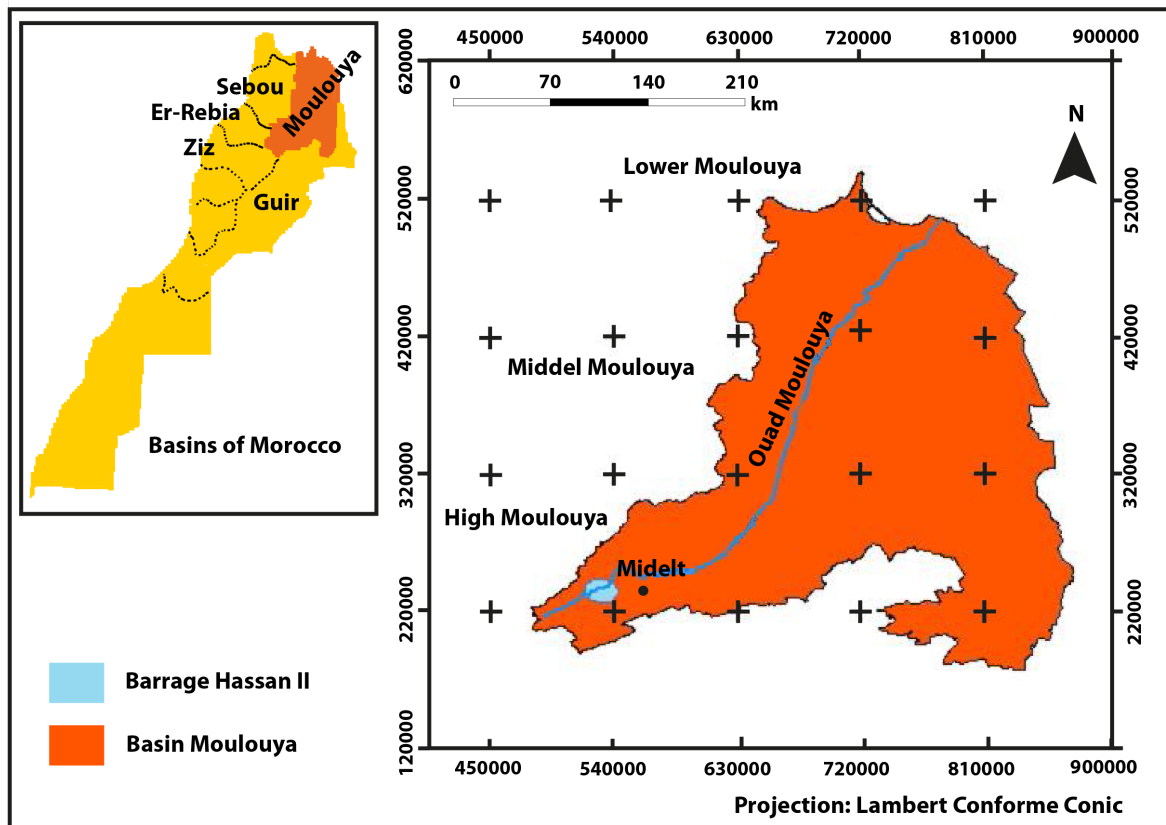


Figure 3.6: Geographical location of the basin La Moulouya, the hydrological area of interest. Left: Location of the existing basins in Morocco with emphasis on the basin la Moulouya. Right: Location of the Hassan II dam near the city of Midelt, where the GPS-R soil moisture and altimetry stations were placed. Source: Beckheinrich et al. (2014).

The Hassan II dam is located in the high Moulouya (Figure 3.6 right). It has a maximum storage capacity of 400 million cubic meters, extended over an area of 12,7 km² enabling it to ensure the annual flow regulation of the Moulouya with a volume of 100 m³ in its upstream part. On the left bank, the major purpose of the dam is the supply of drinking water and irrigation for agricultural plains. Downstream, it protects against potential flooding.

The antenna constellation is similar to the one used in Vietnam (Section 3.1). The three antennas are placed on the balustrade of the Hassan II dam with approximately 30 m height above the reflecting water surface (Figure 3.7A). The water level of the dam is continuously monitored by a laser gauge (Figure 3.7B) that allows for validation of the results (Chapter 5).

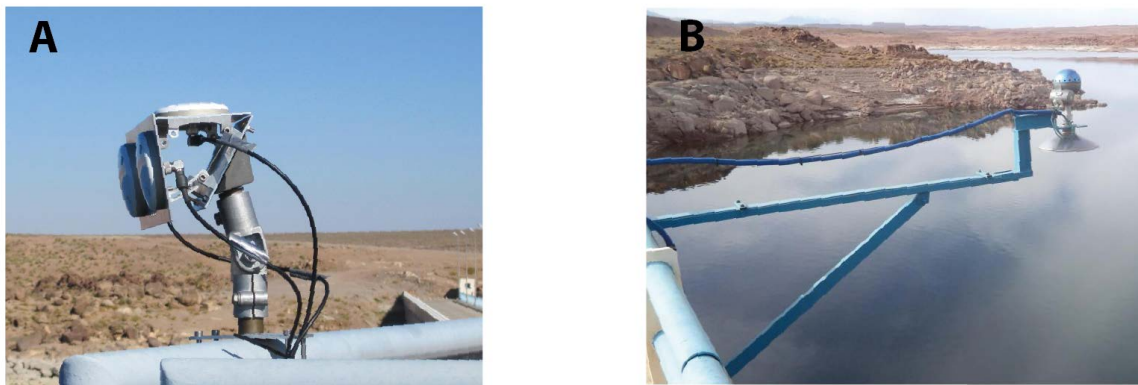


Figure 3.7: **A:** GPS-R altimetric station placed on the balustrade of the Hassan II dam approximately 30 m above the reflecting water surface. **B:** A laser gauge instrument continuously measures the water level height of the reservoir.

3.3 GNSS-Reflectometry Receiver

The GNSS Occultation, Reflectometry and Scatterometry (GORS) receiver is used for the GNSS-Reflectometry phase based altimetry measurements (Figure 3.5C). It is a custom-designed JAVAD Quattro-G3D dual-frequency receiver. It can be either used as a standard geodetic instrument to calculate precise positioning, or for GNSS-R applications through its special interferometric mode. The receiver can process GPS, GLONASS and Galileo signals.

As discussed in Section 2.2.3, two GNSS-R altimetry methods can be distinguished: the code and the carrier phase based approach. The latter is more precise. A new generation of GORS receiver with a modified firmware has been developed in collaboration with the manufacturer JAVAD. The first prototype was a single front-end receiver developed within the German Indonesian Tsunami Early Warning System (GITEWS) project (Helm et al., 2007). Since that time, it has been improved to a four front-end receiver which is able to track separately, the direct and up to three reflected GPS L1/L2C signals.

Up to 10 channels can be used in the GNSS-R application mode. Each channel uses one correlator, called Master, to track the direct signal and up to 3 correlators (one for each connected antenna), called Slave, for the reflected signal (Figure 3.8).

During a reflection event, the direct signal is tracked by the Master in a closed-loop. For the reflected signal of the same GPS satellite, a modified firmware allows for open-loop tracking by the Slave correlators. The direct signal frequency tracked by the Master added with a-priori Doppler frequency and an estimate of the code-delay is used as a reference frequency to process the reflected signal (Figure 3.8 green). The receiver Slave correlator NCO is thus not driven by the reflected observations itself but by the direct signal added with a-priori information. The code delay, $\delta\tau$, accounts for the relative time delay between the time-of-arrival of the direct and the reflected signal. An approximation of the water level height is used as a starting value. The code delay is then adjusted with a chip step of ± 0.1 chip (1 chip \approx 300 m). Concerning the compensation in Doppler space, a correction was not required in our set-up because it is less than 1 Hz which can easily be covered by the receiver's sampling rate of 200 Hz (5 ms).

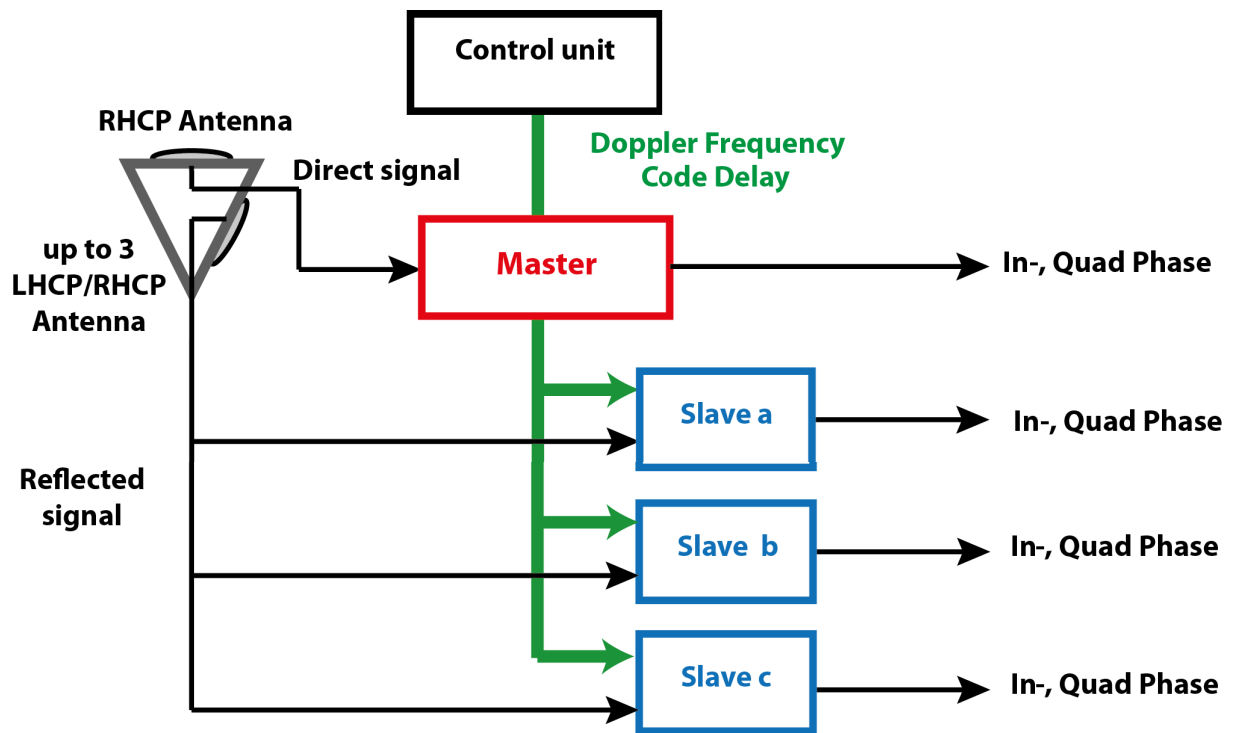


Figure 3.8: Schematic representation of one GORS receiver channel in interferometric mode. The Master tracks the direct signal in closed-loop. Up to three Slave correlators can track the reflected signal in open-loop mode. Up to 10 such channels can be run in parallel so that up to 10 reflection events can be tracked simultaneously.

The output of the receiver is the recorded In-phase (I) and Quadrature correlation sum of the Master and the Slave correlators (Figure 3.8).

Chapter 4

Data Analysis

In order to develop and understand the GPS-R recorded reflection events, representative data samples of the experiment conducted in Vietnam are presented in this chapter. As discussed in Section 2.2.3, coherent observations are a mandatory condition for the use of a phase-based GPS-R altimetry. To filter out coherent reflection events, a new algorithm is presented and analysed in the first section of this chapter (Section 4.1). Based on the as coherent extracted observations, a comparison between the quantity and quality of recorded coherent data between both antenna heights is made (Section 4.2). This in turn, is the motivation for a deeper analysis of the data, in order to find the reasons that caused a high loss of coherency of the data. In this context, it will be shown that the effects of the objects in proximity of the antennas (surroundings) combined with those of the maritime activities on the Mekong Delta are the main factors. The high number of cycle slips in the collected data in Vietnam is also analysed. A clear correlation between the surroundings of the antennas and cycle slips is shown in Section 4.3. As cycle slips lead to a false ambiguity fixing, a detection algorithm is presented. In Section 4.4, the presence of multipath effects is shown and mitigated. The Empirical Mode Decomposition (EMD) method is proposed to filter out reflection events coming from objects other than the water surface. Finally, in the last section of this chapter (Section 4.5), the preprocessing algorithm of the data is illustrated, resuming the different algorithms developed within this chapter.

4.1 Coherent Observation Extraction Algorithm

Continuous and coherent phase observations are mandatory conditions for a GPS-R phase-based altimetry (Section 2.2.3). Since the data are recorded with a high sampling rate of 200 Hz and the coherency of the phase observations is affected by the unpredictable irregularities of the water surface (Section 2.3.1), an automated coherency extraction method is needed.

As explained in Section 3.3, the output of the GNSS Occultation, Reflectometry and Scatterometry (GORS) receiver is the In-phase (I) and Quadrature (Q) correlation sum from which

the amplitude A and the phase ϕ of the signal are calculated

$$A = \sqrt{I^2 + Q^2}, \quad (4.1)$$

$$\Phi = \arctan(Q, I). \quad (4.2)$$

As outlined in Section 2.3.1, incoherency leads to randomly distributed phase values within the interval of $[0, 2\pi]$. In contrast, coherent observations cause a uniform rotation of the phasor within the interval of $[0, 2\pi]$. Figure 4.1 illustrates this effect via simulations calculated for different surface conditions controlled by the addition of a white noise with zero mean and standard deviation σ on the simulated reflected signal. On the left and the right side of the figure, are illustrated the phasor and resulting phases, respectively. For a perfectly mirror-like water surface, the phase changes $\Delta\phi$ and the amplitude between consecutive reflected signals will be nearly constant, causing the circular rotation of the phasor (Figure 4.1A). However, the more the reflecting surface roughness increases, the more the circular rotation of the phasor is destroyed. For $\sigma = 0.5$ cm, the circular rotation of the phasor get an elliptical form (Figure 4.1B). For $\sigma = 1$ cm, fading becomes visible, partially destroying the coherency of the reflected signal (Figure 4.1C). For $\sigma = 1.5$ cm, signal fading dominates causing the incoherency of the reflected signal (Figure 4.1D).

The rotation of the phasor in the complex plane and its resulting phase observations, form the basis for the proposed coherency extraction algorithm presented in the next section.

4.1.1 Ellipse Fitting

Semmling (2012) proposed the idea of using the rotational nature of the phasor during coherent phase observations by applying the following two conditions:

1. The phase cycle passes through all quadrants of the complex plane either in ascending or descending order.
2. The samples within the phase cycle have to be uniformly distributed over the four quadrants.

As discussed by Semmling (2012), the disadvantage of the proposed algorithm is its sensitivity to a temporary loss of amplitude (fading), causing the violation of the first condition and thus the rejection of the observation. To overcome this limitation, a Least-Squares (LS) fitting of the observed phasor cycle to an ellipse is developed and proposed in this thesis. Indeed, the advantage of using a LS based ellipse fitting is that it allows a certain degree of amplitude fading.

Following Bookstein (1979) and Gander et al. (1994), an ellipse can be described by

$$\{(x, y) \in \mathbb{R}^2 \mid F(x, y) = 0\},$$

with

$$F(x, y) = ax^2 + bxy + cy^2 + dx + ey + f = 0, \quad (4.3)$$

where a, b, c, d, e and f are the coefficients of the polynomial F .

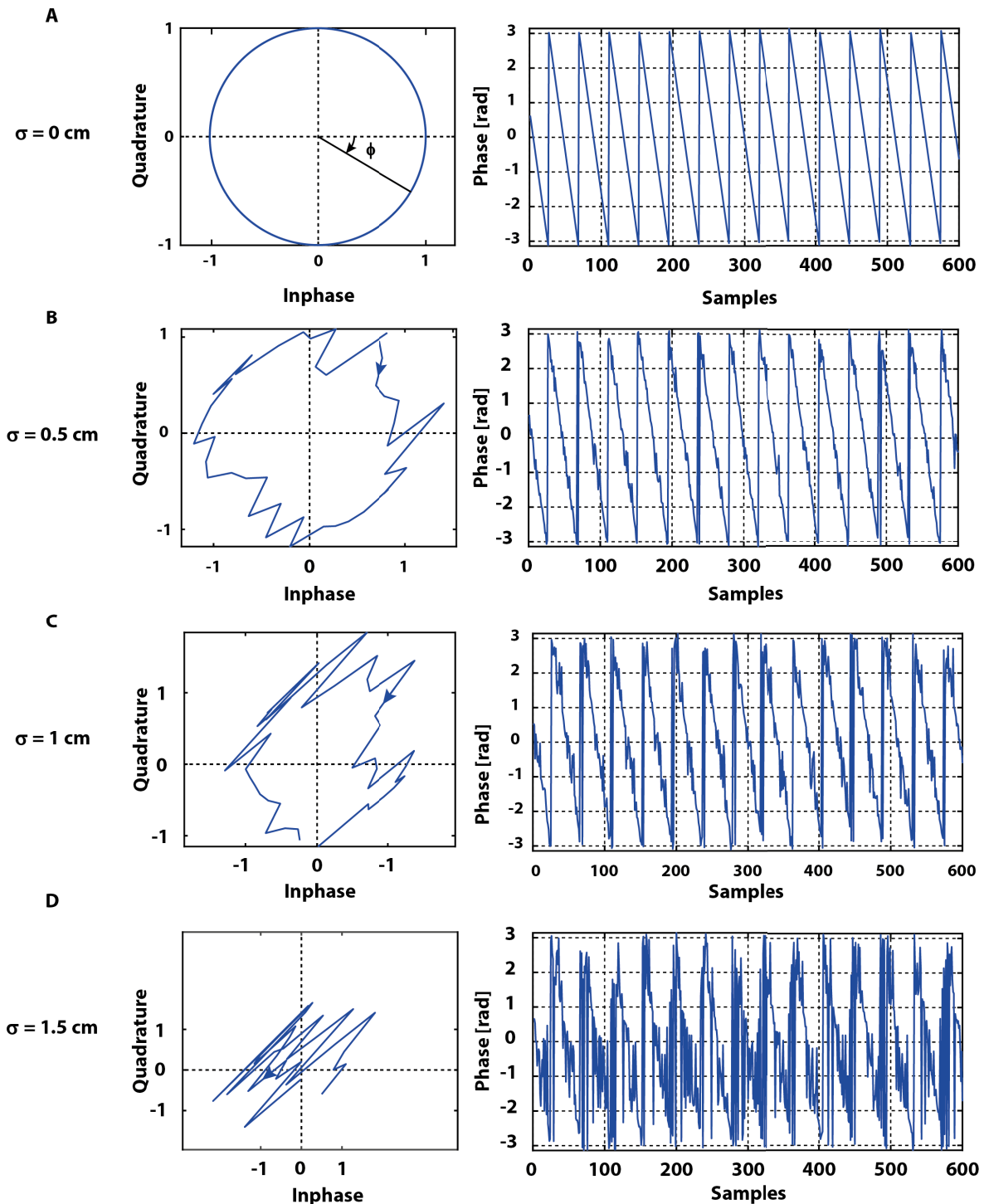


Figure 4.1: I and Q phasor simulation and from it calculated phases for different white noise level with zero mean and standard deviation σ . **A:** For a perfectly mirror-like water surface, the phasor rotates with a constant amplitude and phase. **B:** The circular rotation gets an elliptical form, for $\sigma = 0.5$ cm. **C:** For $\sigma = 1$ cm fading becomes visible, partially destroying the coherency of the reflected signal. **D:** For $\sigma = 1.5$ cm, signal fading dominates causing the incoherency of the reflected signal.

By introducing the vectors

$$\mathbf{a} = [a, b, c, d, e, f]^T, \quad (4.4)$$

$$\mathbf{x} = [x^2, xy, y^2, x, y, 1]^T, \quad (4.5)$$

equation (4.3) can be written in vector form

$$f_{\mathbf{a}}(x, y) = \mathbf{x}^T \cdot \mathbf{a} = 0. \quad (4.6)$$

In the LS method, the fitting of a general conic section to a set of points (x_i, y_i) , $i \in \{1, \dots, N\}$ is solved by minimizing the sum of squared algebraic distances of the observed points to the conic represented by the coefficient vector \mathbf{a}

$$\begin{aligned} \min_{\mathbf{a}} \sum_{i=1}^N |f_{\mathbf{a}}(x_i, y_i)|^2 &= \min_{\mathbf{a}} \sum_{i=1}^N (\mathbf{x}_i \cdot \mathbf{a})^2 \\ &= \min_{\mathbf{a}} \mathbf{a}^T \mathbf{A}^T \mathbf{A} \mathbf{a} \\ &= \min_{\mathbf{a}} \mathbf{a}^T \mathbf{S} \mathbf{a}, \end{aligned} \quad (4.7)$$

where the $N \times 6$ design matrix \mathbf{A} is given by

$$\mathbf{A} = \begin{pmatrix} x_1^2 & x_1 y_1 & y_1^2 & x_1 & y_1 & 1 \\ \vdots & \vdots & \vdots & \vdots & \vdots & \vdots \\ x_i^2 & x_i y_i & y_i^2 & x_i & y_i & 1 \\ \vdots & \vdots & \vdots & \vdots & \vdots & \vdots \\ x_N^2 & x_N y_N & y_N^2 & x_N & y_N & 1 \end{pmatrix}, \quad (4.8)$$

the 6×6 matrix $\mathbf{S} = \mathbf{A}^T \mathbf{A}$ is the scatter matrix and $\mathbf{x}_i = [x_i^2, x_i y_i, y_i^2, x_i, y_i, 1]^T$.

To avoid the trivial solution $\mathbf{a} = \mathbf{0}$, a constraint $\|\mathbf{a}\|^2 = \mathbf{a}^T \mathbf{a} = 1$ is set. However, other constraints can be used, see Zhang (1997); Halir and Flusser (1998); Fitzgibbon et al. (1999). This constraint combined with equation (4.7) describes a Lagrange optimization problem, with a Lagrange operator λ , that can be solved using generalized eigenvectors, with six eigenvalue-eigenvector pairs (λ_i, g_i) . Since

$$\begin{aligned} \min_{\mathbf{a}} \mathbf{a}^T \mathbf{S} \mathbf{a} &= \lambda \mathbf{a}^T \mathbf{a}, \quad \text{and} \\ \mathbf{a}^T \mathbf{a} &= 1, \end{aligned} \quad (4.9)$$

we are looking for the eigenvector \mathbf{a}_i that corresponds to the minimal positive eigenvalue λ_i .

To ensure that only a single phasor rotation is treated each time, phase segments within the interval of $[0, 2\pi]$ are isolated by determining the minima and maxima of the calculated phase observations. For this reason, a maximum jump of π was set. For each isolated phase segment the best fitting ellipse is calculated. Figure 4.2 illustrates this procedure for the simulated observations with varying standard deviations presented in Figure 4.1.

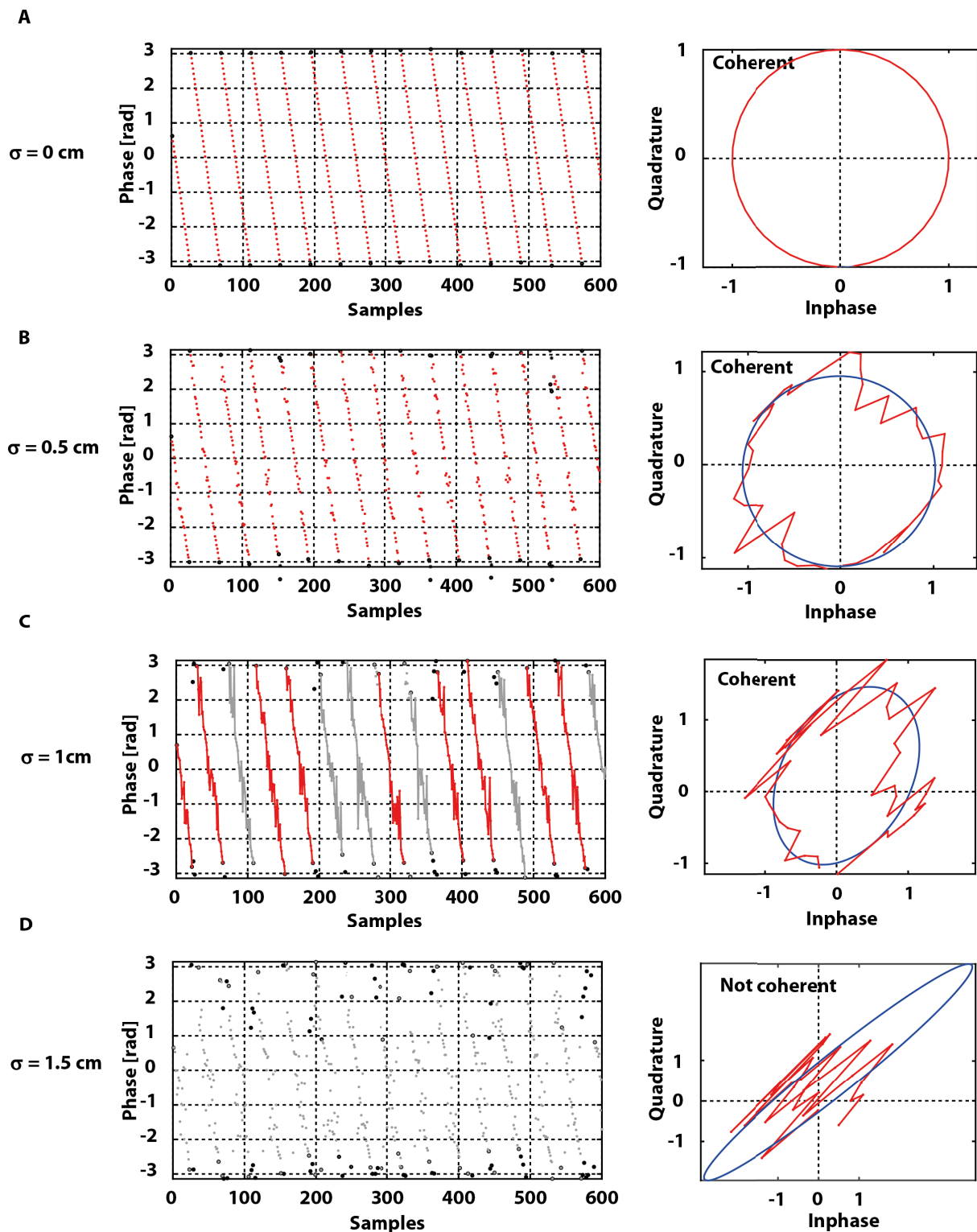


Figure 4.2: Simulation results of the ellipse fitting algorithm to extract coherent phase observations for different white noise levels. **Right:** Isolated phase segments within the interval of $[0, 2\pi]$ (marked with circles in black) flagged as coherent (red) or incoherent (grey). **Left:** For each of the extracted phase segment, the best fitting ellipse is calculated. The ellipse fitting algorithm extracted correctly the coherent and incoherent phase observations for simulated standard deviations of 0, 0.5, 1 and 1.5 cm respectively.

On the left side of the figure, are plotted in red the as coherent flagged phase observations with the calculated maxima and minima defining the single phase segments (black points) used for

the ellipse fitting computation. On the right side of the figure, an example of the computed ellipse (in blue) that bests fits the data (in red).

To exclude non-coherent phase observations, the residuals (and the resulting a-posteriori standard deviation s) are statistically analysed using a chi-square test (χ^2) with a significance level of 95%

$$\chi_f^2 = f \cdot \frac{s^2}{\sigma^2} \quad (4.10)$$

where f is the degree of freedom (the number of observations minus the number of unknown parameters, 6 coefficients in this case), and σ the a-priori standard deviation.

The null hypothesis is $H_0 : s^2 = \sigma^2$,

and the alternative hypothesis: $H_a : s^2 > \sigma^2$.

4.1.2 Performance of the Coherency Extraction Algorithm

To analyse the performance of the proposed coherency extraction algorithm a two class confusion matrix is used (Table 4.1). The confusion matrix, shows the number of correct and incorrect predictions made by the classification algorithm compared to the actual outcomes of the data.

| | | Data | |
|-----------|------------|---------------------|---------------------|
| | | Coherent | Incoherent |
| Algorithm | Coherent | True Positive (TP) | False Positive (FP) |
| | Incoherent | False Negative (FN) | True Negative (TN) |

Table 4.1: Two class confusion matrix.

In this thesis, the entries in the confusion matrix have the following meaning:

1. True Positive (TP) is the number of correctly extracted coherent data.
2. False Positive (FP) is the number of incorrectly extracted coherent data (the number of incoherent observations that were extracted as coherent from the algorithm).
3. False Negative (FN) is the number of missed coherent observations, (the number of coherent observations that were not identified by the algorithm).
4. True Negative (TN) is the number of correctly excluded incoherent observations.

To characterize the performance of the algorithm, several parameters exist (Powers, 2007). The sensitivity or True Positive Rate (TPR) is the proportion of real positive (TP) cases that are

correctly predicted positive by the algorithm

$$\text{sensitivity} = TPR = \frac{TP}{TP + FN} \cdot \quad (4.11)$$

The specificity or True Negative Rate (TNR) is the proportion of real negative (TN) cases that are correctly predicted negative by the algorithm and is computed as

$$\text{specificity} = TNR = \frac{TN}{FP + TN} \cdot \quad (4.12)$$

Thus TPR and TNR reflect how many of the relevant cases the algorithm picks up. This in turn is used in the overall Accuracy (ACC) that gives the rate of correctly classified data related to the total number of data N

$$ACC = \frac{TP + TN}{N} \cdot \quad (4.13)$$

For the comparison, a random selection of 50 hours from the pool of data in 2012 and 2013 was used. To define the coherency status of these reference data, the (at the beginning of this section mentioned) coherency extraction method proposed by Semmling (2012) combined with a visual classification were used. The following confusion matrix was established

| | | Validation Data set | |
|---------|------------|---------------------|------------|
| | | Coherent | Incoherent |
| Ellipse | Coherent | 23214 | 4592 |
| | Incoherent | 8374 | 35912 |

Table 4.2: Results of the confusion matrix used to analyse the performance of the ellipse fitting coherency extraction algorithm.

from which following parameters were calculated

| | TPR | TNR | ACC |
|-----------------|------|------|------|
| Ellipse Fitting | 0.74 | 0.89 | 0.82 |

Table 4.3: Calculated parameter of the confusion matrix. TPR: True Positive Rate, TNR: True Negative Rate and ACC: Accuracy.

From Table 4.3, it can be seen that 82% of the data were extracted correctly using the proposed ellipse fitting algorithm. However, ~ 12% of the coherent data are wrongly rejected and ~ 5% are erroneously marked as coherent. Notably, the set of incoherent data is about 55% of the total observations. The high loss of coherency is the motivation to go deeper into the analysis of the causes in the following section.

4.2 Coherent Data Analysis

To be able to use a phase-based GPS-R as a monitoring flood instrument in the region of the Mekong Delta, the continuity of the as coherent extracted observations is of significant interest. In the following section, the term coherent observations refers to the data that were identified as coherent using the ellipse fitting algorithm presented in the previous Section 4.1.1.

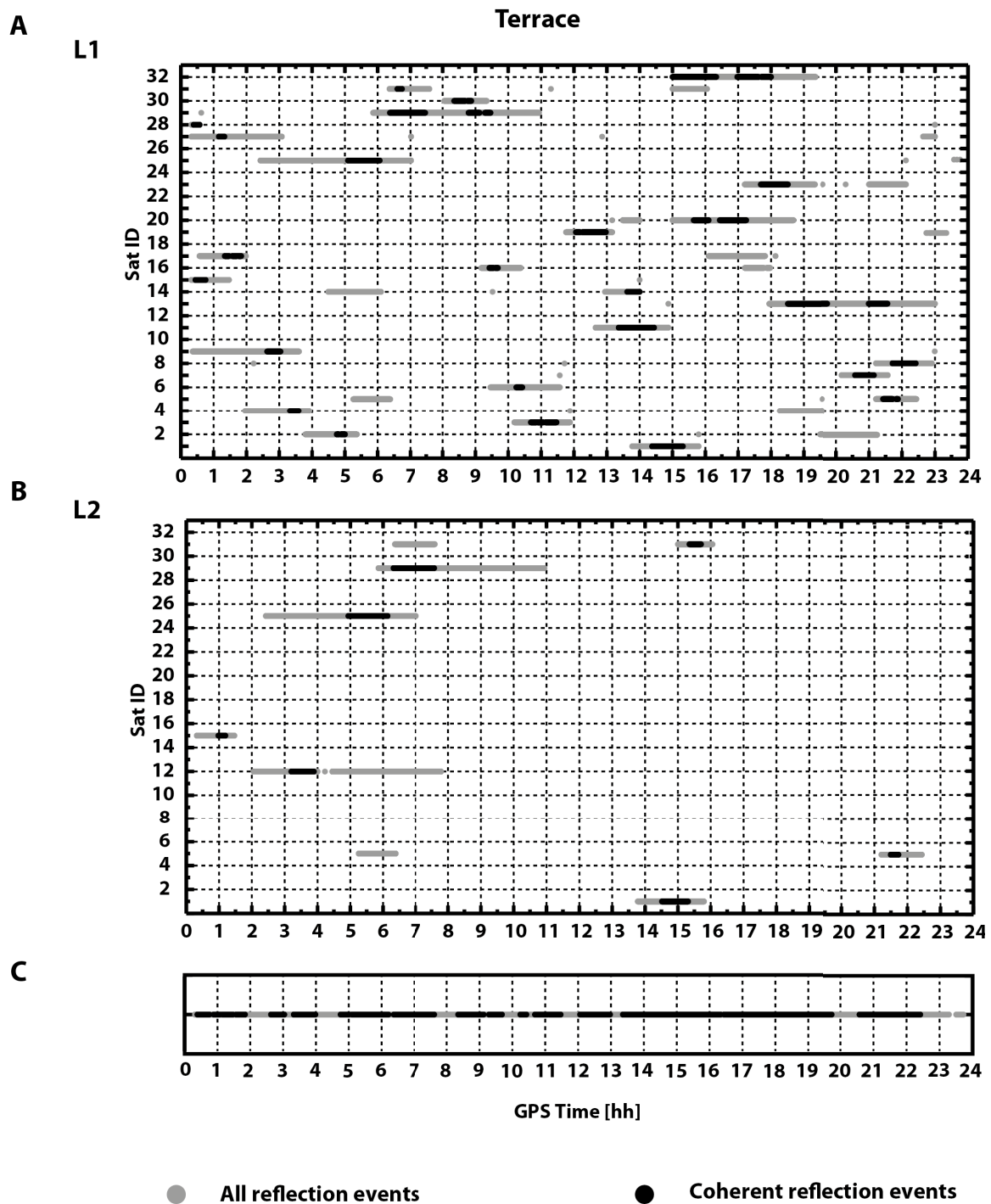


Figure 4.3: Representative example of recorded reflection events over 24 hours. In grey: reflection event. In black: coherent reflection event. **A:** Reflection events for the L1 signals. **B:** Reflection events for the L2 signal. **C:** Sum of reflection events over 24 hours. Data source: February 26, 2012, An Bihn hotel, Terrace, Can Tho City, Vietnam, Terrace.

Figure 4.3 shows a representative example of recorded L1 and L2 reflection events over 24 hours. On average, five L1 reflection events per hour (with a mean length of 2 hours) are tracked in parallel. Concerning the L2 reflections events, on average only 1 reflection event per hour (with a mean length of 2 hours) is tracked simultaneously. If the coherency is also taken into account, interruptions between several seconds and more than one hour can be observed. For this reason, an analysis of the recorded coherent reflected signals during both measurement campaigns in 2012 and 2013 is presented in Table 4.4. Under the category "Reflection events", all the recorded observations are taken into account without consideration for their coherency. Under the category "Coherent observations", all extracted coherent observations are included, without consideration for the continuous time length of their coherency.

| Year | 2012 | | 2013 | |
|---------------------------|-------|-------|-------|-------|
| Antenna height [m] | ~10 | ~20 | ~10 | ~20 |
| Reflection events [h] | ~ 265 | ~ 248 | ~ 202 | ~ 241 |
| Coherent observations [%] | 28.4 | 31.7 | 27.8 | 29.3 |

Table 4.4: Recorded reflection events for the conducted measurement campaigns in 2012 and 2013 in Vietnam, including the percentage of extracted coherent observations depending on the antenna height.

In the case of the first measurement campaign in 2012 and for the antenna placed ~10 m over the reflecting surface, only 28.4% of the recorded reflections are considered as coherent. For the second antennas position with a height of ~20 m, 31.7% of the recorded reflection events are extracted as coherent. A slight increase of around 4% for the higher placed antenna is thus observed. In the case of the second measurement campaign in 2013, for the antenna placed ~10 m over the reflecting surface, only 27.8% of the recorded reflections are considered coherent. Also here no significant difference with the results of the previous campaign can be observed. For the second antennas placement with a height of ~ 20 m, no significant difference can be seen with 29.3% compared to the results obtained in 2012 or with the first antennas position. Based on these results, the data of 2012 and 2013 could be merged. However, to analyse the impact of the antenna heights on remaining errors, namely cycle slips and multipath effects, only the experimental year will be merged together and only the different antennas height are considered.

If the recorded reflections events are analysed considering water surface reflections only, a major factor for the loss of coherency is due to the breadth of the river and the antennas location. The river bank starts approximately 20 m away from the terrace and 25 m from the roof of the hotel. A small garden with a covered terrace and palm trees is located in front of the hotel and many buildings are in the surroundings of the antennas (figures 3.2 and 3.3). The river itself is only ~150 m wide and also surrounded by buildings and palm trees on each side of its banks. Since the selected elevation and azimuth masks do not consider the geometrical behaviour of the river and the surrounding of its banks, incoherent reflection events passing through these areas are also recorded (Figure 4.4). Based on a map of the river, it can be seen

in Figure 4.4 that only 48.1% and 47.6% of the recorded reflection tracks, reflect off the water surface for the antenna placed at 10 m and at 20 m height, respectively. If now the percentage of coherent observations is analysed, nearly 50% of the water reflection events are coherent (Table 4.5).

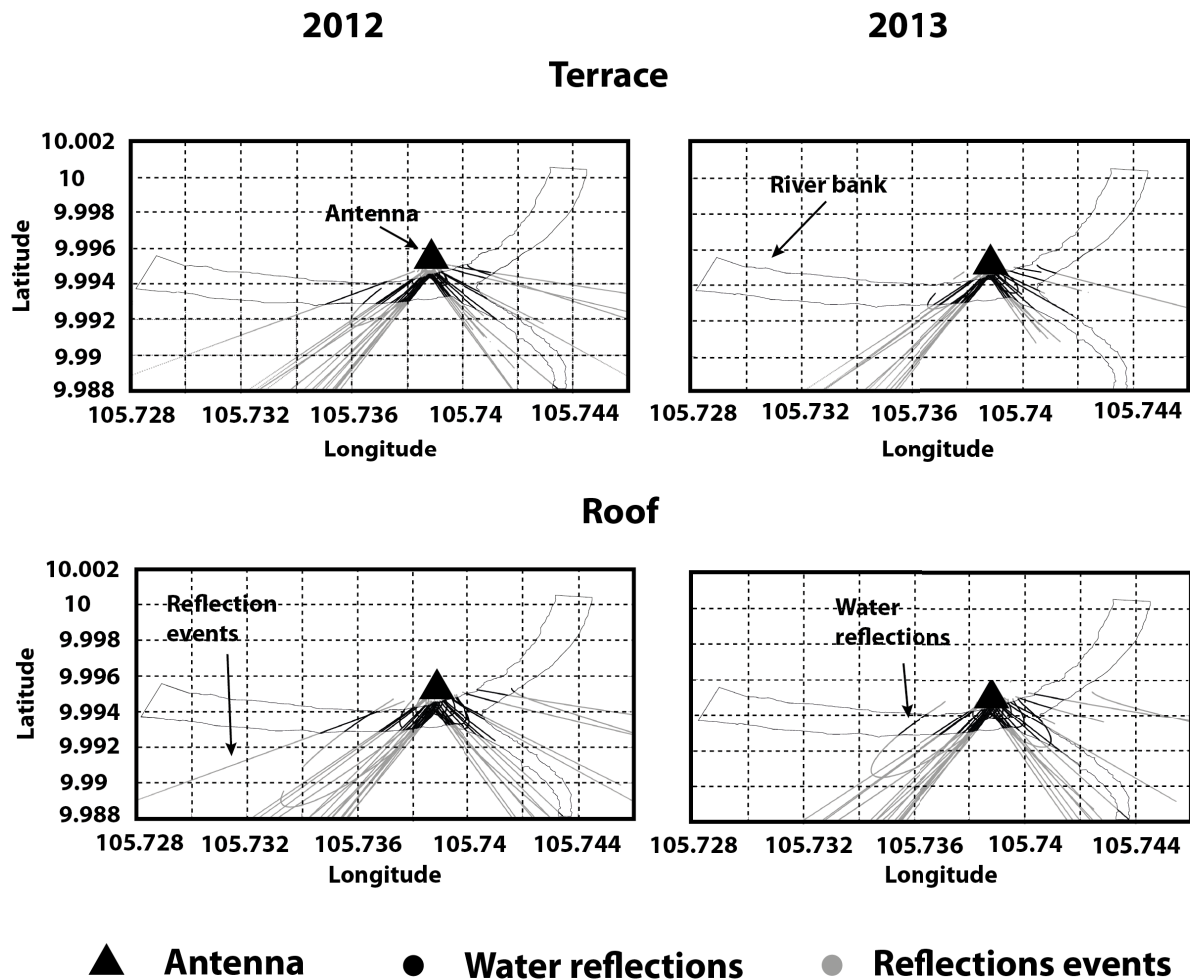


Figure 4.4: Reflection events for the measurement campaigns of 2012 and 2013. In grey all recorded reflection events. In black, expected water reflections based on simulations calculated using a map of the river. Data source: Experimental data from 2012 and 2013, An Bihn hotel, Can Tho City, Vietnam.

| | | |
|----------------------------|--------|--------|
| Antenna height | 10 m | 20 m |
| Water Reflections | 48.1 % | 47.6 % |
| Coherent water reflections | 46.7 % | 48.4 % |

Table 4.5: Recorded water reflection events as well as the percentage of their coherent part for the conducted measurement campaigns in 2012 and 2013 in Vietnam.

If these ~ 50% of water reflected data are analysed, the loss of coherency results from the direct surroundings of the antenna (palm trees and buildings). This effect can be clearly seen in Figure 4.5A and 4.5C, where the coherent and incoherent water reflection events are plotted in black and grey, respectively.

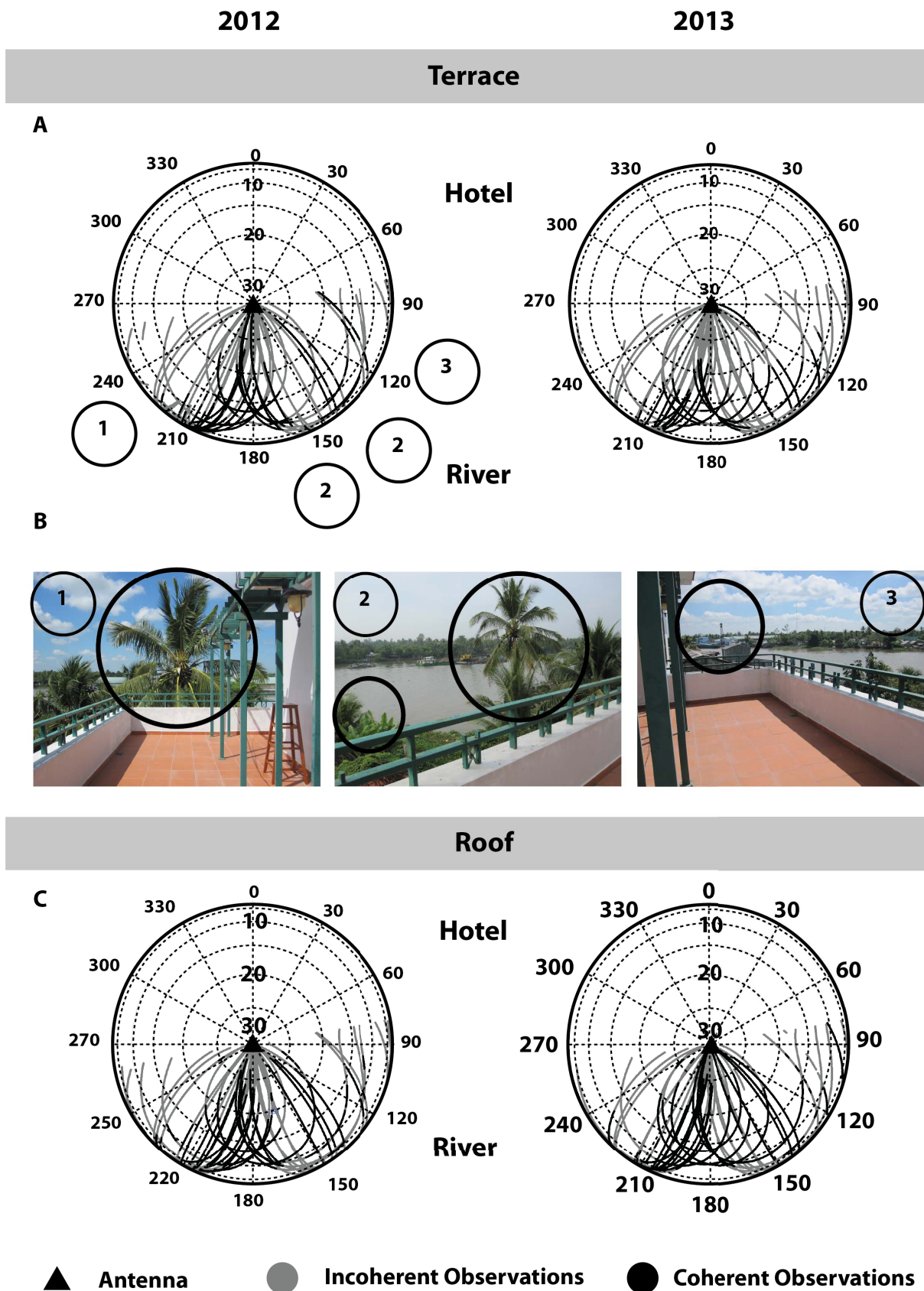


Figure 4.5: Restricted azimuthal view of the antennas. **A:** Observed azimuth of the coherent observations for the antennas placed on the terrace. **B:** Palm trees and buildings obstructing the signals received by the antennas placed on the terrace. **C:** Observed azimuth of the coherent observations for the antennas placed on the roof. Data source: Experimental data of 2012 and 2013, An Bihn hotel, Can Tho City, Vietnam.

Since the antennas placed at the height of 10 m have a more obstructed view than those placed at 20 m height, we can observe more azimuthal sections with no coherent reflection events between: 96 - 98 deg, 108 - 112 deg, 146 - 151 deg, 208 - 212 deg, 216 - 222 deg, and 230 - 260 deg. This azimuth angles coincide with the existing palm trees and buildings in the vicinity of the hotel and consequently of the antennas (Figure 4.5B). Similarly for the second antenna placed at the height of 20 m, a signal obstruction is found at the following azimuth angles: 103 - 105 deg, 217 - 223 deg, 231 - 249 deg and 251 - 260 deg.

Based on the shape of the river and the position of the receiver, a maximal possible horizontal water reflection point distance is simulated to be at 1000 m (grey line in Figure 4.6A). Assuming a planar Earth model, a minimal elevation angle of 0.6 deg and 1.1 deg would be feasible for the antennas placed at 10 m and 20 m height, respectively. However, this simulated reflection track with the maximal reachable horizontal distance comes from the perpendicular arm of the river in front of the hotel. This reflection trace is within the azimuthal mask section of 146-151 deg that in turn is one of the sections of incoherent reflection events.

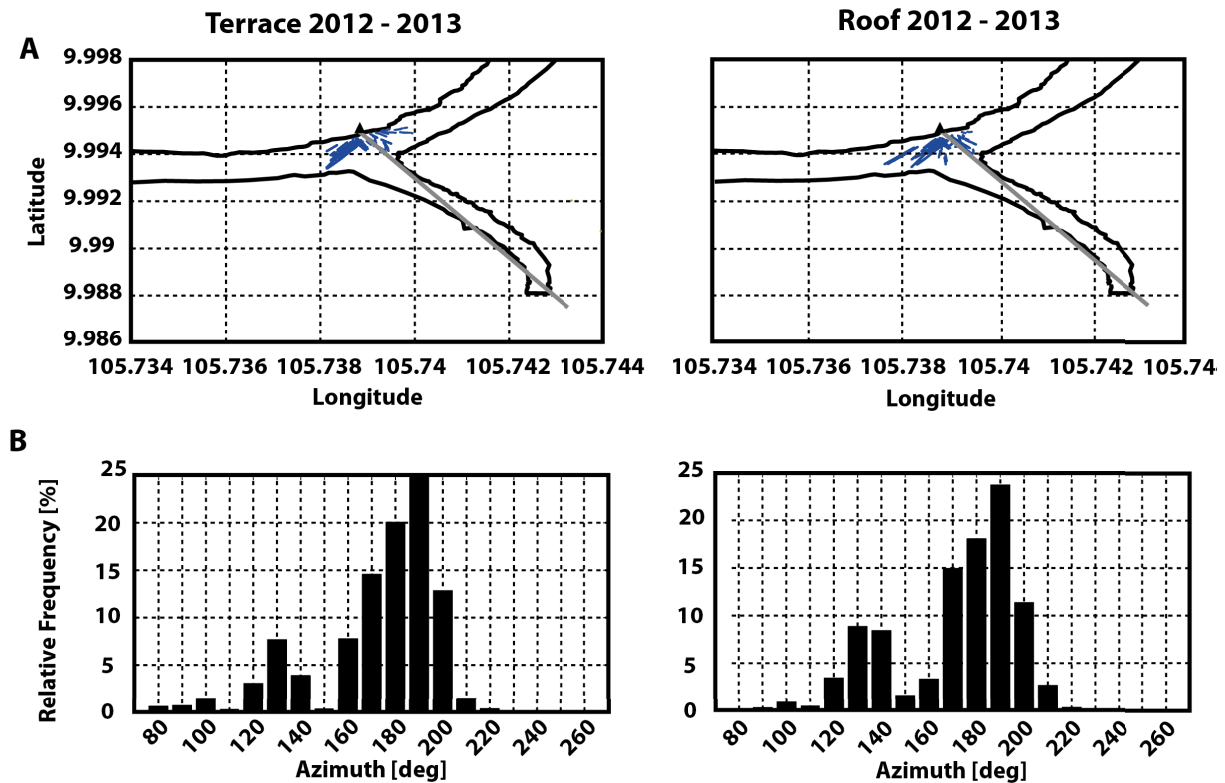


Figure 4.6: Analysis of the observed reflection events regarding their azimuth angle. **A:** Coherent water reflections with simulated maximal horizontal distance. **B:** Relative frequency of the observed azimuthal angles. Data source: Experimental data from 2012 and 2013, An Bihn hotel, Can Tho City, Vietnam.

Regarding the elevation angle, the analysis of the data shows that coherent observations for the antenna placed at 10 m height starts with an elevation angle of 3.2 deg and ends at an elevation angle of 29.1 deg (Figure 4.7). This corresponds to a horizontal distance between 20.3 m and 198 m. For the antenna placed at 20 m height, the elevation angles are between 3.4 - 28.4 deg, corresponding to a horizontal distance between 18.5 m and 168 m.

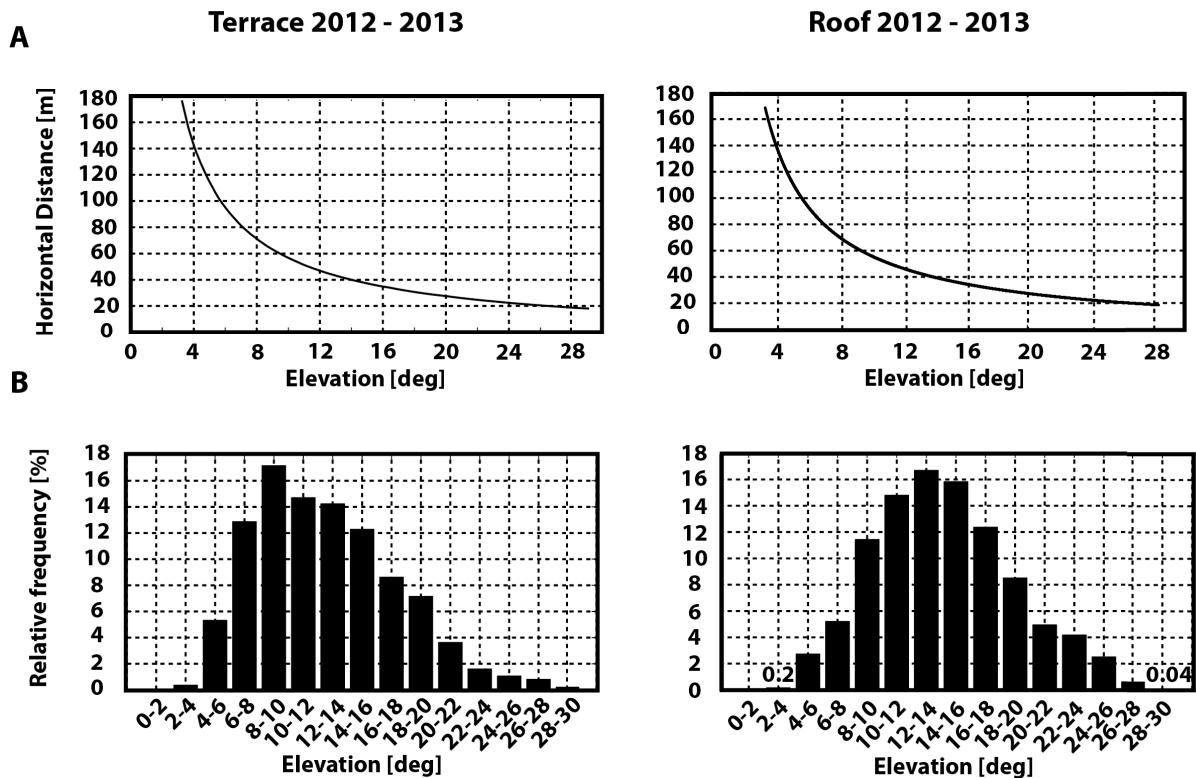


Figure 4.7: Analysis of the elevation and horizontal distance of the coherent water reflections. **A:** Calculated horizontal distances in case of coherent reflection events. **B:** Relative frequency of the observed elevation angles. Data source: Experimental data from 2012 and 2013, An Bihn hotel, Can Tho City, Vietnam.

The reason for the discrepancy between the observed and simulated elevation angles and consequently for the lower observed horizontal distances, is the existing roads, palm trees and buildings on the opposite side of the river. Thereby, the minimum elevation angle is limited by trees and obstacles on the opposite river bank, while the maximum elevation angle by the antenna surroundings. This is again shown in the relative frequency of the observed coherent azimuthal sections that are concentrated in both cases in the 160 - 200 deg range. This corresponds to the free view of the antennas of the river section.

Two further factors can also cause incoherent observations. First, the variation of the water level due to tidal back flow that causes a narrowing of the river up to ~ 3 m from both sides of the river bank (Figure 4.8 Left). Second, the high number of floating vegetation during low tides that disturbs the signal reflection off the water surface (Figure 4.8 Right).



Figure 4.8: **Left:** River narrowing up to 3 m from each side due to low tides. **Right:** High number of floating vegetation due to low tides, disturbing the reflection of the signal off the water surface.

Last but not most influencing factor disturbing the coherency of the phase observations, are the passing ships. Indeed, in addition to its importance as a means of transportation for merchandise and goods, the Mekong Delta is also frequently used by the local population for personal transportation. This leads to an increased roughness of the river and thus additional signal obstruction. To show this, ship movements were recorded during both measurement campaigns using a web-cam. A picture of a fixed section of the river was taken each minute.

Figure 4.9 shows an example of recorded coherent observations reflecting some of the cited reasons why coherency in our experimental set-up was disturbed. At the beginning of the observation (approx. between 2:00 - 2:25 GPS time) there is no coherency because the reflection track passes across the vegetation and buildings surrounding the hotel and crosses the section of dry river bed due to low tides (Figure 4.9A, B and D green box). Coherent phase observations are recorded for about 10 min. (Figure 4.9A). Afterwards, we can observe a sudden loss of coherency that is most likely due to a passing ship, causing ripples on the water surface (Figure 4.9A and D red box).

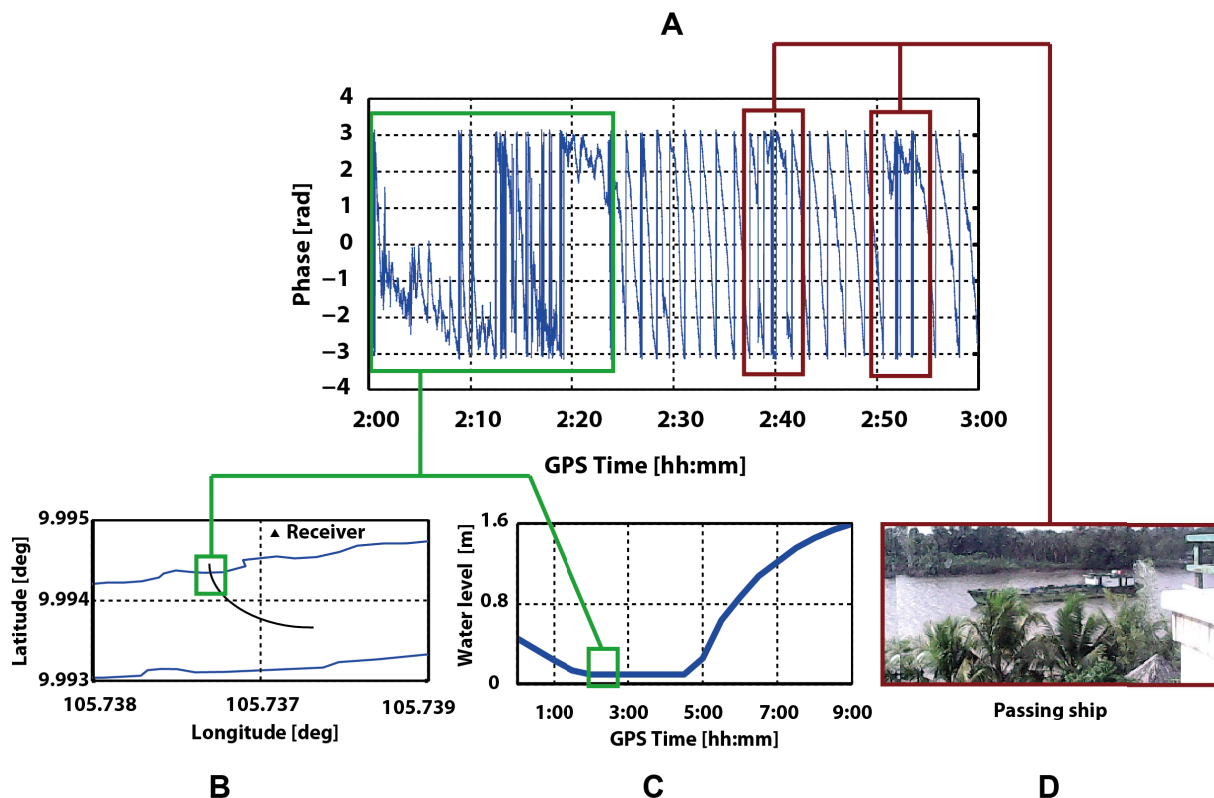


Figure 4.9: Example of recorded observations illustrating some of the factors that disturb the coherency of the reflected signals. **A:** Recorded phase observations. **B:** Reflection track passing through vegetation and buildings in front of the hotel. **C:** Reflection track passing through the section of dry river bed due to low tides. **D:** Sudden loss of coherent phase observations most likely due to a passing ship. Data source: Experimental data from March 3, 2012, An Bihn hotel, Can Tho City, Vietnam.

Continuous coherent phase observations are a mandatory condition to estimate water level and to resolve for the existing ambiguities in the phase observations. For this purpose, the length of continuous coherent water reflections is analysed. Under the category "Coherent observations

> 10 min.", all the continuous coherent fractions longer than 10 min. are included.

| | | |
|--------------------------------|--------|--------|
| Antenna height | ~10 m | ~20 m |
| Coherent observations > 10 min | 77.6 % | 80.0 % |

Table 4.6: Recorded coherent water reflections in function of the length of their continuous recording time of 10 min.

For a reliable ambiguity resolution, not only the length of continuous coherently observed phases is important but also their redundancy. For this reason, first the overlapping of extracted coherent observations regarding the in parallel observed satellites is analysed.

The analysis showed four categories:

1. Coherent observations on the L1 frequency from one satellite.
2. Coherent observations on the L1 and L2 frequency from one satellite.
3. Coherent observations on the L1 frequency by more than one satellites in parallel.
4. Coherent observations on the L1 and L2 frequency by more than one satellites in parallel.

For each of these categories, the percentage of their occurrence is calculated. Under the category "L1", the percentage of L1 coherent observations viewed by one, or simultaneously by two or more satellites, is given. Under the category "L2", the percentage of L2 coherent observations viewed by one, or simultaneously by two or more satellites. Under the category "L1 + L2", the percentage of simultaneously observed dual frequency coherent observations that are from one, or from more than two satellites in parallel is given.

We can notice that for the antenna placed on the terrace during 2012 and 2013 (left side of the Table 4.7), over 65% of the L1 coherent observations were observed from one satellite, around 32% from two satellites simultaneously and in only 2% of the cases from three satellites in parallel. For the L2 coherent observations, 85% are observed by one satellite and the remaining observations from maximal two satellites in parallel. Concerning the dual frequency observations, only 7% of the observations and this during only one single day (3rd March 2013) is observed in parallel from two satellites. The remaining dual frequency coherent observations are all observed from one satellite.

For the antenna placed on the roof of the hotel in 2012 and 2013, over 50% of the L1 coherent observations are observed from one satellite, around 40% from two satellites and about 8% from three satellites in parallel. For the L2 frequency, over 70% of the coherent observations are observed from a single satellite, around 30% from two satellites and under 1% from three satellites simultaneously. Finally, regarding the dual frequencies, over 70% of the coherent observations are observed by a single satellite, over 25% from two satellites in parallel and under 1% from three satellites.

| Terrace | | 1 Sat. | 2 Sat. | 3 Sat. | Roof | | 1 Sat. | 2 Sat. | 3 Sat. |
|------------|---------|--------|--------|--------|------------|---------|--------|--------|--------|
| 2012 02 25 | L1 | 73 % | 26.6 % | 0.4 % | 2012 03 04 | L1 | 64.1 % | 31.1 % | 4.8 % |
| | L2 | 100 % | 0 % | 0 % | | L2 | 65.9 % | 32.6 % | 1.5 % |
| | L1 + L2 | 100 % | 0 % | 0 % | | L1 + L2 | 100 % | 0 % | 0 % |
| 2012 02 26 | L1 | 70.9 % | 29.1 % | 0 % | 2012 03 05 | L1 | 56.4 % | 34 % | 9.6 % |
| | L2 | 100 % | 0 % | 0 % | | L2 | 100 % | 0 % | 0 % |
| | L1 + L2 | 100 % | 0 % | 0 % | | L1 + L2 | 100 % | 0 % | 0 % |
| 2012 02 28 | L1 | 77 % | 23 % | 0 % | 2012 03 06 | L1 | 46.2 % | 44.6 % | 9.2 % |
| | L2 | 96.8 % | 3.2 % | 0 % | | L2 | 38 % | 61.8 % | 0.2 % |
| | L1 + L2 | 100 % | 0 % | 0 % | | L1 + L2 | 38 % | 61.8 % | 0.2 % |
| 2012 03 03 | L1 | 59 % | 36 % | 5 % | 2012 03 07 | L1 | 60 % | 36 % | 4 % |
| | L2 | 95.6 % | 4.4 % | 0 % | | L2 | 54.4 % | 45.6 % | 0 % |
| | L1 + L2 | 100 % | 0 % | 0 % | | L1 + L2 | 54.4 % | 45.6 % | 0 % |
| 2012 03 04 | L1 | 54 % | 46 % | 0 % | 2012 03 08 | L1 | 35.8 % | 64.2 % | 0 % |
| | L2 | 100 % | 0 % | 0 % | | L2 | 100 % | 0 % | 0 % |
| | L1 + L2 | 100 % | 0 % | 0 % | | L1 + L2 | 100 % | 0 % | 0 % |
| 2013 03 18 | L1 | 84.6 % | 15.4 % | 0 % | 2013 03 11 | L1 | 66.5 % | 26.3 % | 7.2 % |
| | L2 | 94.8 % | 5.2 % | 0 % | | L2 | 51.5 % | 36.8 % | 0 % |
| | L1 + L2 | 100 % | 0 % | 0 % | | L1 + L2 | 41.7 % | 58.3 % | 0 % |
| 2013 03 19 | L1 | 58.8 % | 32.1 % | 9.1 % | 2013 03 12 | L1 | 53.6 % | 36.3 % | 10.1 % |
| | L2 | 52.1 % | 47.9 % | 0 % | | L2 | 100 % | 0 % | 0 % |
| | L1 + L2 | 100 % | 0 % | 0 % | | L1 + L2 | 100 % | 0 % | 0 % |
| 2013 03 20 | L1 | 50.5 % | 48.7 % | 0.8 % | 2013 03 13 | L1 | 26.2 % | 61.2 % | 12.6 % |
| | L2 | 41.6 % | 47 % | 11.4 % | | L2 | 52.9 % | 47.1 % | 0 % |
| | L1 + L2 | 39.8 % | 60.2 % | 0 % | | L1 + L2 | 51.7 % | 48.3 % | 0 % |

Table 4.7: Statistical analysis of the redundancy of coherent observations for the antennas placed on the terrace (left) and on the roof of the hotel (right) during the measurement campaign in 2012 and 2013. Data source: Experimental data from 2012 and 2013, An Bihn hotel, Can Tho City, Vietnam.

A comparison between both antennas heights suggests that the antennas positioned on the roof of the hotel and consequently higher, have a better observation constellation than the antenna positioned on the terrace giving more redundant observed satellites in parallel. This is due to the better free view of the antennas over the sensed river section of the Mekong Delta.

If now the percentage of single and dual frequency coherent observations with a continuous length of more than 10 min is analysed, around 95% of the coherent data are observed on a single frequency L1 or L2 (Table 4.8). However, only 5% of the single frequency coherent observations are observed at the L2 frequency. This is due to the GORS firmware where the L2C signal tracking is not optimal i.e. the signal tracking is not aligned with maximum C/N0 (personal communication G. Beyerle, GFZ Potsdam). As a consequence a low percentage of dual frequency coherent observations can be observed. Due to this fact, all the following analysis will concentrate on the L1 single frequency cases only.

| Antenna placement | Terrace | Roof |
|-------------------|---------|-------|
| Single Frequency | 94.6 % | 95.3% |
| Dual Frequency | 5.3 % | 4.7 % |

Table 4.8: Recorded coherent water reflections in function of their in parallel observed frequency and length of their continuous recording time of 10 min.

To get an estimate about the a-priori standard deviation of the L1 frequency phase observations, de-trended unwrapped coherent phase observations are used. The analysis showed a standard deviation of 0.55 rad corresponding to approximately 0.02 m.

4.3 Cycle slips

The carrier tracking loop combined with local frequency replica, enables to measure highly precise phase data with a precision of millimetre. These are obtained from the carrier tracking loop, using a carrier accumulator consisting of the fractional cycle count of the carrier Doppler phase measurement and the integer cycle count (Section 2.1.4).

During the first signal tracking, the number of full cycles between the receiver and satellite is unknown and the receiver can only measure a fraction of it

$$\Phi_{rcv}^{sat_i}(t_r) = \Phi_{rcv}(t_r) - \Phi^{sat_i}(t_r) + N_{rcv}^{sat_i} + \delta, \quad (4.14)$$

where $N_{rcv}^{sat_i}$ is the ambiguity and has the following three properties. First, since the ambiguity is a number of full cycle, it has an integer value. Second, each receiver satellite link has its own ambiguity integer value. Third, as long as no signal interruption has occurred, it stays constant, otherwise the receiver interprets the interruption as a new signal tracking and a new cycle count starts. Therefore, the ambiguities are unknown again. However, to take advantage

of the precise carrier phase observations, the ambiguity has to be solved correctly and thus these signal interruption - the Cycle Slip (CS) - have to be detected.

Many cycle slip detection methods have been developed since the early 1980s. However, all of them use either a combination of dual-frequency observations or a combination of phase and code observations. The advantage given here is that the code observations are not affected by cycle slips. The challenge within this thesis is thus to develop a method that relies only on single-frequency phase observations as more than 95% of the coherently recorded data are on the L1 or L2 frequency. Additionally, many of the existing cycle slip detection methods assume that the carrier phase observations are smooth. This presumption may be incorrect due to the reflection off the signal off the water surface, which increases the noise level of the observations.

4.3.1 Cycle Slip Detection Algorithm

In this section, a cycle slips detection algorithm is proposed based on the widely used Turbo Edit algorithm.

The Turbo Edit algorithm developed by Blewitt (1990) is a recursive algorithm that updates sequentially the wide-lane linear combination of code and phase observations and their variances. Through the use of a recursive average the noisy data are smoothed permitting to better detect cycle slips. For the GPS-R phase based method, the same algorithm is applied with the difference that the de-trended phase observations ϕ are used instead of the wide-lane linear combination.

The recursive average and variances are calculated as follow; c.f. Blewitt (1990)

$$\bar{\phi}(k) = \bar{\phi}(k-1) + \frac{1}{k} [\phi(k) - \bar{\phi}(k-1)] , \quad (4.15)$$

$$\sigma^2(k) = \sigma^2(k-1) + \frac{1}{k} [(\phi(k) - \bar{\phi}(k-1))^2 - \sigma^2(k-1)] , \quad (4.16)$$

where $\bar{\phi}$ is the mean of the de-trended unwrapped phase observations ϕ , σ the standard deviation and k and, $k - 1$ the present and previous epochs, respectively. The choice of the a-priori standard deviation is not critical, as the recursive algorithm rapidly determines variances values which are representative of the data set.

To flag an observation as a cycle slip, the following two conditions have to be fulfilled. First, subsequent epoch estimates $\phi(k+1)$ must lie within $4\sigma(k)$ of the running mean $\bar{\phi}(k)$

$$|\phi(k+1) - \bar{\phi}(k)| \geq 4\sigma(k) . \quad (4.17)$$

Second, two consecutive positive detections must lie within one cycle

$$|\phi(k+1) - \phi(k)| \leq 1 . \quad (4.18)$$

If both conditions are met, a new average is calculated, starting with these two points, until the next two consecutive points are found. If the last condition is not fulfilled (Equation (4.18)), the detected point is flagged as an outlier and is removed from the data.

4.3.2 Algorithm Performance

The performance of the proposed algorithm is examined with simulations. Six different satellites observed within the experiment conducted in Vietnam were used simulating an antenna height of 13 m. The satellites were chosen in the way that the elevation range of the Vietnam experiment was covered (3 - 30 deg). For each satellite, 50 simulations were carry out. To analyse the performance of the algorithm under different level of noise, a white noise with a zero mean and standard deviation σ was added to the de-trended phase observations for each of the 300 simulations. To test the impact of the occurrence time of the cycle slips within the data (at the beginning, middle or end), a cycle slip was randomly set within a predefined time window of one, two or five minutes. To test the sensitivity of the algorithm, cycle slips of different sizes are introduced within the data: 0.25, 0.5, 1 and 2 cycles.

| Noise [m] | Cycle Slip size [cycle] | Time Interval [min] | Found [%] | Not found [%] | False Positive [%] |
|-----------|-------------------------|---------------------|-----------|---------------|--------------------|
| 0.01 | 0.25 ; 0.5 1 ; 2 | 1 ; 2 ; 5 | 100.0 | 0.0 | 0.0 |
| 0.05 | 0.25 | 1 | 35.0 | 31.0 | 24.0 |
| | | 2 | 47.0 | 29.3 | 23.7 |
| | | 5 | 47.7 | 24.0 | 28.3 |
| | 0.5 | 1 | 81.7 | 9.3 | 9.0 |
| | | 2 | 88.0 | 5.0 | 7.0 |
| | | 5 | 93.3 | 0.3 | 6.3 |
| | 1 | 1 | 99.3 | 0.3 | 0.3 |
| | | 2 ; 5 | 100.0 | 0.0 | 0.0 |
| | 2 | 1 ; 2 ; 5 | 100.0 | 0.0 | 0.0 |

Table 4.9: Simulation results using the Turbo Edit algorithm for different cycle slip sizes (0.25, 0.5, 1 and 2 cycles) that occur at different time interval within the data (1, 2 or 5 minutes), under different white noise level of (0.01 and 0.05 m). For standard deviation of the observations of 0.01 m, the proposed algorithm detected all the artificially introduced cycle slips independently of their occurrence time or size. For observations with a standard deviation of 0.05 m, a high detection rate of over 99% could only be reached for cycle slips starting with a size of 1 cycle.

Table 4.9 summarize the results of the simulations obtained with the different cited settings using the Turbo Edit algorithm. The table can be read as follow: the added white noise is displayed in the first column. The time interval at which a cycle slip occurs with the size displayed in the second and third column, respectively. The percent of correctly detected cycle slips,

of missed cycle slips and wrongly flagged observation, are displayed in the following three columns, respectively.

For a standard deviation σ of 0.01 m all the tested cycle slip sizes were successfully found by the algorithm independently on the position of occurrence of the cycle slip within the data (Figure 4.10A). However, differences become evident with an increase in the measurement noise. For a standard deviation σ of 0.05 m, the Turbo Edit algorithm not only fails to detect small cycle slips of the size of quarter a cycle but also shows a high percentage of false positive flagged observations. For cycle slips of half a cycle of size, over 80% was correctly identified by the algorithm. A higher performance is achieved, if at least two minutes of cycle slip free observations are available to initialise the running average and variance. For larger cycle slips, the algorithm showed a hit rate of more than 99% (Figure 4.10B).

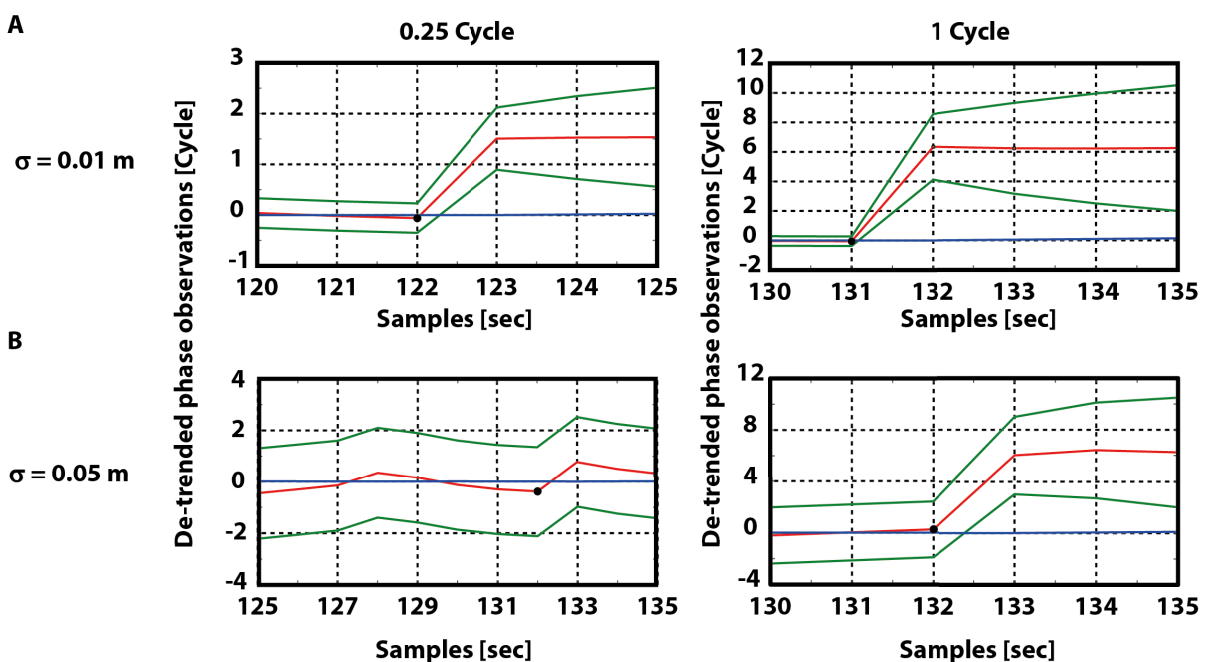


Figure 4.10: Representative examples of the simulation results using the Turbo Edit algorithm. Artificially introduced cycle slip (black point) of 0.25 cycle (left) and 1 cycle (right) size within the first two - three minutes of the data. In green plotted, the 4σ limits for the running mean in blue. In red the de-trended simulated phase observations. **A:** For a σ 0.01 m, all the artificially introduced cycle slips are detected independently of their size. **B:** For a σ of 0.05 m, not all cycle slips are detected especially for small cycle slips (left). For cycle slips bigger than one cycle, almost all cycle slips were detected correctly.

4.3.3 Cycle Slip Occurrence Analysis

Due to the presence of buildings and palm trees in the surrounding of the antennas, the reflected signal undergoes a high number of perturbations leading to a loss of coherency (Section 4.2), but also a high number of cycle slips.

For the conducted measurements, 1380 and 1205 cycle slips were detected for the height of 10 m and the 20 m observation, respectively.

The analysis of the relative frequencies of cycle slips, for both antenna placement, as a function of the elevation angle showed a distinct peak at an elevation angle of 7 deg and 8 deg, respectively (Figure 4.11). In combination with the relative frequency as a function of the azimuth, we can assume that cycle slips are most likely caused by moving palm tree leaves and the buildings in front of and on every side of the hotel, obstructing the reflected water signals.

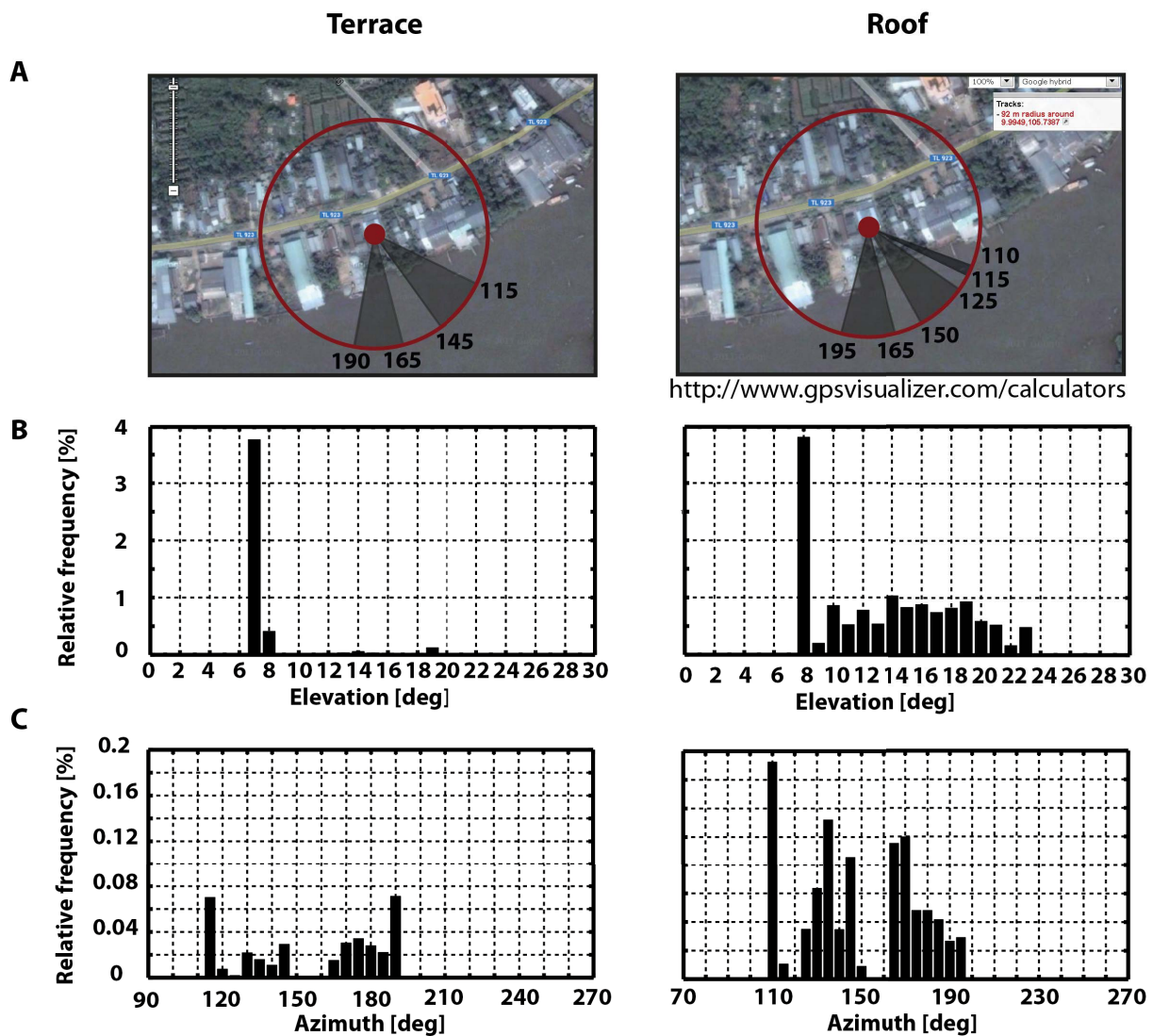


Figure 4.11: Analysis of the occurrence of cycle slips in function of the elevation and azimuth angles. **A:** Azimuthal section with a high occurrence of cycle slips. (Created by freely available GPS visualizer tool¹). **B:** Relative frequency as function of the elevation angle. **C:** Relative frequency as function of the azimuth. Data source: Experimental data from 2012 and 2013, An Bihn hotel, Can Tho City, Vietnam.

An analysis of the resulting water level height (Chapter 5) showed that not all cycle clips could be detected so that there is potential for further improvements. These undetected cycle slips lead to an error of several meters in the estimated water level heights.

¹www.gpsvisualizer.com

4.4 Multipath Effects

The Master-Slave antenna set-up for water level monitoring is based on the following two assumptions. First, only two signals are received: the direct LOS signal and signal reflected from the water surface. Second, these signals are tracked separately: the direct signal by the Master correlator and reflected signal by the Slave correlator. However, the data analysis showed that the Master signals as well as the Slave tracked signals are sometimes disturbed by several multipath. As the signal tracked by the Master serves as a reference for the Slave correlator, reflections affecting the direct signal are mapped into the signal tracked by the Slave (Figure 4.12A and 4.12B). Additionally, since we are interested in monitoring the water level, we have to determine the reflections, which are caused by the water surface only (Figure 4.12C and 4.12D).

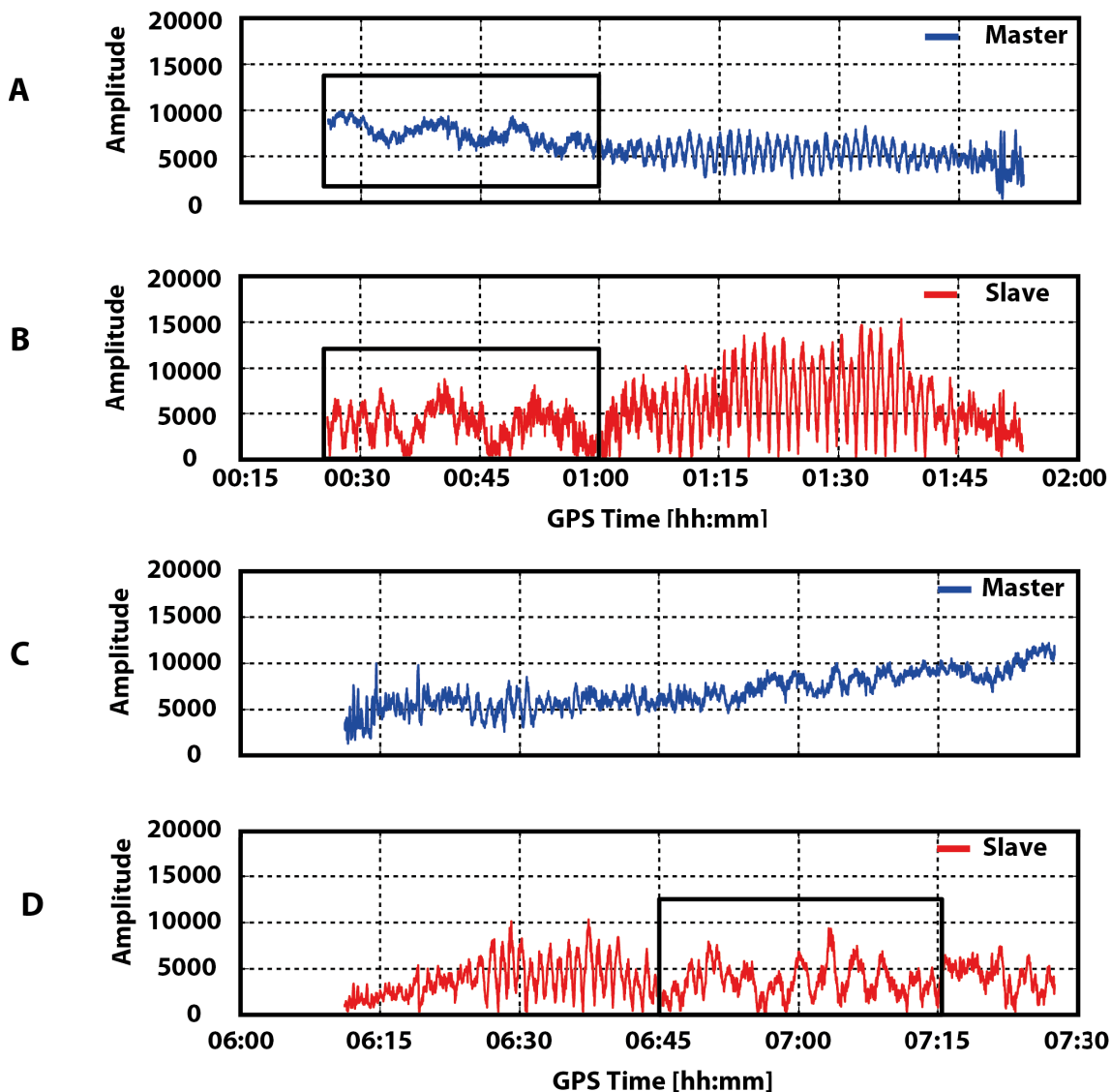


Figure 4.12: Master and Slave amplitude. Master amplitude (A) showing multipath effects (black box) that correlate with the recorded Slave amplitude (B), (black box). Slave amplitude (D) showing multipath effects (black box) that are not correlated with the multipath effects recorded by the Master (C). Data source: February 28, 2012, Can Tho City, Vietnam, A and B PRN 17, C and D: PRN 31.

4.4.1 Empirical Mode Decomposition

To extract the reflections from the water surface, the Empirical Mode Decomposition (EMD) analysis method is applied. It was developed by Huang et al. (1998) and adapted for GNSS multipath estimation for positioning tasks by Hirrle et al. (2012). The main advantage of the EMD method is that it is fully data-driven and can be applied to any complex data set. There is also no need for an a-priori base as for example trigonometric functions in the case of Fourier transform or a mother wavelet in the case of the Wavelet transform. Notably, in the EMD method, the basic functions are directly derived from and based on the input signal itself making it an adaptive method. Additionally, the decomposition is based on the local characteristic time scale of the data and hence applicable to non-linear and non-stationary processes (Hariharan et al., 2006). Thus there are no conditions on data processing in contrast to the Fourier which imposes the linearity and stationarity or Wavelet transform which imposes the linearity of the data. The basis of EMD is the assumption that at any given time, the data may have many coexisting simple oscillatory modes of significantly different frequencies, one superimposed on the other; c.f. Huang and Wu (2008)

$$\begin{aligned} x(t) &= \sum x_i(t) , \\ x_i(t) &= a(t) \sin(\omega(t)t) . \end{aligned} \quad (4.19)$$

The principle of the EMD method is to decompose a signal of multi-components into a finite number of mono-component thus a signal with a single frequency (Hirrle, 2016), called Intrinsic Mode Function (IMF), and that satisfy the following conditions; c.f. Huang and Wu (2008):

1. The number of local extrema and zero crossings must either be equal or differ from one.
2. The mean value of the envelope defined by the local minima and maxima is zero.

Figure 4.13 shows the different steps of the called 'sifting' process decomposing, that decomposes an input signal (Figure 4.13A) into a series of IMFs:

1. Identify all the local extrema (Figure 4.13B red dots) and interpolate between them, using a cubic spline to form the upper envelope env_{max} (Figure 4.13C, green line).
2. Repeat the same procedure as in step 1, but this time for the local minima, defining now the lower envelope env_{min} .
3. Calculate the mean between the upper and the lower envelope (Figure 4.13D, red line)

$$m_1(t) = \frac{(env_{min}(t) + env_{max}(t))}{2} \quad (4.20)$$

and compute the difference between the original signal $x(t)$ and m_1 to build the first "proto-intrinsic mode function" h_1 (Flandrin et al., 2004)

$$h_1 = x(t) - m_1 , \quad (4.21)$$

If h_1 does not fulfill the definition of an IMF, h_1 is treated as the new original signal and

the process is repeated from step 1 to 3

$$h_{11} = h_1 - m_{11}, \quad (4.22)$$

k times until the conditions of an IMF are met

$$IMF_1 = h_{1k}. \quad (4.23)$$

4. Extract the first IMF (IMF_1) from the original signal $x(t)$ (Figure 4.13E)

$$r_1 = x(t) - IMF_1. \quad (4.24)$$

The first IMF includes the highest frequency component of the signal, while the following IMFs contain decreasing frequencies.

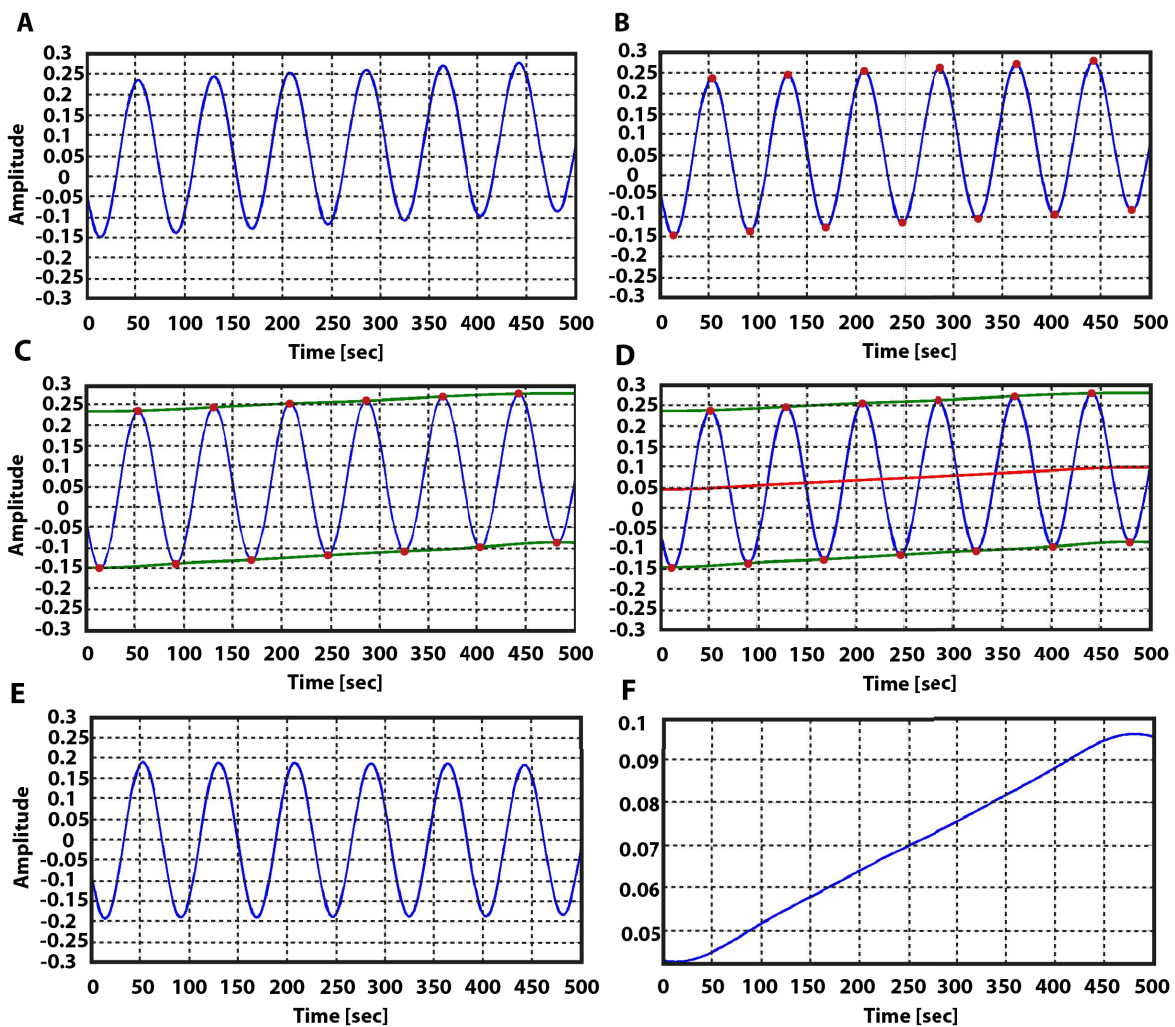


Figure 4.13: Empirical Mode Decomposition (EMD) sifting steps for a simple sinusoidal signal added with a trend. **A:** Composed signal of a simple sinusoidal plus a trend. **B:** Determination of the maxima and minima of the signal (red dots). **C:** Interpolation between the maxima and minima with a cubic spline, building the upper and lower envelope of the signal (green lines). **D:** Computation of the mean between the upper and lower envelope (red line). **E:** First IMF. **F:** Remaining trend.

r_1 is treated as the original signal and the steps from 1 to 3 are repeated until the next IMF is found. The above process is repeated n times until all IMF's are extracted and the residual r_n becomes a monotonic function, with one maximum or one minimum from which no more IMF's can be built (Figure 4.13F)

$$\begin{aligned} r_1 - IMF_2 &= r_2, \\ &\vdots \\ r_n - IMF_{n+1} &= r_{n+1}. \end{aligned} \quad (4.25)$$

The total sum of the IMF's reconstruct the original signal and therefore ensures completeness (Huang et al., 1998)

$$x(t) = \sum_{j=1}^n IMF_j + r_n. \quad (4.26)$$

In contrast to GNSS positioning, the major advantage of GPS-R is the a-priori information about the expected reflection events. Indeed, through the approximate knowledge about the satellite-receiver-reflector geometry, the roughly contribution of the water reflection can be predicted (Chapter 5). This in turn, enables us to calculate the expected phase observation.

Figure 4.14 shows the flowchart of the proposed algorithm which will be explained stepwise in the following.

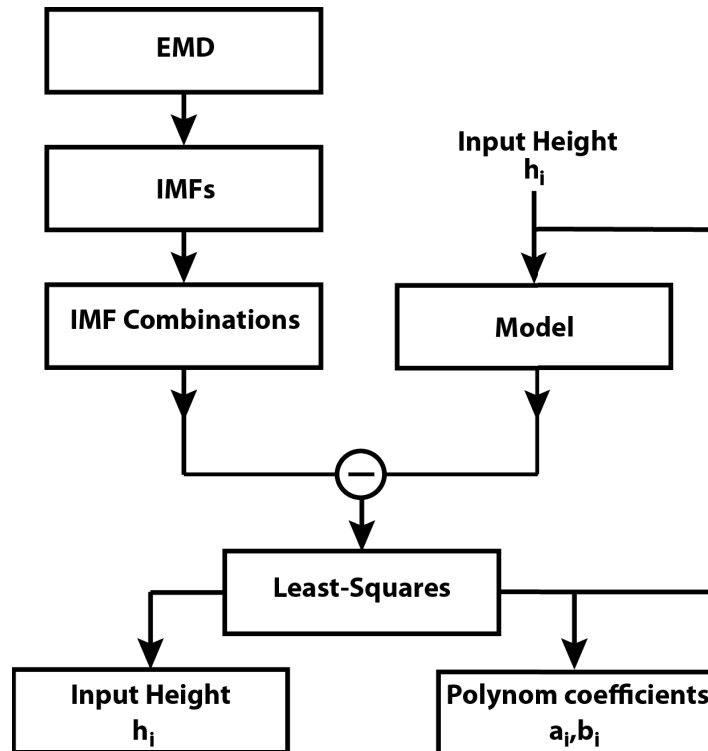


Figure 4.14: Main steps of Multipath processing algorithm. First, the IMFs are extracted using the EMD method. Second, all possible combinations of IMFs are build. In parallel, a model of the expected reflected phase observations is calculated for different input heights. The modelled phases and the IMF phase combinations are unwrapped. The difference between them is computed. In the last step, a LS polynomial fitting of first order is used to determine the IMF combination and the input height that causes the minimum slope of the differenced unwrapped phases.

First, from the I and Q observations, the IMFs are extracted using the EMD method. In a next step, all possible combinations of the IMFs are build. In parallel, the I and Q are modelled based on the satellite and receiver position and a coarse information about the relative height between the receiver and the reflecting water surface (Chapter 5). If the model fits the observations, the difference between them should build a (zero) line with minimal slope.

Figure 4.15 shows simulation results for an antenna placed at 13 m height. On the left side of the figure, the simulated unwrapped phases with a noise level of 0.01 m is indicated. On the right side of the figure, the difference between modelled and simulated unwrapped phases for different input heights between 10 and 15 m with a step of 1 m can be seen. For the input height of 13 m, the difference builds a zero line with minimal slope (purple line).

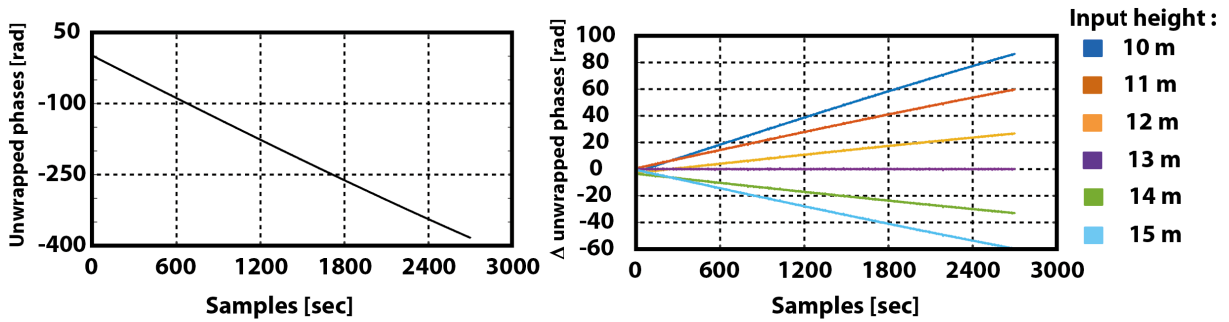


Figure 4.15: Simulation showing that with a LS based polynomial fitting of first degree for different input heights, the difference between the model and the observations builds a zero line. **Left:** Simulated unwrapped phase for an antenna placed at 13 m height above the reflecting surface. **Right:** Difference between the simulated unwrapped phase observations and the modelled unwrapped phases for different input heights between 10 and 15 m. For the input height of 13 m, the difference shows a zero line with minimal slope.

To determine the best fit that causes the minimum slope, a LS polynomial fitting is used. As no complete satellite pass with coherent observations is observed during the conducted experiment, a linear fit of first degree suffice otherwise a polynomial of higher degree should be used. The linear functional model is defined as

$$\begin{aligned}\Delta\varphi_a &= a + bt, \\ x &= [a, b], \\ l &= Ax + v,\end{aligned}$$

where l represents the column vector of $n \times 1$ $\Delta\varphi_a$ (difference between the modelled and observed unwrapped phases), A the $n \times m$ design matrix, x the $m \times 1$ column vector of unknown parameters a and b forming the coefficients of the polynomial, t the $n \times 1$ observations time and v is the $n \times 1$ column vector of residuals.

This procedure is repeated for different input heights. The accumulated IMF sub-signals, that best fit the model, are isolated as the "real" observations caused by the reflections off the water surface. These are stored with the corresponding relative height between the receiver and the water surface that gives a first guest of the water level height.

4.4.2 Efficiency Analysis

In the following section, the efficiency of the proposed algorithm is analysed using simulated phase observations as well as selected observations collected during the experimental setup in Vietnam. To avoid confusion, the term "multipath" is used for the reflections that are not caused by a reflection off the water surface.

Simulations

To analyse the efficiency of the proposed multipath filtering method, following simulations are carried out.

First, to test the ability of the algorithm to isolate the IMF combination that corresponds to the reflection off the water surface, 50 noise free simulations are conducted. For this reason, different reflector types (horizontal (H), vertical (V) or a mix of both(H/V)) and different reflector positions (between 1 and 30 m) are used (Table 4.10).

Second, to analyse the impact of noisy observations on the EMD decomposition method, simulations with different noise level are tested. With this aim, a white noise with zero mean and standard deviation σ of 0.01 m and 0.05 m, respectively is added to the noise free simulated data (Table 4.11).

To be able to compare the results of each time series, the same satellite pass is used for all the conducted simulations, namely the PRN 13 observed on February 25, 2012 at the An Bihn hotel in Vietnam. Additionally, the relative height between the water surface and the receiver antenna is set to 13 m.

Table 4.10 shows a part of the results, obtained with the proposed algorithm, if noise free multipath signals are used. Ideally, the number of extracted IMF should reflect the number of multipath signals composing the signal. In the first simulation series, a single horizontal reflector is simulated (H). In the second simulation, a single vertical reflector is used (V). In the third simulation series, a single horizontal and a single vertical reflector is used (H/V).

The simulations show, that independently of the simulated reflector type, the number of extracted IMF sub-signals, do not coincide with the number of superimposed signals. A correct physical interpretation of the extracted single IMFs is thus not possible. However, the main interest within this thesis is not the interpretation of the obtained IMFs but the isolation of the signals caused by a reflection on the water surface.

Through the use of all possible combinations of IMFs combined with the LS fitting approach, the relative height is mostly estimated correctly. A high discrepancy is found for the simulated multipath signals of which the frequency is close to the frequency of the reflected water signal. In this case, the EMD method is not able to separate correctly between both signals. This phenomena is called the Beat-effect (Hirrlé, 2016).

| Reflector Parameters | | | No. of Extracted IMFs | | Selected IMF combinations that best fit the water reflection model | | Obtained relative height [m] |
|----------------------|---------------|--------|-----------------------|---|--|-------|------------------------------|
| Type | No. H / No. V | h [m] | I | Q | I | Q | |
| H | 1 / 0 | 1 | 2 | 2 | 1 | 1 | 13.0 |
| | | 10 | 5 | 5 | 1+3 | 4+5 | 12.5 |
| | | 30 | 5 | 5 | 2+3 | 2+3 | 13.0 |
| V | 0 / 1 | 1 | 2 | 2 | 1 | 1 | 13.0 |
| | | 10 | 3 | 3 | 1 | 1 | 13.0 |
| | | 30 | 3 | 4 | 1 | 1+3 | 13.6 |
| H/V | 1 / 1 | 1 / 2 | 2 | 2 | 1 | 1 | 13.0 |
| | | 5 / 30 | 4 | 3 | 1+3 | 1 | 13.0 |
| | | 30 / 5 | 3 | 5 | 2 | 2 + 5 | 13.2 |

H: Horizontal reflector

V: Vertical reflector

Table 4.10: Part of the simulation results, aiming to test the ability of the proposed algorithm, to isolate the water reflected signal in case of noise free signals for different types of reflectors: horizontal (H), vertical (V) and a mix of both (H/V) and reflector height between 1 and 30 m. The number of extracted IMFs do not coincide with the number of superimposed signals. Through the use of the LS matching algorithm, the relative height of the water level could be successfully estimated apart from those multipath signals close to the frequency of the reflected water signal.

In the second simulation series, the same signals are used as in the previous time series, but this time a white noise with a zero mean and a standard deviation σ of 0.01 m and 0.05 m, respectively is added (Table 4.11).

The comparison between both simulation series shows that the obtained number of extracted IMFs increased, independently of the simulated reflector type (horizontal (H), vertical (V) or a mix of both (H/V)) or the set distance between the reflector and the water surface. Thus as expected and like in the noise free simulation series, the number of extracted IMFs do not reflected the simulated input number of superimposed signals. A physical interpretation of the single extracted IMF is thus not possible. Compared to the noise free simulation series, the use of all IMF combinations leads to a first relative height estimation between the water surface and the receiver antenna but this time at the decimetre level.

| Noise [m] | Reflector Parameters | | | No. of Extracted IMFs | | Selected IMF combinations that best fit the water reflection model | | Obtained relative height [m] | |
|-----------|----------------------|---------------|---------|-----------------------|---|--|-------|------------------------------|------|
| | Type | No. H / No. V | h [m] | I | Q | I | Q | | |
| 0.01 | H | 1 / 0 | 1 | 7 | 8 | 5+6 | 5+7 | 13.3 | |
| | | | 10 | 8 | 8 | 6+7 | 6+7 | 13.5 | |
| | | | 30 | 7 | 7 | 2+3 | 2+3 | 13.3 | |
| | V | 0 / 1 | 1 | 8 | 8 | 5 | 5 | 13.4 | |
| | | | 10 | 7 | 8 | 5+6 | 6+7 | 12.7 | |
| | | | 30 | 9 | 8 | 5+6 | 5 | 12.7 | |
| | H/V | 1 / 1 | 1 / 2 | 7 | 7 | 6 | 5+6 | 13.3 | |
| | | | 5 / 30 | 7 | 7 | 4 | 4 | 12.6 | |
| | | | 30 / 5 | 3 | 5 | 2 | 2 + 5 | 13.2 | |
| | | | 30 / 25 | 3 | 5 | 2 | 2 + 5 | 13.1 | |
| | 0.05 | H | 1 / 0 | 1 | 7 | 8 | 5+6 | 5+7 | 13.3 |
| | | | | 10 | 8 | 8 | 6+7 | 6+7 | 13.5 |
| 30 | | | | 7 | 7 | 2+3 | 2+3 | 13.3 | |
| V | | 0 / 1 | 1 | 8 | 8 | 5 | 5 | 13.4 | |
| | | | 10 | 7 | 8 | 5+6 | 6+7 | 12.7 | |
| | | | 30 | 9 | 8 | 5+6 | 5 | 12.7 | |
| H/V | | 1 / 1 | 1 / 2 | 7 | 8 | 5+6 | 6 | 12.6 | |
| | | | 5 / 30 | 8 | 8 | 7 | 6+7 | 13.3 | |
| | | | 30 / 5 | 9 | 8 | 6 | 5+6 | 13.6 | |
| | | | 30 / 25 | 8 | 8 | 7 | 6+7 | 12.6 | |

Table 4.11: Part of the simulation results using the EMD method for different reflector types added with a normally distributed white noise with zero mean and standard deviation σ of 0.01 m and 0.05 m, respectively. The number of extracted IMFs do not match the number of superimposed signals and increase due to the noise. The obtained values of the water level height are within the meter level of accuracy.

The remaining IMF signals not only enable to recombine the multipath signals but also the randomly added white noise that can be used to estimate the noise level of the processed signals. The mismatch between the combined IMFs (Figure 4.16 in green) and the simulated signal (Figure 4.16 in red) is due to the use of a cubic spline interpolation.

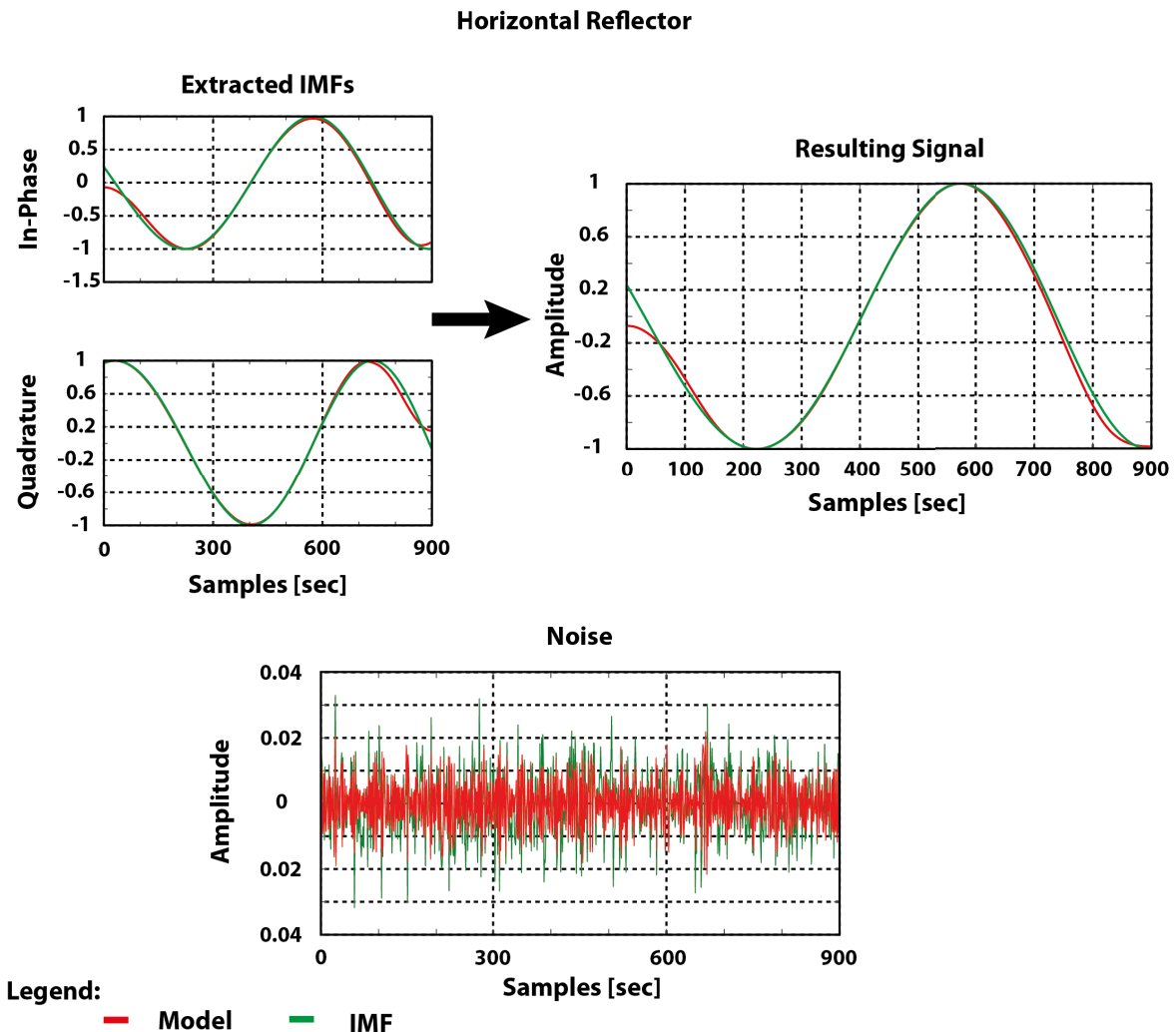


Figure 4.16: **Top:** Sum of the selected IMFs that recombine a simulated horizontal object with a distance of 3 m relative to the water surface. **Bottom:** Sum of the remaining IMFs that give a noise level estimate of the signals for a randomly added white noise of 0.01 m.

Observations

The proposed algorithm was also tested on observations recorded during the conducted experiments in Vietnam.

Figure 4.17 shows an example of an EMD decomposition on recorded data of PRN 1 during the measurement campaign of February 28, 2012. Each of the recorded I and Q were decomposed in seven IMFs ordered in decreasing frequency. In red are marked the selected IMFs combination (IMFs 3 and 4 for both I and Q input signal) that best fit the calculated phase model with an input height of 12.9 m.

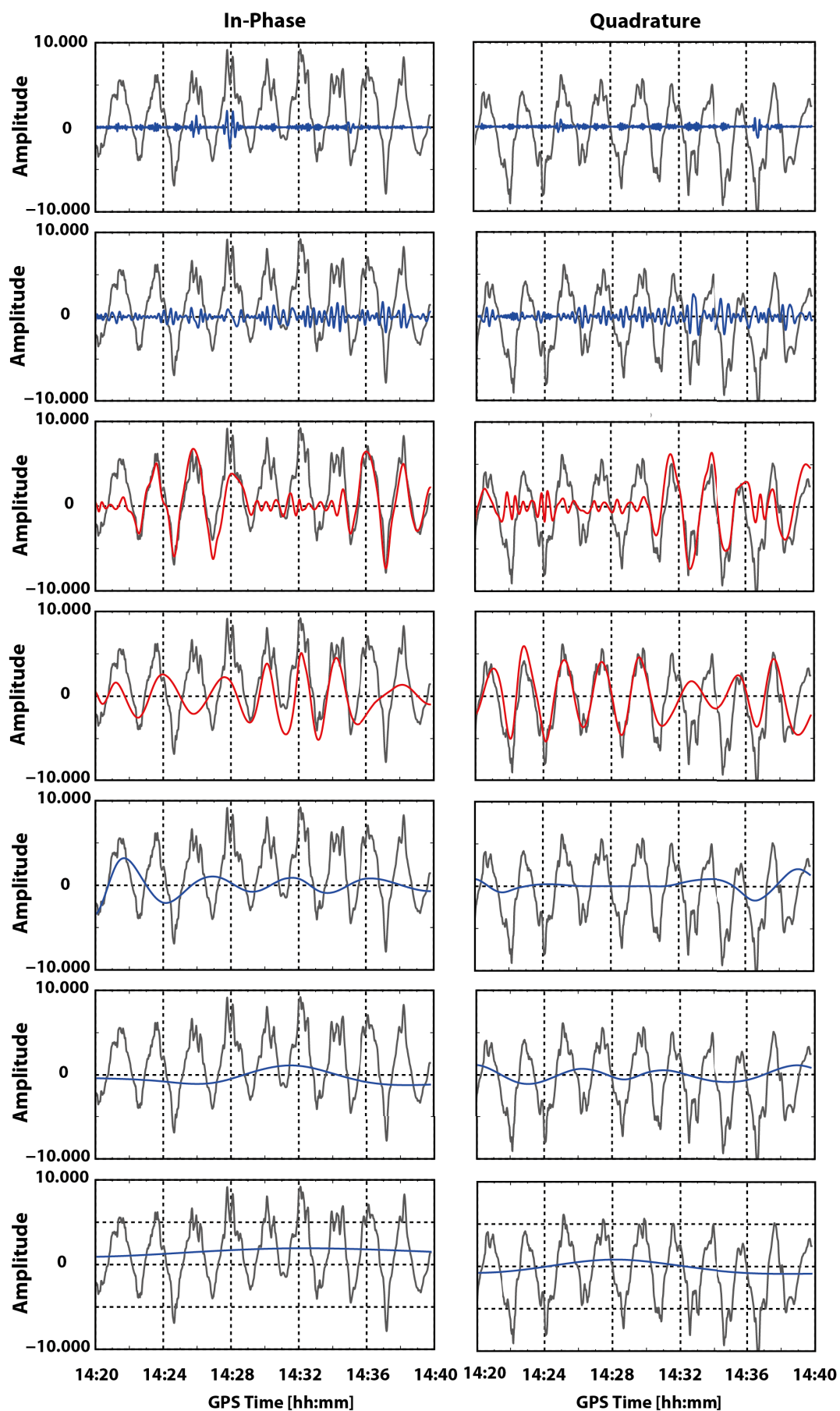


Figure 4.17: Results of the application of the EMD method on the I and Q output signal. In grey, the original input signal. In blue, the IMFs resulting from the EMD decomposition. In red, the sub-signals, that best fit the phase model. Data: Can Tho City, Vietnam, PRN 1, February 28, 2012.

The isolated IMFs of Figure 4.17 are now represented in phase form in Figure 4.18. In red are marked the calculated phase observations from the recorded I and Q observations. In green the selected IMFs (IMFs 3 and 4 that best fit the calculated phase model (in red) for an input height of 12.9 m.

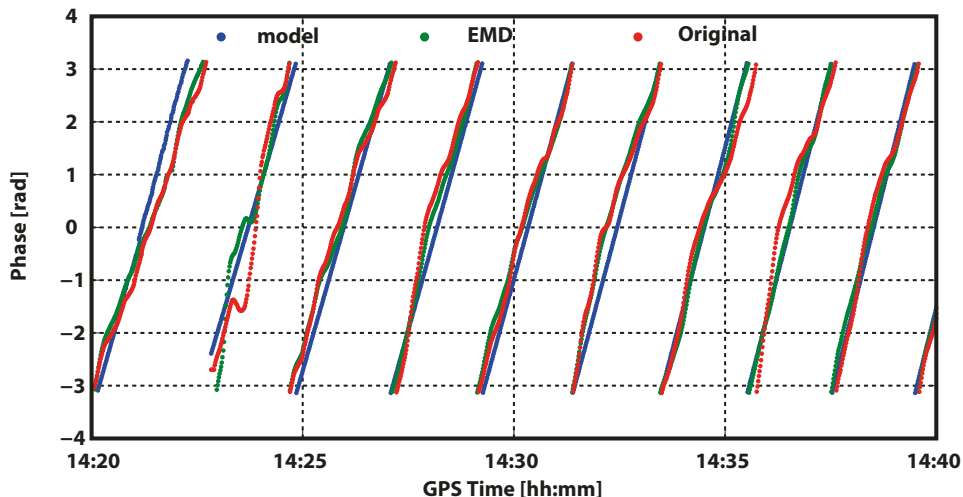


Figure 4.18: Results of the isolated IMF sub-signals that best fit the phase model. In blue, the modelled phase observations. In red, original recorded coherent phase observations. In green, the phase observations obtained by accumulating the IMF sub-signals 3 and 4. Data: Can Tho City, Vietnam, PRN 1, February 28, 2012.

In the next plot (Figure 4.19) an analyse of the remaining accumulated IMFs of Figure 4.17 is made. The residual sub-signals are formed from noise (IMFs 1 and 2 in Figure 4.19A) and other multipath effects probably caused by objects in the surrounding of the antenna (accumulated IMFs 5 and 6) in Figure 4.19B.

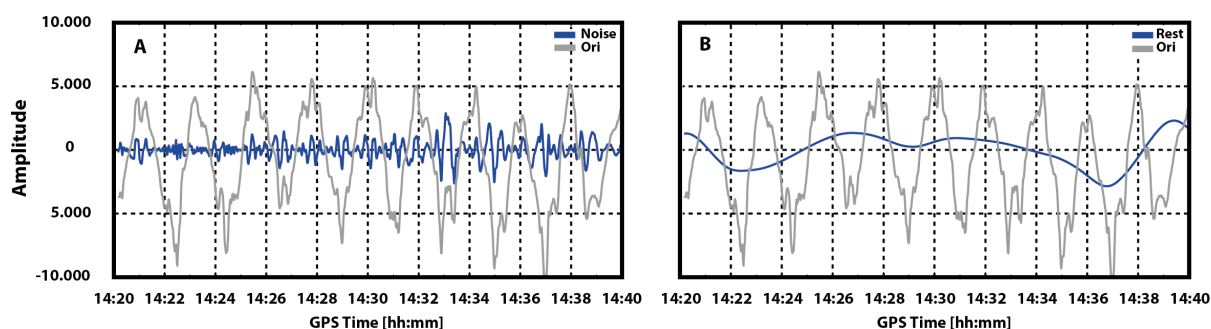


Figure 4.19: Accumulation of residual IMF sub-signals 1,2,5 and 6. **A:** Resulting noise signal by accumulating IMF 1 and 2. **B:** Resulting multipath by accumulating IMF 5 and 6. Data: Can Tho City, Vietnam, PRN 1, February 28, 2012.

As the number of extracted IMFs does not coincide automatically with the number of existing multipath signals, the following can only be an interpretation.

The interpretation of the mean frequency of these two last accumulated IMFs yield to a horizontal reflecting object placed in a radius of 22 m from the antenna. This combined with the mean

observed elevation angle of 9 deg and the mean azimuth angle of 191 deg gives the direction of the incoming multipath signal that coincides with the grass in the neighbouring property to the hotel (Figure 4.20).



Figure 4.20: Interpretation of the accumulated residual IMF sub-signals 5 and 6. The mean frequency yields to an object lying at an horizontal distance of 22 m away from the antenna. This combined with a mean azimuth of 191 deg and a mean elevation of 9 deg, coincides with grass on the banks of the observed river section. Data: Can Tho City, Vietnam, PRN 1, February 28, 2012.

4.5 Preprocessing Algorithm

The analysis of the data within this chapter, shows the necessity to pre-process the recorded data. Indeed, due to objects (buildings, palm trees) in the vicinity of the antennas, multipath effects and Cycle Slips could be detected. Additionally, due to the increased number of passing ships and floating vegetation during low tides, the coherency of the phase observations is disturbed enabling their use in a phase based GPS-R water level height extraction method. With a sampling rate of 200 Hz, an automated coherency extraction method is mandatory. In the following, the different algorithms proposed and methods developed in this chapter are resumed to form the pre-processing algorithm for the receiver output data.

Figure 4.21 shows the algorithm flowchart used in the pre-processing stage. First, the coherent phase observations are extracted using the LS based ellipse fitting algorithm presented in Section 4.1. After this step, the as coherent extracted data are investigated on the presence of Cycle Slips or outliers using the adapted Turbo Edit algorithm proposed in Section 4.3. Finally, the pre-processed data are mitigated on the presence of multipath effects other than those

caused by water reflections. For this purpose, the Empirical Mode Decomposition method described in Section 4.4 is used combined with a model of the expected water reflections. Thereby all the possible combinations of the extracted IMFs are built. The combination of IMFs that best fits the model is isolated as the signal that was reflected off the water surface. For this purpose a LS polynomial fitting is used.

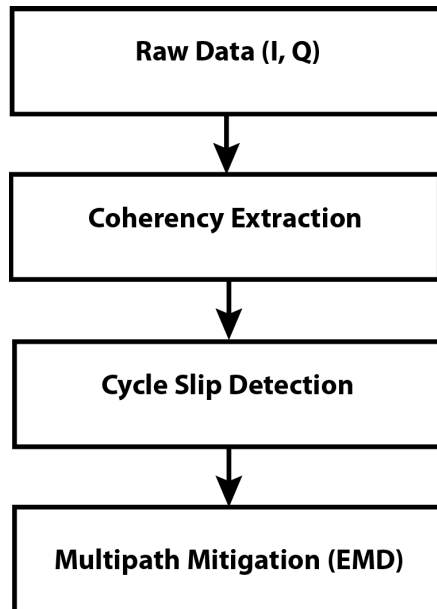


Figure 4.21: Main steps of the preprocessing algorithm of the input data. First coherent observations are extracted base on the ellipse fitting algorithm. Second, the data are verified on the presence of cycle slips. In the last step, the existence of multipath effects other then water reflections are mitigated and filtered out from the phase observations. The extracted IMFs that best fit a model of the expected water reflection is used for this purpose.

Chapter 5

Least-Squares Phase Based GPS-R Altimetry

After the preprocessing steps, described in Chapter 4, water level heights are calculated based on the Least-Squares (LS) method (Figure 5.1). In GPS based positioning, the functional model has been investigated intensively over the past decades (Hofmann-Wellenhof et al., 2008; Xu, 2007). Nevertheless, for GPS-R applications it has to be adapted. In this chapter, the functional model will be developed based on an analysis of the maximal allowed excess path error to reach the set decimetre level of accuracy (Section 5.1). The definition of this mathematical model will lead to the problem of ambiguities that will be outlined in the following Section 5.2. Finally, the obtained water level results will be presented and analysed in the last section of this chapter (Section 5.4).

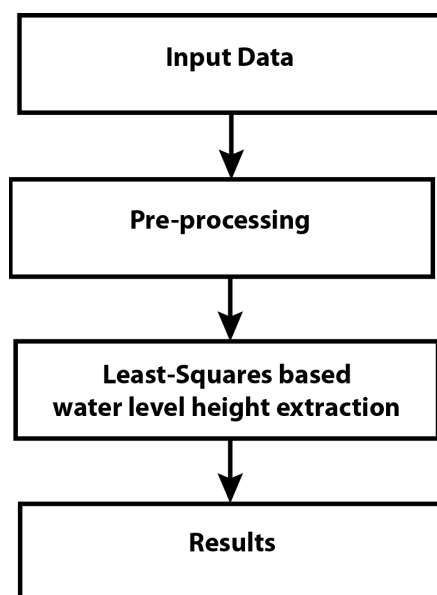


Figure 5.1: Main steps of the used algorithm for the extraction of water level using GNSS-R phase observations. In the first stage, a pre-processing of the input data is made. In a second stage, the water level changes are determined by using a LS based method.

5.1 Functional Model of a Phase Based GPS-R Altimetry

A prerequisite for any Least-Squares (LS) based method is the existence of redundant observations \mathbf{I} thus an excess of measurements compared to the number of unknown parameters (an overdetermined system). So if n is the number of observations and u the number of unknowns, then there is a LS task with a degree of freedom $f = n - u$, if $f \geq 1$. The results and quality of a LS based solution depend on the formulation of two models: the functional and stochastic model.

The functional model $f(\tilde{\mathbf{x}})$ describes the mathematical relationship between the observations $\tilde{\mathbf{I}}$ and the unknown parameters $\tilde{\mathbf{x}}$

$$\tilde{\mathbf{I}} = f(\tilde{\mathbf{x}}) , \quad (5.1)$$

where $\tilde{\mathbf{I}}$ represents the $n \times 1$ column vector of the true value of measured quantities and $\tilde{\mathbf{x}}$ the $u \times 1$ column vector of true unknown parameters.

However, as measurements are always afflicted with some uncertainties, a correction of the observations \mathbf{v} (residuals) has to be accounted for. Additionally, as we have no sole solution but rather an infinite number of them, the true values of the unknown parameters are not known but estimated, so that Equation (5.1) becomes

$$\mathbf{I} + \mathbf{v} = f(\hat{\mathbf{x}}) , \quad (5.2)$$

where \mathbf{v} represents the $n \times 1$ column vector of the correction of the observations and $\hat{\mathbf{x}}$ the $u \times 1$ column vector of the estimated unknown parameters.

To be able to calculate the quantity of interest, namely the relative height h between the receiver and the reflecting surface, the excess path difference $\Delta\rho_{r,d}$ between the direct and the reflected signal is needed. This in turn, can be expressed in terms of the phase difference $\Delta\varphi_{r,d}$ between the direct and the reflected signal (Section. 2.2.3) in metre

$$\begin{aligned} \Delta\varphi_{refl,drct}(t) &= \lambda_i [\varphi_{refl}(t) - \varphi_{drct}(t)] \\ &= \Delta\rho_{refl,drct}(t) + \sigma_{syst}(t) + \lambda_i N_{amb,refl,drct} + \epsilon , \end{aligned} \quad (5.3)$$

where the index *refl* and *drct* stands for reflected and direct, respectively, t is the time of reception of the signal, σ_{syst} are the sum of all systematic errors affecting the GPS observables (Section 2.4), λ_i is the wavelength in dependency of the used frequency i , N_{amb} represents the ambiguity and ϵ stands for the observations noise and remaining not modelled effects. For visibility task, the time of reception t will be left out in the following equations.

However the phase differences $\Delta\varphi_{refl,drct}$ are not directly observed but computed from the output of the Slave correlator, namely from the I and Q

$$\Delta\varphi_{refl,drct} = atan(Q, I) . \quad (5.4)$$

Each element of the mathematical model (Equation (5.3)) has to be related to the unknown parameter h . The systematic errors affecting the GPS observables may be corrected for a-priori. But depending on the specified accuracy, in the case of this thesis the decimetre level, the appropriate model has to be chosen.

5.1.1 Impact of Excess Path Errors on Altimetric Determination

To give a statement on the overall excess path error budget that has to be maintained to reach an altimetric accuracy at decimetre level, the impact of excess path errors $\sigma_{\Delta\rho}$ on the relative height σ_h determination is analysed in the following

$$\sigma_h = \frac{\sigma_{\Delta\rho}}{2 \sin E}, \quad (5.5)$$

where E is the elevation angle.

Figure 5.2 reveals that the precision in range determination is an important factor in the error budget of a GPS-R based altimetric application. Accordingly, an error of 10 cm in the excess path length causes an altimetric error of 0.7 m for an elevation angle of 4 deg.

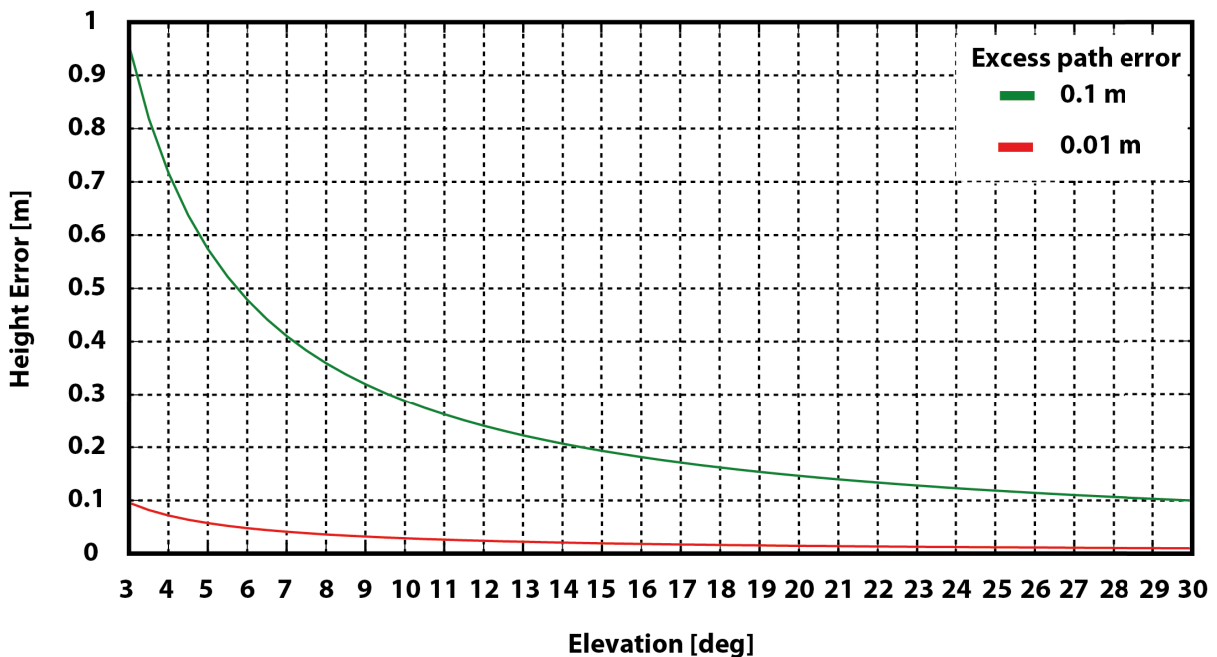


Figure 5.2: Altimetric error height caused by errors in path length determination. For an elevation mask of 3 deg, the total error of the excess path determination should not exceed 1 cm if decimetre level accuracy in the altimetric height has to be reached.

Based on the analysis of the recorded observations during the conducted experiments in Vietnam (Section 4.2), the minimal observed elevation angle is 3 deg. This combined with the targeted altimetric accuracy to decimetre level, a maximal total excess path error budget of 1 cm has to be kept.

5.1.2 Planar versus spherical Earth Model

To decide, whether a planar or a spherical Earth surface model should be used within this thesis, the calculated excess path difference between the two models has been computed for different receiver heights and elevation angles, based on the description of the experimental set-up in Chapter 3 and the elevation angle limits found in Chapter 4.

Figure 5.3 illustrates that for elevation angles greater than 3 deg, an excess path difference between the two models reaches a maximum of 3 mm for receiver heights below 30 m above the water surface. For decimetre level of accuracy, the use of a planar model is thus justified (Chapters 3 and 4).

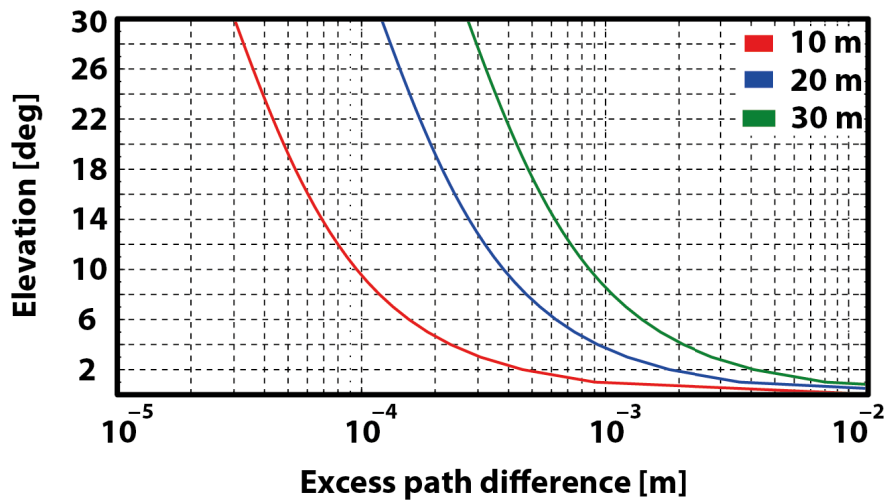


Figure 5.3: Excess path difference in [m] between spherical and planar model for different antenna heights at different elevation angles. For elevation angles greater than 3 deg and receiver heights of less than 30 m over the reflecting surface, the excess path difference between the two models does not exceed 3 mm so that the use of a planar model instead of a spherical one is justified for this kind of receiver reflector constellation if accuracy of decimetre level has to be reached.

5.1.3 GPS-R Mathematical Model

Based on the results of the precedent section, the direct φ_{drct} and the reflected φ_{refl} carrier phase signals can be modelled as follows

$$\varphi_{drct} = \rho_{rcv}^{sat_i} + c(\delta t_{rcv} - \delta t^{sat_i}) - I_{rcv}^{sat_i} + T_{rcv}^{sat_i} + \lambda_i N_{amb,rcv}^{sat_i} + M_{drct} + PCC_{drct}(A, E) + PWU_{drct}(A, E) + \varepsilon_{drct}, \quad (5.6)$$

$$\varphi_{refl} = \rho_{rcv}^{sat_i} + c(\delta t_{rcv} - \delta t^{sat_i}) - I_{refl.Point}^{sat_i} + T_{refl.Point}^{rcv} + T_{refl.Point}^{sat_i} + \lambda_i N_{amb,rcv}^{sat_i} + 2h \sin(E) + M_{refl} + PCC_{refl}(A, E) + PWU_{refl}(A, E) + \varepsilon_{refl}, \quad (5.7)$$

with

| | |
|------------------------------------|---|
| $\varphi_{drct}, \varphi_{refl}$ | carrier phase of the direct and the reflected signal [m], |
| $\rho_{rcv}^{sat_i}$ | geometric range between the receiver and satellite i [m], |
| c | speed-of-light [m/s], |
| $\delta t_{rcv}, \delta t^{sat_i}$ | receiver and satellite i clock error [sec], |
| $T_{rcv}^{sat_i}$ | tropospheric delay from receiver to satellite i [m], |
| $T_{refl.Point}^{sat_i}$ | tropospheric delay from reflection point (refl.Point) to satellite i [m], |
| $T_{refl.Point}^{rcv}$ | tropospheric delay from reflection point to receiver [m], |
| $I_{rcv}^{sat_i}$ | ionospheric delay from receiver to satellite i |
| $I_{refl.Point}^{sat_i}$ | ionospheric delay from reflection point to satellite i [m], |
| PCC_{drct}, PCC_{refl} | phase centre correction for the direct and the reflected signal [m], |
| M_{drct}, M_{refl} | multipath effect for the direct and the reflected signal [m], |
| PWU_{drct}, PWU_{refl} | phase wind up effect for the direct and the reflected signal, |
| $N_{amb,rcv}^{sat_i}$ | ambiguity [m], |
| h | height difference between reflecting surface and receiver [m], |
| E | elevation angle [deg], |
| A | azimuth angle [deg], |
| ε_j | random noise for the direct and the reflected signal [m]. |

By subtracting the reflected (Equation (5.7)) from the direct signal (Equation (5.6)) a model can be obtained that links the receiver phase observations to the unknown relative height h between receiver and reflecting surface (Beckheinrich et al., 2012)

$$\begin{aligned}
\Delta\varphi &= \varphi_{refl} - \varphi_{drct} \\
&= 2h \sin E + \Delta I_{refl,drct} + \Delta T_{refl,drct}^{sat_i} + \lambda_i N_{refl}^{sat_i} \\
&\quad + \Delta M_{refl,drct}(t) + \Delta PCC_{refl,drct}(A, E) + \Delta PWU_{refl,drct}(A, E) + \varepsilon_j.
\end{aligned} \tag{5.8}$$

Due to the short baseline between the Master and the Slave antenna, it is assumed that the remaining ionospheric effect $\Delta I_{refl,drct}$ is negligible (Section 2.4.6). Additionally, as the same receiver is used for the direct and the reflected signal, the receiver clock error δt_{rcv} as well as the satellite clock error δt_{sat_i} are eliminated. The phase wind up effect $\Delta PWU_{refl,drct}(A, E)$ is

corrected following the method described in Section 2.4.2. For the multipath effects $\Delta M_{refl, drct}$, the EMD method, described in Section 4.4, is applied. For the remaining systematic errors namely the tropospheric delay and the phase centre correction, the used models will be treated in the following two subsections.

5.1.4 GPS-R Tropospheric Model

To avoid multipath effects and a higher noise level, observations from low elevation angles are excluded for a GPS based positioning by introducing a cut-off elevation angle lying mostly in the range of [10 - 20] deg above the horizon (Teunissen, 1991). In contrast, in the constellation used within this thesis, GPS-R reflection events from low elevation angles are of interest. Thus accurate Mapping Function (MF)s (Section 2.4.1) are required, such as the Global Mapping Function (GMF) (Boehm et al., 2006) mapping function which is used within this thesis. Additionally, the fact that the GPS-R signal crosses the troposphere twice (from the transmitter down to the reflecting surface then from the reflector to the receiver antenna) have to be accounted for (Figure 5.4).

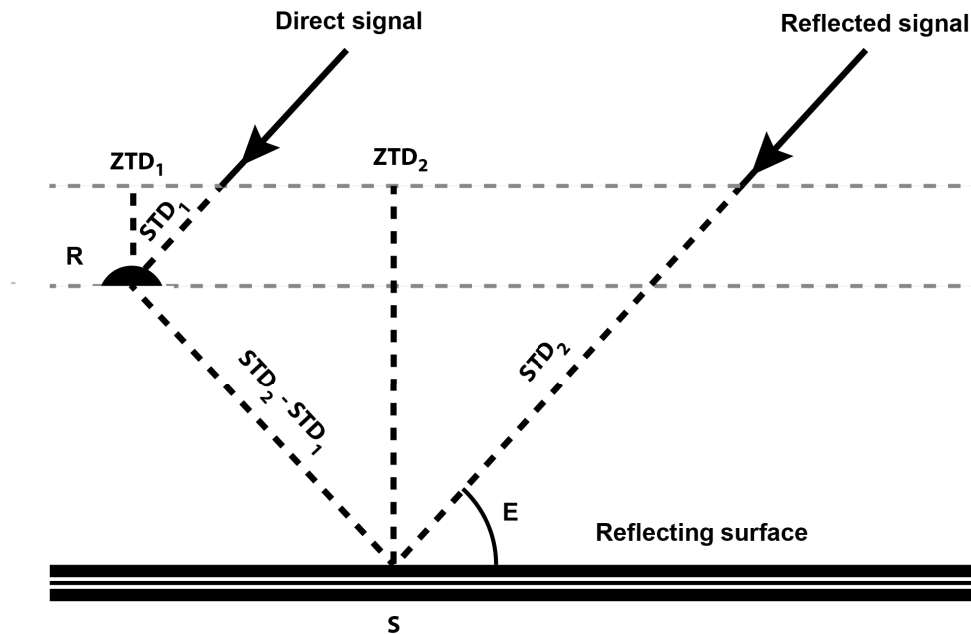


Figure 5.4: Symmetric tropospheric model. Following Cardellach et al. (2011) the tropospheric delays STD_1 and STD_2 are considered to be symmetric so that by building the difference, only twice the $STD_2 - STD_1$ remains.

To account for this, Cardellach et al. (2011) assume the tropospheric layer to be azimuthally symmetric at the reflection point S and propose following model to correct for the tropospheric delay

$$\Delta_{trop} = 2 ZTD MF \left(1 - e^{-\frac{h}{H_{atm}}} \right). \quad (5.9)$$

This model can be derived as follows: let the subscript 1 and 2 stand for the reflection point and the antenna respectively, then the difference between the Slant Total Delay (STD) at the

reflection point (STD_2) and the receiver antenna (STD_1) is approximated by

$$\begin{aligned} 2(STD_2 - STD_1) &= 2(ZTD_2 MF_2 - ZTD_1 MF_1) , \\ &= 2(ZTD_2 - ZTD_1) MF . \end{aligned}$$

Here, it is assumed that the hydrostatic and wet MF are the same and the MF is independent of the height.

The second assumption is that the Zenith Total Delay (ZTD) decreases exponentially with the relative height h between the reflection point and the antenna. Therefore

$$ZTD_1 = ZTD_2 \cdot e^{-\frac{h}{H_{atm}}} , \quad (5.10)$$

where H_{atm} denotes the scale height.

Hence

$$2(STD_2 - STD_1) = 2\left(ZTD_2 - ZTD_2 e^{-\frac{h}{H_{atm}}}\right) MF , \quad (5.11)$$

$$\Delta_{trop} = 2 ZTD_2 MF \left[1 - e^{-\frac{h}{H_{atm}}}\right] . \quad (5.12)$$

In the case ZTD value at the antenna is used, Equation (5.12) becomes

$$\Delta_{trop} = 2 ZTD_1 MF \left[e^{\frac{h}{H_{atm}}} - 1\right] . \quad (5.13)$$

Cardellach et al. (2011) propose setting the ZTD and the H_{atm} to constant values ($ZTD = 2.3$ m and $H_{atm} = 8621$ m). In contrast, Fabra et al. (2012) use a value of $H_{atm} = 7610$ m. The impact of the H_{atm} and the ZTD on the path delay for a station located in Vietnam is analysed in the following.

Based on Equation (5.9), the tropospheric path delays for different receiver antenna heights [2-30 m] and elevation angles [2-30 deg] are calculated. As mapping function the Global Mapping Function (GMF) is used. The GMF is based on data from the global European Centre for Medium-range Weather Forecasts (ECMWF) numerical weather model (Boehm et al., 2006). A priori zenith hydrostatic and wet delays for any site coordinates, day of year and elevation angle can be obtained. As input parameters, only the station coordinates and the day of year are needed and thus no external input files are required. The computed path delays are compared with those obtained by ray-tracing (Zus et al., 2012). The ray-traced model is based on the refractivity extracted from the Global Forecast System (GFS).

Based on the results, described in Section 5.1.1, the following requirements are set to the GNSS-R tropospheric model comparison: the calculated difference between the path model and the ray-traced model should not exceed the centimetre level for an elevation angle > 3 deg and for antenna heights < 30 m (Chapter 3 and 4).

As a model without elevation angle restriction is sought for the conducted experimental set-up in Vietnam, one can recognize from Figure 5.5, that the H_{atm} , proposed by Cardellach et al.

(2011) and Fabra et al. (2012), can not be used.

| A | Input Values | | | B | Input Values | | |
|--|--|------|------|--|--|------|------|
| | $H_{atm} = 8621 \text{ m} ; ZTD = 2.3 \text{ m}$ | | | | $H_{atm} = 7610 \text{ m} ; ZTD = 2.3 \text{ m}$ | | |
| Antenna Height [m] | 10 | 20 | 30 | Antenna Height [m] | 10 | 20 | 30 |
| $\Delta_{trop} > 1 \text{ cm}$ for Elevation [deg] | < 11 | < 23 | < 31 | $\Delta_{trop} > 1 \text{ cm}$ for Elevation [deg] | < 8 | < 14 | < 22 |

ZTD = 2.3 m

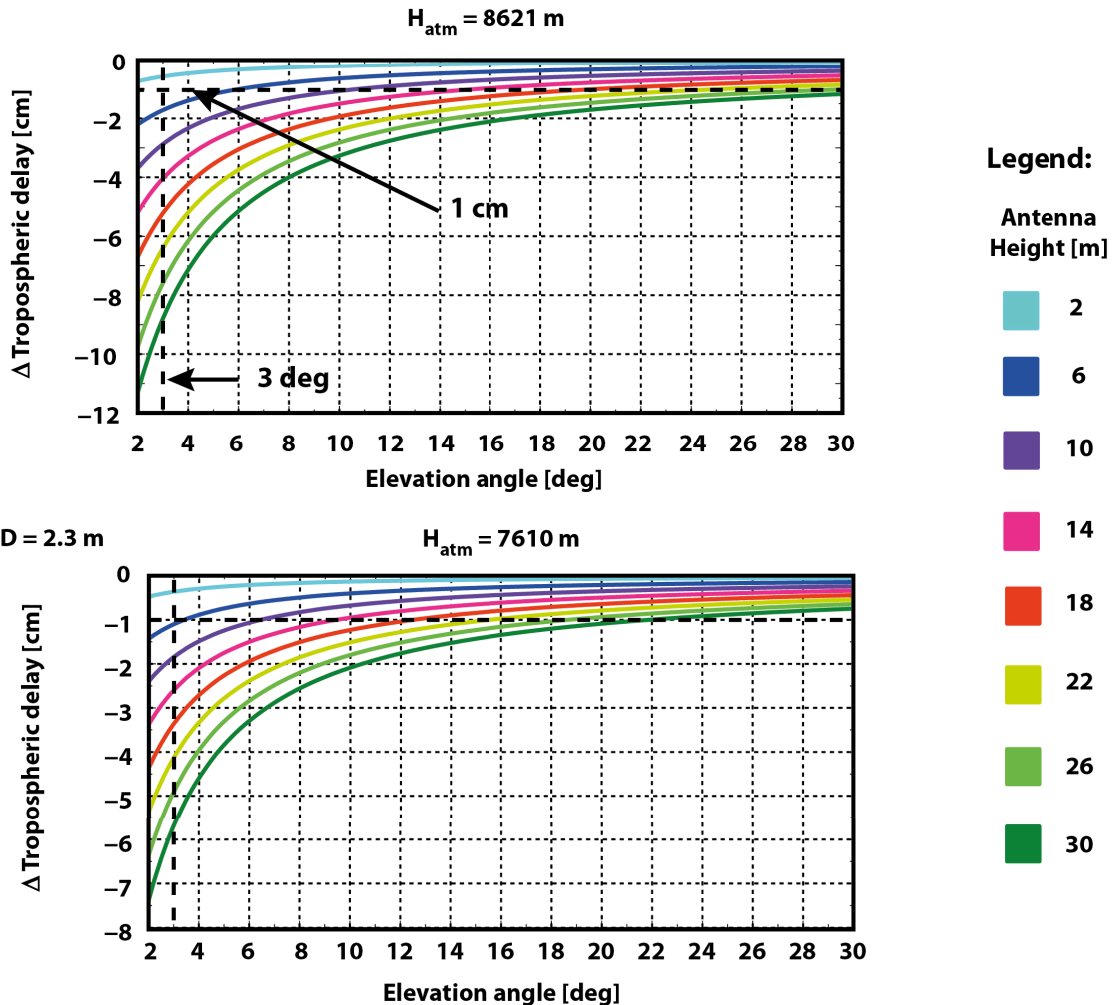


Figure 5.5: Tropospheric delay differences to a ray-traced model for different antenna heights over the reflecting surface using a ZTD value of 2.3 m and H_{atm} values proposed by Cardellach et al. (2011) (8621 m) and Fabra et al. (2012) 7610 m for a station base at An Bihn hotel, Vietnam, February 28, 2012, 12:00 GPS Time. Please note the different scales used in the graphics.

Starting with an H_{atm} value of 8621 m, only for antennas placed below 2 m height, the calculated differences between the ray-traced and the Cardellach et al. (2011) model do not exceed the centimetre regardless of the elevation angle used. In contrast, for antennas placed at 10 m height, a difference of more than one centimetre can be observed for elevation angles under 11 deg. At the set lower limit of 3 deg of elevation, the difference reaches 0.03 m causing a theoretical relative water level height error of 0.3 m (Equation (5.5)). For antennas placed at

20 m height, only for elevation angles larger than 23 deg, the model shows an error below centimetre level. In this case, a difference of 0.06 m can be observed for an elevation angle of 3 deg, causing a relative height error of 0.6 m. For an antenna placed at 30 m height and observed elevation angles between 3 - 30 deg, the model shows a difference of 0.11 - 0.01 m, causing an error of 1 - 0.01 m.

For the H_{atm} value of 7610 m, the difference between the two models starts to exceed the centimetre from an antenna height over 5 m regardless of the elevation angle used. For an antenna placed at 10 m, the model can be used for an elevation angle above 8 deg otherwise an excess path error of 0.01 - 0.025 m occurs, causing an height error of 0.1 - 0.2 m. For an antenna placed at 20 m height, the model can be used for elevation angles above 14 deg; for antennas at 30 m, for elevation angles of more 22 deg.

If now both H_{atm} values are compared, the Cardellach et al. (2011) model used with a value of 7610 m shows, in general, better results. This is an indication that this H_{atm} value better fits the conditions of Vietnam's atmospheric layers.

To analyse the variations in the ZTDs and H_{atm} values, the same ray-tracing model used for the former analysis is used to compute ZTD and H_{atm} for a station based in Vietnam and one in Germany, at different Universal Time Coordinated (UTC) of the day.

Table 5.2 shows the higher variations of the calculated H_{atm} with the time of the day for the antenna placed in Vietnam. These variations are due to the tropical climate of Vietnam. Concerning the ZTD value, it differs by about 0.2 m from the value proposed by Cardellach et al. (2011).

| | | UTC Time [hh] | | | | Mean | STD |
|------------------------|---------------|---------------|-------|-------|-------|-------|------|
| | | 0 | 6 | 12 | 18 | | |
| An Bihn hotel, Vietnam | ZTD [m] | 2.491 | 2.494 | 2.459 | 2.522 | 2.492 | 0.03 |
| | H_{atm} [m] | 6696 | 7321 | 6776 | 6754 | 6887 | 291 |
| GFZ, Potsdam, Germany | ZTD [m] | 2.408 | 2.438 | 2.463 | 2.455 | 2.441 | 0.02 |
| | H_{atm} [m] | 7483 | 7545 | 7569 | 7486 | 7521 | 43 |

Table 5.2: Variation of ZTD and H_{atm} calculated for different UTC time and two different locations: An Bihn hotel, Vietnam and GFZ Potsdam, Germany on February 28, 2012.

Based on this analysis, the calculated ZTDs and H_{atm} for the Vietnam station have been inserted in Equation (5.9) to compute the tropospheric path delays for different antenna altitudes.

Figure 5.6 shows the differences between the Cardellach et al. (2011) model and the ray-tracing based one. For all elevation angles between 2 and 30 deg and a station height under 30 m, the difference does not exceed the centimetre. It can thus be concluded that the Cardellach et al. (2011) model with the corresponding ZTDs and H_{atm} for the Vietnam station can be used.

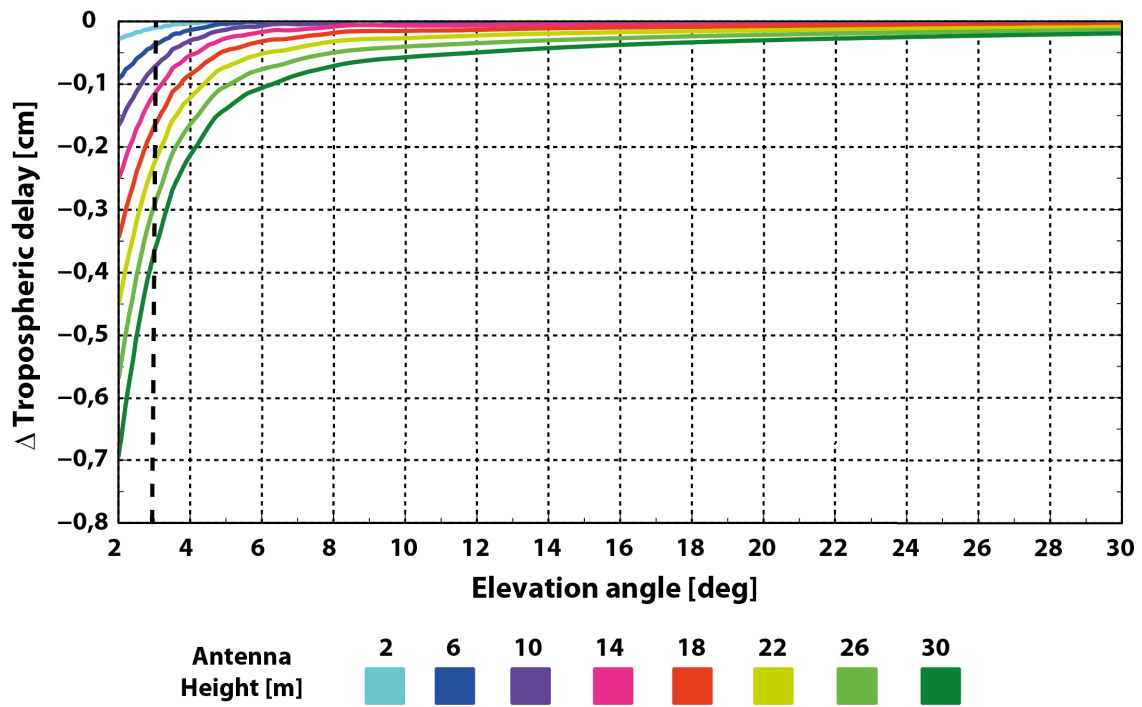


Figure 5.6: Tropospheric delay differences to a ray-traced model for different antenna heights using ZTD and H_{atm} calculated by a ray-tracing model for a station based at An Bihn hotel, Vietnam, February 28, 2012, 12:00 GPS Time.

More details about the used GMF and ray-tracing model can be found in Boehm et al. (2006) and Zus et al. (2012), respectively.

5.1.5 Antenna Phase Centre Offset and Variation

As underlined in Section 2.4.3, the computed geometric distance between satellite and receiver is related to the electrical phase centre of the transmitting GPS satellite antenna and the receiving GPS receiver antenna. These are, however, not identical with the physical centre of the antennas. As these deviations can cause an error of up to 0.1 m in the height component, Phase Centre Correction (PCC)s for the satellite and the receiver antennas have to be applied. The PCC consists of a constant value - the Phase Centre Offset (PCO) - and the elevation, azimuth and frequency dependent value - the Phase Centre Variation (PCV).

The PCC of the tracked satellite is eliminated by building the difference between the direct and the reflected signal (Section 2.4.3). In contrast, for the receiver antenna a calibration is mandatory to determine the PCC values which are made available for commonly used antennas through the IGS-ANTEX file. However, for the Antcom antennas used within this thesis, the PCOs and PCVs are not listed. For this reason, these were determined by a calibration method, called the Hanover concept (Wübbena et al., 1996), that was developed at the Leibniz Universität Hannover at the Institut für Erdmessung in cooperation with the company Geo+++. This method is internationally recognized, standardized and over more than a decade operationally used to calibrate geodetic antennas used in the IGS network. While the antenna to be calibrated is placed on a robot arm, a reference antenna is fixed on a pillar ≈ 7 m away

(Figure 5.7). This short baseline enables the elimination of atmospheric induced systematic errors. In addition, each antenna is connected to a receiver of the same type in order to eliminate instrumental specific systematic errors.

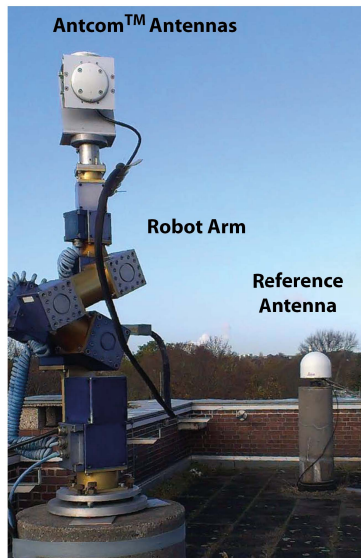


Figure 5.7: Robot arm used to determine the absolute field calibration of the Antcom antenna (PCO and PCV) at the Institut für Erdmessung at the Leibniz Universität Hannover. Picture: Kersten (2013).

For the calibration a Javad Delta TRE-G3T receiver was used. To reduce the individual receiver clock error, the receivers are associated with a frequency normal. Currently, a Stanford Rubidium FS725 is used with a frequency stability of $\sigma_{FS725} < 2 \cdot 10^{-11}$ (Allan variance of 1 sec.) (Kersten, 2014). The robot arm is controlled by a computer unit that twists and tilts the antenna horizontally and vertically with an accuracy of 0.25 mm within a maximal time interval of 1 - 5 sec. (Kersten, 2014). The calibration is fully automated and requires 6 - 8 hours. To get reliable values, the absolute field PCV and PCO calibration was repeated eight times for each antenna. The mean values obtained for the Master and Slave antenna are listed in table form in function of the zenith and azimuth angle, following the IGS-ANTEX format convention. A bi-linear interpolation is used to calculate the in-between values. As two different Antcom antennas types are used, namely a single and a dual polarized antenna (Chapter 3), two absolute field calibrations have been done. The first antenna used to track the reflected signals is a dual polarized RHCP/LHCP GPS L1/L2 antenna with the product number P/N 3G1215RL-AA-XT-1. The second antenna used to track the direct signals is a single polarized RHCP GPS L1/L2 antenna with the product number P/N 3G1215A-XTR-1. To differentiate between the two antennas, also here the term Master is used for the single polarized antenna and the term Slave for the dual polarized one. It should be noted that the Hanover calibration method is only applicable for RHCP antennas. According to Antcom, the RHCP PCO and PCV values found for the dual RHCP/LHCP Slave antenna differ within the millimetre range to the LHCP so that the assumption of same values can be used.

Figure 5.8 shows the obtained PCO and PCV values for the Antcom Master and Slave antenna. The PCO values for the L1 frequency are lower than those for the L2 frequency which reaches around 2 cm. The magnitude of the PCV's found are for the used elevation angles of 3 - 30 deg and the azimuthal interval of 80 - 270 deg within the conducted experiment, under 1.5 cm for the L1 and L2 frequency in the case of the Master antenna and under 2 cm for the L1 and L2 frequency in the case of the Slave antennas.

RHCP Master Antenna

A

PCO L1 [mm]

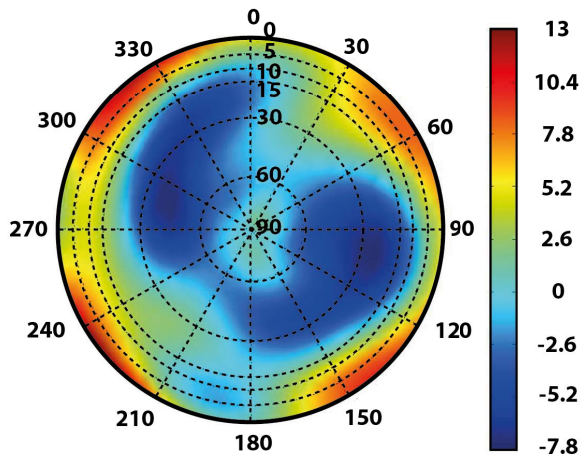
| | | | |
|----------|-------|------|------|
| | North | East | Up |
| PCO [mm] | 0.48 | 0.89 | 5.76 |

B

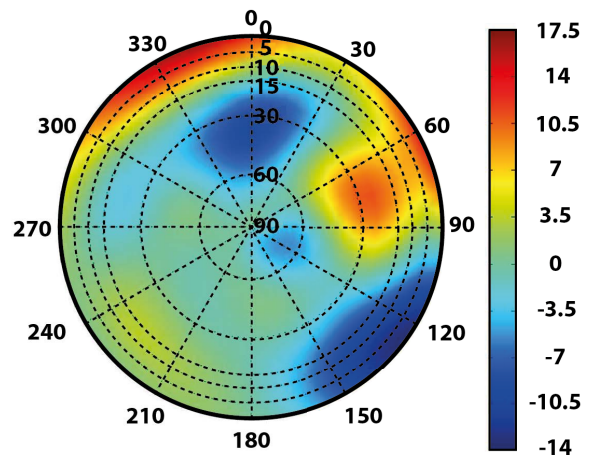
PCO L2 [mm]

| | | | |
|----------|-------|------|-------|
| | North | East | Up |
| PCO [mm] | 2.77 | 1.31 | 18.49 |

PCV L1 [mm]



PCV L2 [mm]



RHCP/LHCP Slave Antenna

C

PCO L1 [mm]

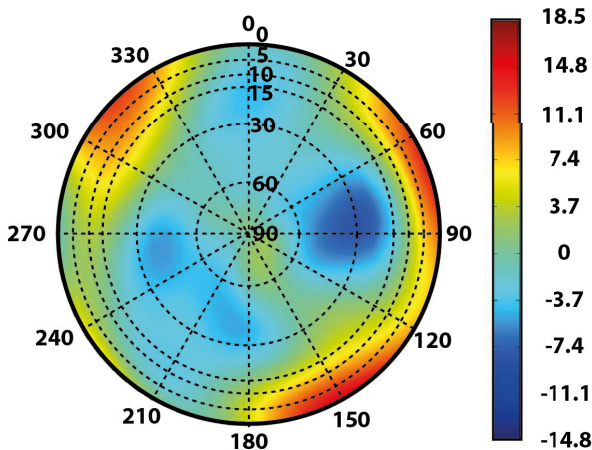
| | | | |
|----------|-------|------|------|
| | North | East | Up |
| PCO [mm] | 4.37 | 4.36 | 2.96 |

D

PCO L2 [mm]

| | | | |
|----------|-------|------|-------|
| | North | East | Up |
| PCO [mm] | 4.19 | 2.10 | 21.95 |

PCV L1 [mm]



PCV L2 [mm]

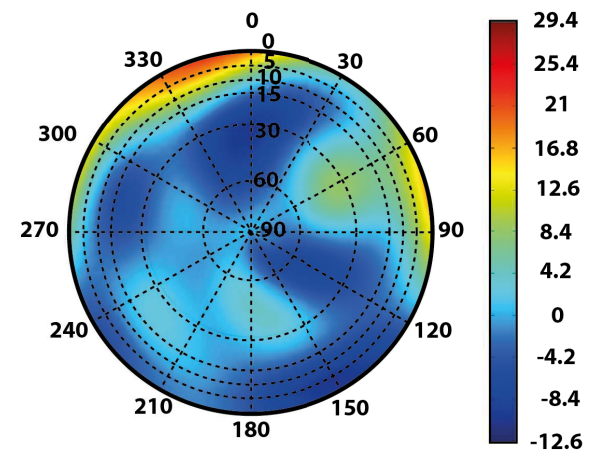


Figure 5.8: The absolute field calibration PCV and PCO values using the Hanover method for the Master (RHCP) and the Slave (RHCP/LHCP) Antcom antennas used during the conducted measurement campaigns. **A** and **B**: PCV and PCO values for the Master RHCP antenna for L1 (left) and L2 (right) respectively. **C** and **D**: PCV and PCO values for the Slave RHCP/LHCP antenna for L1 (left) and L2 (right) respectively. Source: Kersten (2013)

However, in a standard GNSS-R antenna arrangement, mostly two antennas are used: one antenna is placed horizontally to track the direct signals (Master antenna) and the second one is tilted toward the reflecting surface to intercept the reflected signals (Slave antenna).

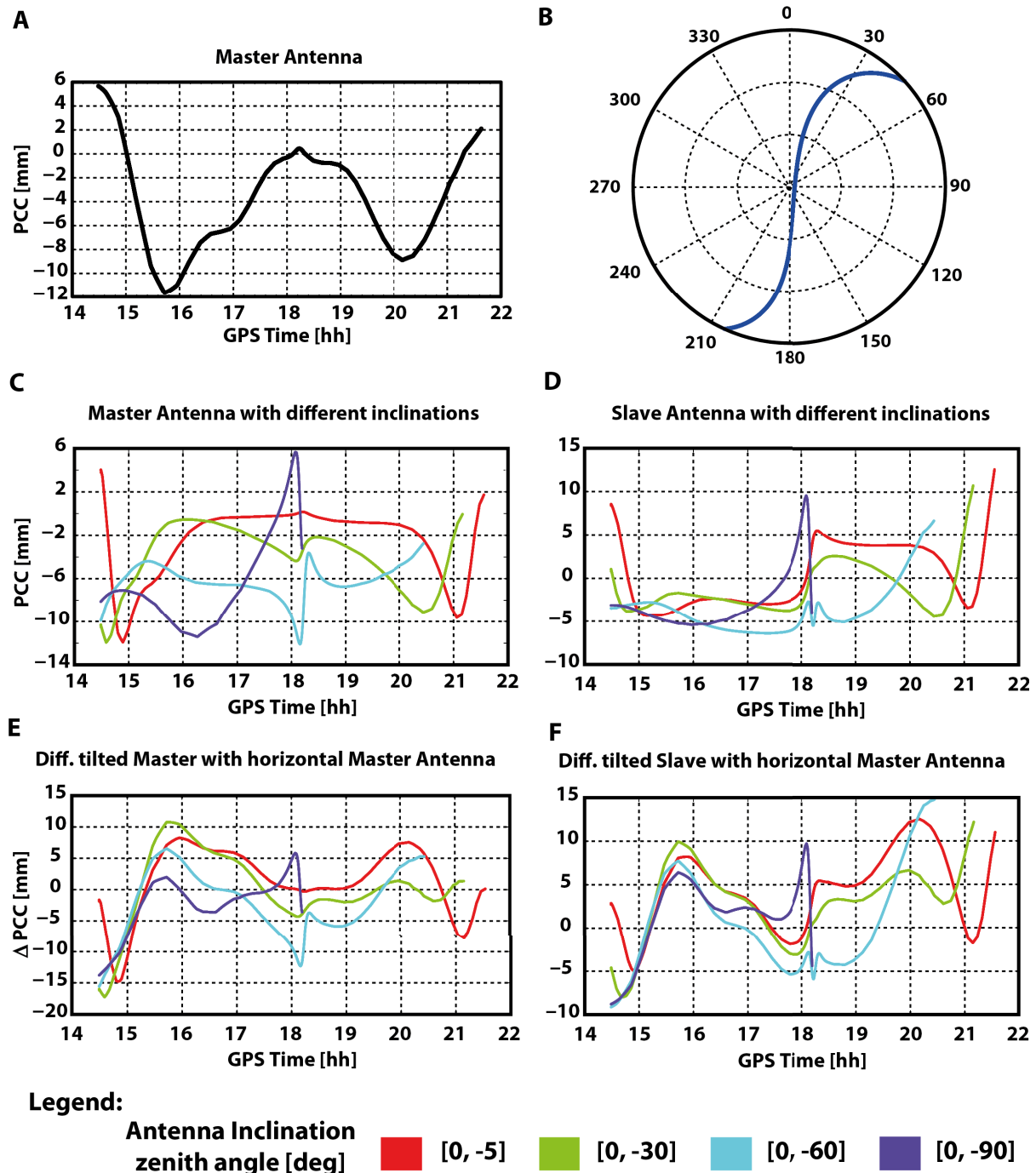


Figure 5.9: Impact of inclination and of different antenna types on the PCC values. **A:** PCC values of the horizontally placed Master RHCP antenna. **B:** Sky-plot of the simulated PRN satellite ID 7 as observed on February 26, 2012 from An Bihn hotel in Vietnam. **C:** PCC values of the tilted Master antenna for different zenith angles [-5, -30, -60 and -90 deg.] **D:** PCC values for an inclined Slave antenna of different type as the Master antenna. **E:** Differences between horizontally placed and inclined Master antenna showing the impact of inclination of antennas of the same type. **F:** Differences between horizontally placed Master and Slave antenna with different inclinations. For visibility tasks the scale of the plots are different. Data source: An Bihn hotel, February 26, 2012, PRN 7.

Due to the inclination of the Slave antennas, the incoming elevation angle of the reflected signal from the specular point to the antenna, differs from the incoming elevation angle of the direct signals to the Master antenna. Concerning the azimuth angle, if the antennas are placed one below the other, as it is the case in the experiment conducted within this thesis, both antennas receive the signals with the same azimuthal angle. Finally, depending on the satellite-receiver-reflection geometry, the reflection of the signal can cause a polarization change (Section 2.3.2), so that two different antenna polarizations and thus types are used.

Figure 5.9 shows simulated PCC values for the Master and the Slave antenna. The simulation was calculated using reflection events for antennas placed 10 m above the Can Tho River in Vietnam using the observed PRN 7 on February 26, 2012.

Panel **A** illustrates the changes in the PCC values for the horizontally placed Master antenna due to different elevation and azimuth angles (Sky-plot in Panel **B**).

To visualise the impact of the inclination of the antenna on the extracted PCC values, different zenith angles were simulated: 5, 15, 30, 60 and 90 deg. Panel **C** and **D** show the resulting PCC values for the Master and the Slave antennas. It can be seen that even if the same antenna type is used, the calculated PCC values differ. To underline this, panel **E** shows the differences experienced by the horizontally and the tilted RHCP Master antenna. Differences of more than one centimetre can be observed. In panel **F**, the antenna constellation used within the Vietnam experiment is simulated. Thus the impact of using two different antenna types combined with the inclination of one of them, the Slave antenna. Also here, the experienced PCC value differences can reach more than one centimetre.

It can thus be concluded that, the PCO and PCV corrections need to be taken into account for the correct determination of GNSS-R based altimetric heights.

5.2 GPS-R Ambiguity Fixing

As underlined in Section 2.2.3, the advantage of using phase observations is that the fraction of the cycle can be measured with a precision better than 1% of the wavelength thus within millimetre range for L-Band frequencies. However the benefit of the phase-based GPS-R method can only be used if the ambiguous integer number of cycles $N_{amb,refl}^{sat_i}$ (Equ. (5.8)) is correctly resolved. Following Teunissen (1998), the GPS ambiguity process consists of resolving the unknown cycle ambiguities of the carrier-phase observation as integers using the following system of linear observations:

$$\mathbf{y} = \mathbf{Aa} + \mathbf{Bb} + \boldsymbol{\epsilon}, \quad (5.14)$$

where \mathbf{y} is the vector of "observed minus computed" phase observations accumulated over a certain number of observation epochs, \mathbf{a} and \mathbf{b} are the unknown parameter vector whether \mathbf{a} contains the integer values of the ambiguities and \mathbf{b} the remaining unknown parameter h (the relative height between the receiver antenna and the reflecting water surface) and finally $\boldsymbol{\epsilon}$ the noise vector.

When using the LS principle, the above system of equations can be solved by means of the minimization problem

$$\min_{\mathbf{a}, \mathbf{b}} (\mathbf{y} - \mathbf{Aa} - \mathbf{Bb})^T \mathbf{Q}_y^{-1} (\mathbf{y} - \mathbf{Aa} - \mathbf{Bb}) \quad , \quad \mathbf{a} \in \mathbb{Z} \quad , \quad \mathbf{b} \in \mathbb{R} \quad , \quad (5.15)$$

with \mathbf{Q}_y the variance-covariance matrix of the observations, \mathbb{Z} the space of integers and \mathbb{R} the space of real numbers. This type of LS problem is a non-standard one due to the integer constraints $\mathbf{a} \in \mathbb{Z}$.

The computation of the solution of Equation (5.15) is mostly made in three steps. In the first step, the integer nature of the ambiguities is ignored and a standard LS adjustment is performed. As a result, the real value number of ambiguities as well as their variance-covariance matrix are obtained

$$\begin{bmatrix} \hat{\mathbf{a}} \\ \hat{\mathbf{b}} \end{bmatrix} \quad , \quad \begin{bmatrix} \mathbf{Q}_{\hat{\mathbf{a}}} & \mathbf{Q}_{\hat{\mathbf{a}}\hat{\mathbf{b}}} \\ \mathbf{Q}_{\hat{\mathbf{a}}\hat{\mathbf{b}}} & \mathbf{Q}_{\hat{\mathbf{b}}} \end{bmatrix} \quad . \quad (5.16)$$

Due to the real-valued nature of the ambiguities $\hat{\mathbf{a}}$, this solution is often called float solution. In the second step, the obtained float ambiguities $\hat{\mathbf{a}}$ and their variance-covariance matrix $\mathbf{Q}_{\hat{\mathbf{a}}}$ are used to estimate the integer ambiguity $\check{\mathbf{a}}$ but this time by solving the constrained integer LS problem

$$\min_{\mathbf{a}} (\hat{\mathbf{a}} - \mathbf{a})^T \mathbf{Q}_{\hat{\mathbf{a}}}^{-1} (\hat{\mathbf{a}} - \mathbf{a}) \quad , \quad \mathbf{a} \in \mathbb{Z} \quad . \quad (5.17)$$

Finally, in the last step, the obtained integer ambiguities $\check{\mathbf{a}}$ are used as fixed values to correct the float estimated unknown parameter $\hat{\mathbf{b}}$ so that the so called fixed and final solution is obtained

$$\check{\mathbf{b}} = \hat{\mathbf{b}} - \mathbf{Q}_{\hat{\mathbf{a}}\hat{\mathbf{b}}} \mathbf{Q}_{\hat{\mathbf{a}}}^{-1} (\hat{\mathbf{a}} - \check{\mathbf{a}}) \quad . \quad (5.18)$$

5.2.1 Ambiguity Fixing Methods

To resolve for the constrained integer LS problem, different strategies have been developed over the past decades. However, mostly linear combinations of L1 and L2 frequencies (like the wide-lane linear combination combined with a narrow-lane combination) is used to build an artificial bigger wavelength. The challenge within this thesis is to resolve the ambiguity using only the L1 phase observations as 95% of the coherent observations are of L1 nature. This leads to a considerable reduction of the usable ambiguity fixing methods that will be outlined in the following.

Integer Rounding

The ambiguity solution is resolved by simply rounding the obtained real-valued ambiguity $\hat{\mathbf{a}}$ computed in the float solution

$$\check{\mathbf{a}}_{IR} = [\hat{\mathbf{a}}] \quad , \quad (5.19)$$

where $[\cdot]$ denotes rounding to the nearest integer and the abbreviation IR stands for Integer Rounding.

However, the non-modelled systematic errors flow in the float estimated ambiguity \hat{a} so that a simple rounding to the nearest integer value can lead to a falsification of the obtained unknown parameter.

Integer Least-Square

As the method is in detailed described in Jonkman (1998) and Teunissen (1994) only the main ideas of the method will be outlined in the following.

The difficulty in fixing the ambiguities to integers, is the high existing correlation between their estimated values. As a consequence the search process of the integer values is very time consuming. To overcome this, Teunissen (1994) developed the Least-squares AMBIGUITY Decorrelation Adjustment (LAMBDA) method. The essence of the method is (Jonkman, 1998):

- the search for the fixed solution $\check{\mathbf{a}}$ is restricted to an ellipsoidal confidence region centred at the float solution $\hat{\mathbf{a}}$
- before the search process is started, the ellipsoidal confidence region is transformed to a circle-like confidence region accelerating the search process.

The search process for the fixed solution around the float solution $\hat{\mathbf{a}}$ that minimizes Equation (5.17), is restricted to an ellipsoidal confidence region

$$\| \hat{\mathbf{a}} - \mathbf{a} \|_{\mathbf{Q}_{\hat{\mathbf{a}}}}^2 < \chi^2 . \quad (5.20)$$

The shape of the ellipsoidal search space is governed by the variance-covariance matrix $\mathbf{Q}_{\hat{\mathbf{a}}}$ and the size of the search space by the constant χ^2 .

To simplify the following explanations, only an ambiguity pair $\mathbf{a} = [a_1 \ a_2]^T$ is considered. From Equation (5.17) the objective function is

$$\begin{aligned} (\hat{\mathbf{a}} - \mathbf{a})^T &= (\hat{a}_1 - a_1) \frac{\sigma_{\hat{a}_2}^2}{\sigma_{\hat{a}_1}^2 \sigma_{\hat{a}_2}^2 - \sigma_{\hat{a}_1 \hat{a}_2}^2} (\hat{a}_1 - a_1) \\ &+ (\hat{a}_2 - a_2) \frac{\sigma_{\hat{a}_1}^2}{\sigma_{\hat{a}_1}^2 \sigma_{\hat{a}_2}^2 - \sigma_{\hat{a}_1 \hat{a}_2}^2} (\hat{a}_2 - a_2) \\ &- 2 (\hat{a}_1 - a_1) \frac{\sigma_{\hat{a}_1 \hat{a}_2}}{\sigma_{\hat{a}_1}^2 \sigma_{\hat{a}_2}^2 - \sigma_{\hat{a}_1 \hat{a}_2}^2} (\hat{a}_2 - a_2) , \end{aligned} \quad (5.21)$$

where $\sigma_{\hat{a}_i}$ denotes the standard deviation of the ambiguities obtained during the float solution and $\sigma_{\hat{a}_1 \hat{a}_2}$ their covariance.

If $\sigma_{\hat{a}_1 \hat{a}_2} = 0$, thus both ambiguities are uncorrelated, Equation (5.21) is reduced to the sum of two scalar objective functions permitting to formulate scalar bounds on the integer ambiguities

a_1 and a_2

$$\begin{aligned} (\hat{\mathbf{a}} - \mathbf{a})^T &= (\hat{a}_1 - a_1) \frac{1}{\sigma_{\hat{a}_1}^2} (\hat{a}_1 - a_1) \\ &\quad + (\hat{a}_2 - a_2)^T \frac{1}{\sigma_{\hat{a}_2}^2} (\hat{a}_2 - a_2) \\ &= \| \hat{a}_1 - a_1 \|_{\sigma_{\hat{a}_1}^2}^2 + \| \hat{a}_2 - a_2 \|_{\sigma_{\hat{a}_2}^2}^2 \end{aligned} \quad (5.22)$$

To reach this decorrelation, a diagonalization of the variance-covariance matrix $\mathbf{Q}_{\hat{\mathbf{a}}}$ is performed using a **LDL** decomposition

$$\mathbf{Q}_{\hat{\mathbf{a}}} = \mathbf{LDL}^T. \quad (5.23)$$

The matrix \mathbf{L} being a lower triangular matrix with diagonal elements of one

$$\mathbf{L}^{-1} = \begin{bmatrix} 1 & 0 \\ -\sigma_{\hat{a}_2 \hat{a}_1} \sigma_{\hat{a}_1}^{-2} & 1 \end{bmatrix}, \quad (5.24)$$

and the \mathbf{D} matrix a diagonal matrix with positive elements

$$\mathbf{D} = \begin{bmatrix} \sigma_{\hat{a}_1}^2 & 0 \\ 0 & \sigma_{\hat{a}_2}^2 - \sigma_{\hat{a}_1 \hat{a}_2}^2 \sigma_{\hat{a}_1}^{-2} \end{bmatrix}. \quad (5.25)$$

By setting Equation (5.23) in Equation (5.17), we obtain

$$(\hat{\mathbf{a}} - \mathbf{a})^T \mathbf{L}^{-T} \mathbf{D}^{-1} \mathbf{L}^{-1} (\hat{\mathbf{a}} - \mathbf{a}). \quad (5.26)$$

By defining the difference vector

$$(\hat{\mathbf{d}} - \mathbf{d}) = \mathbf{L}^{-1} (\hat{\mathbf{a}} - \mathbf{a}), \quad (5.27)$$

and expanding it, we obtain

$$\hat{d}_1 - d_1 = \hat{a}_1 - a_1 \quad (5.28)$$

$$\hat{d}_2 - d_2 = \hat{a}_2 - a_2 - \sigma_{\hat{a}_1 \hat{a}_2} \sigma_{\hat{a}_1}^{-2} (\hat{a}_1 - a_1). \quad (5.29)$$

The unknown d_1 and the estimate \hat{d}_1 are the unknown integer ambiguity a_1 and its LS estimate \hat{a}_1 .

The estimate \hat{d}_2 is the LS estimate \hat{a}_2 conditioned on fixing the ambiguity a_1 to integer value, so that Equation (5.29) reads

$$\| \hat{a}_1 - a_1 \|_{\sigma_{\hat{a}_1}^2}^2 + \| \hat{a}_{2|1} - a_2 \|_{\sigma_{\hat{a}_{2|1}}^2}^2 < \chi^2. \quad (5.30)$$

The search process is executed with following steps

- select all possible integer values \bar{a} within the upper and lower bound defined by

$$\hat{a}_1 - \sigma_{\hat{a}_1} \chi < a_1 < \hat{a}_1 + \sigma_{\hat{a}_1} \chi . \quad (5.31)$$

- for each of this integer values, determine the corresponding integer value for the second ambiguity with

$$\hat{a}_{2|1} - \sigma_{\hat{a}_{2|1}} \left(\chi^2 - \frac{(\hat{a}_1 - \bar{a}_1)^2}{\sigma_{\hat{a}_1^2}} \right)^{\frac{1}{2}} < a_2 < \hat{a}_{2|1} + \sigma_{\hat{a}_{2|1}} \left(\chi^2 - \frac{(\hat{a}_1 - \bar{a}_1)^2}{\sigma_{\hat{a}_1^2}} \right)^{\frac{1}{2}} . \quad (5.32)$$

The pair of integer values (\bar{a}_1, \bar{a}_2) that minimize Equation (5.17) is selected as the fixed solution $\check{\mathbf{a}}$.

Still the ellipsoidal search space is not optimal due to the mostly elongated form of the ellipsoidal confidence region. A more circle-like search space is sought. A so called Z-transformation is introduced before the search process is started.

A re-parametrization of the integer LS problem is made with

$$\min_{\mathbf{a}} \|\hat{\mathbf{a}} - \mathbf{a}\|_{\mathbf{Q}_{\hat{\mathbf{a}}}}^2, \quad \mathbf{a} \in \mathbb{Z} \iff \min_{\mathbf{z}} \|\hat{\mathbf{z}} - \mathbf{z}\|_{\mathbf{Q}_{\hat{\mathbf{z}}}}^2, \quad \mathbf{z} \in \mathbb{Z}, \quad (5.33)$$

with

$$\mathbf{z} = \mathbf{Z}^T \mathbf{a}, \quad \hat{\mathbf{z}} = \mathbf{Z}^T \hat{\mathbf{a}}, \quad \mathbf{Q}_{\hat{\mathbf{z}}} = \mathbf{Z}^T \mathbf{Q}_{\hat{\mathbf{a}}} \mathbf{Z}, \quad (5.34)$$

where \mathbf{Z} represents the sought transformation matrix.

The \mathbf{Z} matrix should satisfy following conditions

- the transformation should still decorrelate the variance-covariance matrix $\mathbf{Q}_{\hat{\mathbf{a}}}$
- the entries of the \mathbf{Z} matrix are integers,
- the inverse of the \mathbf{Z} matrix exist and its entries are integers.

If we take the first condition, the matrix \mathbf{L} achieves a full decorrelation of the ambiguity estimates but its entries are not of integer nature so that the second and the third conditions are not fulfilled. A compromise between decorrelation of the ambiguity estimates and the preservation of the integer constraints can be made by rounding the elements of the \mathbf{L} matrix

$$\mathbf{Z}^T = \begin{bmatrix} 1 & 0 \\ -\left[\sigma_{\sigma_{\hat{a}_1} \sigma_{\hat{a}_2} \sigma_{\hat{a}_1}^{-1}} \right] & 1 \end{bmatrix}, \quad (5.35)$$

Once the transformed fixed solution has been identified, the original solution $\check{\mathbf{a}}$ is recovered with

the inverse transformation

$$\check{\mathbf{a}} = \mathbb{Z}^T \check{\mathbf{z}}. \quad (5.36)$$

The Matlab code implementation of the LAMBDA method is freely available¹.

5.2.2 Analysis of the Vietnam Data with Regard to the Ambiguity Problematic

As showed in Section 4.2, during the conducted experiment in Vietnam, four observation constellations could be distinguished:

1. Coherent observations on a single frequency L1 from a single satellite
2. Coherent observations on a single frequency L1 simultaneously from different satellites
3. Coherent observations on dual-frequency L1 and L2 from a single satellite
4. Coherent observations on dual-frequency L1 and L2 simultaneously from different satellites

However, the analysis showed also that 95% of the as coherent extracted observations, are on the single L1 frequency, so that the following analysis will be restrained on the first and the second observation constellation. Depending on the available redundancy of the satellite constellation, one of the ambiguity strategies proposed in Section 5.2.1 can be used.

To overcome the lack of redundant satellites, the information content of the relative receiver-satellite geometry and its changes over the time is used. In the following subsections, the minimum observation time span needed to reach the set water level height accuracy at the decimetre is analysed in dependency of the number of observed satellites and the used ambiguity estimator strategy. For this purpose, observations for an antenna placed at 10 m height above the reflecting surface with an elevation mask of 3 - 30 deg are simulated over a whole day. To analyse the impact of the water surface roughness on the obtained results, varying white noise with zero mean and standard deviations of 0.1 m and 0.05 m are used.

For each simulated constellation of available satellites, the redundant observations are first solved as float solution using the standard LS method. Here, it is assumed that the mathematical model is well defined, thus all systematic errors are corrected. Furthermore it is assumed that no cycle-slips occurred. Based on this results, the ambiguity is fixed applying one of the different presented estimators and finally used to compute the final relative height between the antenna and the reflecting surface.

For all simulated approaches, the computed solution is considered to be correct, if the obtained relative height lies continuously within the target accuracy of ± 1 dm otherwise the results are excluded.

¹<http://http://gnss.curtin.edu.au/research/lambda.cfm>

Case of Single Satellite

In the single satellite with a single-frequency L1 case, only a single ambiguity per satellite is present in the model

$$\phi_i^{sat_j}(t) = 2h(t) \sin(E(t)) + \lambda_i N_i^{sat_j}. \quad (5.37)$$

The number of unknown parameters to be estimated are: $1 + n$ where n represents the number of parallel observed satellites j and i the used frequency. Thereby, the number of unknown parameters to be determined is two: the relative height and a single ambiguity.

As no ambiguity correlation exists, the Integer Rounding (IR) estimator is used to fix for the ambiguity.

To get an estimate on the minimal time span needed to resolve for the ambiguity, so that the solution lies within $\pm 1 dm$, the relative frequency of successfully obtained solution for intervals of 5 min are calculated and illustrated in Figure 5.10 for the different used noise level. On the left side, the obtained relative frequencies based on a float solution are plotted, and on the right side, the relative frequencies obtained by using the IR estimator.

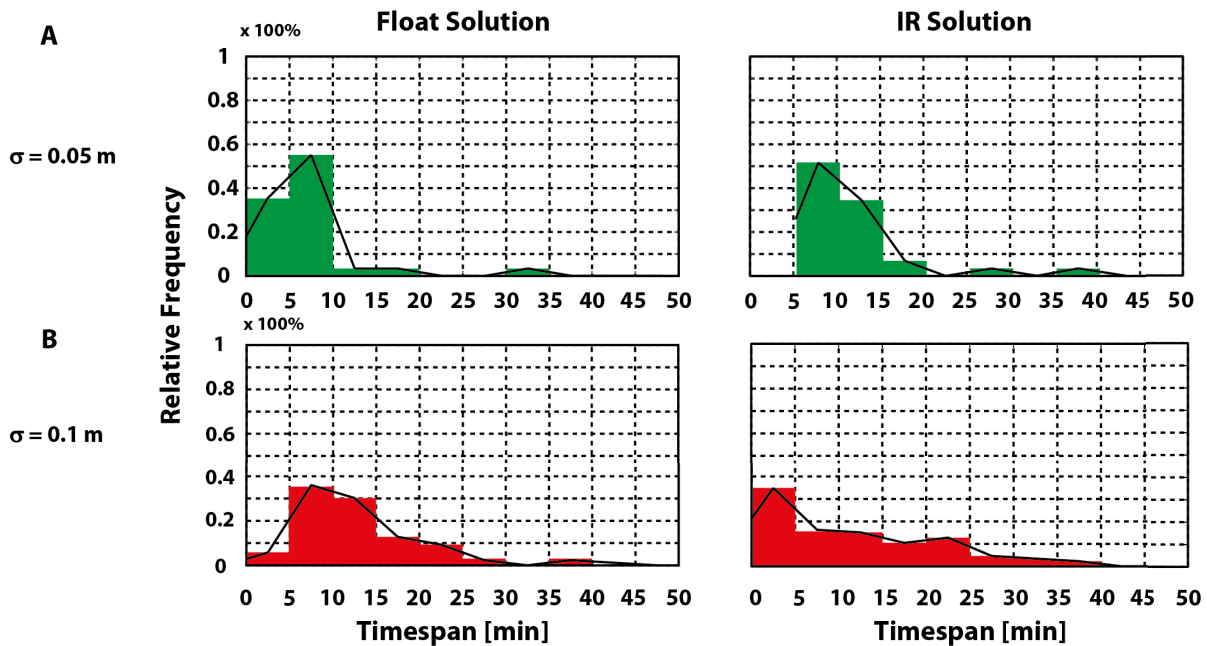


Figure 5.10: Time span relative frequency of successfully calculated water level height solutions within $\pm 1 dm$ for different observation variances (0.1 m and 0.05 m) if only a single satellite with a single frequency L1 is available. **Left:** Relative frequency for the float solution. **Right:** Relative frequency using the IR based solution. The simulations are based on satellites observed at An Bihn hotel, Vietnam for an antenna placed at 10 m height and an elevation mask between 3 - 30 deg on February 25, 2012.

For a standard deviation of 0.05 m, the float solution shows a peak at the interval of 5 - 10 min with a median value of 7 min. If the ambiguity is fixed using the IR estimator, the biggest relative frequency is reduced to the time span interval of 0 - 5 min with a median value at 5 min. However, if the polygon of the obtained relative frequencies is analysed, more than 95%

of the float and the fixed solution lie within the time span interval of 0 - 25 min. Thus to reach the set decimetre level of accuracy, an initializing time of at least 5 min but better of 25 min of continuous observations are needed.

Similarly, for a standard deviation of 0.1 m, more than 95% of the float and the fixed solution is within the interval of 0 - 30 min. For the float solution with a peak at the interval of 5 - 10 min and a median value at 11 min. For the fixed solution, the biggest relative frequency is within the interval of 0 - 5 min and a median value of 9 min.

As expected, due to the slowly changing receiver-satellite geometry combined with the use of a unique satellite with a single frequency, a long data span is necessary in order to accumulate sufficient geometric information to resolve for the correct solution. This effect is reinforced with an increasing standard deviation of the observations. For the estimated standard deviation of the as coherent extracted observations of 0.05 m combined with the fact that in the rare cases more than 10 min of continuous coherent phase observations are available (Section 4.2), it is thus expected that the decimetre level of accuracy will not always be reached. For the case of a single satellite with a single frequency, a minimum time span of 10 min will be set.

Case of Multiple Satellites

As only a single frequency is available, n ambiguities equivalent to the number of parallel observed satellites have to be solved. Thereby the number of unknown parameter to be determined is: $n + 1$. In this case, correlation between the float estimated ambiguities \hat{a} exist so that the LAMBDA estimator can be used.

In the case of multiple available satellites with a single frequency, during the conducted experiment in Vietnam, a maximum of three satellites was observed in parallel (Section 4.2). Based on this results, simulations are calculated for respectively two and three simultaneously observed satellites. As in the former subsection, the simulations are conducted for an antenna placed at 10 m height and for two different standard deviations of 0.05 m and 0.1 m (Figure 5.11).

In comparison to the precedent analysis the use of two satellites instead of one, shows a reduction of the needed timespan for the float as well as for the fixed solution using the LAMBDA estimator. Indeed, in the case of a standard deviation of 0.05 m, 95% of the float and the fixed solutions need a timespan of [0 - 10 min] only compared to [0 - 25 min] if only a single satellite is available. If a standard deviation of 0.5 m is simulated, the float solution needs [0 - 20 min] and the fixed solution [0 - 10 min] to get 95% of the solutions within the decimetre limits. Thus the use of the LAMBDA estimator combined with a high noise level reduces the timespan to the half.

As expected, the possibility to fix the ambiguity increases the reachable accuracy considerably even though only a single frequency is available. This fact is underlined in the case where three satellites are available. Indeed, compared to the precedent analysis the simulations show that nearly 100% of the results within the decimetre limits, lie within the timespan interval of

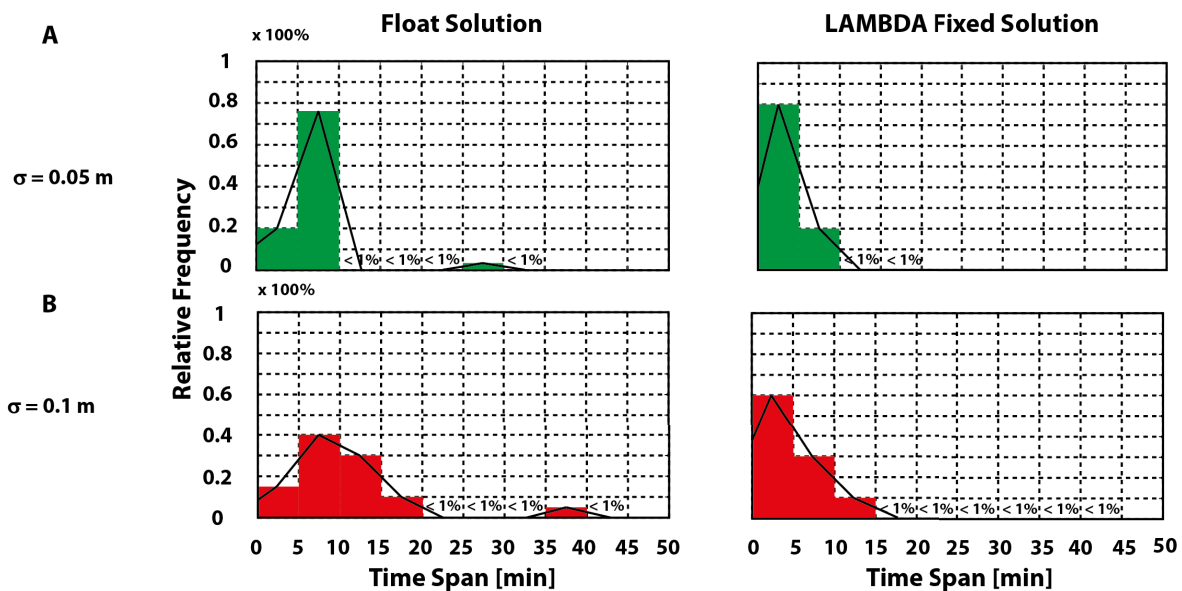


Figure 5.11: Simulations to determine the impact of using two satellites instead of one for different observation variances. **Right:** The calculated relative frequency for the float based solution. **Left:** the obtained relative frequency using the LAMBDA method. **A:** Simulations for a standard deviation of 0.05 m. **B:** Simulations with a standard deviation of 0.1 m. Simulations are based on satellites observed at An Bihn hotel, Vietnam, over three days in February 25, 2012 for an antenna placed at 10 m height.

[0 - 10 min] for the float as well as for the fixed solution if a standard deviation of 0.05 m is simulated (Figure 5.12A). For a standard deviation of 0.1 m on the other hand, the needed timespan for 95% of the float and the fixed solution lie within the same timespan as by the use of two satellites. However, the median value for the float solution reduces from 7 min to 6 min and for the fixed solution from 4 min to 2 min.

The overall conclusion that can be drawn from these simulation is that with increasing roughness and consequently the standard deviation of the observations, quite a number of epochs has to be taken into account to reach the decimetre level of accuracy if only a single frequency of a unique satellite is available. Although the simulations show that at least 25 min of coherent observations should be used to reach the decimetre level of accuracy with a high reliability, the timespan will be set to 10 min forced by the fact that mostly only around 10 min of continuous coherent observations are available in the data collected in Vietnam. It is thus expected that the decimetre level will not always be reached. On the other hand, in the case multiple satellites are available, an ambiguity fixing is possible so that the use of a timespan of 10 min showed that mostly 95% of the results could be solve within the decimetre level of accuracy.

5.3 Water Level Height Determination

Having now all the necessary background information, the second stage of the algorithm is processed. In this stage, the EMD isolated sub-signals are used as an input for the LS based water level height extraction algorithm using the mathematical model presented in Section 5.1. In this step, a float solution is first calculated. The results of the coherency analysis (Section 4.2)

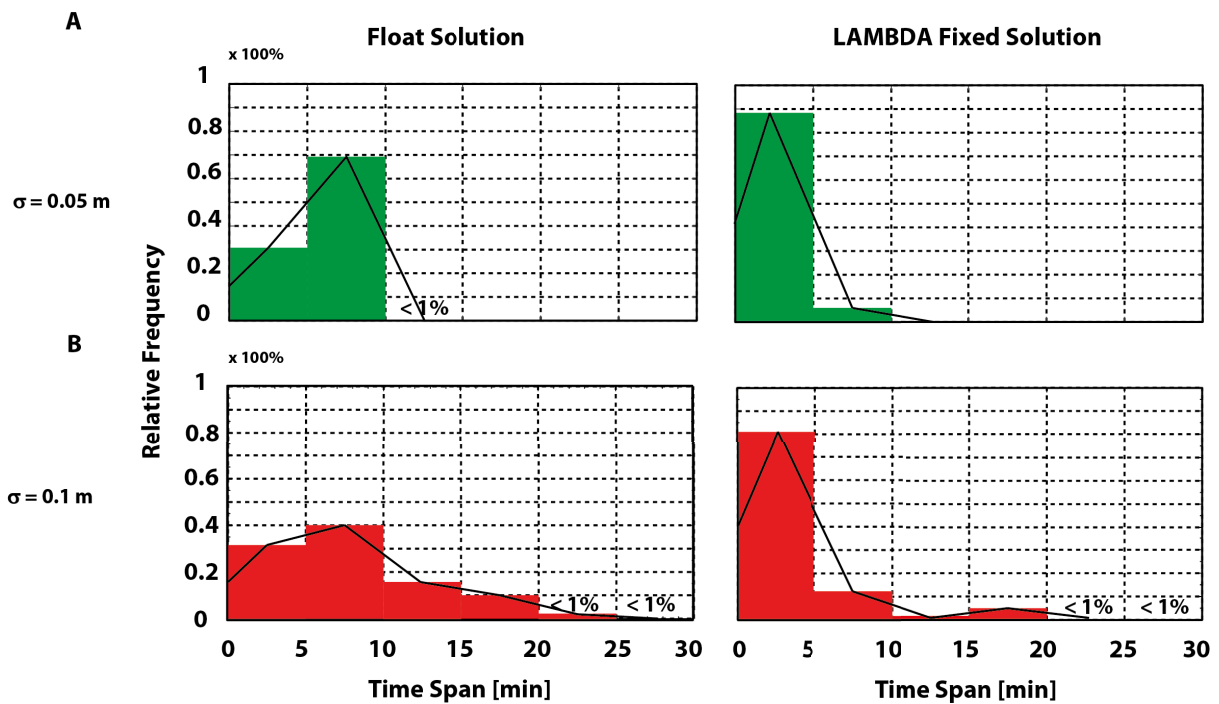


Figure 5.12: Simulations to determine the impact of using three satellites for different observation variances. **Right:** The calculated relative frequency for the float based solution. **Left:** the obtained relative frequency using the LAMBDA method. **A:** Simulated standard deviation of 0.01 m. **B:** Simulated standard deviation of 0.5 m. Simulations are based on satellites observed at An Bihn hotel, Vietnam, over a whole day in February 25, 2012 for an antenna placed at 10 m height.

showed that 95% of the as coherent extracted phase observations are on the L1 frequency. Based on this results, only single L1 frequency observations are processed. If more then one satellite is simultaneously available, the float solution is used as an input for the LAMBDA based ambiguity (Section 5.2.2) (Figure 5.13). The output of the algorithm, is the estimated relative height between the receiver and the reflecting water surface for the observed timespan of 10 minutes.

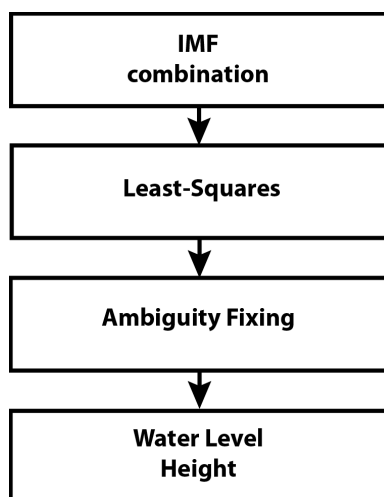


Figure 5.13: Flow diagram of the second main stage of the used algorithm to extract water level height changes. The IMF's isolated from the first main stage of the algorithm are used as input for the LS based water level height extraction algorithm. The output of the algorithm is a float solution. In a next step, if more than one satellite is available, the integer value of the ambiguity is fixed using the LAMBDA estimator. Otherwise, the float based solution is used as the final relative height between the receiver and the reflecting water surface.

5.4 Result Analysis

In this section, the results obtained by applying the proposed algorithms are shown. For this purpose, several representative days will be analysed in detail in order not only to demonstrate the feasibility of the algorithm but also its limits, namely the impact of:

- the loss of phase observations coherency leading to solution gaps that can reach several hours (Section 5.4.1),
- undetected cycle slips in the phase observations causing a water level height error of several decimetres (Section 5.4.2),
- the lack of satellite redundancy enabling the fixing of the ambiguity of the phase observations and with it decreasing the reachable accuracy (Section 5.4.4),
- the suggested Empirical Mode Decomposition (EMD) method to isolate multipath effects other than water reflections (Section 5.4.3).

Since the local water level height observations from the GPS-R based tide gauge are relative to the position of the antennas and the reference water level height changes from the tide gauge instrument are referred to the mean sea level of the year, mean values were removed from each time series. This allows to compare the obtained results avoiding any biases. Additionally, each least squares solution uses 10 minutes of data (starting at the full hour).

5.4.1 Solution gaps

Figures 5.14 and 5.15 show the results obtained for several successive days from Day of the Year (DOY) 56 until DOY 62 (February 25 until March 2) during the experiment conducted in 2012 at the An Bihn hotel in Can Tho City, Vietnam. Whatever, extremely big outliers are first excluded from these solutions (Subsection 5.4.2).

In both figures the sections where a solution gap occurred are outlined in blue and red, respectively. These solution gaps, that can reach several hours, have various reasons.

First, multiple general power cut in Vietnam and receiver hardware problems (Figure 5.14, red). To resolve the power cut problems, a battery with a capacity of ten hours was used during the measurement campaign of 2013 in Vietnam and 2014 in Morocco. Concerning the GORS receiver hardware, the encountered problems could not be reproduced under simulation conditions conducted at the GFZ in Potsdam, Germany. One assumption is a programming error of the receiver by the attempt to track Galileo satellites ephemeris. An error, that were unfortunately first detected and resolved after the experiment conducted in Morocco, so that these kind of solution gaps will be encountered in all the results presented within this thesis.

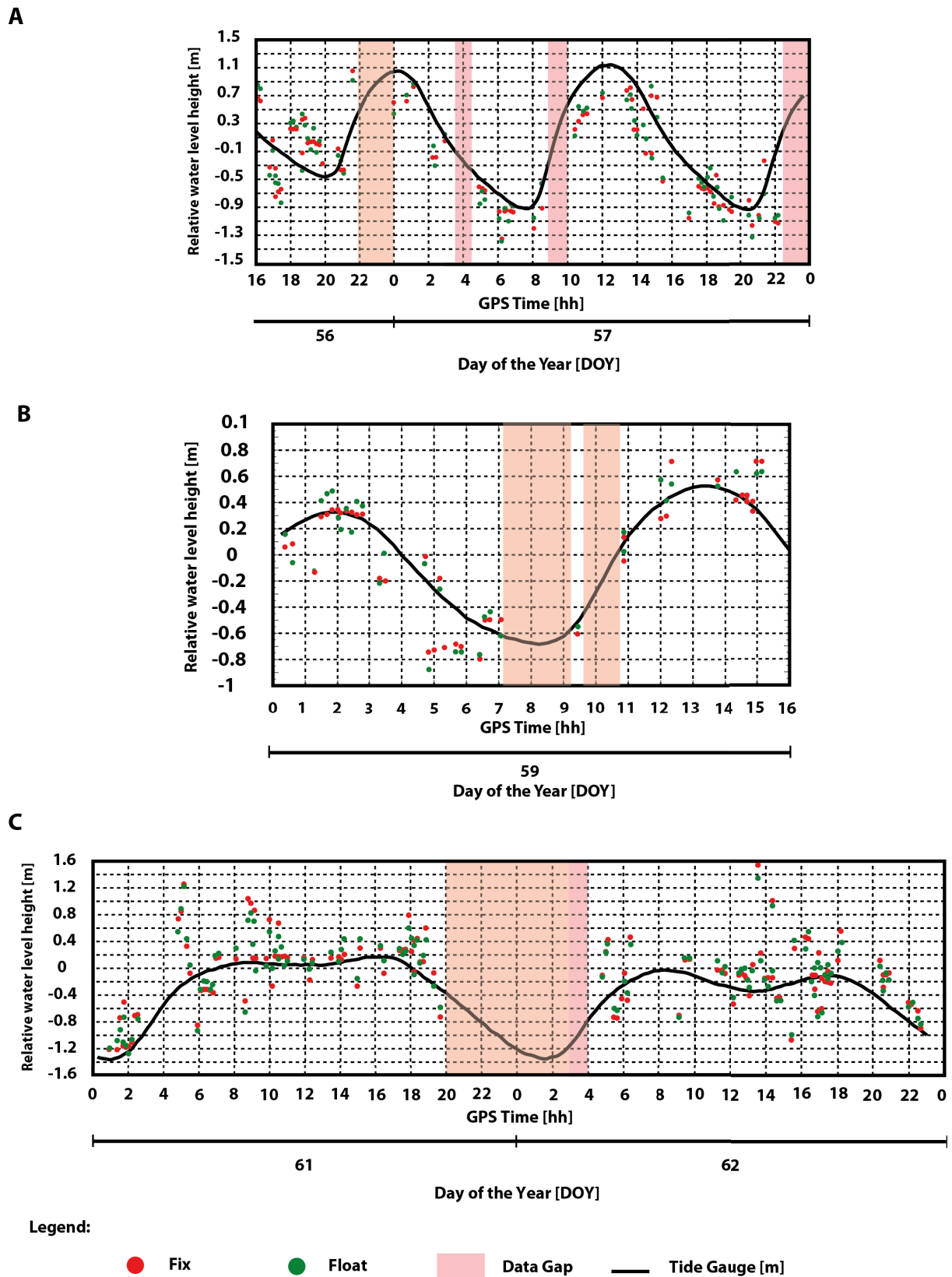


Figure 5.14: Data gaps due to multiple general power cut and hardware problems during the measurement campaign in Vietnam. Data source: February 25, 2012 until March 2, 2012 (DOY: 56 - 62), Terrace, An Bihn hotel, Can Tho City, Vietnam.

Second, the loss of coherency that are mostly due to an increase of the water surface roughness caused by vegetation floating and passing ships but also due to the objects surrounding

the antennas disturbing the reflected signals (Figure 5.15, blue). All effects, that can not be influenced by the proposed algorithm. If only those kind of solution gaps are considered, the proposed method can not be used in the frame of the Vietnam experiment as a monitoring instrument as the goal of a monitoring system is to have continuous measurements results.

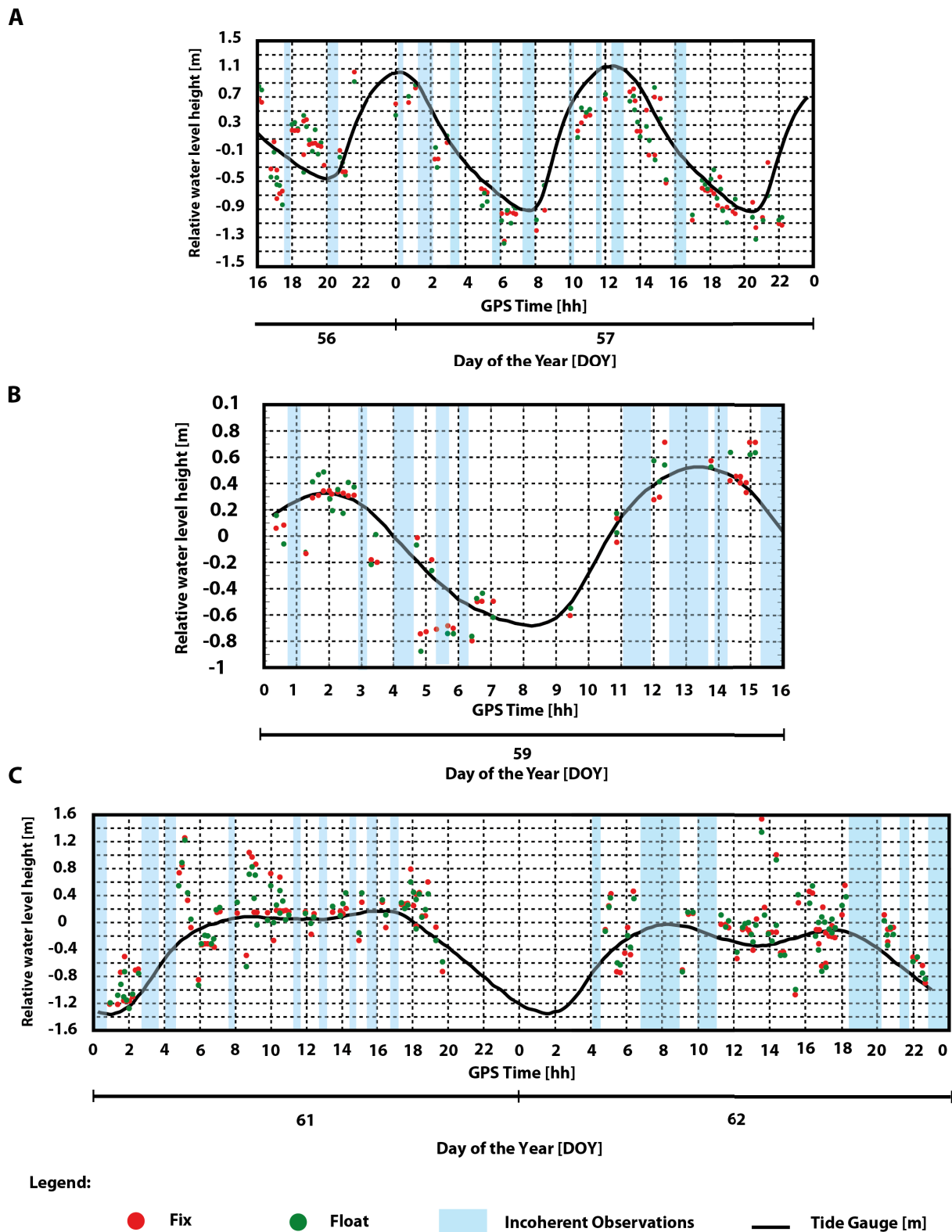
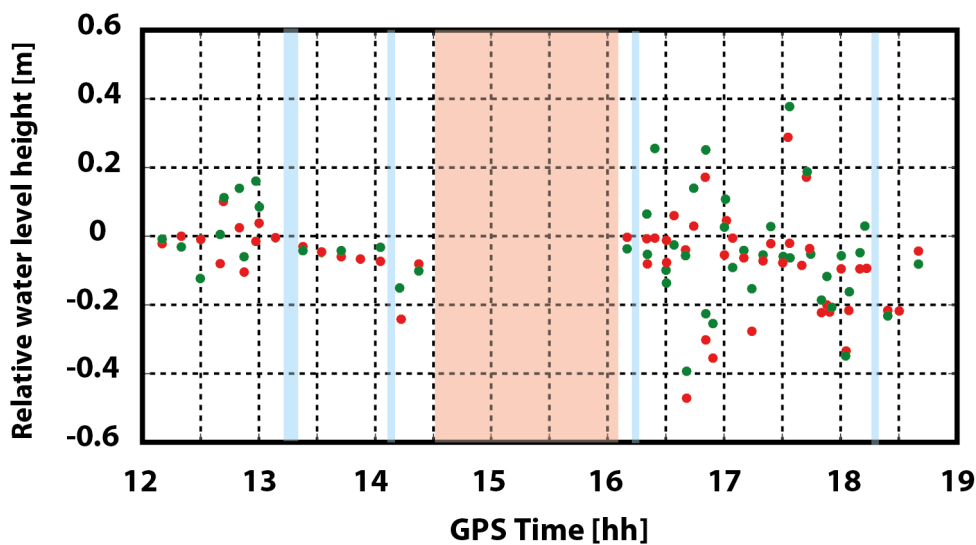


Figure 5.15: Data gaps due to a loss of coherent phase observations. Data source: February 25, 2012 until March 2, 2012 (DOY: 56 - 62), Terrace, An Bihn hotel, Can Tho City, Vietnam.

If a comparison is made to other conducted experiments with similar water roughness properties (Löfgren et al., 2011; Löfgren, 2014), the main difference (except of course from the used receiver), is the antenna.

During the Vietnam experiments, value was attached to the use of low cost equipments, including a low cost antenna. A higher gain antenna could increase the number of coherently recorded observations.

Nevertheless, if the GORS receiver hardware problems are ignored (section marked in red in Figure 5.16), the data collected in Morocco show that under smooth water conditions, nearly all the phase observations are coherent in spite of the use of a low cost antenna.



Legend:

● Fix ● Float ■ Incoherent Observations ■ Hardware problem

Figure 5.16: Results obtained during the measurement campaign conducted in Morocco. In Blue: Data gaps due to a loss of coherent phase observations. In red: Data gaps due to hardware problems of the GORS receiver. Data source: December 16, 2013, Dam Hassan II, Midelt, Morocco.

5.4.2 Impact of undetected Cycle slips

Figure 5.17 shows now the obtained results for the same days as in Figures 5.14 and 5.15 but this time including extremely big outliers (encircled in black) that can reach several metres.

The analysis of these outliers showed that all of them are due to undetected CS by the modified Turbo Edit detection algorithm proposed in Section 4.3.

As an example, Figure 5.18A shows an undetected cycle slip of the size of one cycle, on DOY 59 (February 28, 2012), at the observation epoch 4760 for the satellite with PRN 27. The proposed detection algorithm fails to detect the CS due to an increased noise level of the phase observations. As counter example, Figure 5.18B shows a successfully detected CS of the size of two cycles on the phase observations of PRN 29 at DOY 59, at the epoch 22690. These two

selected examples coincide with the results obtained with simulated data in Section 4.3.2.

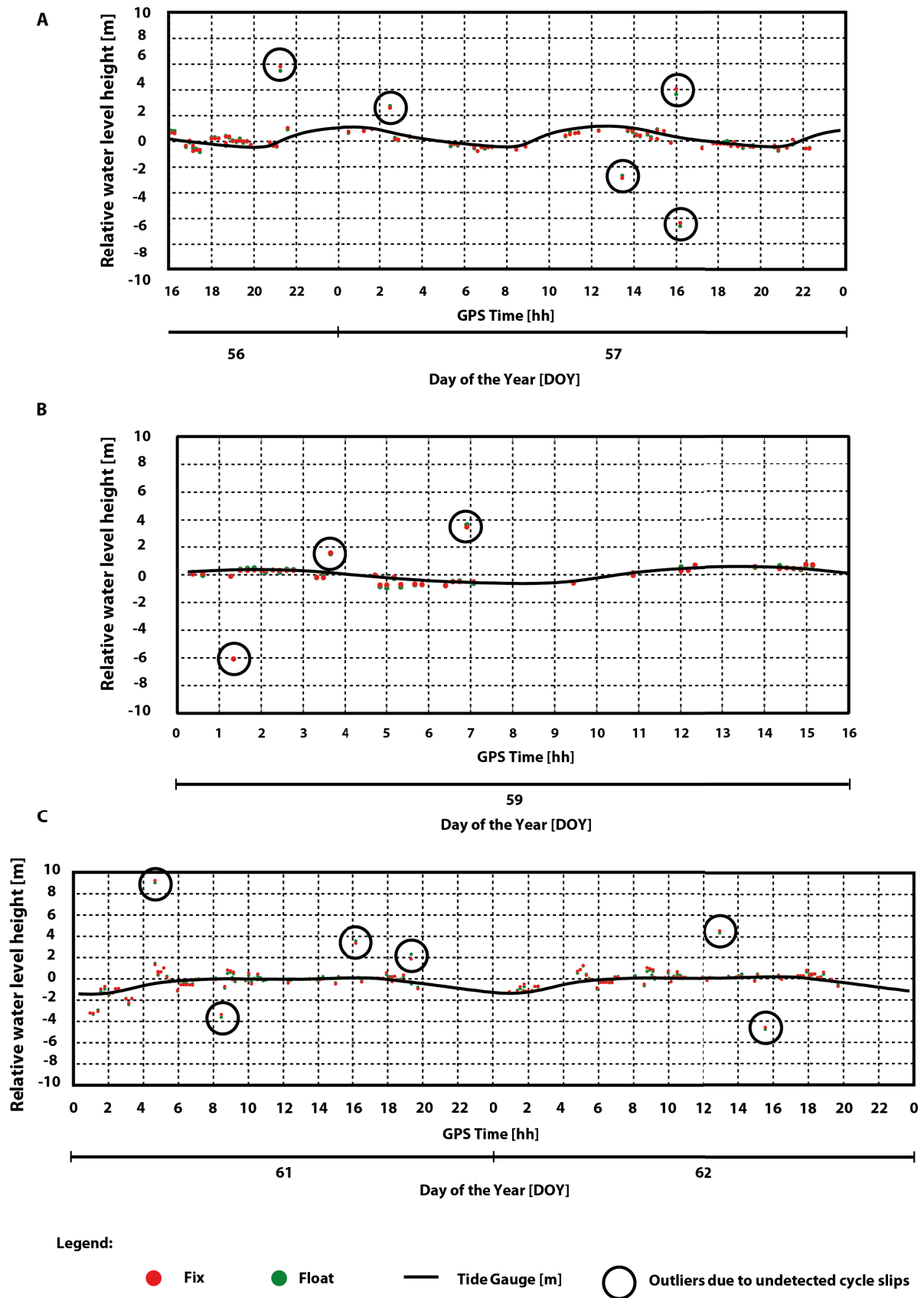


Figure 5.17: Undetected CS can cause a water level height error of several metres. Data source: February 25, 2012 until March 2, 2012 (DOY: 56 - 62), Terrace, An Bihn hotel, Can Tho City, Vietnam.

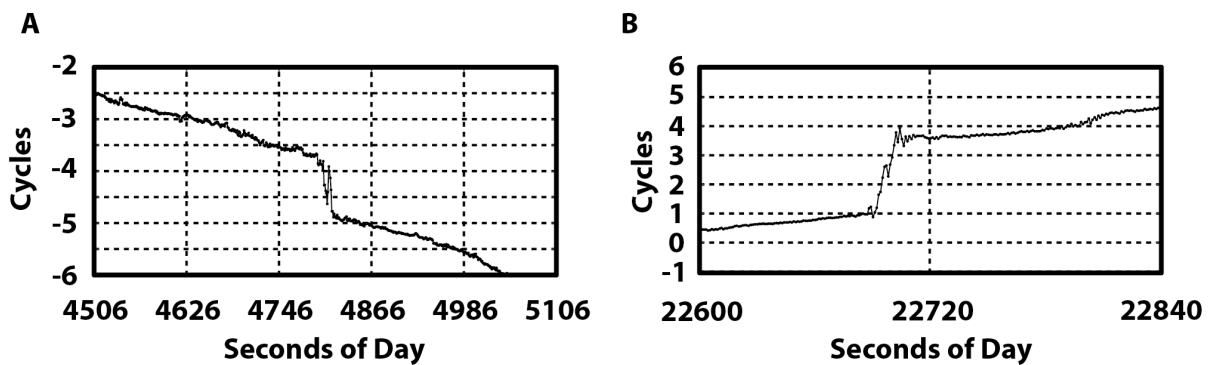
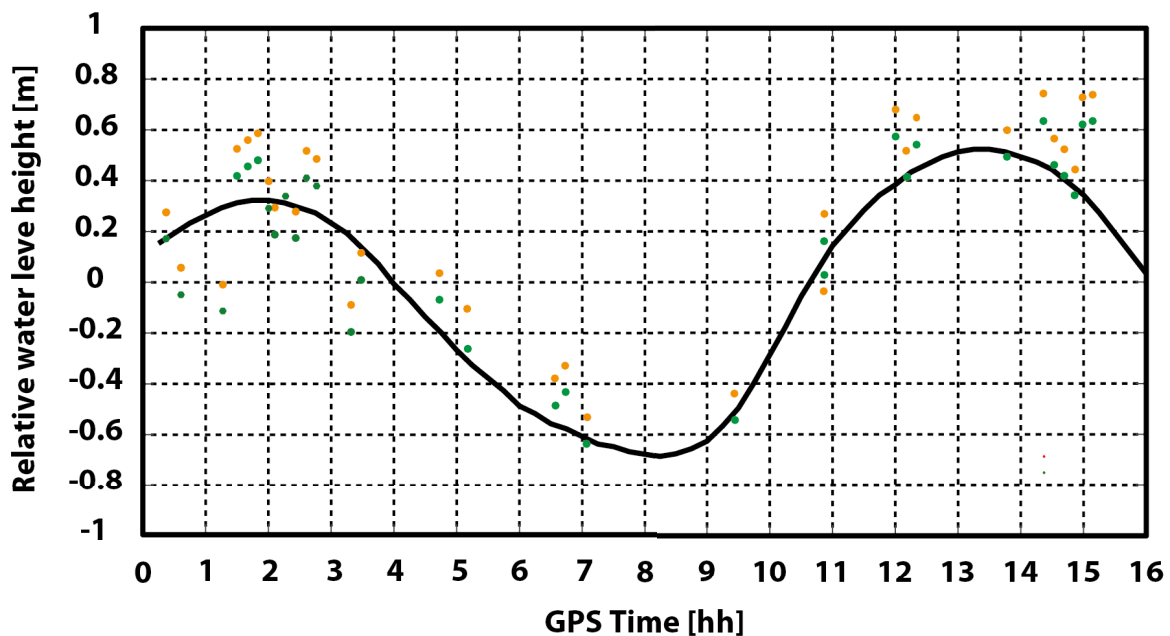


Figure 5.18: Example of a successfully detected and a missed cycle slip using the proposed cycle slip algorithm. **A:** Undetected cycle slip of the size of one cycle on the phase observations of PRN 27 at the epoch 4760 due to an increased noise level of the observations. **B:** Successfully detected cycle slip on PRN 17 at the epoch 22690 of the size of two cycle.

5.4.3 Impact of the proposed Empirical Mode Decomposition Method on the results

In Section 4.4, the Empirical Mode Decomposition (EMD) method is proposed to isolate multipath effects other than those caused by reflections off the water surface. Figure 5.19 shows the impact of using the EMD as a preprocessing tool on the acquired water level height changes. In this case, the standard deviation of the calculated L1 based float solution improves from 0.18 m to 0.14 m.



Legend: ● without EMD ● with EMD

Figure 5.19: Impact of filtering multipath effects on the water level height changes. In green: Float solution without EMD preprocessing. In orange: Float solution using a preprocessing with the EMD method. Data source: February 28, 2012, An Bihn hotel, Can Tho City, Vietnam.

Although, a closer look to single calculated water level height changes, shows also a deterioration of some solutions if a preprocessing of data with the EMD method is made. An analysis of these events shows that their common ground is the relative higher noise level of the phase observations and the use of a single satellite for the calculation of the water level height changes.

On the basis of an example, this phenomena will be illustrates. For the first computed water level height changes in Figure 5.19, the preprocessing of the phase observations leads to an amelioration of the results of almost 1 cm. However, for the next ten minutes, the opposite can be observed. Figure 5.20 illustrates the comparison between the quality of the used data for the calculation. In the first period between the GPS time 0:20 and 0:30, the quality of the recorded phase observations is very good. On the other hand, the second period between the GPS time 0:30 and 0:40, a worsening of the data quality can be observed that is reflected in the obtained results.

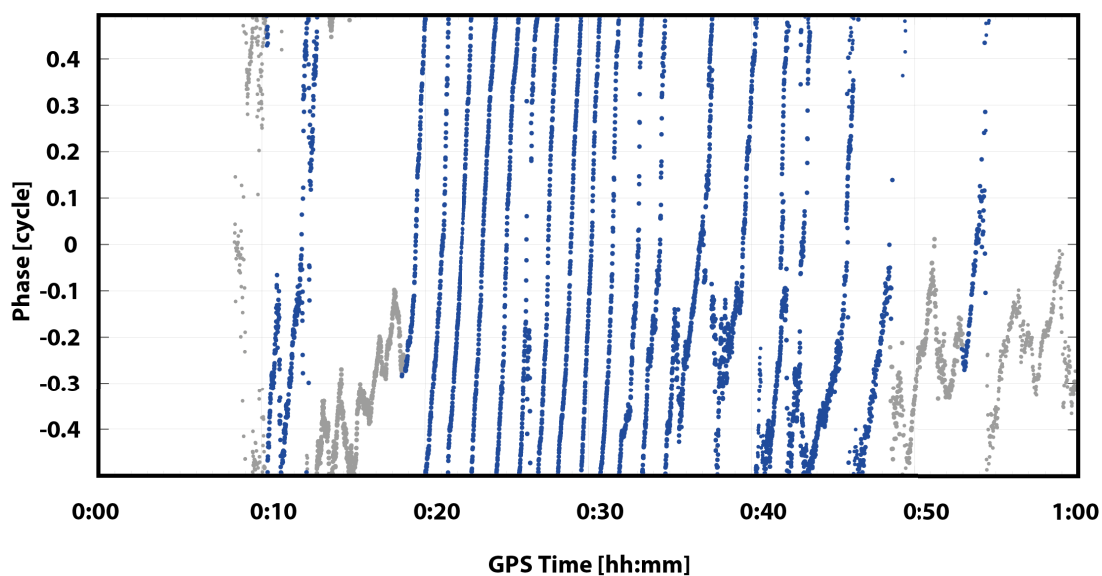


Figure 5.20: In grey: As not coherent extracted phase observations. In blue: As coherent extracted phase observations. In the observation period between 0:30 and 0:40, a higher noise level can be observed, compared to the coherent phase observations recorded between 0:20 and 0:30. This leads to a deterioration of the performance of the proposed EMD multipath filtering method. Data source: February 28, 2012, An Bihn hotel, Can Tho City, Vietnam.

5.4.4 Impact of the available satellite redundancy

In the following section, the impact of the available number of satellites that can be observed in parallel on the obtained water level height accuracy is analysed. For a better visualisation, at the first, one representative day of the plotted results in Figure 5.15 is selected, namely the obtained water level height changes of DOY 59 thus for the February 28, 2012. Figure 5.21A shows the acquired water level height changes for this specific day, if all the available satellites in view (single or redundant) are employed, if all the available frequencies (L1 and L2) are used and if the three outliers caused by the undetected CS are excluded from the solution (Figure 5.17B). In this case, the float solution (green dots) is calculated with a standard deviation of 0.17 m (1σ) and the fixed solution (red dots) with a standard deviation of 0.13 m (1σ). If now only the

results obtained using the L1 frequency are used, a standard deviation of 0.14 m is reached for the float solution and a standard deviation of 0.08 m for the fixed solution. The deterioration of the results by including the L2 frequency observations is due to their higher noise level (Section 4.2). Due to this fact and the fact that the percentage of L2 coherent phase observations are very low (5%), only L1 phase observations are used.

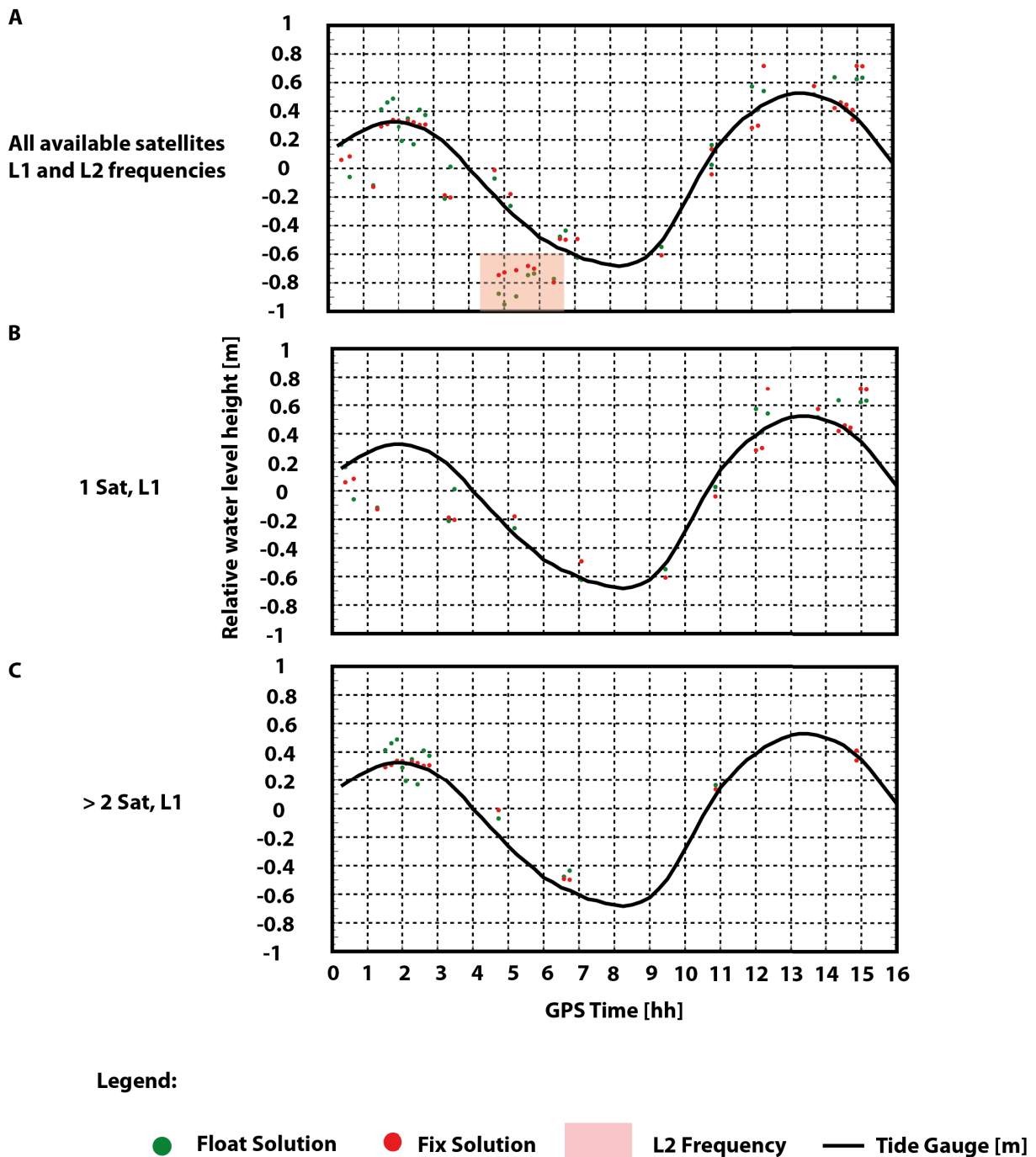


Figure 5.21: Results obtained on February 28, 2012, An Bihn hotel, Can Tho City, Vietnam. **A:** Water level height changes using all available satellites and all frequencies L1 and L2. In green the float solutions and in red the ambiguity fixed solutions. **B:** Results obtained if only a unique satellite is available using a single frequency L1. **C:** Results obtained if more than one satellite is observed in parallel using the single frequency L1. Data source: February 28, 2012, An Bihn hotel, Can Tho City, Vietnam. A mean is removed from each time series.

Furthermore, the Figures underline the impact of redundant satellite observations on the achievable water level height changes accuracy. Panel **B**, illustrates the obtained results if only a unique satellite with L1 frequency is used. In this case, the float solution is calculated with a standard deviation of 0.11 m and the fixed solution, using the IR estimator (Section 5.2), with a standard deviation of 0.12 m.

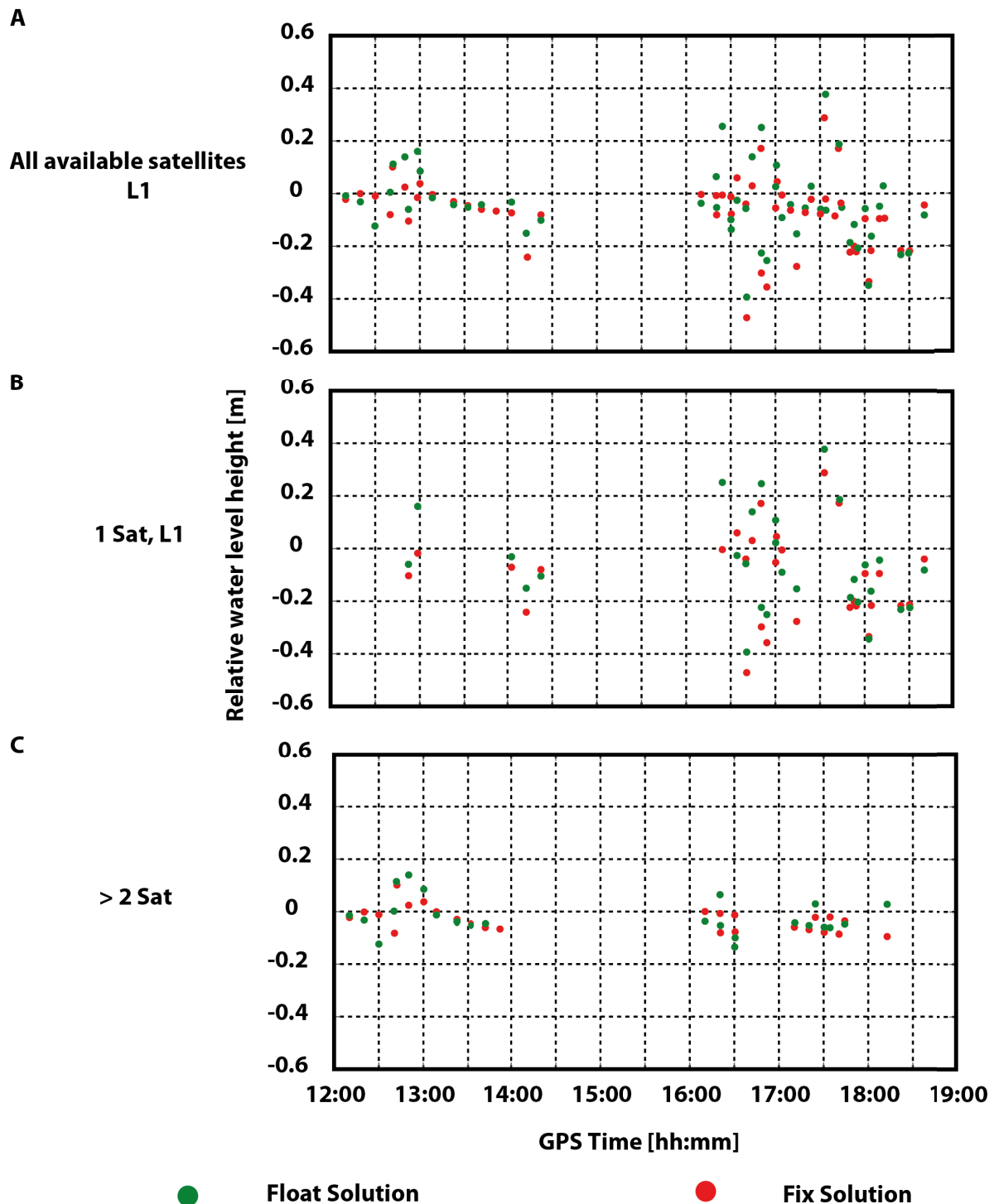
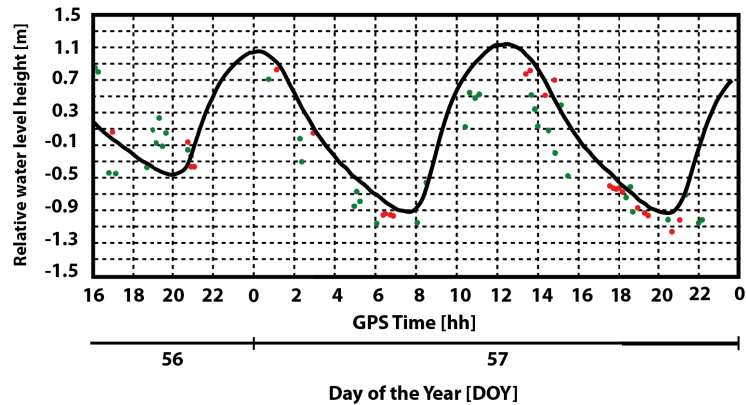


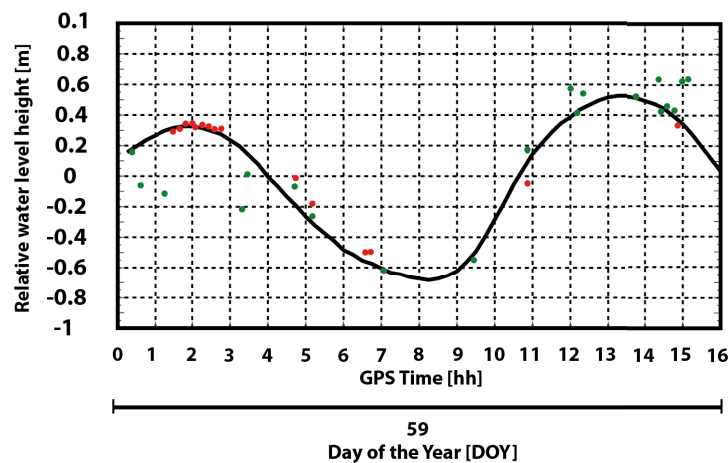
Figure 5.22: Results obtained on December 16, 2013, Dam Hassan II, Midelt, Morocco using more than two satellites. The relative water level height changes could be estimated with a standard deviation of 0.06 m. Data source: December 16, 2013, Dam Hassan II, Midelt, Morocco.

Despite this minimal improvement, the probability of correct integer estimation using the IR estimator to fix the ambiguity is particularly low (Teunissen et al., 1999). Therefore, in the case only one satellite is available, the float solution is used. Panel **C** shows the results obtained if more than one satellite is observed in parallel (maximum of 3 satellites) and the ambiguities are fixed using the LAMBDA method. The standard deviation of the fixed solution in this case is 0.05 m.

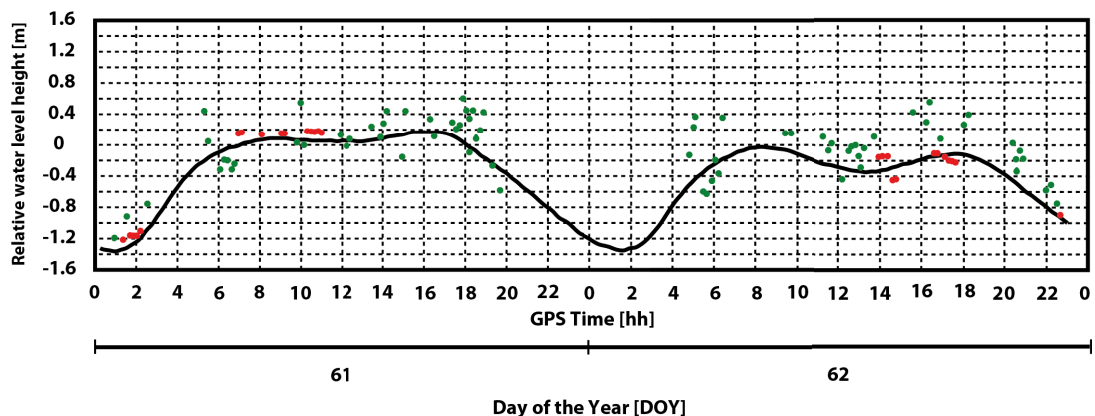
A



B



C



Legend:

● Fix ● Float — Tide Gauge [m]

Figure 5.23: Calculated water level height changes for several successive days. In green: If only one satellite is visible, the float solution will be used. If redundant satellites are available, the fixed solution will be used. Data source: February 25, 2012 until March 2, 2012 (DOY: 56 - 62), Terrace, An Bihn hotel, Can Tho City, Vietnam.

The use of redundant satellites improves as expected, the accuracy of the extracted water level height changes up to several centimetres.

The importance of the satellite redundancy is again underlined in the results obtained in the experiment conducted in Morocco, where up to four satellites could be observed in parallel. In this case, the standard deviation using all the available satellites with the L1 frequency is 0.11 m for the float solution and 0.10 m for the fixed solution. If the results are analysed from the point of view of redundant satellites, a standard deviation of 0.17 m for the float solution and 0.13 m for the fixed solution is acquired if only one satellite with L1 frequency is used. In the case redundant satellites are available, the obtained results show this time a standard deviation of 0.05 m using the LAMBDA method over periods of more than an hour.

The increase in satellite redundancy during the measurement campaign conducted in Morocco was due to the following two reasons. First, the open view of the receiver antenna on the area of interest that gives the possibility to track satellites on a larger elevation range than in the constellation of Vietnam. Second, the dam water surface was smooth so that the coherency of the signals was maintained over longer observation period.

Figures 5.23 show the final results for all the selected days based on the following findings: only L1 phase observations are used, if only one satellite is available the float solution will be used otherwise the fixed solution based on the LAMBDA method is used. In this case, the overall standard deviation of the solutions is 0.18 m. However, for the float solutions, a standard deviation of 0.20 m is found and for the fixed solutions a standard deviation of 0.07 m.

Chapter 6

Conclusion and Outlook

In the last years extreme flood events occur more frequently in Vietnam. Global Positioning System-Reflectometry (GPS-R) reveals new perspectives for water level monitoring. To test the possibility of using this innovative technique as a gauge instrument, two measurement campaigns were conducted in Can Tho City in Vietnam in 2012 and 2013.

Compared to code observations, the use of phase observations has the potential to offer more accurate results. However, its use depends on the coherency of the phase observation and on the resolution of the ambiguity. To test the impact of the antenna geometry on the quality and quantity of the recorded coherent phase observations two different antenna heights with a difference in altitude of 10 m were used. A thorough analysis of the recorded observations showed that for both antenna position, data coherency was partially or entirely destroyed due to the heavy ship traffic on the observed section of the Mekong Delta River so that the recorded data could not be directly used. Given the high number of recorded reflection events with a sampling rate of 1 Hz, an automated method was developed to isolate coherent data. For this purpose, a Least-Squares (LS)-based ellipse fitting was used, showing a rate of correctly classified data of 82%.

The analysis of the as coherent extracted phase observation showed that only around 50% of the recorded data could be used and that 95% of them are on the L1 frequency only with a continuous recording time of at least 10 min. The challenge was thus to develop a complete algorithm based on the L1 phase observation only. A further analysis showed also a high number of cycle slips as well as multipath effects other than the reflections off the water surface. All mostly caused by the objects surrounding the antennas. The proposed algorithm has therefore two main steps: a preprocessing step to correct for the cycle slips and the multipath effects and a processing step that enables the calculation of the sought water level height.

In the preprocessing step, first the presence of cycle slips are mitigated. Restricted to the use of single frequency phase observations and the fact that the phase observations showed a mean noise level of 0.05 m, the proposed algorithm based on a running mean could not always properly differentiate between small cycle slips and noise. This phenomenon has been demonstrated in the analysis of the results where outliers of several metres appeared in the

calculation of water level height due to undetected cycle slips. The proposed method could be improved by the addition of code observation as they are not affected by cycle slips. In a second step, the presence of multipath effects is mitigated by using the Empirical Mode Decomposition (EMD) method. The main advantage of the EMD method is that it is fully data-driven and can be applied to any complex data set. There is also no need for an a-priori base, as with, for example, trigonometric functions in the case of the Fourier transform or a mother wavelet in the case of the Wavelet transform. There is also no condition set to the data such as linearity or/and stationary. The EMD method decomposes the input signal into sub-signals called Intrinsic Mode Function (IMF). Simulation results showed that the extracted number of IMFs do not reflected the number of multipath signals. The proposed strategy to overcome this problem, is to use a phase model based on the approximate satellite-receiver-reflector geometry information. The IMF combination that best fitted the model are isolated as the "real" water reflections. By applying this filter, it was possible to achieve an improvement of several centimetres on the estimated altimetric information showing the high potential of this method. However, also here the proposed method can be improved like the use of a more complex method to define more accurately the upper and the lower envelop used to extract the single IMFs or the use of the (Noise Assisted Data Analysis) (NADA) EMD-method to isolate more correctly each single multipath effects in a single IMF (Hirrlinger, 2016).

After these pre-processing steps, the water level height was calculated using the LS method. As only L1 phase observation from a unique satellite were available, a model for all remaining systematic errors has to be selected carefully to be able to reach the set decimetre level of accuracy. Due to the short horizontal distances between the antennas and the reflection events, a planar model of the Earth surface sufficient as the difference to the more sophisticated spherical model shows a difference of only 3 mm for the used antenna constellation. To correct for the tropospheric delay, the model developed by Cardellach et al. (2011) can be used if the corresponding ZTDs and H_{atm} for the Vietnam station which has been determined within this thesis are used. Simulations showed also the necessity to correct for the Antenna Phase Centre (APC) and Phase Centre Offset (PCO) as well as for the Phase Wind Up (PWU) (Beyerle, 2009). Indeed, due to the inclination between the horizontally placed antenna and the antenna tilted toward the reflecting water surface, the built difference between direct and reflected incoming signal do not eliminate these systematic errors although a zero baseline is used.

The advantage of using phase observations is that the fraction of the incoming cycle can be measured within the millimetre. However this benefit can only be used if the ambiguous integer number of cycles is correctly resolved. As mostly only coherent phase observations on the L1 frequency from a single satellite are available, the geometric changes of the satellite is used for this aim. Simulations showed that the minimum time span of observation needed to reach the decimetre level was 5 min but to get more reliable results a timespan of 25 min should be used. However, as mostly only around 10 min of continuous coherent phase observation are available, the timespan was set to 10 min. As a consequence, water level height output are also given in this frequency under the condition of coherent phase observation.

The proposed algorithm demonstrates that altimetric information about the reflecting water surface can be recovered with an Root Mean Square (RMS) of 0.28 m. Furthermore, it was also shown that the use of redundant satellites improved the water level results to an RMS of 0.05 m, even if only a single frequency was used. This shows the potential that a GPS-R phase-based method could significantly contribute to altimetry applications where observation with high spatial and dense temporal resolution are needed.

However, in the case study of the Can Tho river section of the Mekong Delta, the use of phase-based GPS-R as a flood-monitoring instrument is not possible, as continuous monitoring of water levels is necessary. Thus an important task for the future is to reduce the amount of data gaps in the time series to get a reliable monitoring instrument. This could be done by carefully choosing the placement of the antennas. Additionally, to overcome the high loss of coherency due to the roughness of the reflecting surface, GPS-R still requires further research especially in the optimization of receivers and antennas for GPS-R applications (Löfgren et al., 2011). This will enable improvement in information extraction and analysis.

Bibliography

- Andrei, C.-O. and Chen, R.: Assessment of time-series of troposphere zenith delays derived from the Global Data Assimilation System numerical weather model, *GPS Solutions*, 13, 109 – 117, doi:10.1007/s10291-008-0104-1, 2009.
- Apel, H., Hung, N., Thoss, H., and Schöne, T.: GPS buoys for stage monitoring of large rivers, *Journal of Hydrology*, 412-413, 182–192, doi:10.1016/j.jhydrol.2011.07.043, 2010.
- Arras, C., Wickert, J., Beyerle, G., Heise, S., and Schmidt, T.: A global climatology of ionospheric irregularities derived from GPS radio occultation, *Geophys. Res. Lett.*, 35, L14 809, 1–4, doi:10.1029/2008GL034158, 2008.
- Beckheinrich, J., Beyerle, G., Schön, S., Apel, H., Semmling, A. M., and Wickert, J.: WISDOM: GNSS-R based flood monitoring, in: *IEEE Workshop on Reflectometry Using GNSS and Other Signal of Opportunity (GNSS+R)*, pp. 1–6, Purdue, USA, doi:10.1109/GNSSR.2012.6408257, 2012.
- Beckheinrich, J., Ouazzar, D., Touzani, A., Hasnaoui, M. D., and Nsandamoun, T.: PMARS: The Use of GNSS Reflectometry for water level Monitoring and soil moisture extraction, *Internal Report*, 2014.
- Beckmann, P. and Spizzichino, A.: *The scattering of electromagnetic waves from rough surfaces*, Artech House, Incorporated, 1987.
- Beyerle, G.: Carrier Phase wind-up in GPS reflectometry, *GPS Solutions*, 13, 3, 191–198, doi:10.1007/s10291-008-0112-1, 2009.
- Beyerle, G., Schmidt, T., Michalak, G., Wickert, J., and Reigber, C.: GPS radio occultation with GRACE: Atmospheric profiling utilizing the zero difference technique, *Geophys. Res. Lett.*, 32, 1–5, doi:10.1029/2005GL023109, 2005.
- Bisnath, S. B.: Efficient, Automated Cycle-Slip Correction Of Dual-Frequency Kinematic GPS Data, in: *Proceedings of the 13th International Technical Meeting of the Satellite Division of The Institute of Navigation (ION GPS 2000)*, pp. 145–154, Salt Lake City, UT, 2000.
- Blewitt, G.: An Automatic Editing Algorithm for GPS data, *Geophys. Res. Lett.*, 17, 199–202, doi:10.1029/GL017i003p00199, 1990.
- Boehm, J., Niell, A., Tregoning, P., and Schuh, H.: *Global Mapping Function (GMF): A new*

- empirical mapping function based on numerical weather model data, *Geophys. Res. Lett.*, 33, L07 304, 1–4, doi:10.1029/2005GL025546, 2006.
- Bookstein, F. L.: Fitting Conic Sections to Scattered Data, *Computer Graphics and Image Processing*, 9, 56–71, 1979.
- Businger, S., Chiswell, S., Bevis, M., Duan, J., Anthes, R., Rocken, C., Ware, R., Exner, M., Van Hove, T., and Solheim, F.: The promise of GPS in atmospheric monitoring, *Bulletin of American Meteorological Society*, 77, 5–18, 1996.
- Cai, C., Liu, Z., Xia, P., and Dai, W.: Cycle slip detection and repair for undifferenced GPS observations under high ionospheric activity, *GPS Solutions*, 17, 247–260, doi:10.1007/s10291-012-0275-7, 2013.
- Cardellach, E., Ao, C. O., de la Torre Juárez, M., and Hajj, G. A.: Carrier phase delay altimetry with GPS-reflection/occultation interferometry from low Earth orbiters, *Geophys. Res. Lett.*, 31(L10402), 1–4, doi:10.1029/2004GL019775, 2004.
- Cardellach, E., Fabra, F., Nogués-Correig, O., Oliveras, S., Ribó, S., and Rius, A.: GNSS-R ground-based and airborne campaigns for ocean, land, ice, and snow techniques: Application to the GOLD-RTR data sets, *Radio Sci.*, 46, RS0C04, doi:10.1029/2011RS004683, 2011.
- Cardellach, E., Rius, A., Martín-Neira, M., Fabra, F., Nogues-Correig, O., Ribo, S., Kainulainen, J., Camps, A., and D Addio, S.: Consolidating the Precision of Interferometric GNSS-R Ocean Altimetry Using Airborne Experimental Data, *IEEE Trans. Geosc. Remote Sens.*, 52, 4992–5004, 2014.
- Cox, C. and Munk, W.: Measurement of the Roughness of the Sea Surface from Photographs of the Sun's Glitter, *J. Opt. Soc. Am.*, 44, 838–850, doi:10.1364/JOSA.44.000838, 1954.
- Danh, V. T. and Mushtaq, S.: Environmental Change and Agricultural Sustainability in the Mekong Delta, vol. 45 of *Advances in Global Change Research*, chap. 11, pp. 181–204, Springer, 2011.
- de Jonge, P.: A processing strategy for the Application of the GPS in networks, Master's thesis, Technical University of Delft, The Netherlands, 1998.
- Doberstein, D.: GPS Signal Structure and Use, chap. 3, pp. 39–54, Springer, 2012.
- Dunn, M. J.: Interface Specification, IS-GPS-200H, Tech. rep., Global Positioning Systems Directorate Systems Engineering & Integration, 2013.
- Egido, A., Caparrini, M., Ruffini, G., Paloscia, S., Santi, E., Guerriero, L., Pierdicca, N., and Flouy, N.: Global Navigation Satellite Systems Reflectometry as a Remote Sensing Tool for Agriculture, *Journal Remote Sensing*, 4, 2356–2372, doi:10.3390/rs4082356, 2012.
- Eissfeller, B.: Ein dynamisches Fehlermodell für GPS Autokorrelationsempfänger, vol. 55 of

- Schriftenreihe Universität der Bundeswehr München. Studiengang Vermessungswesen*, Universität der Bundeswehr München, 1997.
- Fabra, F., Cardellach, E., Rius, A., Ribó, S., Oliveras, S., Nogués-Correig, O., Rivas, M., Semmling, M., and D'Addio, S.: Phase Altimetry With Dual Polarization GNSS-R Over Sea Ice, *IEEE Transactions on Geoscience and Remote Sensing*, 50, 2112–2121, doi:10.1109/TGRS.2011.2172797, 2012.
- Fitzgibbon, A., Pilu, M., and Fisher, R. B.: Direct Least Square Fitting of Ellipses, *Pattern Analysis and Machine Intelligence*, *IEEE Transactions on*, 21, 476–480, doi:10.1109/34.765658, 1999.
- Flandrin, P., Gabriel, R., and Goncalves, P.: Empirical Mode Decomposition as a Filter Bank, *IEEE Signal Processing Letters*, 11, 112–114, doi:10.110/LSP.2003.821662, 2004.
- Flock, W. L.: Propagation Effects on Satellite Systems at Frequencies Below 10 GHz : A Handbook for Satellite System Design, no. 1108 in Scientific and Technical Information Division, National Aeronautics and Space Administration, NASA, 1987.
- Foelsche, U. and Kirchengast, G.: A New Geometric Mapping Function for the Hydrostatic Delay at GPS Frequencies, *Phys. Chem. Earth*, 26, 153–157, 2001.
- Fu, L.-L., Chelton, D., Le Traon, P.-Y., and Morrow, R.: Eddy dynamics from satellite altimetry, *Oceanography*, 23, 14–25, doi:10.5670/oceanog.2010.02, 2010.
- Gander, W., Golub, G. H., and Strebel, R.: Fitting of Circles and Ellipses, *BIT*, 34, 558–578, 1994.
- Garrison, J. L. and Katzberg, S. J.: The Application of Reflected GPS Signals to Ocean Remote Sensing, *Remote Sensing of Environment*, 73, 175–187, 2000.
- Gebhard, S., Kuenzer, C., Huth, J., Wehrmann, T., Schetter, I., and Schmidt, M.: The WISDOM project - A Water-related Information System for the Mekong Delta, Vietnam, in: 13th Int. Water Resources Assoc, (IWRA) World Water Congr., Montpellier, France, 2008.
- Gendt, G., Dick, G., Reigber, C., Tomassini, M., Liu, Y., and Ramatschi, M.: Near Real Time GPS Water Vapor Monitoring for Numerical Weather Prediction in Germany, *Journal of Meteorological Society of Japan*, 82, 361–370, doi:10.2151/jmsj.2004.361, 2004.
- Gleason, S. and Gebre-Egziabher, D.: GNSS Applications and Methods, chap. 16: Remote Sensing Using Bistatic GNSS Reflections, pp. 399–436, Artech House, 2009.
- Grasso, V. F.: Early Warning Systems: State-of-Art Analysis and Future Directions, Tech. rep., United Nations Environment Programme (UNEP), 2012.
- Halir, R. and Flusser, J.: Numerically Stable Direct Least Squares Fitting of Ellipse, in: 6th International Conference in Central Europe on Computer Graphics and Visualisation WSG'98, pp. 125–132, 1998.

- Hall, C. and Cordy, R. A.: Multistatic Scatterometry, in: IEEE Geoscience And Remote Sensing Symposium (IGARSS), vol. 1, pp. 561–562, doi:10.1109/IGARSS.1988.570200, 1988.
- Hannah, B. M.: Modelling and simulation of GPS Multipath propagation, Ph.D. thesis, Queensland University of Technology, Australien, 2001.
- Hariharan, H., Gribok, A., Abidi, M. A., and Koshan, A.: Image Fusion and Enhancement via Empirical Mode Decomposition, *J. Pattern Recognition Research*, 1, 16–31, 2006.
- Hashimoto: Environmental issues and recent infrastructure development in the Mekong Delta: Review, analysis and recommendations with particular reference to large-scale water control projects and the development of coastal areas, Tech. rep., Australian Mekong Resource Centre, 2001.
- Helm, A.: Ground-based GPS altimetry with the L1 OpenGPS receiver using carrier phase-delay observations of reflected GPS signals, Ph.D. thesis, Technische Universität Berlin, Germany, Scientific Technical Report STR: 08/10, GFZ Potsdam, Germany, doi:10.2312/GFZ.b103-08104, 2008.
- Helm, A., Stosius, R., Beyerle, G., Montenbruck, O., and Rothacher, M.: Status of GNSS reflectometry related receiver developments and feasibility studies within the German Indonesian Tsunami Early Warning System, in: IEEE Geosci. Remote Sensing Symp. IGARSS, pp. 5084–5087, 2007.
- Hirrlé, A.: Zur Reduzierung des mehrwegebedingten GNSS-Trägerphasenmessfehlers durch Anwendung der Hilbert Huang Transformation auf Signalqualitätsparameter, Ph.D. thesis, University of Dresden, 2016.
- Hirrlé, A., Jentschel, H.-J., and Michler, O.: Estimation of multipath parameters using hilbert huang transform, in: 25th Intern. Technical Meeting of the Satellite Division of the Institute of Navigation, ION, pp. 67–78, 2012.
- Hofmann-Wellenhof, B., Lichtenegger, H., and Collins, J.: GPS Theory and Practice, Springer-Verlag Wien, 5th rev. ed. 2001 edn., 2008.
- Huang, N. E. and Wu, Z.: A Review on Hilbert-Huang Transform: Method and its Applications to Geophysical Studies, *Reviews of Geophysics*, 46, 1–23, doi:2007RG000228, 2008.
- Huang, N. E., Shen, Z., Long, S. R., Wu, M. C., Shin, H., Zheng, Q., Yen, N. C., Tung, C. C., and Liu, H. H.: The Empirical Mode Decomposition and the Hilbert Spectrum for nonlinear and non-stationary time series analysis, *Proc. R. Soc. Lond. A.*, 454, 903–995, 1998.
- Ibouhouten, H., Zielhofer, C., Mahjoubi, R., Kamel, S., Linstädter, J., Mikdad, A., Bussmann, J., Werner, P., Härtling, J. W., and Fenech, K.: Archives alluviales holocènes et occupation humaine en Basse Moulouya (Maroc nord-oriental), *Géomorphologie : relief, processus, environnement* [Online], doi:10.4000/geomorphologie.7812, URL <http://geomorphologie.revues.org/7812>, 2010.

- ICD-GPS-200D: Global Positioning System Wing (GPSW), Systems Engineering and Integration, Interface Specification, IS-GPS-200, Revision E, Navstar GPS Space Segment/Navigation User Interfaces, Tech. rep., Global Positioning Systems Directorate, URL <http://www.gps.gov/technical/icwg/IS-GPS-200E.pdf>, 2010.
- Ilcev, S. D.: Global Mobile Satellite Communication, For maritime, Land and Aeronautical Applications, Springer, 2005.
- Irsigler, M.: Multipath Propagation, Mitigation and Monitoring in the Light of Galileo and the Modernized GPS, Ph.D. thesis, Universität der Bundeswehr München, Germany, 2008.
- Jakowski, N., Stankov, S. M., Mayer, C., Becker, C., and Schlüter, S.: SWACI-ein neuer Ionosphären-Wetterdienst, in: Zweiter Nationaler Workshop zum Weltraumwetter, 2005.
- Jonkman, N. F.: Integer GPS-ambiguity estimation with the receiver-satellite geometry, Ph.D. thesis, Delft University of Technology, Faculty of Civil Engineering and Geosciences, Department of Mathematical Geodesy and Positioning, 1998.
- Kaplan, E. and Hegarty, C. J.: Understanding GPS: Principles and Applications, Artech House, Boston, second edn., 2006.
- Karaim, M. O., Karamat, T. B., Noureldin, A., Tamazin, M., and Atia, M. M.: Real-time Cycle-slip Detection and Correction for Land Vehicle Navigation using Inertial Aiding, in: Proceedings of the 26th International Technical Meeting of The Satellite Division of the Institute of Navigation (ION GNSS+ 2013), pp. 1290 – 1298, Nashville, TN, USA, 2013.
- Karaim, M. O., Karamat, T. B., Noureldin, A., and El-Shafie, A.: GPS Cycle Slip Detection and Correction at Measurement Level, British Journal of Applied Science & Technology, 4, 4239–4251, doi:9734/BJAST/2014/11850, 2014.
- Kersten, T.: Calibration Report: GNSS (GFZ) Reflectometry Antenna Mount, Tech. rep., Institut für Erdmessung, Leibniz Universität Hannover, Germany, 2013.
- Kersten, T.: Bestimmung von Codephasen-Variationen bei GNSS-Empfangsantennen und deren Einfluss auf die Positionierung, Navigation und Zeitübertragung, Ph.D. thesis, Leibniz Universität Hannover, Germany, URL <http://dgk.badw.de/fileadmin/docs/c-740.pdf>, 2014.
- Klobuchar, J. A.: Ionospheric Time-Delay Algorithm for Single Frequency GPS Users, IEEE Transactions on Aerospace and Electronic Systems, 23, 325–331, doi:10.1109/TAES.1987.310829, 1987.
- Kouba, J.: A simplified yaw-attitude model for eclipsing GPS satellites, GPS Solutions, 13, 1–12, doi:10.1007/s10291-008-0092-1, 2009.
- Larson, K. M., Gutmann, E. D., Zavorotny, V. U., Braun, J. J., Williams, M. W., and Nievinski, F. G.: Can we measure snow depth with GPS receiver, Geophys. Res. Lett., 36(17), doi:10.1029/2009GL039430, 2009.

- Larson, K. M., Braun, J. J., Small, E. E., Zavorotny, V. U., Gutmann, E. D., and Bilich, A. L.: GPS Multipath and Its Relation to Near-Surface Soil Moisture Content, *IEEE J. Sel. Topics Appl. Earth Observ.*, 3, doi:10.1109/JSTARS.2009.2033612, 2010.
- Löfgren, J. S.: Local Sea Level Observations Using Reflected GNSS Signals, Ph.D. thesis, Department of Earth and Space Sciences, Space Geodesy and Geodynamics, Chalmers University of Technology, Sweden, URL <http://publications.lib.chalmers.se/records/fulltext/191472/191472.pdf>, 2014.
- Löfgren, J. S., Haas, R., Scherneck, H.-G., and Bos, M. S.: Three months of local sea level derived from reflected GNSS signals, *Radio Sci.*, 46, 2011.
- Long, N. T. and Trong, B. D.: Flood monitoring of Mekong River Delta, Vietnam using ERS SAR data, in: *Asian Conference on Remote Sensing*, 2001.
- Lowe, S. T., Zuffada, C., Chao, Y., Kroger, P., and Young, L. E.: 5-cm-Precision aircraft ocean altimetry using GPS reflections, *Geophys. Res. Lett.*, 29, 1–4, doi:10.1029/2002GL014759, 2002.
- Lowe, S. T., Meehan, T., and Young, L.: Direct Signal Enhanced Semicodeless Processing of GNSS Surface-Reflected Signals, *IEEE JSTARS*, 7, 1469–1472, doi:10.1109/JSTARS.2014.23130, 2014.
- Lyons, R. G.: *Understanding Digital Signal Processing*, 2nd edn., 2004.
- Magnan, A., Garnaud, B., Billé, R., Gemenne, F., and Hallegatte, S.: *La Méditerranée au futur: Des impacts du changement climatique aux enjeux de l'adaptation*, Tech. rep., Institut du développement durable et des relations internationales, 2009.
- Manh, N. V., Dung, N. V., Hung, N. N., Kummu, M., Merz, B., and Apel, H.: Future sediment dynamics in the Mekong Delta floodplains: Impacts of hydropower development, climate change and sea level rise, *Global and Planetary Change*, 127, 22–33, 2015.
- Martín-Neira, M.: A PASSive Reflectometry and Interferometric System (PARIS): Application to ocean altimetry, *ESA Journal*, 17, 331–355, 1993.
- Martín-Neira, M., Caparrini, M., Font-Rossello, J., Lannelongue, S., and Vallmitjana, C. S.: The PARIS concept: an experimental demonstration of sea surface altimetry using GPS reflected signals, *IEEE Trans. Geosc. Remote Sens.*, 39, 142–150, doi:10.1109-36.898676, 2001.
- Martín-Neira, M., d'Addio, S., Buck, C., Floury, N., and Cerdeira, R. P.: The PARIS ocean altimeter In-Orbit demonstrator, *IEEE Trans. Geosci. Remote Sensing*, 49, 2209–2237, doi:10.1109/TGRS.2010.2092431, 2011.
- Misra, P. and Enge, P.: *GPS: An Overview*, chap. 2, pp. 29–69, Ganga-Jamuna Press, 2011.
- Parkinson, B. W.: Introduction and Heritage of NAVSTAR, the Global Positioning System, chap. 1, pp. 3–28, American Institute of Aeronautics and AstroAmerica, Inc., 1996.

- Powers, D. M. W.: Evaluation: From Precision, Recall and F-Factor to ROC, Informedness, Markedness & Correlation, Tech. Rep. SIE-07-001, School of Informatics and Engineering, 2007.
- Pröller, G. W.: Physik des erdnahen Weltraums, Springer-Verlag, 2004.
- Requier-Desjardins, M.: Impacts des changements climatiques sur l'agriculture au Maroc et en Tunisie et priorités d'adaptation, Tech. Rep. 56, CIHEAM, IAM Montpellier, 2010.
- Rius, A., Aparicio, J. M., Cardellach, E., Martín-Neira, M., and Chapron, B.: Sea surface state measured using GPS reflected signals, *Geophys. Res. Lett.*, 29, 2122–2127, doi:10.1029/2002GL015524, 2002.
- Rius, A., Nogue-Correig, O., Ribo, S., Cardellach, E., Oliveras, S., Valencia, E., Park, H., Tarongi, J. M., Camps, A., van der Marel, H., van Bree, R., Altena, B., and Martín-Neira, M.: Altimetry with GNSS-R interferometry: first proof of concept experiment", *GPS Solutions*, 16, doi:10.1007/s10291-011-0225-9, 2012.
- Rothacher, M.: Estimation of station heights with GPS, in: IAG Symposium, edited by Drewes, H., Dodson, D., Fortes, L., Sanchez, L., and Sandoval, P., vol. 124, pp. 81–89, Springer, 2001.
- Roussel, N., Frappart, F., Ramillien, G., J., D., Desjardins, C., Gegout, P., Perosanz, F., and Biancale, R.: Simulations of direct and reflected wave trajectories for ground-based GNSS-R experiments, *Geoscientific Model Development*, 7, 2261–2279, doi:10.5194/gmd-7-2261-2014, 2014.
- Ruffini, G., Soulat, F., Caparrini, M., Germain, O., and Martín-Neira, M.: The Eddy Experiment: Accurate GNSS-R ocean altimetry from low altitude aircraft, *Geophys. Res. Lett.*, 31, L12306, 1–4, doi:10.1029/2004GL019994, 2004.
- Schmid, R., Rothacher, M., Thaller, D., and Steigenberger, P.: Absolute phase centre correction of Satellite and receiver antennas: Impact on global GPS solutions and estimation of azimuthal phase centre variations of the satellite antenna, *GPS Solutions*, 9, 283–293, doi:10.1007/s10291-005-0134-x, 2005.
- Schön, S. and Kersten, T.: On adequate Comparison of Antenna Phase Center Variations, in: American Geophysical Union Fall Meeting 2013, URL http://www.academia.edu/5512179/On_adequate_Comparisons_of_Antenna_Phase_Center_Variations, poster, 2013.
- Semmling, A. M., Beyerle, G., Stosius, R., Dick, G., Wickert, J., Fabra, F., Cardellach, E., Ribo, S., Rius, A., Helm, A., Yudanov, S., and d'Addio, S.: Detection of Arctic ocean tides using interferometric GNSS-R signals, *Geophys. Res. Lett.*, 38, 1–4, doi:10.1029/2010GL046005, 2011.
- Semmling, M.: Altimetric Monitoring of Disko Bay using Interferometric GNSS observations on L1 and L2, Ph.D. thesis, Technical University Berlin, Germany, 2012.

- Semmling, M., Schön, S., Beckheinrich, J., Beyerle, G., Ge, M., and Wickert, J.: Carrier phase altimetry using Zeppelin based GNSS-R observations and water gauge reference data, in: European Geosciences Union (EGU), 2014.
- Smyrnaio, M., Schön, S., and Nicolas, M. L.: Multipath Propagation, Characterization and Modeling in GNSS, *Geodetic Sciences - Observations, Modeling and Applications*, chap. 5, pp. 1–40, InTech, doi:10.5772/54567, URL <http://www.intechopen.com/books/geodetic-sciences-observations-modeling-and-applications/multipath-propagation-characterization-and-modeling-in-gnss>, 2013.
- Son, T. P. H. and Tung, N. T.: *Environmental Change and Agricultural Sustainability in the Mekong Delta*, Springer, doi:10.1007/978-94-007-0934-8, 2011.
- Soulat, F., Caparrini, M., Germain, O., Lopez-Dekker, P., Taani, M., and Ruffini, G.: Sea state monitoring using coastal GNSS-R, *Geophys. Res. Letters*, 31, doi:10.1029/2004GL020680, I21303, 2004.
- Spilker Jr., J. J.: *Global Positioning System: Theory and Applications: Overview of GPS Operation and Design*, vol. 1, chap. 3, pp. 57–119, American Institute of Aeronautics and AstroAmerica, Inc., 1996a.
- Spilker Jr., J. J.: *GPS Navigation Data*, chap. 4, pp. 121–176, American Institute of Aeronautics and AstroAmerica, Inc., 1996b.
- Spilker Jr., J. J.: *Overview of GPS Operation and Design*, chap. 2, pp. 29–55, American Institute of Aeronautics and AstroAmerica, Inc., 1996c.
- Spilker Jr., J. J.: *Global Positioning System: Theory and Applications Volume I*, vol. 163, chap. 13: Tropospheric Effects on GPS, pp. 517–546, American Institute of Aeronautics and AstroAmerica, Inc., 1996d.
- Teunissen, P. J. G.: *Differential GPS: Concepts and Quality Control*, invited Lecture for the Netherlands Institut of Navigation (NIN), 1991.
- Teunissen, P. J. G.: *Least-Squares Estimation of the Integer GPS ambiguities*, in: LGR Series, Delft University, vol. 6, pp. 59–74, Delft Geodetic Computing Centre, 1994.
- Teunissen, P. J. G.: *On the Integer Normal Distribution of the GPS Ambiguities*, *Artificial Satellites*, 33, 47–62, 1998.
- Teunissen, P. J. G. and Kleusberg, A.: *GPS for Geodesy*, Springer, Berlin, 1998.
- Teunissen, P. J. G., Joosten, P., and Odijk, D.: *The Reliability of GPS Ambiguity Resolution*, *GPS Solut*, 2, 63–69, 1999.
- Treuhaft, R. N., Lowe, S. T., Zuffada, C., and Chao, Y.: 2-cm GPS altimetry over Crater Lake, *Geophys. Res. Lett.*, 28(23), 4343–4346, doi:10.1029/2001GL013815, 2001.

- Tsui, J. B.: *Fundamentals of Global Positioning System Receiver: A software Approach*, Wiley, New York, 2nd edn., 2005.
- Urquhart, L., Nievinski, F. G., and Santos, M. C.: Assessment of tropospheric mapping functions using three-dimensional ray tracing, *GPS Solutions*, 18, 345–354, doi:10.1007/s10291-013-0334-8, 2013.
- Van Dierendonck, A. J., Fenton, P., and Ford, T.: Theory and Performance of Narrow Correlator Spacing in a GPS Receiver, *Navigation: Journal of the Institute of Navigation*, 39, 265–283, 1992.
- Ward, P. W., Betz, J. W., and Hegarty, C. J.: *Understanding GPS: Principles and Applications*, chap. 5: Satellite Signal Acquisition, Tracking, and Data Demodulation, pp. 153–241, Artech House, Inc., 2nd edn., 2006.
- Wassmann, R., Hien, N. X., Hoanh, C. T., and Tuon, T. P.: Sea Level rise affecting the Vietnamese Mekong Delta: Water elevation in the flood season and implications for rice production, *Climatic Change*, 66, 89–107, 2004.
- Wübbena, G., Menge, F., Schmitz, M., Seeber, G., and Völksen, C.: A New Approach for Field Calibration of Absolute Antenna Phase Center Variations, *Proceedings of the International Technical Meeting, ION GPS-96*, Kansas City, Missouri, pp. 1205–1214, URL <http://www.geopp.com/pdf/ion96.pdf>, 1996.
- Wübbena, G., Schmitz, M., and Bachmann, M.: Zur Absoluten Kalibrierung von Referenzstationen: Grundlagen, Anwendungen und das Hannoversche Verfahren, URL http://www.gib.uni-bonn.de/forschung/gnss/antennen-workshops/2002AWS/aws02_v12.pdf, 2002.
- Weill, L. R.: Differences between Signal acquisition and Tracking, URL <http://www.insidegnss.com/node/2432>, 2011.
- Wickert, J., Michalak, G., Schmidt, T., G., B., Cheng, C., Healy, S., Huang, C., Jakowski, N., Köhler, W., Mayer, C., Offiler, D., Ozawa, E., Pavelyev, A., Rothacher, M., Tapley, B., and Arras, C.: GPS Radio Occultation: Results from CHAMP, GRACE and FORMOSAT-3/COSMIC, *Terr. Atmos. Oceanic Sci.*, 20, 35–50, 2009.
- Wickert, J., Egido, A., Elgered, G., Fuller, S., Gauss, M., Jongman, R., Martin-Puig, C., and Monks, P.: Novel GNSS applications for GEE0 and GEOSS, *Tech. rep.*, Public Report of the GfG2 project, European Union, FP7-ENV-2010 GA No. 265098, 2012.
- Wu, J. T., Wu, S. C., Hajj, G. A., Bertiger, W. I., and Lichten, S. M.: Effects of antenna orientation on GPS carrier phase, *manuscripta geodaetica*, 18, 91–98, 1993.
- Xu, G.: *GPS Theory, Algorithms and Applications*, Springer, Berlin, 2nd edn., 2007.
- Zavorotny, V. U., Larson, K. M. and Braun, J. J., Small, E. E., Gutmann, E. D., and Bilich, A. L.: A physical model for GPS multipath caused by land reflections: Toward bare soil moisture retrievals, *IEEE J. Sel. Topics Appl. Earth Observ.*, 3, 100–110, doi:10.1109/JSTARS.2009.2033608, 2010.

Zhang, Z.: Parameter Estimation Techniques: A Tutorial with Application to Conic Fitting, Image and Vision Computing, 15, 59–76, 1997.

Zus, F., Bender, M., Deng, Z., Dick, G., Heise, S., Shang-Guan, M., and Wickert, J.: A methodology to compute GPS slant total delays in a numerical weather model, Radio Sci., 47, 1–15, doi:10.1029/2011RS004853, URL <http://onlinelibrary.wiley.com/doi/10.1029/2011RS004853/pdf>, 2012.